GAS-SURFACE INTERACTIONS WITH SP^2 CARBON IN EXTREME ENVIRONMENTS

by

Vanessa Jean Murray

A dissertation submitted in partial fulfillment
of the requirements for the degree

of

Doctor of Philosophy

in

Chemistry

MONTANA STATE UNIVERSITY
Bozeman, Montana

April 2018

© COPYRIGHT

by

Vanessa Jean Murray

2018

All Rights Reserved

DEDICATION

I dedicate this work to my mother, Ute Jantz. She has instilled in me the necessary work ethic to make anything possible. Without her, I would not have come this far.

ACKNOWLEDGEMENTS

There have been many people that have helped make this dissertation possible. First, I would like to thank Professor Timothy K Minton. Without his considered advice, this work would not have been possible. His guidance has allowed me to develop into an independence scientist. Additionally, he has presented me with numerous opportunities for growth and professional development that have prepared me well for life after graduate school. I would also like to thank my group members for their help with data collection and analysis. Chenbiao Xu was a pillar of support; without him, I would not have been able to complete my final series of experiments. Eric J. Smoll Jr. has been an invaluable team member who has greatly facilitated data analysis and constantly challenged me to think deeper and more critically about science. Brooks C. Marshall aided with numerous experiments and helped me develop the mechanical skills necessary to keep the Big Machine operational. I am indebted to Bill Hostler for his efforts involved in fixing what was thought to be unfixable. Last, but not least, I would like to thank Nichole Wolf for keeping me sane and well caffeinated throughout this entire journey.

To my friends who have stood by me even though I had secluded myself in the lab: thank you for always being there and providing kind advice or a shoulder to lean on. To Amanda Knick, Heather Ireland, and Dr. Melissa McIntyre I express my sincerest gratitude for reminding me what is important in life. To Dr. Nicole Schonenbach, thank you for providing motivation when mine had waned. To my family, thank you for understanding and supporting my drive to pursue higher education. And while it may seem silly, thank you to my cat Leela for being a constant source of joy and love.

Finally, I am grateful for financial support from the Department of Defense (DoD) through the National Defense Science & Engineering Graduate Fellowship (NDSEG) Program.

TABLE OF CONTENTS

1. INTRODUCTION 1

1.1 Atmospheric Entry of Hypersonic Vehicles 3
1.2 Gas-Surface Interactions for the Analysis of Tenuous Atmospheres 6
1.3 Synopsis of Molecular Beam Scattering Experiments 11

2. BASICS OF MOLECULAR BEAM-SURFACE SCATTERING 13

2.1 Nonreactive Scattering 15
2.1A Impulsive scattering 15
2.1B Thermal Desorption and Detailed Balance 19
2.1C Nonactivated Adsorption/Desorption 21
2.1D Activated Adsorption/Desorption 24
2.1E Thermal Desorption at High Temperature 26
2.1F Thermal Desorption Following a Residence Time on the Surface 26
2.2 Reactive Scattering 28
2.2A Eley-Rideal Reactions 28
2.2B Hot Atom Reactions 29
2.2C Langmuir-Hinshelwood Reactions 29

3. INELASTIC AND REACTIVE SCATTERING
DYNAMICS OF HYPERTHERMAL O AND O_2
ON HOT VITREOUS CARBON SURFACES 31

Contribution of Authors and Co-Authors 31
Manuscript Information Page 32
Abstract 33
3.1 Introduction 34
3.2 Experimental Methods 41
3.2A Temperature Dependence of Surface Reactivity 45

TABLE OF CONTENTS CONTINUED

3.2B Investigation of Surface Thermal Roughening 46
3.2C O/O_2 Beam-Surface Interactions 47
3.3 Results and Analysis 48
3.3A Reactivity as a Function of Surface Temperature 49
3.3B Inelastic Scattering of Ar 53
3.3C Inelastic and Reactive Scattering Dynamics during O/O_2 Bombardment 56
3.4 Discussion 67
3.5 Conclusion 79
Acknowledgments 80

4. DYNAMICS OF GRAPHITE OXIDATION
AT HIGH TEMPERATURE 81

Contribution of Authors and Co-Authors 81
Manuscript Information Page 82
Abstract 83
4.1 Introduction 84
4.2 Experimental Methods 89
4.2A Experimental Design 89
4.2B Temperature Dependence of the
Non-Reactive and Reactive Product Signals 91
4.2C Temperature-Dependent Hysteresis in the Surface Reactivity 92
4.2D Dynamical Behavior of Scattered or Desorbed Products 93
4.3 Results and Analysis 94
4.3A Gas-Surface Interaction Mechanisms and their Scattering Signatures 94
4.3B Temperature Dependence of Non-Reactive and Reactive Products 95
4.3C Time-Dependence of the Surface Reactivity 97
4.3D Scattering Dynamics of O atoms 99
4.3E Scattering Dynamics of O_2 106
4.3F Scattering Dynamics of CO 107

TABLE OF CONTENTS CONTINUED

4.3G Scattering Dynamics of CO_2 114
4.4 Discussion 116
4.4A Impulsive Scattering of O and O_2 117
4.4B Thermal Desorption of O Atoms 119
4.4C Effect of O-Atom Desorption on the LH CO and CO_2 Reactions 124
4.4D ER/HA Reaction Mechanisms for CO and CO_2 125
4.5 Conclusion 128
Acknowledgements 130

5. GAS-SURFACE SCATTERING DYNAMICS APPLIED TO CONCENTRATION OF GASES FOR MASS SPECTROMETRY IN TENUOUS ATMOSPHERES 131

Contribution of Authors and Co-Authors 131
Manuscript Information Page 132
Abstract 133
5.1 Introduction 134
5.2 Methods 141
5.2A Experimental Methods 141
5.2B Computational Methods 148
5.3 Results 156
5.3A Experimental Results 156
5.3B Computational Results 168
5.4 Discussion 176
5.5 Conclusions 189
Acknowledgements 190

6. SCATTERING DYNAMICS OF N_2 FROM HIGHLY ORIENTED PYROLYTIC GRAPHITE 192

TABLE OF CONTENTS CONTINUED

Contribution of Authors and Co-Authors....192
Manuscript Information Page....193
Abstract....194
6.1 Introduction....195
6.2 Experimental Methods....200
6.3 Results....202
6.4 Discussion....209
6.5 Conclusion....212
Acknowledgments....213

7. SCATTERING DYNAMICS OF NITROMETHANE AND METHYL FORMATE FROM HOPG....214

Contribution of Authors and Co-Authors....215
Manuscript Information Page....216
Abstract....217
7.1 Introduction....219
7.2 Experimental Methods....221
7.3 Results and Analysis....221
7.3A Scattering Dynamics of the Total Flux....223
7.3B Scattering Dynamics of the Total Flux....228
7.3C Separation of IS and QT Components....235
7.4 Discussion....235
7.5 Conclusions....242
Acknowledgements....243

8. CONCLUDING REMARKS....244

APPENDIX....250
REFERENCES CITED....256

LIST OF TABLES

Table Page

4.1 Selected fitting parameters for $\beta(E_T, \theta_f)$, and $S(E_T, \theta_f)$ 104

5.1 Experimental conditions for Au, SiO_2, and HOPG 143

5.2 SPARCS scattering parameters 170

5.3 C_a and percentage of primary impacts at 0° angle of attack 173

6.1 Characteristics of the angular distributions for N_2 scattering from HOPG 209

LIST OF FIGURES

Figure Page

1.1. Schematic diagram of the processes occurring during hypersonic flight....3

1.2 Schematic of the gas concentration inlet....7

1.3 Gas-surface scattering from a flat and corrugated potential energy surface....9

2.1 Example time-of-fight (TOF) distribution....14

2.2 Simplified schematic of the molecular beam-surface scattering experiments....14

2.3 Example one-dimensional potential energy surface with no barrier to adsorption....16

2.4 Conceptual representation of scattering in the thermal regime and structure regime....16

2.5 The final energy of the scattered atoms, E_f, normalized by the incidence energy, E_i, the thermal and structure regime....18

2.6 An example angular distribution for atoms scattering via the IS channel....18

2.7 Example angular distributions for atoms exiting the surface via the thermal desorption channel....20

2.8 Translational energy distribution for products desorbing from the surface after absorbing via a nonactivated process....21

2.9 The $\beta(E_T, \theta_i)$ for K sticking on a W(110) surface....23

LIST OF FIGURES CONTINUED

Figure Page

2.10 The effective temperature of Ar scattering from a hydrogen covered tungsten surface....23

2.11 Example one-dimensional potential energy surface with a barrier to adsorption....25

2.12 Translational energy distribution for products desorbing from the surface over a barrier....25

2.13 The effective temperature and flux of Ar scattering from a Pt(111) surface....27

2.14 Translational energy distribution for products with residence time, τ....27

3.1 Schematic diagram of the experimental setup and sample mount used to heat the vitreous carbon....42

3.2 Translational energy distributions of the energy-selected O/O_2 and Ar incident beams....44

3.3 TOF distributions, collected with surface temperatures from 600 to 2100 K, for O, O_2, CO and CO_2 scattering from the vitreous carbon surface....49

3.4 Integrated flux of O, O_2, CO, and CO_2 products as a function of vitreous carbon surface temperature....51

3.5 Dependence of scattered flux on time for CO, O, and O_2 after a sudden increase in the vitreous carbon surface temperature from 800 - 1875 K....52

3.6 TOF distributions for Ar scattering from vitreous carbon surface....54

LIST OF FIGURES CONTINUED

Figure Page

3.7 Representative TOF and angular distributions for Ar atoms scattering from a vitreous carbon surface....55

3.8 Representative TOF, translational energy, and flux-integrated angular distributions for O atoms scattering from a vitreous carbon surface....57

3.9 Representative TOF, translational energy, and flux-integrated angular distributions for O_2 scattering from a vitreous carbon surface at 800 - 1875 K....60

3.10 Average fractional energy transfer as a function of deflection angle, χ, for IS O atoms or O_2 on a vitreous carbon surface....63

3.11 Representative TOF and angular distributions for CO molecules scattering from vitreous carbon....64

3.12 Representative TOF distribution for CO_2 molecules scattering from a vitreous carbon surface at 800 K....67

3.13 Representative TOF and angular distributions for CO_2 scattering from a vitreous carbon surface....68

4.1 TOF distributions for scattered O, O_2, CO, and CO_2, scattering from the HOPG with surface temperatures from 1200 - 2300 K....96

4.2 Temperature dependent flux of O, CO, and CO_2 exiting the HOPG surface with surface temperatures from 1200 - 2300 K....97

4.3 Time dependence of the scattered CO flux after the HOPG temperature was increased suddenly from 1300 K - 1800 K....98

LIST OF FIGURES CONTINUED

Figure Page

4.4 Representative TOF distributions for O atoms exiting the HOPG surface for temperatures of 1100, 1300, and 1900 K....99

4.5 The calculated mean final translational energies TD O atoms as a function of θ_f....104

4.6 Angular distributions for IS and TD) O atoms, for surface temperatures of 1100, 1300, and 1900 K....105

4.7 Angular distributions of scattered O_2 molecules from the HOPG surface....107

4.8 Angular distributions for CO molecules exiting the HOPG surface....108

4.9 Representative TOF distributions for CO molecules exiting the HOPG surface....110

4.10 The calculated mean total final translational energies, of the desorbing CO as a function of θ_f....111

4.11 Energy dependent desorption functions, $S(E_T, \theta_f)$, for CO produced by thermal reaction mechanisms at surface temperatures of 1100 and 1300 K....113

4.12 Total flux angular distributions and angular dependence of the average total final energies, for CO_2 molecules exiting an HOPG surface at 1100 and 1300 K....115

5.1 Schematic diagram of the experimental apparatus....141

5.2 AFM images for surface of pristine Au, Si(100), and HOPG....145

LIST OF FIGURES CONTINUED

Figure Page

5.3 Scattering models represented in SPARCS.....152

5.4 Example geometry showing particles propagating toward the exit of a cone concentrator.....154

5.5 Representative TOF distributions angular distributions for O and O_2 scattering from Au.....157

5.6 Representative TOF distributions and angular distributions for O and O_2 scattering from the oxidized silicon surface.....157

5.7 Representative TOF distributions and angular distributions for O and O_2 scattering from an HOPG surface.....158

5.8 E_f / E_i of IS O and O_2 as a function of final angle following collision with the Au surface.....162

5.9 E_f / E_i of inelastically scattered O, O_2 and Ar as a function of θ_f following collision with HOPG.....164

5.10 Representative TOF distributions and angular distributions for O and O_2 scattering from an HOPG surface for T_w = 873 K.....166

5.11 Representative TOF distributions and angular distributions for Ar scattering from the HOPG surface exposed and unexposed to O atom for T_w = 873 K.....167

5.12 Concentrator geometries utilized in the DSMC simulations.....168

LIST OF FIGURES CONTINUED

Figure Page

5.13 Beam-surface scattering data compared with modeled scattering distributions for O atoms on Au, SiO_2, and HOPG....170

5.14 Three O-atom trajectories through a 10° half-angle cone constructed from Au, SiO_2, and HOPG....172

5.15 C_a as a function of angle of attack....174

5.16 Effect of energy accommodation for an HOPG cone with a half-angle of 15° and an HOPG annular ring concentrator....175

6.1 Representative TOF distributions for the incident molecular beam and the scattered N_2....204

6.2 The ratio of $\langle E_f \rangle$ / $\langle E_i \rangle$ of the scattered N_2 molecules as function of θ_f....205

6.3 Flux angular distributions for N_2 molecules scattering from the HOPG surface....206

7.1 Schematic of the molecular beam machine....220

7.2 Representative TOF distributions for NM and the dominant mass fragment scattering from the surface....222

7.3 Angular distributions and E_f / E_i for the total scattered flux of NM and MF....225

7.4 *I(parent)* / *I(fragment)* for the molecular beam and the NM and MF molecules scattering from the surface....228

7.5 Example of the fit of the IS component with a shifted Maxwell Boltzmann (MB) distribution for a TOF distribution....230

LIST OF FIGURES CONTINUED

Figure Page

7.6 Angular distributions for the IS and QT components for NM and MF....231

7.7 Fraction of molecules scattering via the IS and QT channels for NM and MF....232

7.8 *I(parent)* / *I(fragment)* for the molecular beam, IS, and QT components of NM and MF....233

7.9 Angular dependence of E_f / E_i for the IS and QT components for NM and MF....234

7.10 Potential energy surface for NM and MF with HOPG....238

8.1 Summary of the results for the oxidation of vitreous carbon by O(^3P)....245

8.2. Summary of the results for the oxidation of HOPG by O(^3P)....246

8.3 Summary of the results presented in Chapter 6....247

8.4 Summary of the results presented in Chapters 6 and 7....248

A.1 Sphere-sphere scattering model of gas-surface collisions....251

A.2 Newton diagram for IS of hyperthermal O atoms on a squalane surface....254

ABSRACT

Molecular beam scattering experiments can determine the relative importance of reactive and non-reactive processes that occur when a surface is bombarded with high energy atoms and molecules. The mechanisms by which these processes proceed are inferred by analyzing the angle-resolved flux and energy distributions of the scattered products. The studies presented in this thesis have been conducted with a crossed molecular beams machine reconfigured for surface scattering. Two molecular beam sources were used. One uses a laser detonation process to produce high translational energy O atoms in the ground electronic state, and the other uses a supersonic expansion to produce continuous beams of N_2, nitromethane, or methyl formate. In the first two studies presented in this thesis, the oxidation of dynamics vitreous carbon and highly oriented pyrolytic graphite (HOPG) held at surface temperatures in the range of 800 – 2300 K by O atoms with a translational energy of ~ 500 kJ mol^{-1} are presented. These two studies revealed that the reactivity is suppressed at high temperature because O atoms desorb from the surface before they react to form CO and CO_2. Even though the translational energy of the O atoms was high, the surface reactions proceeded primarily through reactions that occurred in thermal equilibrium with the surface. The third study focuses on the scattering dynamics of O, O_2, and Ar with the surfaces of a gold thin-film, SiO_2, and HOPG. The results of the experiments were used to evaluate the efficacy of a proposed gas concentrator. The strong forward scattering on the HOPG surface made it the most suitable surface for the gas concentrator. The fourth study examines the non-reactive scattering dynamics of N_2 with HOPG. At high surface temperature, the residence time of N_2 is too short for the molecule to fully accommodate to the surface. Thus, even if the molecule suffers multiple collisions with the surface, it will scatter into the vacuum before it can come into thermal equilibrium with the surface. The results have been used in conjunction with theoretical calculations by a collaborator to investigate the relationship between the potential energy surface and the scattering dynamics. In order determine the usefulness of an HOPG concentrator with complex molecules, the scattering dynamics of methyl formate and nitromethane on HOPG were studied. These molecules do not shatter upon impact with the surface and they both scatter strongly in the forward direction through direct and indirect mechanisms, suggesting that the proposed HOPG concentrator should perform as desired. In all studies described in this thesis, the fundamental gas-surface scattering dynamics were elucidated from molecular beam experiments, and these fundamental results have direct links to modeling the performance of hypersonic vehicles and designing a gas concentrator for mass spectrometry in tenuous atmospheres.

CHAPTER ONE

INTRODUCTION

The investigation of gas-surface interactions that occur in extreme environments can reveal a wealth of information regarding the fundamental processes that govern the reactivity of a surface. Reaction pathways with high barriers that are not accessible at ambient conditions open when the incidence energy (50 – 1000 kJ mol^{-1}) and surface temperature (1000 – 2000 K) are high. These pathways may be unusual and have unexpected product angular and internal energy distributions which may be difficult to predict. Furthermore, competition between surface diffusion and reactions will become increasingly important as the energy of the system is increased. The study of these interactions can reveal the rich details of the chemical and physical processes occurring where a material is subjected to high collision energy and temperature. While such extreme conditions may seem exotic, there are numerous situations where the dynamics of these interactions will influence the outcome of practical endeavors, such as the case of a vehicle moving at hypersonic velocity through a gaseous medium. The data presented in this dissertation, in conjunction with computational models, lend substantial understanding to the processes that underlie these applications and provides a foundation upon which to develop new experimental tools and models.

Objects traveling through an atmosphere are subjected to continual bombardment by reactive and nonreactive gases. The inelastic interactions between the impinging species and the surface will determine the eventual fate of the gas particle. A gaseous atom or

molecule may undergo an impulsive collision with the surface and retain most its incidence energy,[1] or it may come into thermal equilibrium with the surface before desorbing.[2] In the latter mechanism, known as thermal desorption (TD), the atom or molecule transfers most of its incidence energy into the surface. This mechanism often precedes a Langmuir-Hinshelwood reaction, which also occurs in thermal equilibrium with the surface.[3] Eley-Rideal reactions, where an incoming gaseous atom or molecule abstracts an atom or other chemical moiety from the surface, can also occur.[3] The relative probabilities of impulsive and thermal mechanisms, both reactive and non-reactive, are determined by several factors, including the surface structure,[4] the potential energy surface between the incoming species and the surface,[5] and the incident energy of the incoming gas particles.[6]

The work presented in this dissertation focuses on the reactive and nonreactive gas-surface interactions for two different scenarios relevant to atmospheric entry. Experiments aimed at understanding atmospheric entry of hypersonic objects, where the incidence energy of the incoming gas is greater than 100 kJ mol^{-1} and the surface temperature is elevated (T_s > 1000 K) will be described first. For these extreme conditions, ablation of the surface is probable. The second half of this dissertation presents experiments that were used to inform the design of a gas concentrator that has been proposed to facilitate the identification of tenuous atmospheres. These experiments analyze the dynamics of atoms and molecules with low incidence energy (30 – 100 kJ mol^{-1}) scattering from candidate concentrator materials.

1.1 Atmospheric Entry of Hypersonic Vehicles

Objects travelling through a dense atmosphere at Mach 5 and higher are subjected to extreme heat fluxes originating from the thin shock wave that forms on the leading surfaces at hypersonic velocities (Figure 1.1). The temperature in the shock layer can reach 10,000 K. For hypersonic flight through Earth's atmosphere, air gases dissociate within the shock wave to form highly reactive O atoms. To survive this environment, the vehicle requires a thermal protection system (TPS) constructed of materials that can withstand high heat fluxes and surface temperatures greater than 2000 K. In addition to extreme heat fluxes, the TPS is continually bombarded with O atoms present in the shock layer which can lead to oxidation of the TPS material.

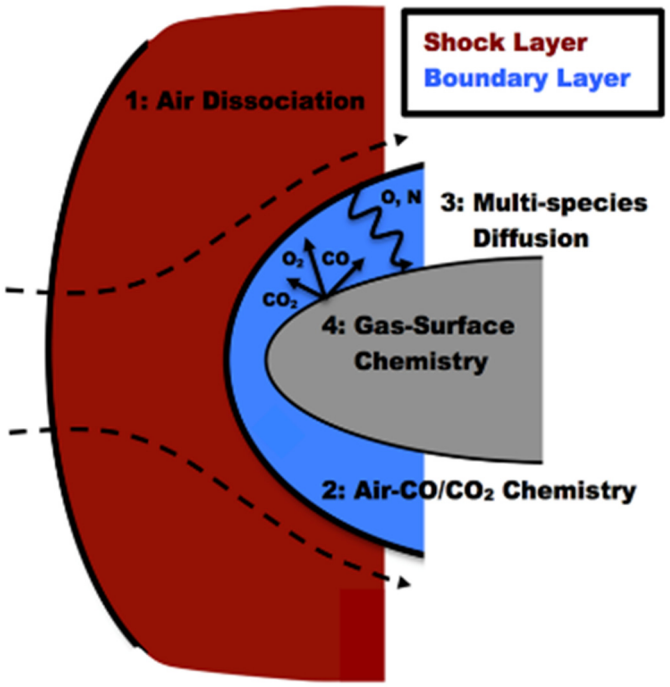


Figure 1.1. Schematic diagram of the processes occurring during hypersonic flight. Figure courtesy of Professor Tom Schwartzentruber, University of Minnesota.

Many TPS systems are constructed from carbon-carbon composites;[7] thus, the reactive products evolved from the surface following exposure to O atoms include CO and CO_2. Reactive products that do not result in a net mass loss of the surface, such as the recombination of O atoms to form O_2, can also occur.[8-9] Reactions can proceed via Eley-Rideal (ER) or Langmuir-Hinshelwood (LH) mechanisms. In the former mechanism, most of the energy evolved from the reaction is carried away by the product molecule, with a only small fraction of the reaction energy deposited into the surface.[10-11] In an LH mechanism, the reaction occurs in thermal equilibrium with the surface and the reaction energy is deposited into the surface. Thus, the mechanisms by which the gas-surface reactions proceed will affect the heat flux to the surface.[3] Furthermore, the reactive and nonreactive products can scatter back into the bound layer, where they may undergo further reactions, thus changing the chemistry in the shock layer.[12] Currently, the gas-surface reactions that occur on TPS surfaces in a hypersonic flow environment are poorly understood. A thorough understanding of the product distributions and gas-surface reaction mechanisms at surface temperatures relevant to hypersonic flight would enable more accurate modeling of the heat flux to and mass loss from the surface as well as the gas-phase chemistry occurring in the shock layer. Additionally, more accurate modeling of these parameters will allow for the improved design of TPSs.

Highly oriented pyrolytic graphite (HOPG) and vitreous carbon can serve as experimental models for the fibers and matrix, respectively, of carbon-carbon composites. Both materials are composed of sp^2 bonded carbon. HOPG is a mosaic crystal composed of layered graphene crystallites, which can be tens of microns in length, that have their *c*

axes oriented parallel to the surface normal of the overall crystal.[13] Vitreous carbon is composed of randomly oriented, graphite crystallites.[14-15] HOPG is a smooth and ordered surface that allows for the precise study of fundamental reaction processes that lead to surface ablation. Vitreous carbon, on the other hand, has a rough and disordered surface. Comparing the gas-surface interactions of O with these surfaces allows us to determine the effect of the surface structure on the chemical reactivity of the surface.

O atoms readily react with HOPG and vitreous carbon, though vitreous carbon has been shown to be more reactive than HOPG.[16-17] Oxidation of HOPG is initiated by the formation of epoxy groups on the surface.[18] At room temperature, these epoxy groups can undergo cyclic recombination to form O_2,[8] or they can migrate to semi-quinone and lactone defect sites on the surface, where they catalyze chemical reactions that form either CO and CO_2 that proceed via LH mechanisms.[19] O_2, CO, and CO_2 can also be formed by ER reactions upon bombardment of HOPG by O atoms with translational energy of 500 kJ mol^{-1}.[9,20]

Little is known about the reaction mechanisms that can occur at surface temperatures relevant to hypersonic flight. The mass loss of graphite filaments oxidized by O and O_2 with thermal energies was found to have a non-Arrhenius temperature dependence in the range of 1000 – 2000 K.[21] The rate of carbon removal was highest for a surface temperature of 1600 K. Increasing the surface temperature beyond this point resulted in a lower probability of carbon removal. A non-Arrhenius temperature dependence was also observed for the flux of CO produced when HOPG was oxidized by O_2.[22] The non-Arrhenius temperature dependence of the mass loss and CO production was

explained by invoking a two-site model for surface reactivity. This model proposed that at high temperatures, one of the reactive sites was inactivated as the result of surface annealing, thus limiting the reactivity of the surface. However, these studies only detected the total product flux or mass loss and could not determine detailed reaction mechanisms by which surface oxidation proceeded.

Molecular beam scattering experiments have been conducted in an attempt garner an understanding of the reactions mechanisms that occur between carbon surfaces (HOPG and vitreous carbon) and O atoms for conditions relevant to atmospheric entry at hypersonic velocities. A laser detonation source was used to generate a molecular beam of O atoms with a mean translational energy of ~500 kJ mol^{-1} that was directed at heated HOPG and vitreous carbon surfaces. The translational energy distributions, $P(E_T)$, of the scattered products were measured using a rotatable mass spectrometer. From these distributions, the relative flux of specific products were determined as a function of final angle, θ_f, for a given incidence angle, θ_i. The scattering dynamics of the products have been analyzed for a surface temperature range of 600 – 2000 K and reveal a complex interplay between reactive and non-reactive interactions that is mediated by the temperature of the surface. These results have been included in several computational fluid dynamics models that study ablation during atmospheric re-entry.[12,23-24]

1.2 Gas-Surface Interactions for the Analysis of Tenuous Atmospheres

Mass spectrometers carried on board atmospheric entry probes are used to study the chemical and isotopic composition of tenuous atmospheres of exoplanets in our solar system.[25-27] The number densities of low pressure atmospheric constituents range from 10^3

– 10^{10} molecules cm^{-3}. The constituents of these rarified gaseous environments are difficult to distinguish from those that outgas from the probes housing the mass spectrometer. In order to accurately identify the composition of a tenuous atmosphere, a suitable gas concentration method must be employed in order to increase the signal of the atmospheric gases. Such a method must provide sufficient signal to overcome the inherent background present in the instrument and have fast transmission times through the apparatus such that spatial distributions of the atmosphere can be determined. In addition, the device must remain inert to the neutral atoms and molecules that are sampled. To this end, a concept for a conical gas-concentration inlet coupled with a spherical accommodation chamber for a mass spectrometer has been developed.

A schematic of the gas concentration inlet geometry is shown in Figure 1.2. The gas concentrator has a large opening and a small exit that leads to the accommodation chamber, whereas the accommodation chamber has a large exit that leads to the mass spectrometer instrumentation. This geometry allows for accumulation and thermal

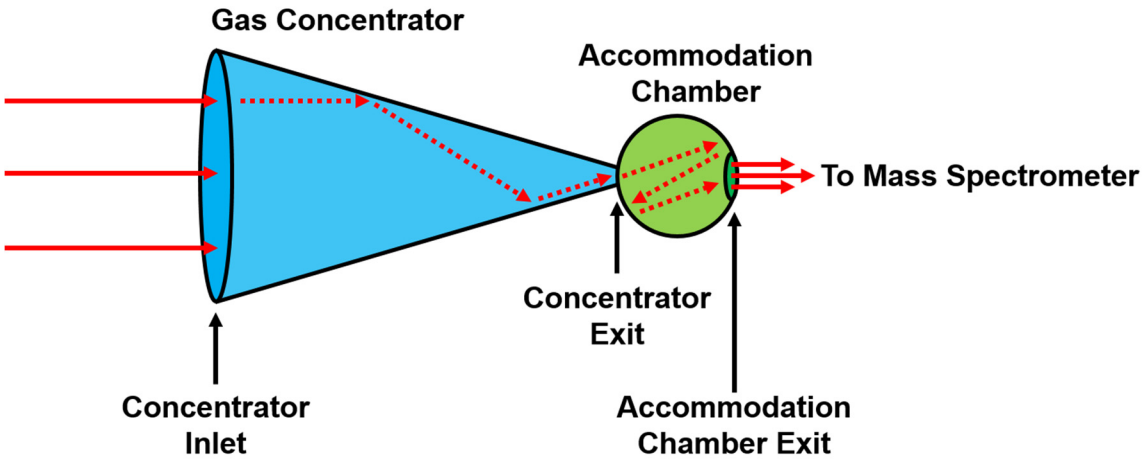


Figure 1.2. Schematic diagram of the gas concentration inlet and the accommodation chamber.

equilibration of atmospheric analytes within the accommodation chamber before the molecules exit to the mass spectrometer. This technique increases the signal-to-noise ratio for the atmospheric constituents to be studied while maintaining low transmission times.

The efficiency of the concentrator is determined by the gas-surface interactions between the incoming molecules and the concentrator surface. Impulsive collisions that focus the scattered molecules at or beyond the specular angle ($\theta_i = \theta_f$) will lead to a higher concentration factor, whereas interactions that lead to trapping desorption will diminish the flux of molecules that enter the accommodation chamber. High relative velocities between the atmospheric gases and the concentrator surface will promote impulsive scattering that will lead to well-defined, lobular angular distributions and reduce the number of molecules that trap on the surface. Molecular beam scattering experiments can investigate the outcome of the gas-surface collisions and allow for the identification of the ideal concentrator surface. Both the surface roughness and the potential energy surface between the incoming molecule and the surface will determine the outcome of the gas-surface collision.[4-5] A rough or disordered surface will promote multiple gas-surface interactions, which yield broad angular distributions for the scattered molecules. A rough surface will also promote energy transfer which can promote trapping of the incoming molecules on the surface. By contrast, molecules will scatter over a narrow angular range with little energy transfer from a smooth and well-ordered surface.

The potential energy surface between the incident atoms or molecules and the surface will also affect the width of the angular distributions of the scattered products (Figure 1.3).[6] If the potential is smooth, the incoming molecules will retain their parallel

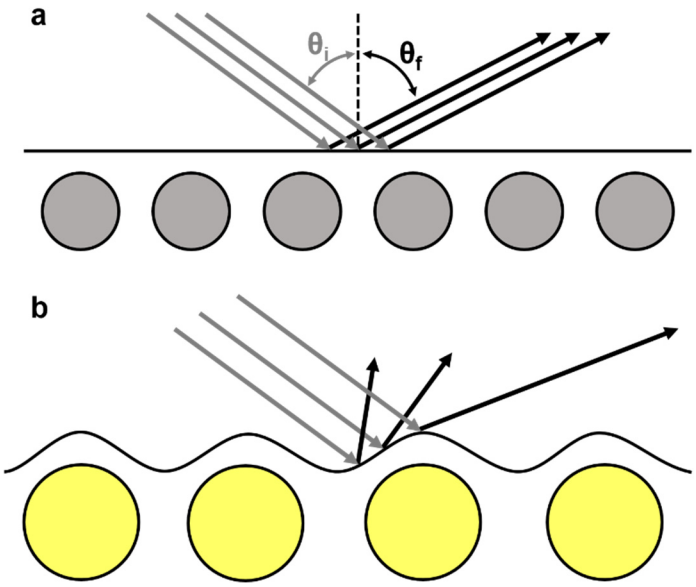


Figure 1.3. Gas-surface scattering from a) a flat potential energy surface and b) a corrugated potential energy surface.

momentum during the surface collision which will lead to well-defined, lobular angular distributions. Conversely, a corrugated potential will lead to broad angular distributions because the incident molecule has a distribution of local impact parameters that lead to a wide range of θ_f for the scattered products. Thus, the potential energy surface between the incident gas species and the surface must be carefully considered when choosing a material for the concentrator.

Using beam-surface scattering techniques, samples of gold, SiO_2, and HOPG were evaluated for their potential as concentrator surfaces. The results of the molecular beam experiments were used in Statistical Program for Aerodynamic and Radiation Pressure Coefficient Simulation (SPARCS) calculations that modeled the trajectories of atoms and molecules passing through the concentrator. The distributions of scattered O, O_2, and Ar from HOPG yielded the highest concentration factor in the simulated concentrator. Further work was conducted for the scattering of N_2 from HOPG. Comparison of molecular

dynamics simulations and experiments revealed that even if the incident molecule suffered multiple collisions with the surface, it retained enough energy to scatter from the surface in a well-defined, lobular angular distribution.

Initial studies for the concentrator focused on the scattering dynamics of atoms and diatomic molecules from the surface. However, life-signature organic molecules must also be able to be detected if the concentrator is to serve its ultimate purpose. Not only is it important that the larger organic molecules scatter in the forward direction when they collide with a concentrator surface, but it is also important that they survive the energetic gas-surface collisions without dissociating. When molecules collide with a surface, some of the incidence energy can be partitioned into internal modes of the molecule.[28-29] If the incidence energy of the molecule is sufficiently high, the energy partitioned into internal modes can cause the molecule to shatter during or after the impact.[30-32] It would be difficult to distinguish the shattering products from the atmospheric constituents in the mass spectra collected during a fly-by mission, which would complicate the identification of the atmospheric composition. The gas-surface interactions of nitromethane and methyl formate with HOPG were studied to determine if these molecules of similar mass but different chemical structure would have desirable scattering dynamics on a proposed HOPG concentrator surface when the incidence energy is ~100 kJ mol^{-1}. The experimental results indicated that the molecules do not shatter when they collide with the surface and they have scattering dynamics that are amenable to gas concentration. However, the results also show slight differences in their scattering dynamics that suggest the unique scattering dynamics of individual species must be considered when deriving relative abundances of atmospheric

constituents from a mass spectrometer equipped with a gas concentrator. Nevertheless, a concentrator constructed from HOPG is likely to be a feasible method for improving the detection efficiency of polyatomic molecules.

1.3 Synopsis of Molecular Beam Scattering Experiments

The work presented in this thesis has investigated the types of gas-surface interactions that can occur in when the relative velocity between the incident gas particle and the surface is high. Chapter 2 gives a broad overview of gas-surface scattering mechanisms. Chapters 3 and 4 focus on the reactive and non-reactive interactions that occur when high-temperature vitreous carbon and HOPG surfaces are bombarded with ~500 kJ mol^{-1} O atoms. By analyzing the scattering dynamics of both reactive and non-reactive products, the effect of the surface temperature on the surface reactivity has been ascertained. The subject of Chapter 5 is the development of a gas concentrator that will facilitate the identification of tenuous atmospheres. The preliminary design of the concentrator was guided by experiments that investigated the interactions of O, O_2 and Ar with gold thin film, SiO_2, and HOPG surfaces. The experimental work presented in Chapter 6 investigates the inelastic scattering of N_2 from an HOPG surface. The experimental results are briefly compared to molecular dynamics simulations that were conducted by our collaborators at the University of Illinois, Urbana-Champaign. While the experimental results indicate that N_2 scatters from the surface after a single, impulsive collision, the calculated trajectories show that a large fraction of the molecules suffer multiple collisions before recoiling from the surface. This mechanism has been referred to as quasitrapping and is relevant for the scattering of polyatomic molecules, namely methyl formate and

nitromethane, from HOPG, which is the subject of Chapter 6. Chapter 8 summarizes the conclusions drawn in Chapters 3 – 7.

CHAPTER TWO

BASICS OF MOLECULAR BEAM-SURFACE SCATTERING

Experiments analyzing the kinetics of carbon oxidation provide information on the overall reaction rate of CO and CO_2 formation and mass loss.[21-22,33] However, these experiments do not reveal *how* the surface reactions proceed. Molecular beam-surface scattering experiments can determine the atomic level details of gas-surface interactions.[34] The flux and energy distributions of the scattered atoms and molecules can also provide qualitative information about the potential energy surface which governs the fate of a molecule that collides with the surface. By studying the outcome of gas-surface interactions, we can develop an atomistic understanding of the mechanisms by which reactive and nonreactive processes proceed.

In the experiments described in this thesis, the number density of the scattered products is measured as a function of flight time, $N(t)$. These plots are commonly referred to as time-of-flight (TOF) distributions, an example of which is shown in Figure 2.1. The TOF distributions are collected for specific final angles, θ_f, corresponding to an incidence angle, θ_i. A schematic of the experimental set up is shown in Figure 2.2. The flux of the scattered products is determined from the TOF distributions by integrating $N(t)/t$. A plot of the scattered flux as a function of θ_f is referred to as an angular distribution. The average energy of the scattered products is determined from translational energy distributions, $P(E_T)$, which are proportional to flux and derived from the TOF distributions by using a simple density-to-flux conversion[35-36]

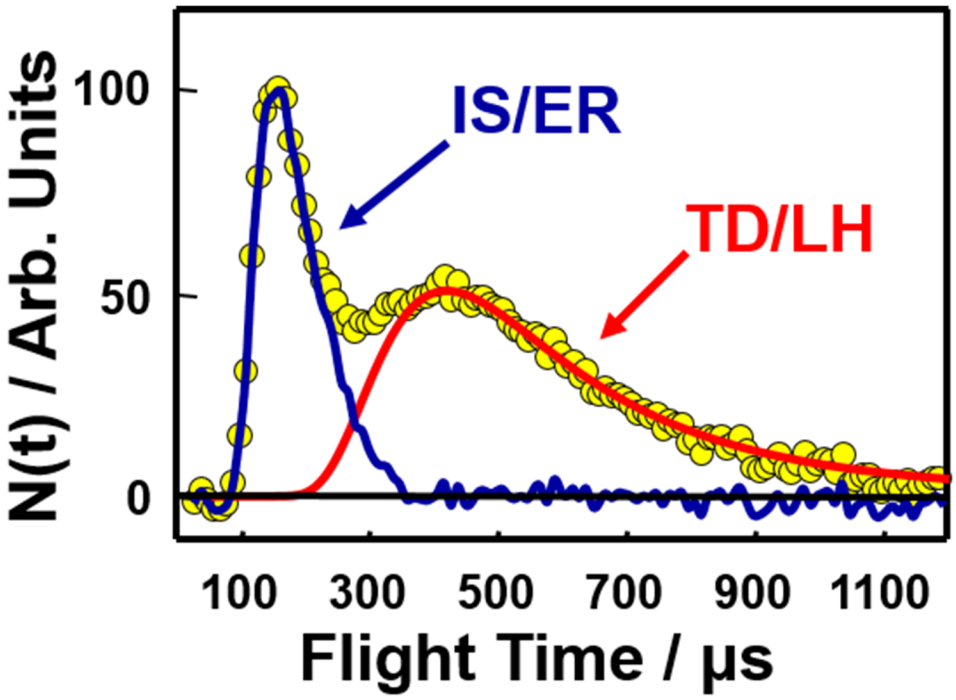


Figure 2.1. Example time-of-fight (TOF) distribution. The yellow symbols represent the total signal, *N(t)*. The blue line represents the impulsive scattering (IS) or Eley-Rideal (ER) signal. The red line represents the thermal desorption (TD) or Langmuir-Hinshelwood (LH) signal.

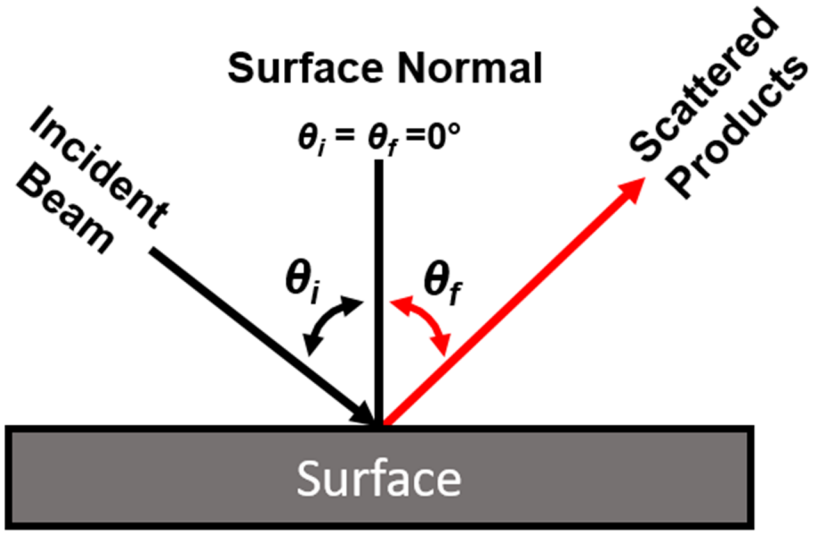


Figure 2.2. Simplified schematic of the molecular beam-surface scattering experiments showing the orientation of the incidence angle, θ_i, of the molecular beam and the final angle, θ_f, of the scattered products.

$$P(E_T) \propto t^2 N(t) \tag{2.1}$$

The translational energy, E_T, is given by

$$E_T = \frac{1}{2} m \left(\frac{d}{t}\right)^2 \tag{2.2}$$

where m is the mass of the detected product and d is the distance from the surface to the detector. By scrutinizing the shapes of the TOF distributions, angular distributions, and the $P(E_T)$ distributions, the dynamics of the scattered products can be determined. The remainder of this chapter will give a brief introduction to the unique experimental features of the gas-surface scattering mechanisms that are relevant to this thesis.

2.1 Nonreactive Scattering

2.1A Impulsive scattering

Atoms and molecules that scatter from the surface after one or a few collisions without reacting are said to undergo impulsive scattering (IS). The molecules have sufficient incidence energy, E_i, that they scatter from the repulsive wall of the potential energy surface without becoming trapped in the potential well (Figure 2.3, blue curve). The IS products retain most of their E_i and appear at short flight times in the TOF distribution (Figure 2.1, blue line).

The angular dependence of the final energy, E_f, for molecules that scatter via the IS channel can be divided into the thermal and structural scattering regimes.[6] When the E_i of the incident molecule is low, the turning point of the collision for the molecule is far from the surface and the molecule experiences a smooth potential energy surface (Figure 2.4,

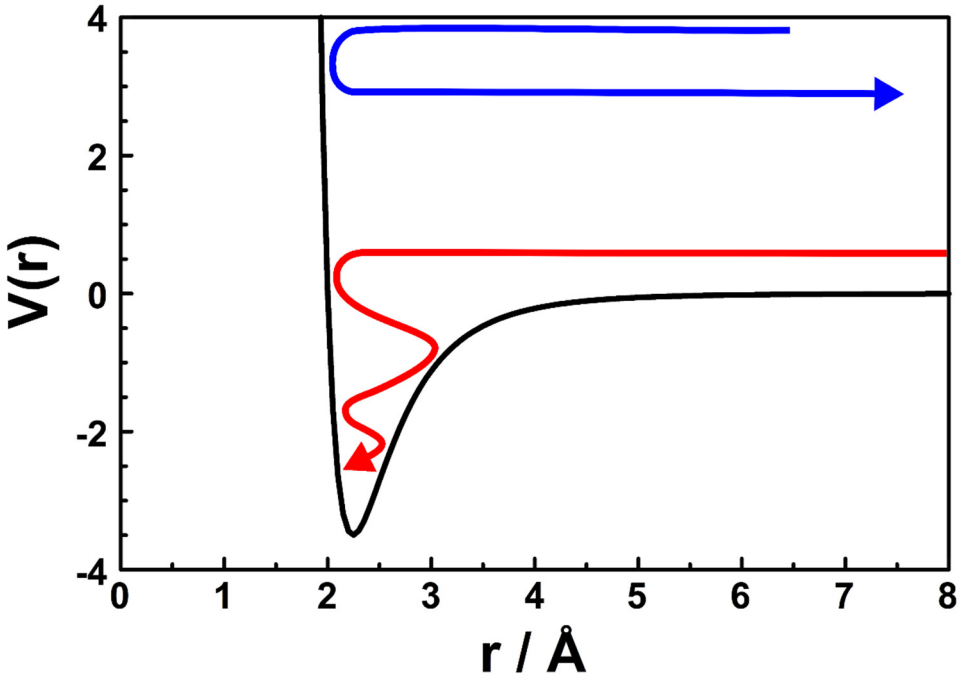


Figure 2.3. Schematic representation of a one-dimensional potential energy surface with no barrier to adsorption; r is the distance between the molecule and the surface. The position of the surface is defined as r = 0 Å. The blue line represents molecules that scatter via an IS mechanism. The red line represents molecules that stick to the surface before exiting the surface via a TD mechanism.

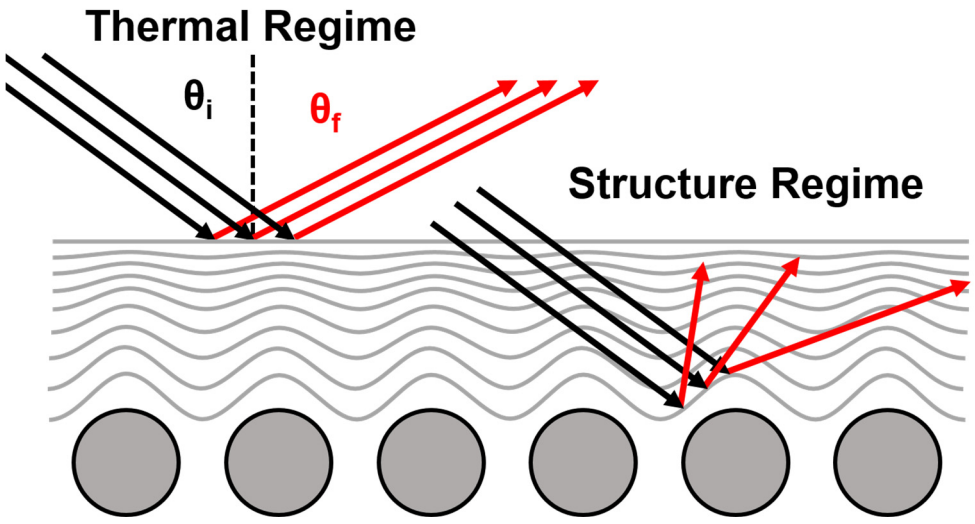


Figure 2.4. Schematic representation of scattering in the thermal and structural scattering regime. The gray circles represent the ion cores of the surface atoms. The grey lines represent the surface potential as a function of distance from the ion cores.

left side). The parallel momentum of the molecule is conserved during the collision because there are no in-plane forces acting on the incoming molecule during the collision. The angular dependence of E_f follows the trend (Figure 2.5, black line)

$$\frac{E_f}{E_i} = \frac{\sin^2(\theta_i)}{\sin^2(\theta_f)}. \tag{2.3}$$

As E_i is increased, the molecule can penetrate deeper into the potential and sample the corrugation of the individual ion cores of the surface (Figure 2.4, right side). The parallel momentum of the molecule is no longer conserved during the collision, and the E_f will increase with θ_f (Figure 2.5, blue symbols). Several models have been developed to model the energy transfer for scattering in the structural regime,[37] including the soft sphere model described in the Appendix and employed in Chapter 3.[38]

The angular distributions for IS molecules are lobular, with a maximum flux at θ_f away from the surface normal (Figure 2.6). The IS angular distributions are asymmetric about the surface normal ($\theta_f = 0°$). As E_i is increased, the width of the angular distributions will grow broader as the molecule samples more of the surface corrugation. Additionally, the angular distributions will grow broader as the surface roughness of the sample increases. The angular distributions shift past the specular angle ($\theta_i = \theta_f$) as the molecule loses more normal energy, E_n, to the surface. As the surface temperature increases, the angular distributions grow broader as the thermal vibrations of the surface cause more of the molecules to scatter toward the surface normal.[1]

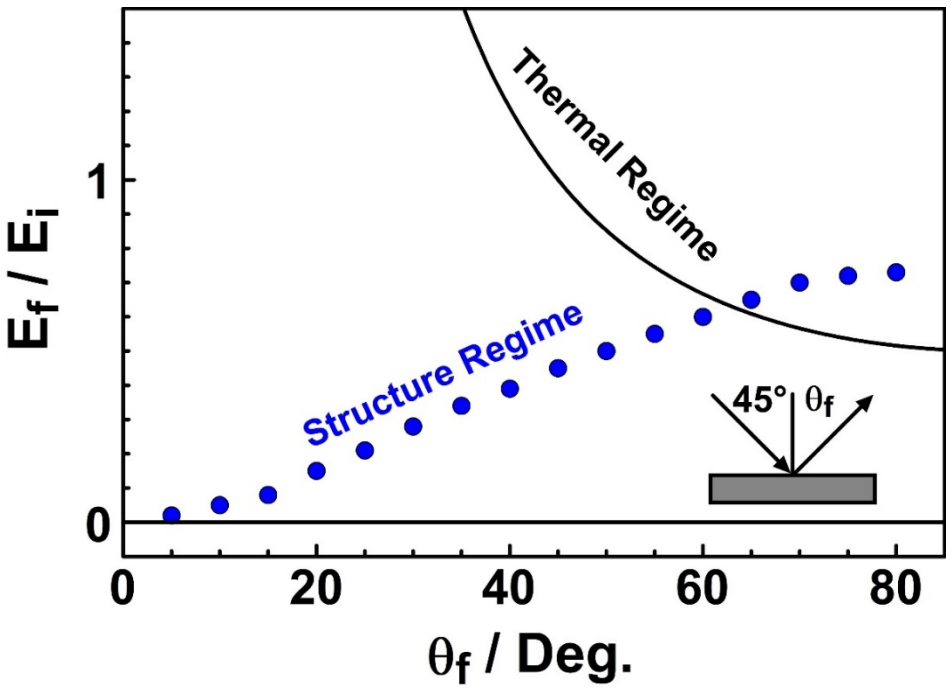


Figure 2.5. The final energy of the scattered molecules, E_f, normalized by the incidence energy, E_i, for molecules with θ_i = 45°. The black line represents E_f / E_i typical of scattering in the thermal regime (from eq 2.3). The blue symbols represent E_f / E_i characteristic of scattering in the structural regime.

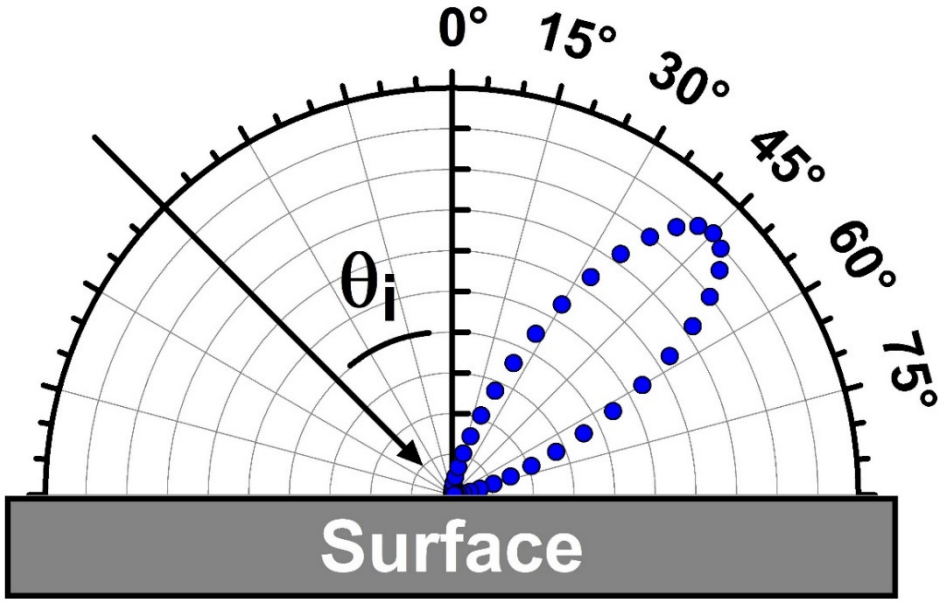


Figure 2.6. An example angular distribution for molecules scattering via the IS channel.

2.1B Thermal Desorption and Detailed Balance

If the incident molecule transfers a substantial amount of energy during the collision, it can "stick" or "trap" in the well of the potential energy surface (Figure 2.3, red curve). If the surface temperature is high enough, the particle can desorb into the vacuum.[2] This scattering mechanism is referred to as thermal desorption (TD). The TD molecules have low translational energies and appear as a broad feature in the TOF distributions (Figure 2.1, red curve). If there is no dependence of the sticking probability on E_i or θ_i, the $P(E_T)$ distribution can be described by a Maxwell Boltzmann distribution of energies (eq 2.4) characterized by the surface temperature, T_s, and the angular distribution of the scattered flux can be described by a $\cos(\theta_f)$ distribution that is symmetric about the surface normal (Figure 2.7, blue curve).

$$P(E_T)_{TD} = E_T \exp\left(-\frac{E_T}{2RT_s}\right) \tag{2.4}$$

These observations, referred to as Knudsen's Cosine Law, can be explained using the principle of detailed balance which states that at equilibrium, the flux of particles with velocity v_i incident on the surface is matched by an equal, but opposite, flux leaving the surface with $v_f = v_i$. The flux of molecules on the surface is proportional to the perpendicular *velocity* of the incoming particle:

$$I_i = v_i \cos(\theta_i) \tag{2.5}$$

By the principle of detailed balance, the flux of the desorbing particles, which is equal but opposite to the incoming particles, must also be proportional to $\cos(\theta_f)$ and $v_f = v_i$.

Knudsen's Cosine Law applies when the sticking probability of the molecules on the surface, $D(E_T, \theta_i)$, does not depend on E_i or θ_i. However, in most systems, $D(E_T, \theta_i)$

depends on the incident conditions of the incoming particles. Thus, the flux of particles that adsorb to (or desorb from) the surface is a product of the incident (or desorbing) flux, which is described by a Maxwell-Boltzmann distribution of energies in eq 2.4 (Figure 2.8, dashed green curve), and the energy- and angle- dependent sticking probability, $D(E_T, \theta_i)$[39-40]

$$P(E_T, \theta_f) dE_T d\theta_f = E_T \exp\left(-\frac{E_T}{RT_s}\right) D(E_T, \theta_i) dE_T d\theta_i \qquad (2.6)$$

where E_T is the translational energy (eq 2.2). $D(E_T, \theta_i)$ is determined by varying the E_i or θ_i and measuring the fraction of molecules that stick to the surface. This curve can be used to predict the $P(E_T)$ distribution for the desorbing molecules using eq 2.6 as is shown in Figure

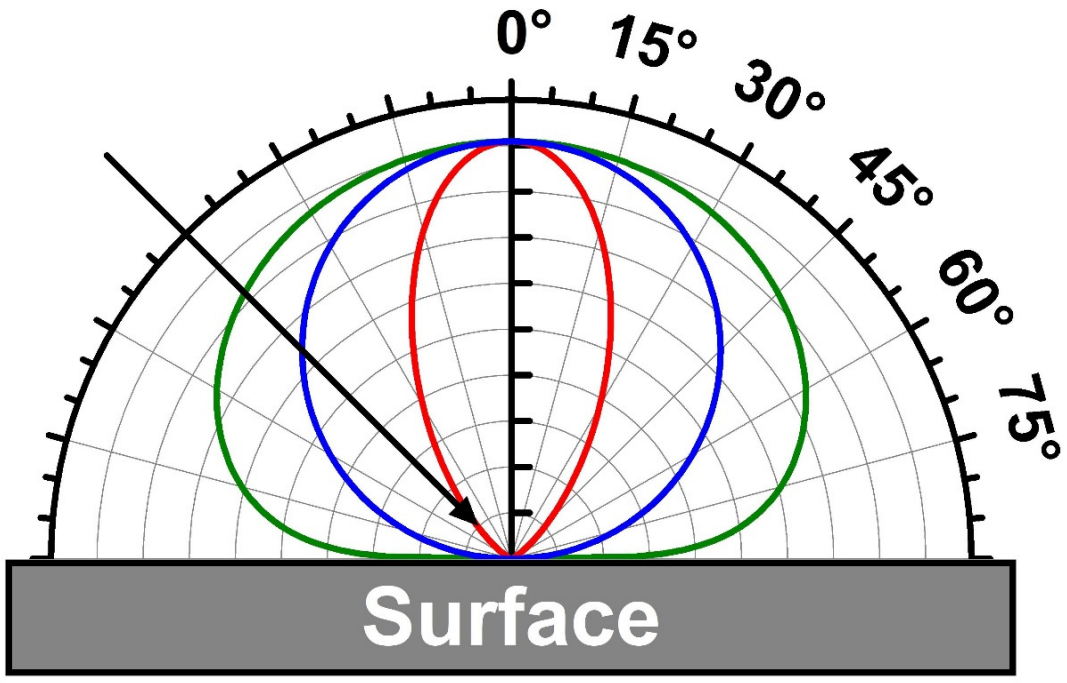


Figure 2.7. Representative angular distributions for molecules exiting the surface via the thermal desorption channel. The blue line represents the angular distribution when the sticking probability does not depend on E_i or θ_i. The green line represents an angular distribution when the sticking probability follows the trend described by $\beta(E_T, \theta_i)$. The red line represents an angular distribution when the sticking probability follows the trend described by $S(E_T, \theta_i)$.

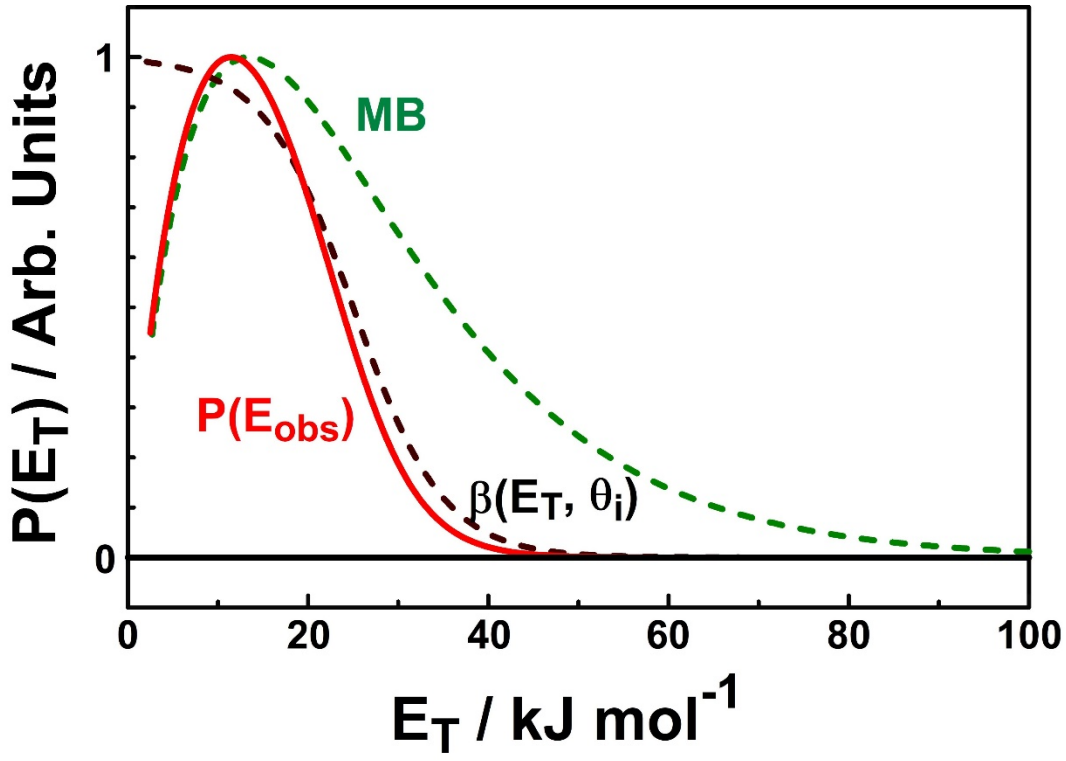


Figure 2.8. Translational energy distribution for products desorbing from the surface after adsorbing via a nonactivated process (red line). The red line is the product of a MB distribution characterized by the surface temperature (dashed green line) and the energy dependent sticking probability for a nonactivated adsorption process, $\beta(E_T, \theta_i)$ (dashed black line).

2.8 and 2.12. The functional form of $D(E_T, \theta_i)$ depends on whether the adsorption process is nonactivated or activated.

2.1C Nonactivated Adsorption/Desorption

If the adsorption process is nonactivated (represented in Figure 2.3, red curve), the number of molecules that adsorb to the surface will decrease as E_i exceeds the magnitude of the well depth of the potential energy surface. Thus, lower energy particles will stick preferentially on the surface. Accordingly, the desorbing particles will appear to have a $P(E_T)$ distribution that is shifted to lower E_T than predicted by a MB distribution

characterized by the surface temperature (Figure 2.8, red curve). For an idealized surface, the sticking probability for nonactivated adsorption, $\beta(E_T, \theta_f)$, will be unity until E_i is raised above a critical energy, E_c, where it will fall to zero. This step function is smoothed out by thermal vibrations of the surface and can be expressed by the functional form[39] (Figure 2.8, dashed black curve)

$$D(E_T, \theta_i) = \beta(E_T, \theta_i) = A\left[1 + \exp\left(\frac{E_{eff} - E_c}{X}\right)\right]^{-1} \tag{2.7}$$

where A is a normalization constant (unitless), E_c is the critical energy above which the sticking probability falls to zero (kJ mol^{-1}), and X determines the width of the curve (kJ mol^{-1}). Eq 2.7 depends on the E_i and θ_i by the term E_{eff}:

$$E_{eff} = E_T \cos^n \theta_i \tag{2.8}$$

where n is unitless and can have values from 0 to 2. When n = 0, the sticking probability does not depend on E_i or θ_i, and particles with any energy and orientation will trap with equal probability. For desorbing particles, this means that the E_f will be constant with θ_f and the angular distribution that can be described by a cos(θ_f) distribution, as discussed above. When n = 2, only energy oriented normal to the surface, E_n, must be dissipated for the particle to trap. The sticking probability increases with θ_i because the particles need to dissipate less energy as θ_i becomes more grazing (Figure 2.9). Accordingly, the desorption of particles that initially adsorbed in a nonactivated process will lead to an angular distribution that is broader than cosine (Figure 2.7, green curve). Simply put, because more molecules adsorb at large θ_i, the flux of desorbing particles will increase with θ_f.

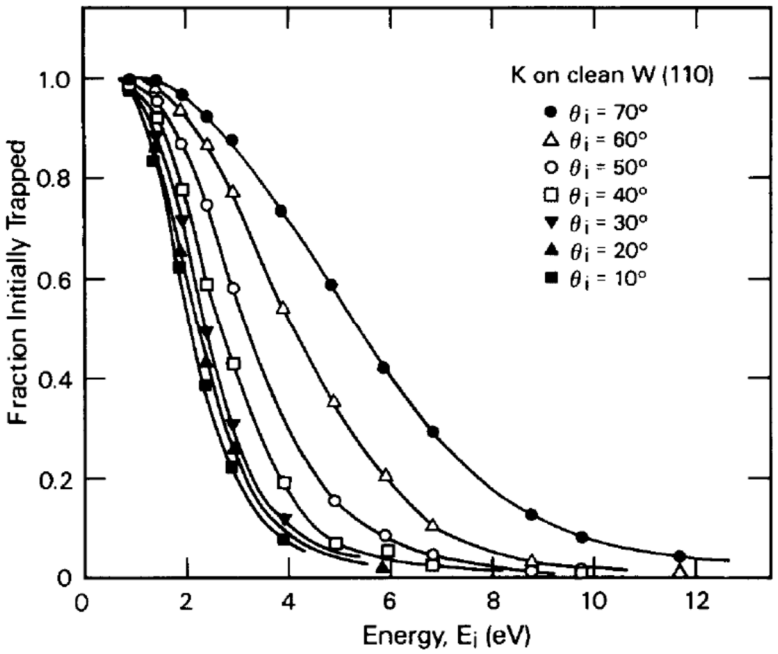


Figure 2.9. The $\beta(E_T, \theta_i)$ for K sticking on a W(110) surface held at a temperature of 1150 K. (Figure from Ref [44]. Data displayed is from Ref. [189] and [190].)

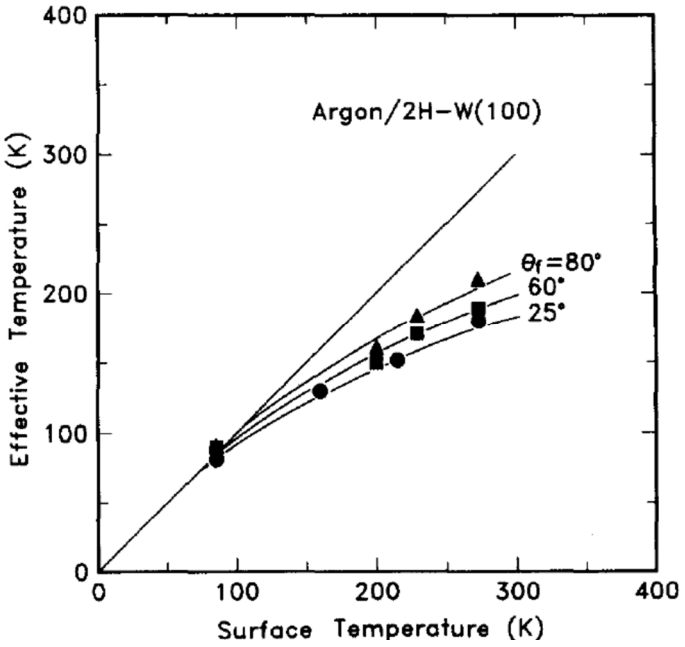


Figure 2.10. The effective temperature of Ar scattering from a hydrogen covered tungsten surface for $\theta_f = 25°$, 60°, and 80°. The E_f of the scattered atoms is proportional to T_{eff}. The energy of the surface, E_s, is equal to $2RT_s$. The black line indicates E_f when it is fully accommodated to E_s. The E_f for $\theta_f = 80°$ is greater than E_f for $\theta_f = 25°$. Figure is from Ref. [39].

Additionally, because the energy oriented parallel to the surface is retained during the collision and only E_n is accommodated, E_f will increase with θ_f (Figure 2.10).

2.1D Activated Adsorption/Desorption

For an activated adsorption process, also referred to as chemisorption, the molecules must surmount a barrier in order enter the potential well (Figure 2.11, red curve). For an ideal surface, the sticking probability, $S(E_T, \theta_i)$, will be a step function that has a value of zero until E_i exceeds the magnitude of the barrier, E_0. For a real surface, thermal vibrations and defects will smooth out the step function and $S(E_T, \theta_i)$ can be expressed by the functional form[41] (Figure 2.12, dashed black line)

$$D(E_T, \theta_f) = S(E_T, \theta_f) = \frac{A}{2}\left[1 + \tanh\left(\frac{E_{eff} - E_0}{W}\right)\right] \quad (2.9)$$

where E_0 represents the barrier for desorption (kJ mol^{-1}), W is related to the range of desorption barriers arising from the variety of surface sites available for desorption (kJ mol^{-1}), A is a normalization factor (unitless), and E_{eff} is given by eq 2.4. Molecules with high E_i adsorb preferentially to the surface. Accordingly, the desorbing particles will appear to have a $P(E_T)$ distribution that is shifted to higher translational energies than predicted by a MB distribution (Figure 2.12, green line). For adsorption over a barrier, only products with sufficient E_n surmount the barrier and the flux of adsorbed particles will increase as θ_i approaches the surface normal ($\theta_i = 0°$). It follows that the flux of particles that desorb over the barrier will be focused toward the surface normal ($\theta_f = 0°$) and the angular distribution will be narrower than cosine (Figure 2.7, red curve).

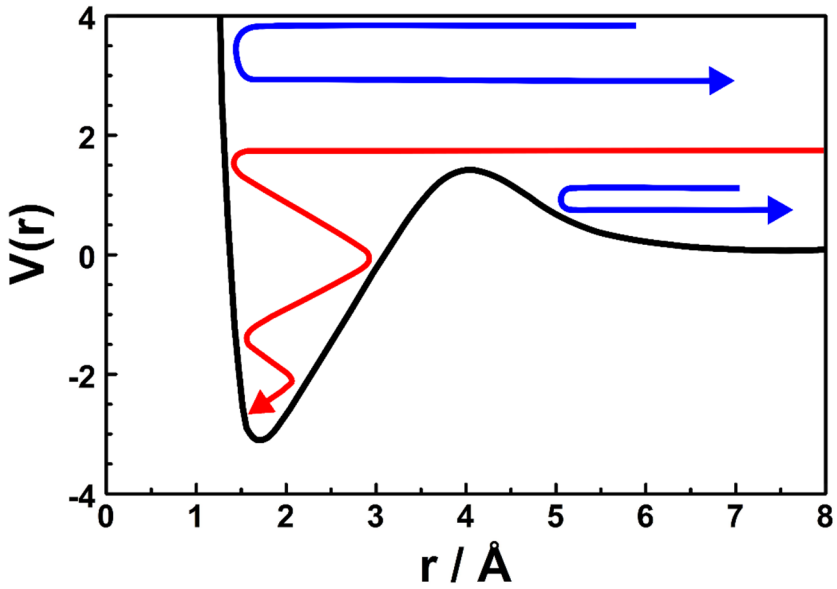


Figure 2.11. Example of a one-dimensional potential energy surface with a barrier to adsorption; r is the distance between the molecule and the surface. The position of the surface is defined as r = 0 Å. The blue line represents molecules that scatter via an IS mechanism from the repulsive wall of the chemisorption well (top blue curve) and from the barrier (dashed blue curve). The red line represents molecules that stick to the surface before exiting the surface via a TD mechanism.

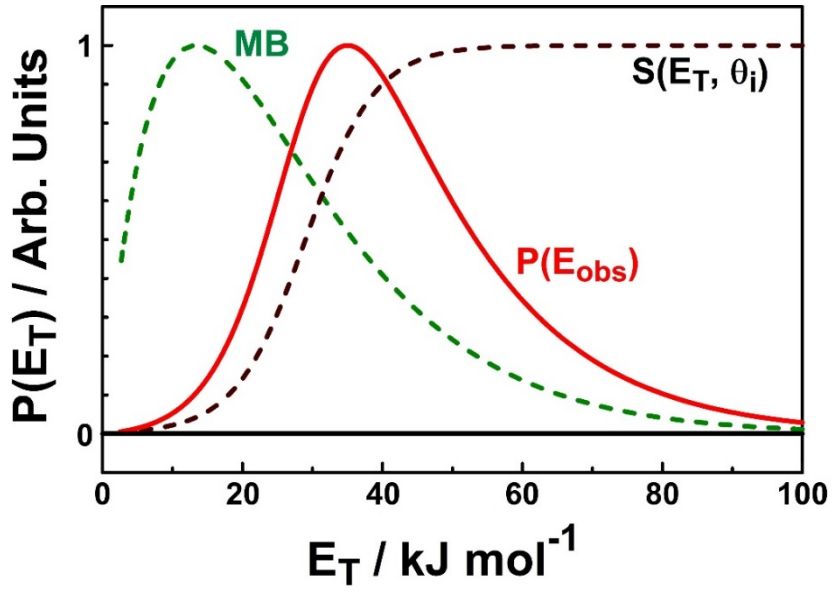


Figure 2.12. Translational energy distribution for products desorbing from the surface after absorbing via an activated process (red line). The red line is the product of a MB distribution characterized by the surface temperature (dashed green line) and the energy dependent sticking probability for a nonactivated adsorption process, $S(E_T, \theta_i)$ (dashed black line).

2.1E Thermal Desorption at High Temperature

In order for a molecule to accommodate to the surface, both the momentum oriented normal and parallel to the surface must be fully dissipated. The normal momentum has been shown to accommodate rapidly, often during the first gas-surface interaction. On a smooth surface, the parallel momentum is accommodated on a much longer time scale because there are few no in plane forces acting on the molecule.[42] At low surface temperature, the residence time of the molecule on the surface is sufficiently long to dissipate the parallel momentum. Thus, the molecule loses all memory of its incidence conditions and the desorbing molecules can be described using the procedure in 2.1C, as described in the previous section. At high temperatures, the residence time decreases and the molecules can escape the surface before the parallel momentum is fully accommodated. Thus, the molecule retains some memory of its incidence conditions and scatters with a lobular distribution that is directed away from the surface normal (Figure 2.13a).[42-43] The E_f will increase with θ_f because the molecule retains its parallel momentum (Figure 2.13b). This mechanism has been referred to as "quasitrapping".

2.1F Thermal Desorption Following a Residence Time on the Surface

The molecule may reside on the surface for some time after coming into thermal equilibrium.[44] The residence time, τ, can decouple the desorption time from the time at which an incident molecule strikes the surface (Figure 2.14, inset). Thus, the scattered particles will appear to have $P(E_T)$ distributions that are shifted to lower translational energies than predicted by a MB distribution (Figure 2.14, red curve). The residence time can be determined from a gas-surface scattering experiment that employs a pulsed

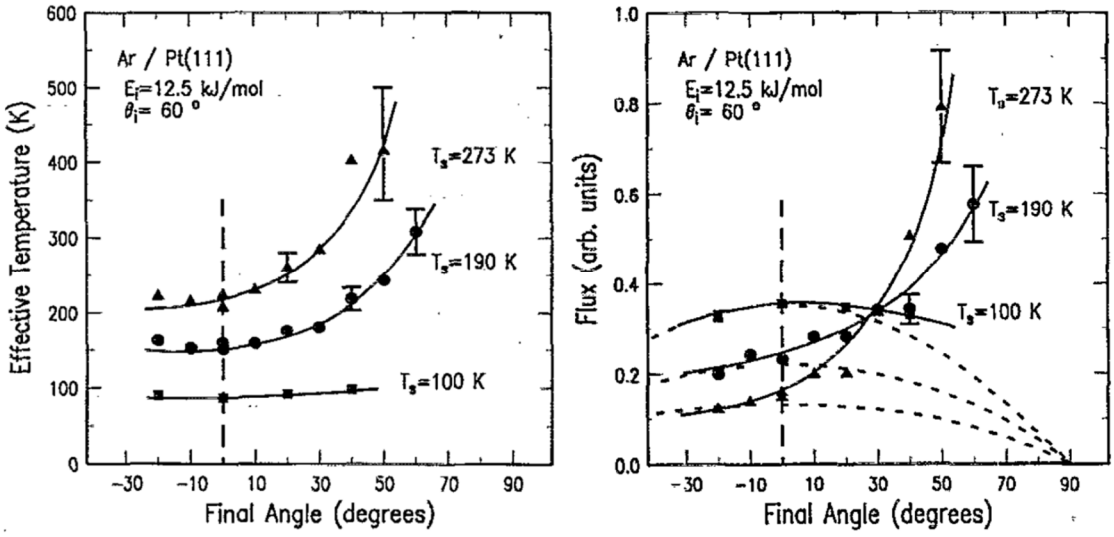


Figure 2.13. The effective temperature (left panel) and flux (right panel) of Ar scattering from a Pt(111) surface held at a temperature of 100, 190, 273 K. The E_f of the scattered atoms is proportional to T_{eff}. Figures are from Ref. [42].

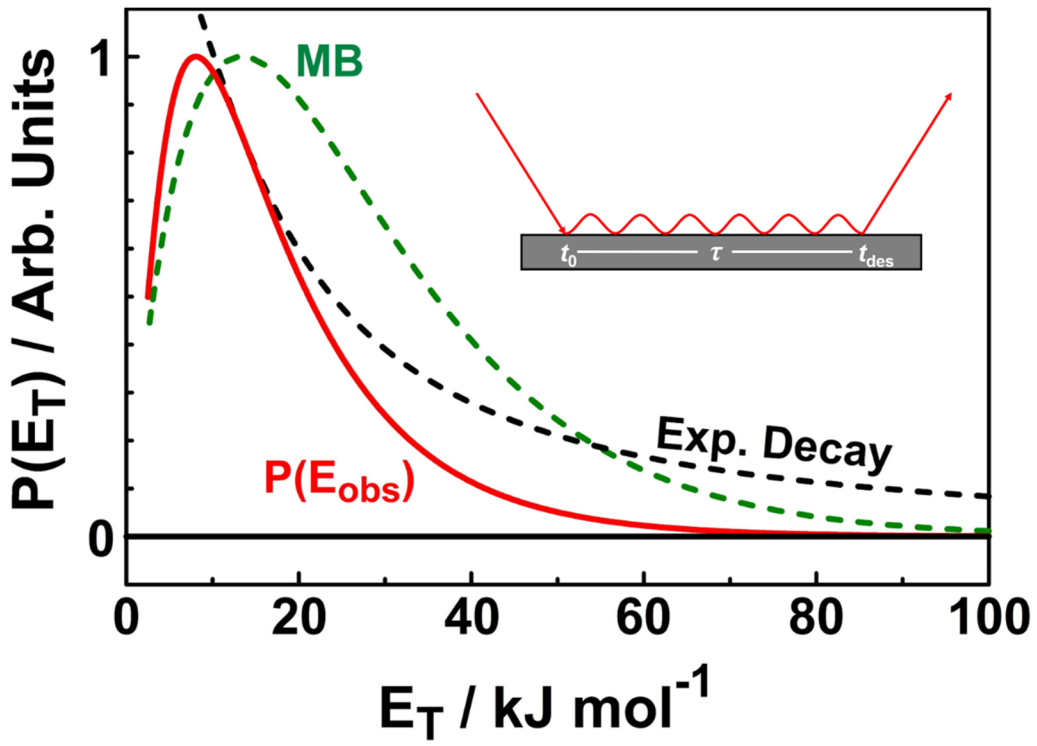


Figure 2.14. Translational energy distribution for products with residence time, τ, desorbing from the surface (red line). The red line is the product of a MB distribution characterized by the surface temperature (dashed green line) and a first order, exponential decay (dashed black line).

molecular beam, as is described in Chapters 3, 4, and 5. The residence time can be determined by fitting the scattered $P(E_T)$ distribution with the product of a first order exponential decay (Figure 2.14, dashed black curve) and a MB distribution (Figure 2.14, dashed green curve). To determine the true scattered flux and E_f of the scattered products, which depend directly on the flight time (t), the TOF distributions must be corrected for the residence time of the molecule on the surface.

2.2 Reactive Scattering

The reactive analogues of IS and TD mechanisms are Eley-Rideal (ER) and Langmuir-Hinshelwood (LH) reactions, respectively. A third reactive process, referred to as a "hot atom" (HA) reaction, is also possible. These reactions have distinct dynamical signatures that can be generally distinguished using beam-surface scattering techniques.

2.2A Eley-Rideal Reactions

In an ER reaction, a gas-phase atom abstracts an atom adsorbed on the surface.[3] ER reactions are probable when the surface coverage of the adsorbate is high and the adsorbate is weakly bound to the surface.[10,45] The incident atom and product molecule do not come into thermal equilibrium with the surface; therefore, the product flux does not depend on surface temperature.[46] Products that are formed by an ER mechanism have memory of the incident reactant's trajectory and have lobular angular distributions (see example in 2.6). The molecules are highly translationally excited, [10-11] and appear at short flight times in the TOF distributions (Figure 2.1, blue curve). Additionally, a large fraction of the E_i and

reaction energy is deposited into internal modes of the molecule. Thus, molecules that are produced by an ER mechanism are highly vibrationally excited.[10-11]

2.2B Hot Atom Reactions

During an HA reaction, the incident atom enters a quasi-bound state and skips along the surface before reacting with an adsorbate.[47] This reaction does not occur in thermal equilibrium with the surface and the rate is independent of the surface temperature.[46] Products formed by an HA mechanism also have a lobular angular distribution and are translationally and internally excited. [10-11] Consequently, products of ER and HA reactions are difficult to distinguish without aid from simulations. However, HA reactions are favored over ER reactions when the surface coverage is low and when the adsorbate is tightly bound to the surface.[10,45]

2.2C Langmuir-Hinshelwood Reactions

An incident atom must first come into thermal equilibrium with the surface before it can react with an adsorbate via a LH reaction mechanism.[3] The reaction occurs in thermal equilibrium with the surface and the product flux depends directly on the temperature of the surface. The energy released during the reaction is deposited into the surface and the product molecules have a translational and internal energy distribution that are in equilibrium with the surface. Accordingly, the products desorb into the vacuum with low translational energies and appear at large flight times in the TOF distributions (Figure 2.1 red curve). If there is no barrier to desorption, the product molecule desorbs with a cosine angular distribution and E_f that follow Knudsen's Cosine Law (Figure 2.7, blue curve). If there is a barrier to desorption, the product molecule has an angular distribution that is

narrower than cosine and energies that are greater than expected by a MB distribution as described in section 2.1D.[40] If there is a residence time associated with the reaction, the product molecules will appear to be exiting the surface with energies lower than predicted by a MB distribution and the analysis described in Section 2.1F must be followed.[44]

CHAPTER THREE

INELASTIC AND REACTIVE SCATTERING DYNAMICS OF HYPERTHERMAL O AND O_2 ON HOT VITREOUS CARBON SURFACES

Contribution of Authors and Co-Authors

Manuscript in Chapter 3

Author: Vanessa J. Murray

Contributions: Performed molecular beam scattering experiments and conducted data analysis. Prepared both the figures and the manuscript for publication.

Co-Author: Brooks C. Marshall

Contributions: Helped with data collection and provided feedback on data interpretation.

Co-Author: Philip J. Woodburn

Contributions: Helped with data collection.

Co-Author: Timothy K. Minton

Contributions: Provided crucial insight regarding the experimental procedure and the interpretation of the collected data. Aided in the preparation of the manuscript and figures.

Manuscript Information Page

Vanessa J. Murray, Brooks C. Marshall, Philip J. Woodburn, and Timothy K. Minton

Journal of Physical Chemistry C

Status of Manuscript:
____ Prepared for submission to a peer-reviewed journal
____ Officially submitted to a peer-review journal
____ Accepted by a peer-reviewed journal
__×__ Published in a peer-reviewed journal

Published by the American Chemical Society
In Volume 119, Issue 26, pp 14780-14796 (2015)

Reproduced with permission from ACS – the American Chemical Society

INELASTIC AND REACTIVE SCATTERING DYNAMICS OF HYPERTHERMAL O AND O_2 ON HOT VITREOUS CARBON SURFACES

Vanessa J. Murray, Brooks C. Marshall, Philip J. Woodburn, and Timothy K. Minton*

Department of Chemistry and Biochemistry, Montana State University, 103 Chem/Biochem Bldg., Bozeman, MT, 59717

Abstract

We have undertaken a series of experiments to learn the mechanisms of carbon oxidation over a wide range of temperatures that extend to the conditions encountered during atmospheric re-entry, with a particular interest in understanding how these mechanisms change with temperature. We report here the hyperthermal scattering dynamics of ground-state atomic oxygen, $O(^3P)$, and molecular oxygen, $O_2(^3\Sigma_g^-)$, on vitreous carbon surfaces at temperatures from 600 to 2100 K. A molecular beam containing neutral O and O_2 in a mole ratio of 0.97:0.07 was prepared with a nominal velocity of 7760 m s^{-1}, corresponding to a translational energy of 481 kJ mol^{-1} for atomic oxygen. This beam was directed at a vitreous carbon surface, and angular and translational energy distributions were obtained for inelastically and reactively scattered products with the use of a rotatable mass spectrometer detector. Unreacted oxygen atoms exited the surface through both impulsive scattering and thermal desorption. The preferred scattering process changed from impulsive scattering to thermal desorption as the surface temperature increased. O_2 scattered mainly impulsively from the surface, and its scattering dynamics were essentially unaffected by surface temperature. The predominant reactive product was carbon

monoxide (CO). Carbon dioxide (CO_2) was also formed at lower surface temperatures. The flux of the CO product rose with temperature to a maximum at approximately 1500-1900 K, depending on heating rate, and then decreased with increasing surface temperature. The CO_2 flux dropped dramatically with increasing surface temperature and was below detectable limits above 1100 K. A minor reactive pathway was identified that produced O_2, presumably through a direct Eley-Rideal reaction of an incident oxygen atom with an O atom residing on the surface. Decreased oxygen surface coverage at higher temperatures was found to limit the reactivity of the surface by inhibiting the production of CO and CO_2 at very high surface temperatures. The observed inelastic and reactive scattering behavior reveal a complex interplay between reactivity and surface temperature.

3.1 Introduction

Space vehicles that enter the Earth's atmosphere at hypersonic speeds require a thermal protection system (TPS) to shield the vehicle from high heat loads. In the re-entry environment, the boundary layer in contact with the hot surface consists of partially dissociated air, with N_2, O_2, and O being the dominant species for vehicles re-entering from low Earth orbit (LEO). These species collide with the TPS surface and may scatter without reaction back into the boundary layer. Atomic and molecular oxygen can also react to form volatile products that either scatter directly or desorb thermally into the boundary layer. The deposition of energy into the surface or the boundary layer depends critically on the details of the gas-surface interaction dynamics, which are largely unknown under such extreme conditions. A thorough understanding of these dynamics would enable more

accurate modeling of thermal loads during atmospheric re-entry and therefore mitigate the need for overly conservative TPS designs.

TPS materials for applications where shape change is undesirable are typically carbon-carbon composites that oxidize in air at high temperatures (>800 K) and are designed to ablate during the hypersonic flight period, where the surface may reach temperatures well above 2000 K. Vitreous carbon, also referred to as glassy carbon, can serve as an experimental model for such materials. This material has both a high melting point and high thermal conductivity, as well as a low coefficient of thermal expansion.[7] These characteristics have motivated its use as the matrix in carbon-carbon composites on vehicle nose-cones and leading edges in the past.[7]

The structure of vitreous carbon has been subject to debate. It has been shown to consist largely of sp^2 bonded carbon with fullerene structures.[48] However, neutron diffraction measurements have shown that fullerene structures are present only in trace amounts in vitreous carbon, suggesting instead that it consists of a graphite-like structure with short range order.[49] Additional studies have reported that vitreous carbon is composed of crystallites that consist of small, randomly oriented stacks of curved graphene sheets.[14-15] The disordered orientation of the crystallites encloses small voids.[50-52] Consequently, the density of vitreous carbon (1.42 g cm^{-3}) is lower than that of pyrolytic graphite (2.25 g cm^{-3}). Nevertheless, vitreous carbon is considered to be non-porous because it has been shown to be impermeable to both H_2 and He.[50-51]

The oxidation of vitreous carbon by molecular oxygen revealed pores that had been initially closed to the atmosphere.[53] X-ray photoelectron spectroscopy (XPS) studies have

shown that O_2 dissociatively chemisorbs on vitreous carbon at edge carbon atoms, with the formation of single bonds between surface carbon atoms and adsorbed O atoms, possibly in an epoxide formation over carbon bridges.[54-55] Additional temperature programmed desorption (TPD) studies have found that the production of CO and CO_2 in the temperature range of 723-873 K corresponded to the decomposition of carboxylate and ether-like species on the surface.[54] Vitreous carbon etching by atomic oxygen was observed upon exposure to suprathermal O atoms at 299 K.[16] The probability of a carbon atom being removed by a suprathermal O atom from vitreous carbon was $2.1 \pm 1.2 \times 10^{-2}$. This probability is nearly twice as high as the value for pyrolytic graphite, which was 1.3×10^{-2},[17] indicating that vitreous carbon is the more reactive substance. This enhanced reactivity is presumably the result of the porous structure of vitreous carbon.

Highly oriented pyrolytic graphite (HOPG) has often been used as a model surface for investigating the degradation of carbon-based materials. HOPG is composed of graphene crystallites that are microns to tens of microns in length and oriented along the basal plane, with their *c* axis being parallel to the surface normal of the overall crystal.[13] Studies of the oxidation of HOPG can be helpful in the understanding of O and O_2 reactions on vitreous carbon, as both these sp^2 allotropes of carbon may undergo oxidation and etching through similar mechanisms, albeit with different rates.[16] The oxidation of HOPG has been studied extensively in environments relevant to LEO, where the dominant chemical species are O atoms that can collide with the ram surfaces of orbiting spacecraft with high relative velocities corresponding to O atoms with ~500 kJ mol^{-1} striking the surfaces. Laboratory experiments of these hyperthermal O-atom interactions, such as the

experiment described in this article, typically expose surfaces to O_2 as well as O. Nevertheless, O_2 is only weakly reactive with HOPG and probably also with vitreous carbon. O_2 can physisorb on a pristine graphite surface, but it is bound by a low barrier of ~0.1 eV.[56-58] Furthermore, O_2 has a low sticking coefficient with HOPG: $1.53 \pm 0.35 \times 10^{-14}$ on pristine surfaces, increasing slightly to 10^{-10} on defect sites.[59] The reaction of O_2 with HOPG occurs mainly through dissociative chemisorption, which follows a low-barrier path only when O_2 binds at defect sites.[60-62] However, the low defect density of an HOPG surface (3 to 4 μm^{-2})[63] keeps the overall reactivity with O_2 low. Even at hyperthermal incidence energies, O_2 would be expected to scatter inelastically with high probability and not contribute significantly to the removal of carbon.[64] In contrast, the reactivity of hyperthermal O atoms is high and extends beyond defect sites. Post-exposure characterization of room-temperature HOPG subjected to hyperthermal O and O_2 bombardment revealed that C-O, C=O or O-C-O, and O-C=O functional groups populated the surface.[65] In the same study, scanning tunneling microscopy studies showed that the surface became rough and formed hillock-like structures. Nicholson, Minton, and Sibener conducted a series of experiments that studied the chemical reactivity of HOPG in the range of 300-500 K when exposed to higher fluences of hyperthermal O atoms.[66-67] They observed the etching of HOPG and found that the reaction probability nearly tripled – from one C atom removed for every 22 incident O atoms to one C atom removed for every 8 incident O atoms – when the surface temperature was increased from 298 to 493 K. In addition, they observed the formation of shallow circular etch pits that grew in diameter with increasing oxygen atom fluence, indicating that O atoms reacted preferentially with

carbon atoms at the edges of the graphene planes, most likely through thermal mechanisms – i.e., in thermal equilibrium with the surface. At elevated temperatures of ~200 °C and above, the circular etch pits did not form, and the surface became randomly rough, presumably through the coalescence of individual etch pits. Molecular beam scattering studies that utilized a beam containing hyperthermal O atoms were conducted in an attempt to probe the details of the mechanisms that lead to the removal of carbon from HOPG.[20] CO and CO_2 products were observed from an HOPG surface at 503 K, and they exited the surface with similar yields via thermal and nonthermal mechanisms.

Theoretical studies have shown that the gasification of carbon by O atoms occurs mainly at specific reactive sites involving semiquinone or lactone functional groups, which form at defect sites during O-atom bombardment. When pristine HOPG is exposed to hyperthermal O atoms, the incident O atoms add to carbon bridges to form epoxide groups, with calculated adsorption energies in the range of 0.95-3.2 eV depending on the surface coverage and level of theory being used.[56,68-70] These epoxide groups can migrate across the surface over low diffusion barriers, calculated to be in the range of 0.36 to 0.38 eV.[68-69] The migration of epoxide groups to the vicinity of semiquinone or lactone sites promotes the formation of CO or CO_2 by decreasing the barrier to reaction.[8,20,61-62,71] The excess oxygen surrounding a reactive site was found to saturate the remaining dangling bonds around carbon vacancies created during the reaction.[19] Theoretical studies have found that the dominant reaction at an HOPG surface during hyperthermal O-atom bombardment is the abstraction of a surface-adsorbed O atom by an impinging oxygen atom to produce O_2 through a direct (Eley-Rideal) reaction.[9,20,72] Reactions of this type do not lead directly to

the removal of carbon, but they may limit the reaction rate by removing adsorbed O atoms, which would otherwise be available to facilitate the production of CO or CO_2. The theoretical studies have not identified an Eley-Rideal abstraction pathway through which CO or CO_2 might be formed.

Two noteworthy theoretical studies have investigated the effect of surface temperature on the interaction of hyperthermal O atoms with carbon surfaces. ReaxFF calculations by van Duin and coworkers probed the reaction dynamics of O atoms with HOPG.[72] It was shown that an increase in the surface temperature resulted in a larger amount of carbon removed from the surface, although the fraction of the carbon atoms removed as CO or CO_2 as a function of temperature was not discussed. Morón et al. conducted calculations on O-atom collisions with a pre-oxidized HOPG surface with the use of a flexible periodic LEPS potential energy surface based on density functional theory.[9] They found that inelastic scattering of O and a direct Eley-Rideal reaction of an incident O atom with a surface adsorbed O to form O_2 were the two main processes observed with surface temperatures of 100 and 900 K and with incident O-atom energies up to 2.0 eV. For unreacted O atoms, they observed direct scattering and thermal desorption, and they found that thermal O-atom desorption processes became more significant at the higher temperatures with incidence energies in the range of 1-2 eV. The desorbing oxygen atoms resulted from weakly bound (E_{ads} = 0.68 eV) adatoms on carbon bridges that were removed when an incident O atom from the gas phase adsorbed at a nearby site.[9] They also reported the observation of some events where the inelastic scattering of an impinging atom induced the thermal desorption of a pre-adsorbed O atom

at a nearby site, although such events were only significant at a high temperature of 1500 K. The theoretical studies by Morón et al. did not address the possible formation of CO or CO_2.

Experiments conducted on surfaces at very high temperatures have only focused on the interaction of thermal O and O_2 with graphite. Rosner and Allendorf studied the probability of thermal O and O_2 reactions with a graphite filament at temperatures ranging from 1000 to 2000 K.[33] The reaction did not follow Arrhenius behavior in the temperature range studied, as the reaction probability for carbon removal increased with temperature and reached a maximum at approximately 1600 K before decreasing as the temperature was increased further. Similar non-Arrhenius behavior was observed by Olander et al., who monitored the CO reaction product when HOPG was exposed to O_2 over a similar temperature range.[22] In addition to the non-Arrhenius behavior, they noted a hysteresis in the temperature dependence, where the reaction probabilities with increasing temperatures were higher than the reaction probabilities with decreasing temperatures over the same temperature range. These observations were attributed to the reduction of surface reactive sites resulting from annealing at high temperature.

The research described herein is part of a broad effort to elucidate the dynamics of carbon oxidation, where we intend to identify both common and unique features particular to different reagent species (O or O_2), surface temperatures, and incidence energies. We begin here with the investigation of the dynamics of the interactions of O and O_2 with vitreous carbon surfaces at hyperthermal velocities (~7.8 km s^{-1}, corresponding to ~500 kJ mol^{-1} for O atoms). These studies were conducted with the use of a beam-surface scattering

technique in which angle- and velocity-resolved distributions of mass-selected products are obtained. The surface temperatures cover a range from 600 to 2100 K, with detailed dynamical scattering data collected for two widely spaced temperatures of 800 and 1875 K. Thus, the important temperature-dependent inelastic and reactive scattering dynamics may be ascertained and investigated in detail. The use of hyperthermal O and O_2 provides for a highly localized interaction at the surface,[38] which can reveal details about surface changes at the atomic level during oxidation. In addition, hyperthermal incident species allow for a clear distinction between nonthermal and thermal processes at the surface, as products of processes that occur in thermal equilibrium with the surface will desorb with much slower velocities than products that exit the surface nonthermally after a hyperthermal impact. Furthermore, the relative importance of thermal vs. nonthermal processes found with hyperthermal incident species may reveal whether surface temperature or incidence energy has the stronger influence on the oxidation reactions at the surface. From the detailed dynamical data that have been obtained combined with information gleaned from relevant studies in the literature, the essential mechanisms of the high-temperature oxidation of vitreous carbon have been inferred and are presented below.

3.2 Experimental Methods

The experiments were performed with the use of a crossed molecular beams apparatus reconfigured for surface scattering.[73-75] Briefly, a pulsed beam containing high-translational-energy (or "hyperthermal") O and O_2 was directed at a heated vitreous carbon surface (Figure 3.1a). Volatile reaction products were monitored with a mass spectrometer that rotated about the same axis as the surface in the plane defined by the surface normal

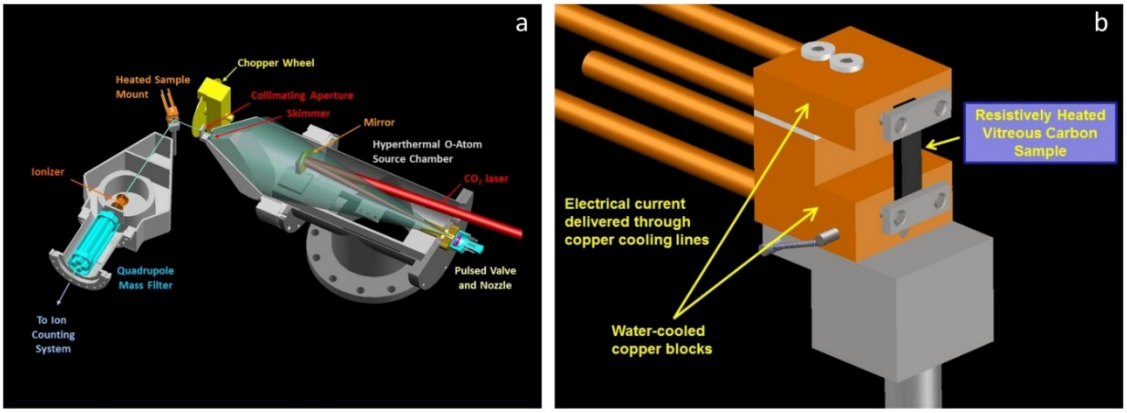


Figure 3.1. (a) Schematic diagram of the experimental setup, including the hyperthermal beam source, heated sample mount, and rotatable mass spectrometer detector. (b) Sample mount used to heat the vitreous carbon sample resistively.

and the beam. Products were detected at a variety of final scattering angles, θ_f, for two angles of incidence, $\theta_i = 45°$ and 60°. All angles are in the same plane and referenced to the surface normal, with positive final angles being on the opposite side of the surface normal from the incidence angles. Products that entered the detector were ionized in an electron-impact ionizer,[76] filtered with a quadrupole, and detected with a Daly-type ion detector[77] in a pulse-counting mode. The ion pulses were accumulated by a multichannel scaler. The distributions collected with the multichannel scaler are number density distributions of scattered products as a function of their flight times over the 33.7 cm distance from the surface to the electron-impact ionizer. These *N(t)* distributions are commonly called time-of-flight (TOF) distributions. Translational energy distributions, $P(E_T)$, of the scattered products, which are proportional to flux, are derived from the TOF distributions with the use of a simple density-to-flux conversion that assumes a monoenergetic incident beam.[74,78] When total relative flux is desired, the $P(E_T)$ distribution is integrated. The base pressure of the main scattering chamber was 4×10^{-7} Torr, and the

operating pressure during the experiment was 6×10^{-7} Torr. The detector was triply differentially pumped such that the region containing the electron-impact ionizer had a base pressure of $<10^{-11}$ Torr that did not rise during data collection.

The laser-detonation source used to generate hyperthermal O and O_2 is based on an original design by Physical Sciences, Inc.[79] that was further refined in our lab and has been described in detail elsewhere.[80] Translational energy distributions and component fluxes of the hyperthermal beam were obtained by lowering the sample out of the beam path and directing the beam into the detector. The beam passed through a 2.0 mm diam. skimmer that was 77 cm from the nozzle orifice. The beam was further collimated by a 1.3 mm diameter aperture that was 3.54 cm from the skimmer. The sample surface was 97.75 cm from the nozzle orifice. The source was operated at a repetition rate of 2 Hz. A synchronized chopper wheel, with three equally spaced slots of 1.5 mm width and a rotation rate of 300 Hz, was used to select a narrow distribution of velocities from the beam. The beam was composed of 93% $O(^3P)$[81] and had an average translational energy of 481.6 kJ mol^{-1} and an energy width (full width at half maximum) of 55 kJ mol^{-1} (Figure 3.2). The remainder of the beam was $O_2(^3\Sigma_g^-)$[82] and had a translational energy of 962.4 kJ mol^{-1} and an energy width of 160 kJ mol^{-1}.

Grade 22 SPI-Glas™ vitreous carbon samples were obtained from SPI, Inc.[83] The samples were used as is from the manufacturer, with no additional post-processing. The samples had dimensions of 25 mm × 7 mm × 1 mm. Before introduction into the vacuum chamber, each vitreous carbon sample was cleaned with a mixture of trichloroethylene and ethanol (0.75:0.25 by volume). The vitreous carbon samples were heated using the sample

mount illustrated in Figure 3.1b. The basic components of the mount are two water-cooled copper blocks that are electrically isolated by alumina spacers. The vitreous carbon surface was clamped to the front of the copper blocks, thus completing an electrical circuit. Current was delivered through copper water-cooling tubes and passed through the sample, heating it resistively. The desired surface temperature was achieved by adjusting the current, which ranged from 10 to 45 A, resulting in sample temperatures from 600 to 2100 K. The surface temperature was not measured directly; instead, the surface temperature was determined by fitting the TOF data from thermally scattered products to a Maxwell-Boltzmann (MB) distribution of translational energies, with temperature as an adjustable parameter. One

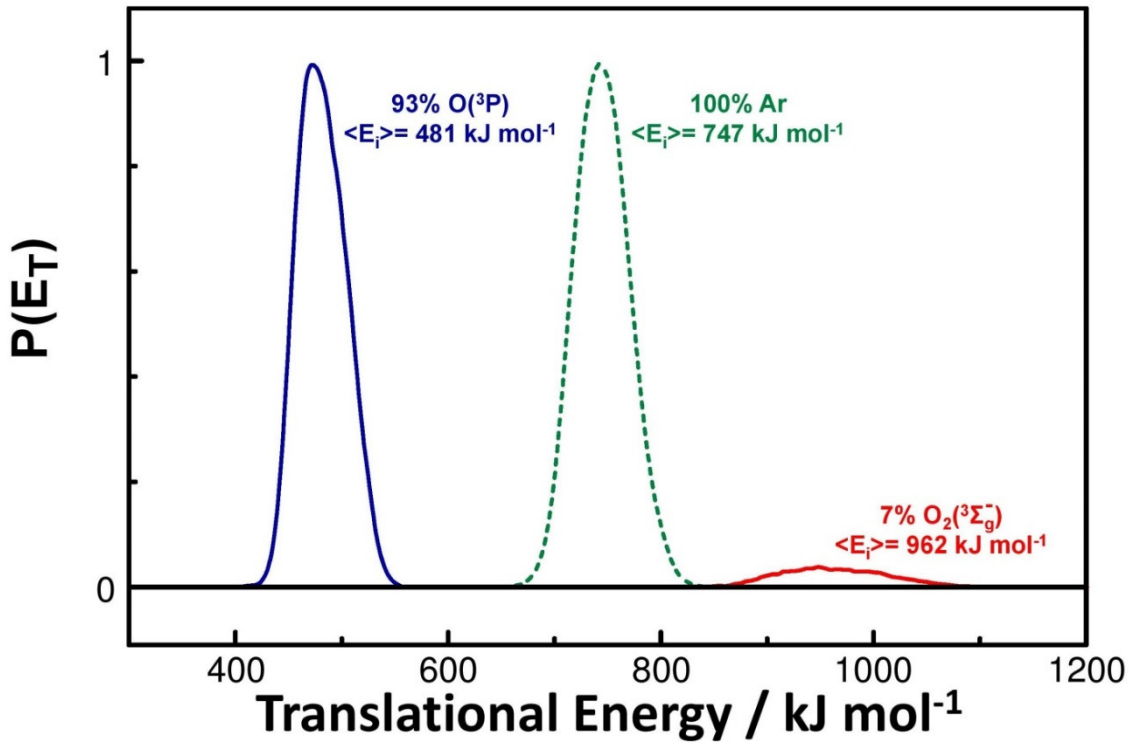


Figure 3.2. Translational energy distributions of the energy-selected hyperthermal atomic and molecular oxygen components of the incident beam (solid lines) and the hyperthermal argon beam (dashed line). The O and Ar curves have been normalized to 1.0, and the areas of the O_2 and O curves reflect the relative mole fraction of O_2 in the beam compared to O.

sample was used for most of the data presented here, and this sample was subjected to one temperature cycle from 600 K to 2100 K and then back to 600 K for 24 hours before data collection began. The sample surface was assumed to be free of contamination based on earlier results in our lab on Ar-atom interactions with HOPG surfaces, which exhibited scattering dynamics that were indicative of a clean surface even at the relatively low temperature of 503 K.[84]

3.2A Temperature Dependence of Surface Reactivity

The effect of surface temperature on the reactivity of the surface was investigated over a broad range of temperatures for fixed incidence and final angles ($\theta_i = 45^\circ$ and $\theta_f = 45^\circ$; $\theta_i = 60^\circ$ and $\theta_f = 0^\circ$). Individual TOF distributions were collected at mass-to-charge ratios (m/z) of 16 (O^+), 32 (O_2^+), 28 (CO^+), and 44 (CO_2^+) for 250, 250, 500, and 500 beam pulses, respectively, for each temperature. This temperature survey began with the surface at 600 K, and the temperature was increased in steps of about 100 K with a hold time of roughly 16 minutes at each temperature during which time TOF distributions were collected at the various m/z ratios. After the temperature had reached 2100 K, the sample temperature was decreased at the same rate, with TOF distributions again being collected at each temperature step. Data were collected for two full temperature cycles from 600 to 2100 K. Each temperature cycle took about 12 hours to complete.

In order to elucidate the time required to reach a steady state of oxidation at a high surface temperature (1875 K, one of the focus temperatures of our studies), the sample was held at 800 K and exposed to the hyperthermal beam for thirty minutes to ensure that the surface had reached a steady state of oxidation. Then the surface temperature was increased

suddenly, in a matter of <30 seconds, to 1875 K. TOF distributions were collected sequentially for *m/z* = 28, 16, and 32 repeatedly until it was observed that the TOF distributions for *m/z* = 28 (CO^+) no longer changed with time, which took about 200 minutes.

3.2B Investigation of Surface Thermal Roughening

To investigate the effects of thermal roughening of the surface on the scattering dynamics, a beam of hyperthermal argon was directed at the surface. Ar is a useful experimental probe for studying surface roughness at the atomic level because of its relatively weak attractive potential with the surface, which makes it possible to isolate the collision dynamics to hard-sphere-like interactions. The hyperthermal Ar beam was generated using the laser-detonation source, and the synchronized chopper wheel was used to select a beam with a translational energy of 747 kJ mol^{-1} and an energy width of 60 kJ mol^{-1} (Figure 3.2). A pristine vitreous carbon sample was used for the experiments with hyperthermal Ar.

The effect of surface temperature on the scattering dynamics of hyperthermal Ar was first investigated with a procedure similar to that described in Section 3.2A. The incidence angle of the beam and the final angle of the scattered Ar were fixed at 45˚ and 60°, respectively, while the temperature was varied from 600 to 2100 K. Data were collected for 250 beam pulses per temperature.

Angular distributions of Ar, over the full range of accessible final angles, were also collected with θ_i = 45˚ for surface temperatures of 800 K and 1875 K. Individual TOF distributions were accumulated for 250 pulses. Long-term drift in the experiment was

compensated for by sequentially varying the final detection angle from lowest to highest and then highest to lowest until two TOF distributions were collected at each final angle for a whole set of final angles. This procedure was done twice (two angular cycles) for a total of four TOF distributions for each final angle. The TOF distributions corresponding to each final angle were summed before being analyzed.

3.2C O/O_2 Beam-Surface Interactions

Scattering dynamics for both inelastically and reactively scattered species were measured with θ_i = 45° and 60° over the full range of accessible angles at surface temperatures of 800 K and 1875 K, during bombardment by the hyperthermal O/O_2 beam. TOF distributions for m/z = 16 (O^+), 32 (O_2^+), 28 (CO^+), and 44 (CO_2^+) were collected for totals of 1500, 1500, 3000, and 3000 beam pulses, respectively, for each final angle when the surface temperature was 800 K. When the surface temperature was held at 1875 K, TOF distributions were collected for totals of 1000, 1000, and 2000 beam pulses for m/z = 16 (O^+), 32 (O_2^+), and 28 (CO^+), respectively. Long-term drift was compensated for in the same way described in Section 3.2B, with three angular cycles for 800 K and two angular cycles for 1875 K. The data sets at the two temperatures were normalized to take into account the different accumulation times. The m/z = 16 (O^+) TOF distributions were corrected for dissociative ionization of O_2 during data processing by subtracting the O_2 component that fragments to m/z = 16 in the electron-impact ionizer (11% of the number density measured for $m/z = 32(O_2^+)$). The resulting TOF distributions corresponding to m/z = 16 thus represent O atoms only.

3.3 Results and Analysis

Four species were observed leaving the vitreous carbon surface: O, O_2, CO, and CO_2. The relative abundance of each product depended strongly on the surface temperature. The scattering of volatile species was considered in terms of two limiting cases: (1) impulsive or nonthermal scattering (IS for nonreactively scattered O and O_2) and (2) thermal desorption (TD).[78,85-86] Thermal desorption is assumed to correspond to desorbing species that can be described with a MB distribution of translational energies characterized by the surface temperature. This MB distribution is typically distinguished in the TOF distributions as a broad component at relatively long flight times. A MB distribution of translational energies, $P(E_T)$, is converted to a number density distribution as a function of flight time, $N(t)$, and the result is compared with the TD component of the TOF distribution. The temperature of the calculated $N(t)$ distribution is scaled to match the shape of the TD component. The IS/nonthermal component of a TOF distribution arises from products that scatter from the surface with translational energies that are significantly higher than the average energy in a MB distribution at the surface temperature. Products with high translational energies may come from inelastic or reactive events on the surface that occur on a time scale too short for thermal equilibrium to be attained. They may also come from species that are initially in thermal equilibrium with the surface but desorb over a barrier.[87] The IS/nonthermal component typically appears in a TOF distribution as a narrow peak at relatively short flight times. The TOF distribution of the IS/nonthermal component is obtained by taking the difference between the overall TOF distribution and the calculated, best-fit MB distribution.

3.3A Reactivity as a Function of Surface Temperature

The scattered products were monitored as the temperature of the surface was varied. Figure 3.3 shows TOF distributions for O, CO, O_2, and CO_2 that were collected for different surface temperatures. The TOF distributions in Figure 3.3 were collected during a single pass from low to high temperature (one-half cycle, based on the description in Section 3.2A). Time zero in the TOF distributions corresponds to the time at which O atoms with the average incidence energy of 481 kJ mol^{-1} collided with the surface. The most probable interaction of O atoms with the vitreous carbon surface was a nonreactive collision (Figure 3.3a). At lower temperatures, the TOF distributions of scattered O atoms are dominated by

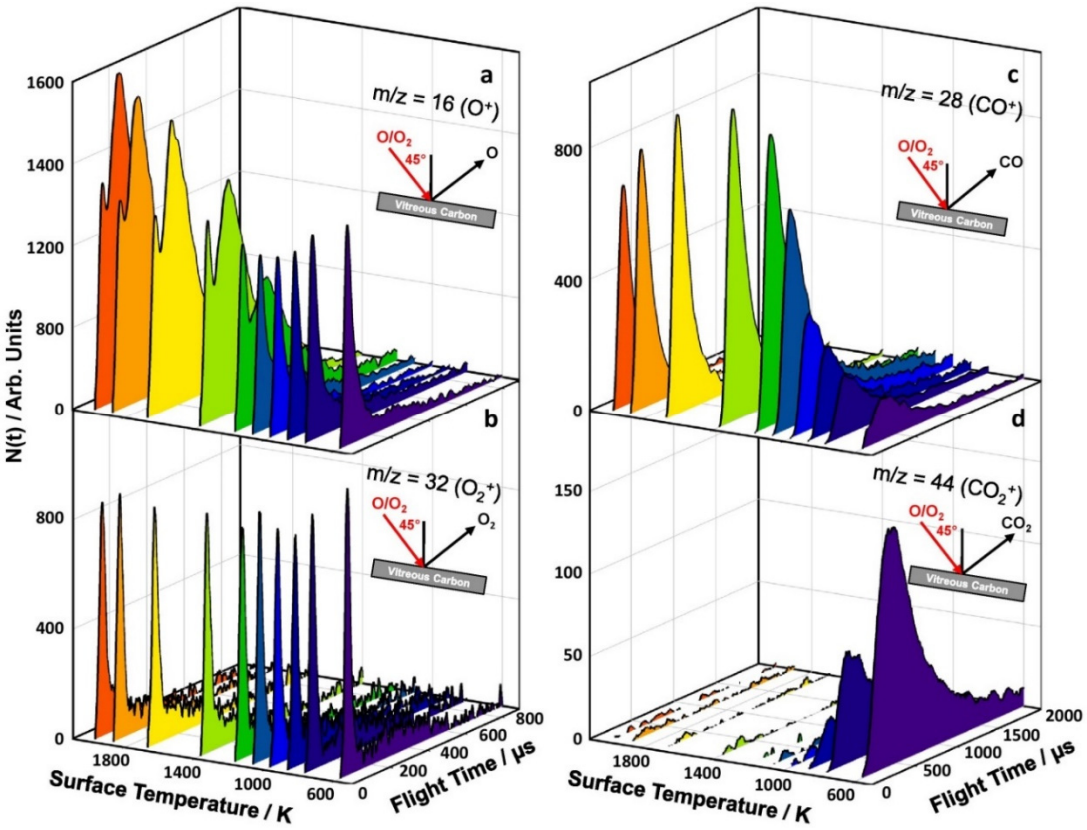


Figure 3.3. Time-of-flight (TOF) distributions, collected with surface temperatures from 600 to 2100 K, for the four scattered products observed following bombardment of the vitreous carbon surface with the O/O_2 beam described in Figure 3.2, at an angle of incidence, θ_i, of 45° and a final angle, θ_f, of 45°.

IS. Above 1200 K, the TD signal begins to dominate and continues to increase with increasing temperature, whereas the IS component appears to be nearly invariant with surface temperature. The TD O atoms thus account for an increase in the overall O-atom flux as the surface temperature increases. Conversely, the TOF distributions for O_2 showed almost no change with surface temperature (Figure 3.3b), with IS being overwhelmingly dominant. The main reactive product was CO, and the magnitude of the TOF distributions for CO depended strongly on surface temperature. In contrast to the O and O_2 TOF distributions, the CO TOF distributions do not exhibit distinct nonthermal and TD components. The initial increase in temperature resulted in an increase in the CO signal; however, the signal reached a maximum at 1400 K and decreased when the surface temperature increased further. An increase in temperature did not enhance the signal from scattered CO_2. When the surface temperature was 600 K, the flux of CO and CO_2 were comparable: $I(t,\mathrm{CO})/I(t,\mathrm{CO_2}) = 1.6$. Above this temperature, the CO_2 signal dropped dramatically and was below detectable limits at temperatures above 1100 K.

Figure 3.4 displays the integrated flux of the scattered products as a function of temperature. Each data point represents the average of two measurements, as the data were collected for two passes from low to high temperature and for two passes from high to low temperature. The scattered flux of CO exhibited a hysteresis in its dependence on the surface temperature, whereas essentially no hysteresis was observed for O, O_2, and CO_2. The flux of the scattered CO was lower when the surface temperature was incremented from high to low than it was when the surface temperature was incremented from low to high. However, the magnitude of the hysteresis was dependent on the rate at which the

temperature was increased when going from low to high temperature, with a slower rate of temperature change resulting in a reduced hysteresis (not shown). Figure 3.5 shows the change in the CO, O, and O_2 signals after a sudden increase in the surface temperature from 800 to 1875 K, as described in Section 3.2A. The CO flux decreased to the values on the lower hysteresis loop gradually over time, with the biggest drop in flux occurring in the first hour after the temperature spike. The flux was stable after about 200 minutes. Thus, the hysteresis in the temperature-dependent CO flux will disappear when the temperature is changed very slowly, in which case the flux will follow the lower curve in Figure 3.4c.

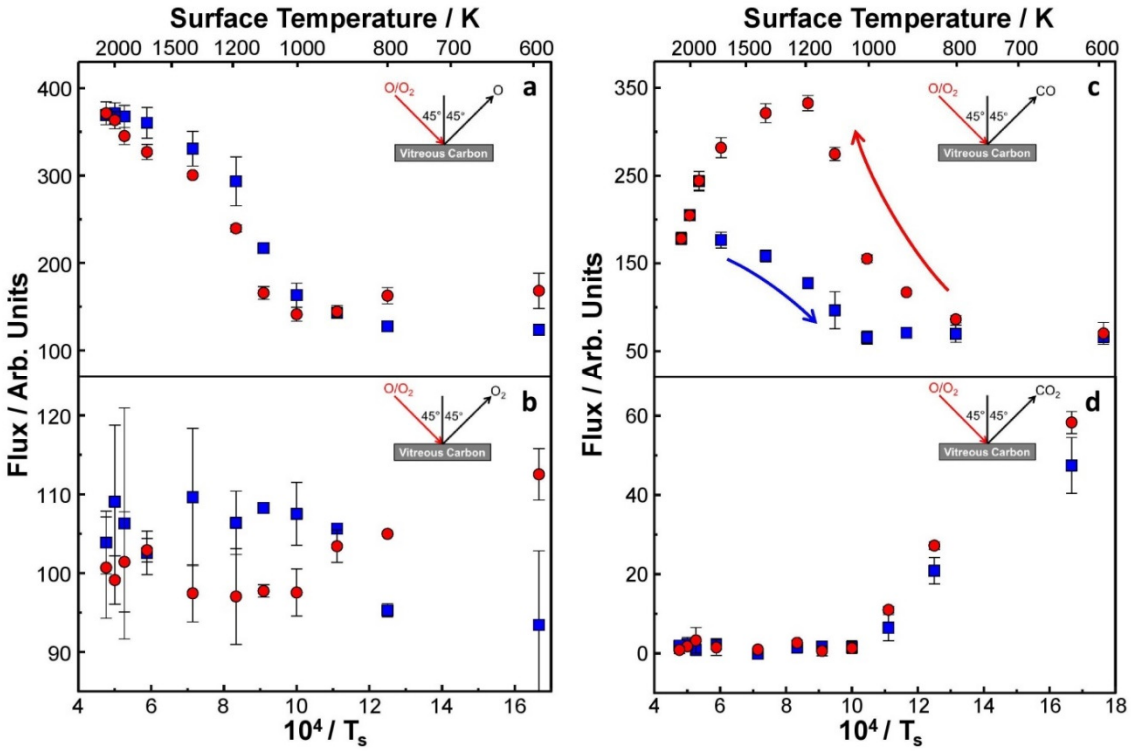


Figure 3.4. Integrated flux of (a) O, (b) O_2, (c) CO, and (d) CO_2 products as a function of surface temperature, following bombardment of the vitreous carbon surface with the O/O_2 beam at $\theta_i = \theta_f = 45°$. For each point, data were accumulated for a total of 500 (O and O_2) and 1000 (CO and CO_2) beam pulses. The time taken to cover the whole temperature range (either low to high or high to low) was ~200 minutes. The fluxes represented by the red points correspond to increasing surface temperature, and the fluxes represented by the blue points correspond to decreasing surface temperature.

Regardless of the rate of temperature change, the CO product flux reaches a maximum as the temperature is increased and then starts to decrease at higher temperatures. Note that when the surface temperature is increased the temperature of maximum flux may vary from ~1300 to ~1900 K depending on the rate at which the temperature is changed. The angle-dependent TOF distributions during O/O_2 bombardment, described below in Section 3.3C,

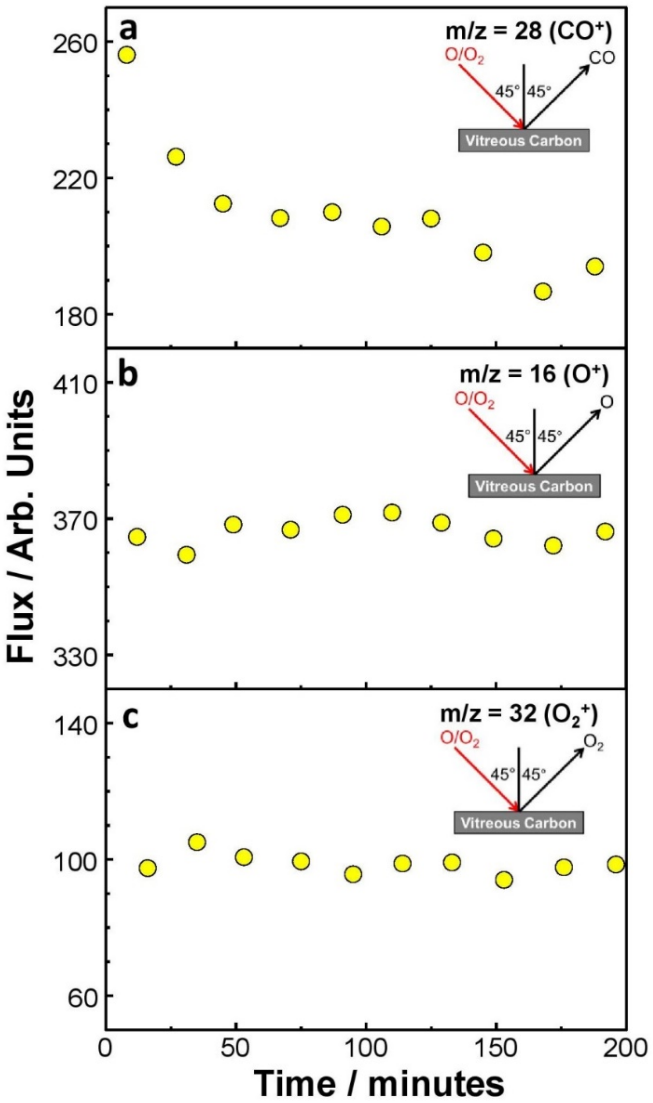


Figure 3.5. Dependence of scattered flux on time for (a) CO, (b) O, and (c) O_2 after a sudden increase in the surface temperature from 800 K to 1875 K, during bombardment of the vitreous carbon surface with the O/O_2 beam at $\theta_i = \theta_f = 45°$. For each point, data were accumulated for 500 (O and O_2) and 1000 (CO) beam pulses.

were collected long after a steady-state had been reached, and one of the focus temperatures was 1875 K, which is very close to the temperature of maximum CO flux under steady-state conditions.

3.3B Inelastic Scattering of Ar

In order to determine if the TD O atoms described above were the result of a physical change in the surface brought about by its elevated temperature, a beam of hyperthermal Ar atoms was directed at the surface. Figure 3.6 displays representative TOF distributions for Ar scattering from surfaces at three temperatures, with $\theta_i = \theta_f = 45°$. The surface temperature had little effect on the scattering of hyperthermal Ar. TOF distributions for every final angle and every surface temperature sampled from 600 to 2100 K only contained an IS feature. The absence of a peak at slow times (~400 μs) in the TOF distributions indicated that Ar atoms did not scatter thermally from the surface. As seen in Figure 3.7, the peak flight times decreased with increasing final angle, which is indicative of structural scattering.[88] The flux-integrated angular distributions for Ar scattering from both the 800 and 1875 K surfaces were nearly identical (Figure 3.7b,d) and had maxima well beyond the specular angle. It is not surprising that the IS dynamics are mostly independent of surface temperature, as the interaction time between the impinging atom and the surface is so short that thermal motions hardly affect the outcome of the collision. The main effect of the increasing temperature is expected to be from the physical roughening (thermal roughening) of the surface, which would enhance multiple-bounce scattering and perhaps drive incident atoms toward thermal equilibrium. While increased thermal roughening apparently does not result in full thermalization of hyperthermal Ar

atoms, both angular distributions are somewhat broad, with a full width at half maximum of about 45°, indicating that the surface is rough in comparison to HOPG, which was shown to have a sharply peaked angular distribution beyond the specular direction.[84] In addition, the TOF distributions in Figure 3.6 show a slight broadening with increasing temperature,

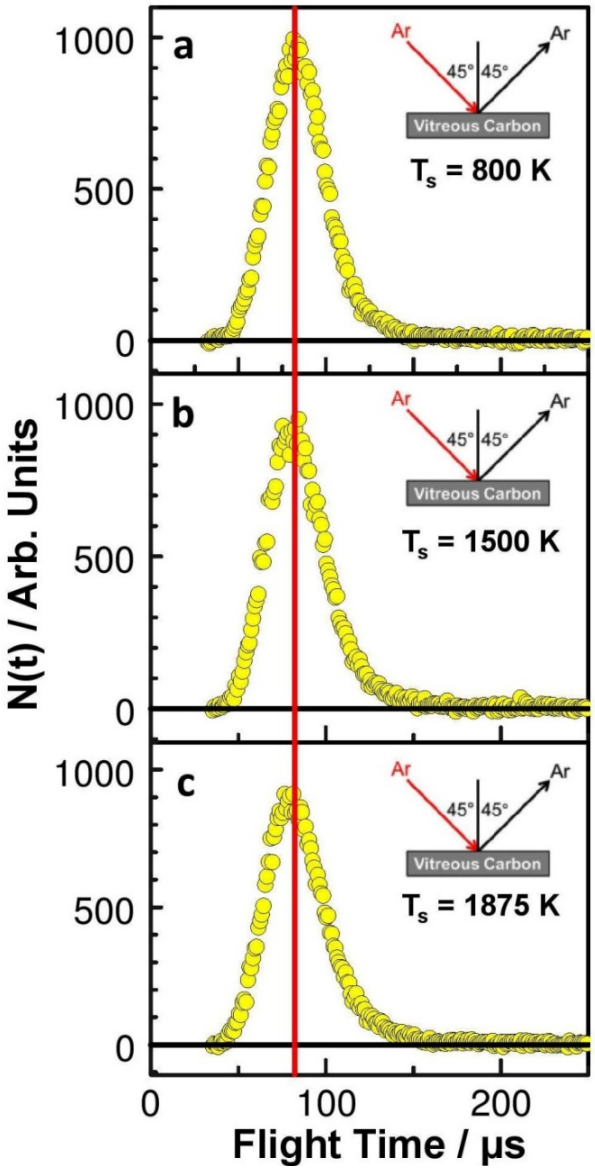


Figure 3.6. TOF distributions for Ar scattering from vitreous carbon surface for θ_f = 45° at the indicated surface temperatures, following bombardment with the O/O_2 beam at θ_i = 45°. The vertical red line has been inserted to emphasize the near invariance of the TOF distributions with surface temperature.

indicative of a larger range of energy transfers at the surface, albeit for IS and not TD processes. Although effects of thermal roughening can be observed in the scattering dynamics of hyperthermal Ar, there is no evidence that physical changes in the surface associated with temperature lead to significant energy loss and enhanced thermal desorption. Thus, such physical changes cannot explain the large TD signals observed in the O-atom TOF distributions in Figure 3.3 at higher surface temperatures.

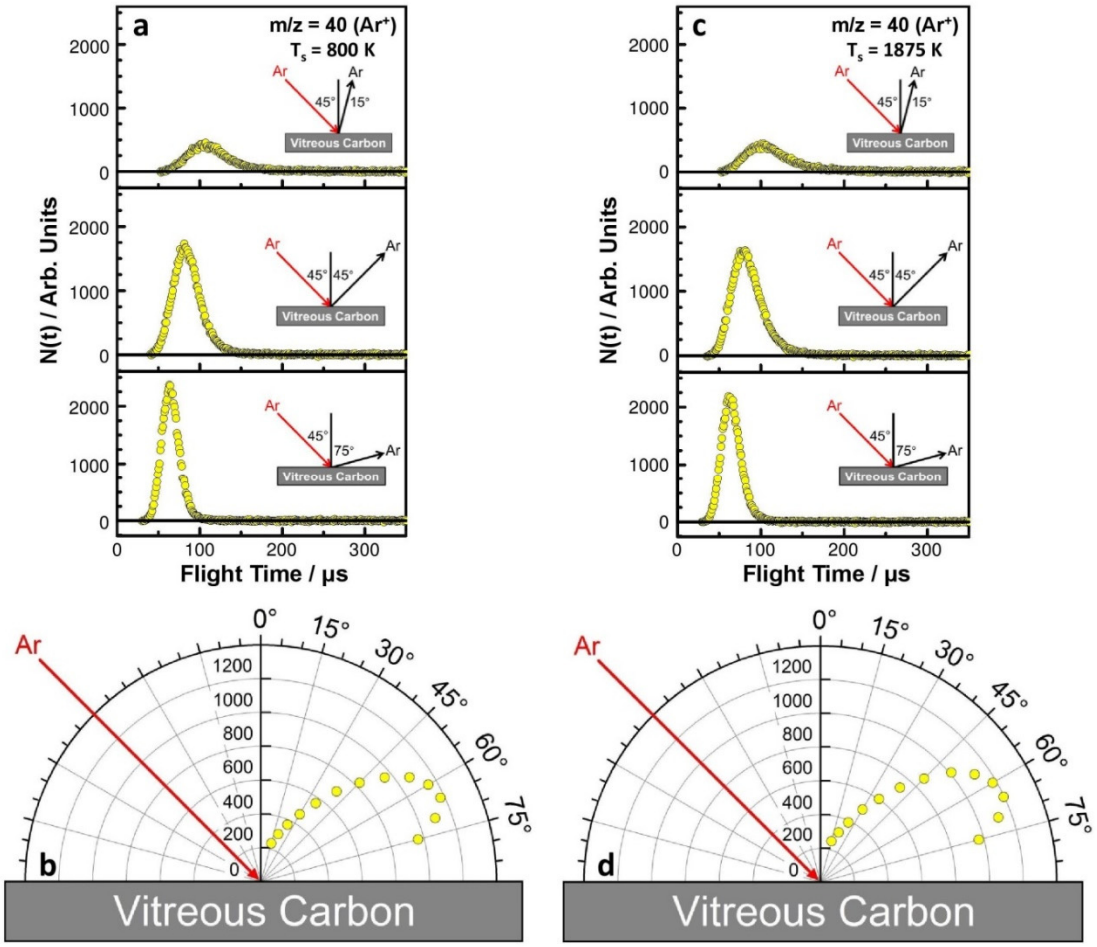


Figure 3.7. Representative TOF (a,c) and flux-integrated angular distributions (b,d) for Ar atoms scattering from a vitreous carbon surface at 800 K (left) and 1875 K (right), following bombardment with the Ar beam, whose energy distribution is shown in Figure 3.2, at θ_i = 45°. The corresponding final angles are indicated beside each TOF distribution.

3.3C Inelastic and Reactive Scattering Dynamics during O/O_2 Bombardment

Figure 3.8 displays representative TOF distributions, corresponding translational energy distributions, and flux-integrated angular distributions for O atoms that exited vitreous carbon surfaces held at 800 and 1875 K after colliding with $\theta_i = 45°$. The flux of IS O atoms increases with final angle and reaches a maximum near 50° before decreasing again. While the dynamical behavior and signal magnitude of the IS O atoms hardly change with surface temperature, the signal magnitude of the thermally desorbed O atoms increases dramatically at the higher temperature, as discussed above. The angular distributions of the TD O atoms appear to have maxima at the surface normal and are fit well by a $\cos^n\theta_f$ distribution, with n = 1.55 and 1.46 for surface temperatures of 800 and 1875 K, respectively. The TOF signal at long flight times does not return to zero, because of the effusive background from the source chamber; a high density of O atoms ($\sim 10^{-3}$ Torr) is produced in the source chamber with each beam pulse, and some of these O atoms can slowly effuse through the skimmer and thermally scatter from the surface into the detector before they are pumped away by the source diffusion pump.[74] The distorted slow tail in the TOF distribution makes it difficult to determine the temperature of the surface by fitting a MB distribution to the thermal desorption component in the O-atom TOF distributions. The "apparent" surface temperature is accurate to +/- 100 K, meaning that the TOF distributions for the TD components could be fit well by MB distributions with temperatures from 700 to 900 K or from 1775 to 1975 K. These O-atom TOF distributions were used to determine the nominal temperatures of 800 K and 1875 K, respectively. Translational energy distributions for the IS and TD components were derived from the

separated TOF distributions under the assumption that the hyperthermal O-atom beam was monoenergetic.[74,78] It has been shown that the translational energy distributions resulting from this procedure are broader than they should be. Furthermore, the monoenergetic beam approximation breaks down for direct inelastic scattering at angles far from surface normal

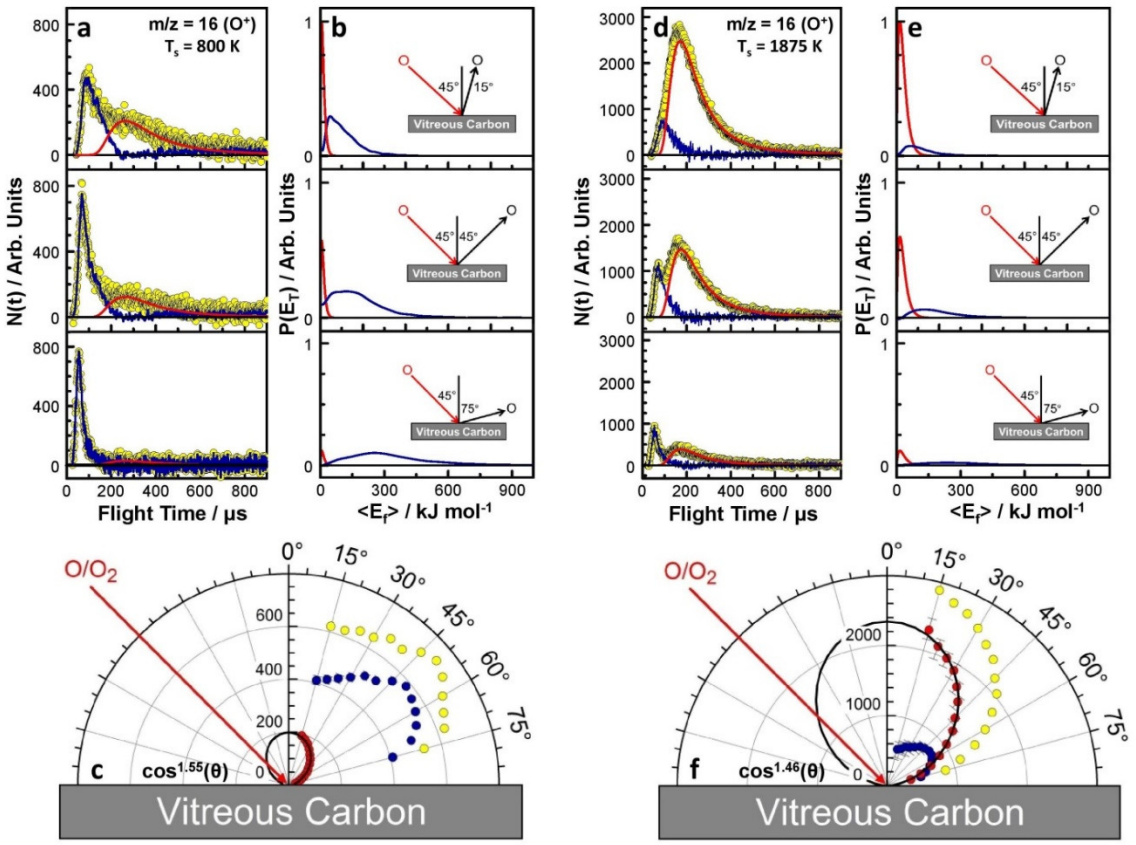


Figure 3.8. Representative TOF (a,d), translational energy (b,e), and flux-integrated angular distributions (c,f) for O atoms scattering from a vitreous carbon surface at 800 K (left) and 1875 K (right), following bombardment with the O/O_2 beam at $\theta_i = 45°$. The corresponding final angles are indicated beside each translational energy distribution. Total values [for number density (a,d), energy (b,e), or flux (c,f)], nonthermal scattering (IS), and thermal desorption (TD) are represented by yellow, blue, and red colors, respectively. The TD components in (c) and (f) have been fit to $\cos^n\theta_f$ distributions, with n given in the respective panels. The translational energy distributions (b,e) have been plotted such that their TD components are normalized to 1.0; therefore, only the shapes, and not relative fluxes, of the translational energy distributions may be compared between plots of data collected at different angles or temperatures.

when little kinetic energy is lost by the inelastically scattered atoms or molecules. This breakdown can be seen in the final translational energy distributions for nonreactive species where there are nonzero probabilities for final translational energies greater than the average translational energy of the beam. Nevertheless, the errors caused by the monoenergetic beam approximation are small, and the average final energies of the scattered species are accurate.[78] Similar to the scattered Ar atoms (Figure 3.7), the IS O atoms become faster at larger final angles, again indicative of structural scattering.[88] The translational energy distributions for the IS O atoms are quite broad, again suggesting that the sample surface is rough on an atomic level. The angular distributions for IS O atoms (Figure 3.8c,f) are broader than those observed for the scattering of Ar atoms (Figure 3.7b,d), which indicate scattering from a rougher surface and might be the result of a relatively high surface coverage of O atoms.[9] Another possible contribution to the broad angular distribution of IS O atoms in comparison with that of Ar might be the stronger atom-surface interaction potential of O. However, the effect of the interaction potential is apparently small compared to the effect of the surface roughness, as evidenced by the similarity between the angular distributions for IS O atoms and those for the much weaker-interacting IS O_2 molecules, which will be discussed below. The angular distribution for IS O atoms is narrower at a surface temperature of 1875 K than of 800 K, suggesting that the surface became smoother at the higher temperature. Thus, it is plausible that the oxygen surface coverage decreases at higher temperatures. A decreasing oxygen coverage (i.e., less sticking) at higher surface temperatures would be consistent with the increasing TD signals for O at the higher surface temperature (compare Figure 3.8d with Figure 3.8a).

In contrast to the scattering of O atoms, IS of O_2 was dominant at low and high surface temperatures, with TD becoming less important at the higher temperature (Figure 3.9). Using the estimate of 800 K for the lower-temperature surface, a MB distribution fits the slow tail of the TD component well (Figure 3.9a). Subtracting the MB fit at 800 K from the overall TOF distribution leads to an apparently bimodal IS component, and this bimodality is especially prominent in the corresponding translational energy distribution (Figure 3.9b). It is not likely that the slower "bump" in the IS component is the result of an error in the temperature used in the MB fit of the TD component. An unrealistic MB temperature of 1050 K is required to eliminate the slow bump when the MB component is subtracted from the overall TOF distribution, but when this temperature is used, the fit to the slow tail of the TD component is poor. Thus, we chose to use the temperature of 800 K for the lower-temperature MB fit, because it is consistent with the fit to the slow tail of the O_2 TOF distributions, the results for O-atom desorption, and the observation of a dull-red glow from the sample surface that was only visible when the lights in the laboratory were turned off. The presence of two parts in the IS component suggests two dynamical pathways. The faster (or higher-energy) part of the bimodal IS component exhibits dynamics that are very similar to the IS component of the O_2 signal from the higher temperature surface (Figures 3.9d,e). The behavior of this component is analogous to that of IS O atoms (Figure 3.8), and we conclude that it arises from impulsive scattering of O_2, which is a significant component of the incident beam (7 mole percent). The slower part of the IS component appears in the data for the lower-temperature surface but is essentially absent in the data for the higher-temperature surface. We assign this extra feature to O_2

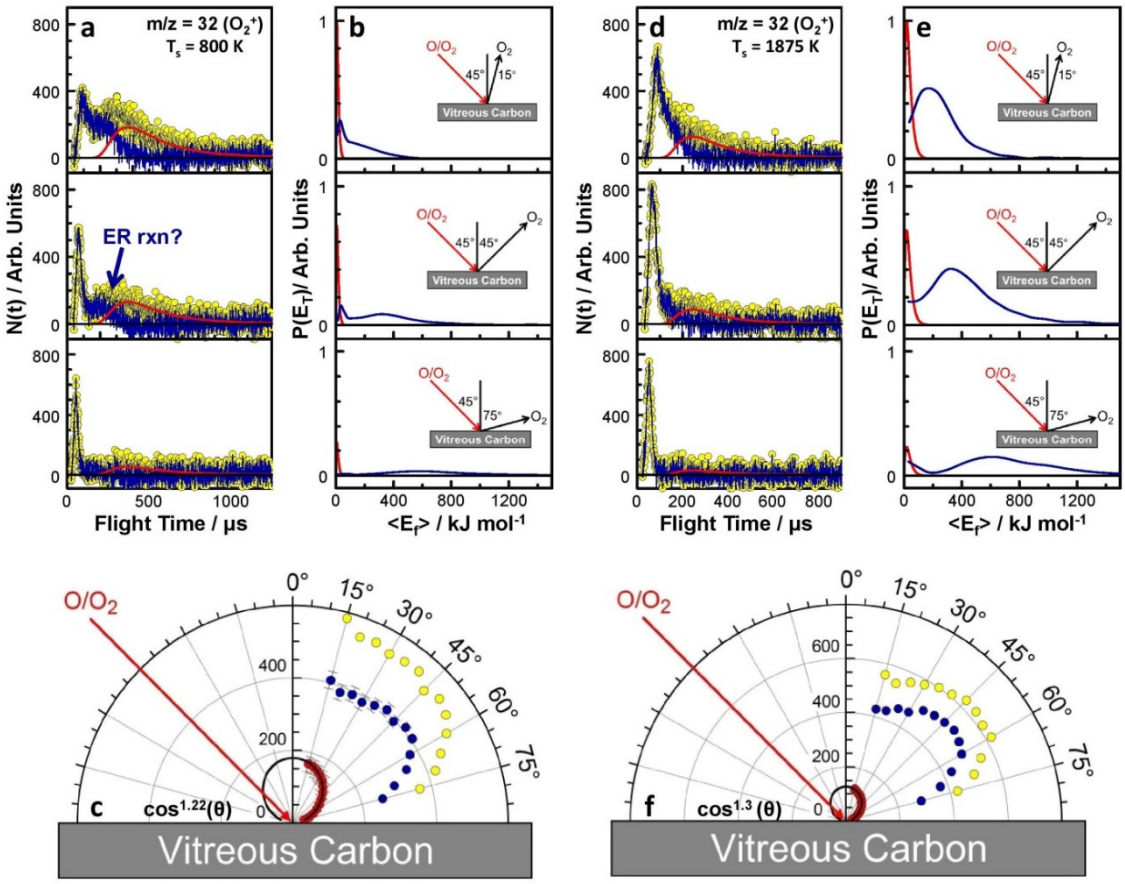


Figure 3.9. Representative TOF (a,d), translational energy (b,e), and flux-integrated angular distributions (c,f) for O_2 molecules scattering from a vitreous carbon surface at 800 K (left) and 1875 K (right), following bombardment with the O/O_2 beam at θ_i = 45°. The corresponding final angles are indicated beside each translational energy distribution. Total values [for number density (a,d), energy (b,e), or flux (c,f)], nonthermal scattering (IS), and thermal desorption (TD) are represented by yellow, blue, and red colors, respectively. The TD components in (c) and (f) have been fit to $\cos^n\theta_f$ distributions, with n given in the respective panels. The slower nonthermal signal with a surface temperature of 800 K is believed to arise from a direct Eley-Rideal reaction of an incident O atom with an O atom that is resident on the surface. The translational energy distributions (b,e) have been plotted such that their TD components are normalized to 1.0; therefore, only the shapes, and not relative fluxes, of the translational energy distributions may be compared between plots of data collected at different angles or temperatures.

produced through a direct Eley-Rideal reaction between incident O atoms and O atoms residing on the surface. The disappearance of such Eley-Rideal reaction products at the higher temperature is consistent with evidence of reduced oxygen coverage at increasing surface temperatures, which implies fewer reagent O atoms at the surface. While the angular distribution of the IS O_2 molecules from the higher-temperature surface (Figure 3.9f) resembles that for O atoms scattering from lower- and higher-temperature surfaces (Figure 3.8c,f), with a broad maximum near $\theta_f = 55°$, the angular distribution for the apparent IS O_2 molecules that scatter from the lower-temperature surface (Figure 3.9c) is nearly constant from the minimum final angle of 15° to about 55°, where it then decreases rapidly with increasing final angle. Assuming that the dynamics of IS O_2 are mostly independent of surface temperature, as would be expected for this nonthermal scattering process and which was confirmed by Ar- and O-atom scattering data in Figures 3.7 and 3.8, the angular distribution for the slower IS bump in the lower-temperature O_2 data could be approximated by subtracting the overall nonthermal O_2 angular distribution from the IS angular distribution obtained from the higher-temperature surface. The result suggests that the Eley-Rideal O_2 products scatter closer to the surface normal than the IS O_2, with a maximum flux at roughly $\theta_f = 20°$. The translational energies of the Eley-Rideal products are tens of kJ mol^{-1} (i.e., hyperthermal), but these energies are much lower than those for the IS O_2, which tend to be around 200 kJ mol^{-1} or higher, depending on the final angle. Scattering closer to the surface normal with significant internal excitation is typical for Eley-Rideal reaction products.[9,11,75,89]

The average fractional energy transfers of O and O_2 as a function of deflection angle, $\chi = 180 - (\theta_i + \theta_f)$ are indicative of sphere-like scattering on an atomically rough surface. Figure 3.10 shows the dependence of the average fractional energy transfer of IS O atoms and O_2 molecules as a function of χ, at two surface temperatures for O and at the higher temperature for O_2. (Data for O_2 scattering from the lower-temperature surface were not used because of the difficulty in distinguishing the IS O_2 from the O_2 reaction products of an Eley-Rideal reaction.) The data for O-atom scattering in Figure 3.10a,b were described well by a soft-sphere model, which allows for excitation of internal modes, whose energy is designated as E_{int}, of a collection of recoiling surface atoms with an effective mass, m_s.[38] The model uses two parameters, m_s and E_{int}/E_i, where E_{int}/E_i is the fraction of the incidence translational energy that goes into internal excitation of the localized collection of surface atoms and, in the case of molecular scattering, the internal excitation of the scattered molecule. In the limit of no such internal excitation, then a hard-sphere scattering model would apply. In fact, a hard-sphere model describes well the average fractional transfer of the impulsively scattered O_2 as a function of χ (Figure 3.10c). Although the higher mass and energy of incident O_2 might be expected to promote more internal excitation than O with the localized group of colliding surface atoms, the strong interaction potential of O compared with O_2 may contribute to the larger E_{int}/E_i for impulsive scattering of O.

The dominant reaction product was CO (see Figure 3.11). The shape of the TOF distributions for CO scattering from low- and high-temperature surfaces was independent

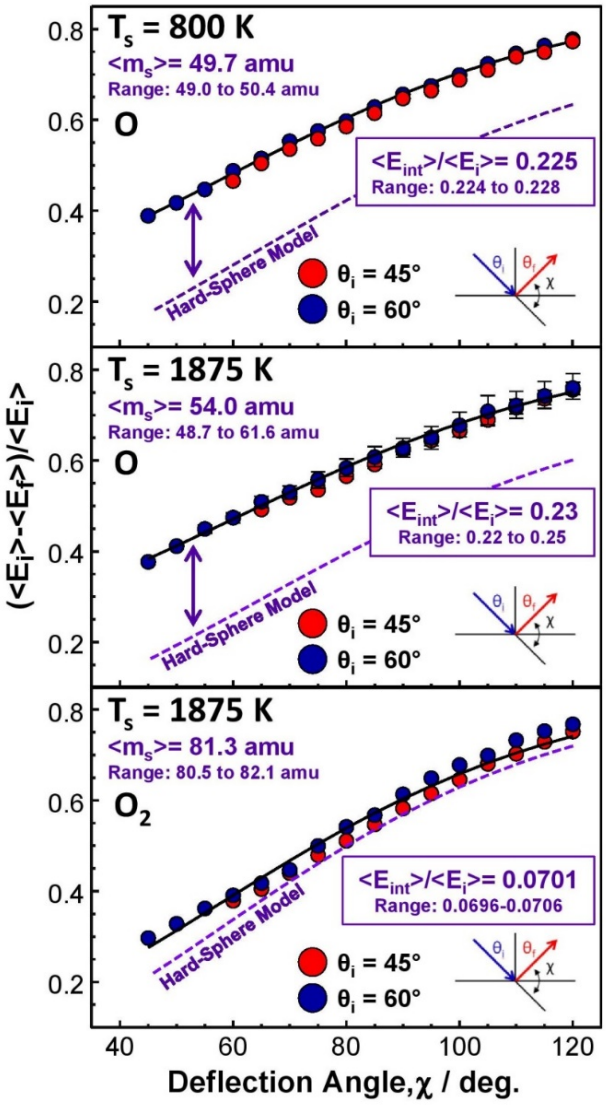


Figure 3.10. Average fractional energy transfer as a function of deflection angle, χ, for impulsively scattered (IS) O atoms or O_2 molecules on a vitreous carbon surface at the temperatures indicated, following bombardment by the O/O_2 beam at θ_i = 45° (red symbols) or θ_i = 60° (blue symbols). The solid lines in give the prediction of the "soft-sphere" model, where the incident atom interacts with a region of the surface with effective mass, m_s, and this region may absorb internal energy in the center-of-mass reference frame. The m_s value and the ratio of the average internal excitation to average incidence energy ($\langle E_{int}\rangle/\langle E_i\rangle$) that yield the best fit to the data are shown in each panel. The dashed lines give the prediction of the hard-sphere model with the same respective m_s but where the interacting surface fragment (and scattered molecule in the case of O_2) is(are) assumed to absorb no internal energy in the center-of-mass frame.

of θ_f and consisted of a broad, structureless peak at relatively long flight times, signifying scattering dynamics that are drastically different from those of non-reactively scattered O and O_2. The TOF distributions for CO were separated into nonthermal and thermal components in a manner analogous to the separation of the IS and TD components in the TOF distributions for O and O_2, using the estimated temperatures of 800 and 1875 K for the two surface temperatures. Given these temperatures, the TOF distributions appeared to

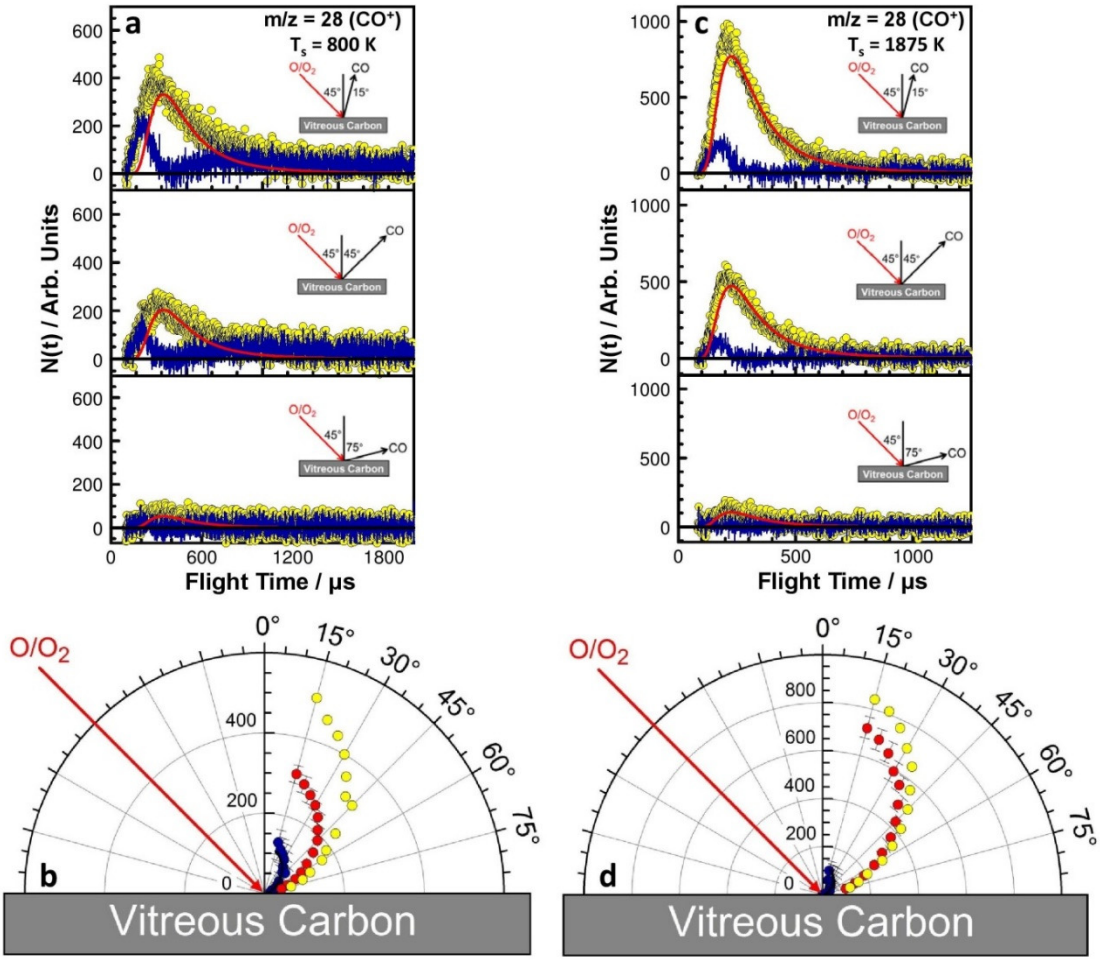


Figure 3.11. Representative TOF (a,c) and flux-integrated angular distributions (b,d) for CO molecules scattering from a vitreous carbon surface at 800 K (left) and 1875 K (right), following bombardment with the O/O_2 beam at θ_i = 45°. The corresponding final angles are indicated beside each TOF distribution. Total values [for number density (a,c) or flux (b,d)], nonthermal scattering, and thermal desorption are represented by yellow, blue, and red colors, respectively.

reflect mostly thermal scattering, but there was additional unresolved signal at short flight times that could not be accounted for by thermal scattering at these temperatures. While this signal constitutes a nonthermal scattering component in our analysis, it is possible that a larger fraction of the CO products observed could be the result of thermal desorption if the surface temperature used for the MB distribution were in error. The CO TOF distributions from the higher temperature surface can be fit well by a MB distribution with a temperature of 2120 K, although the distributions from the lower temperature surface cannot be fit by a single MB distribution at any temperature. The very high MB temperature needed to fit the higher-temperature distributions and the impossibility of fitting the lower-temperature distributions suggest that at least some fraction of CO molecules do not exit the surface in a simple thermal desorption process. The angular distributions for the total CO flux and for its assumed nonthermal and thermal components seem to have maxima toward the surface normal (Figure 3.11b,d). The angular distributions are very similar in shape for CO exiting the lower- and higher-temperature surfaces, but the CO flux is roughly double from the higher-temperature surface. Although the TOF distributions for CO suggest that the CO product is largely thermal, the angular distributions are much narrower than the expected $\cos\theta_f$ distribution for thermal desorption, again suggesting a complex and possibly nonthermal process that leads to CO.

While the TOF distributions of CO scattering from the lower- and higher-temperature surfaces are similar, there is a key difference in the tails of the distributions at long flight times. The TOF distribution for CO from the higher-temperature surface goes to zero at long times, and the shape of this long tail can be fit well by a MB distribution.

On the other hand, the TOF distribution for CO from the lower-temperature surface does not return to zero at long times, indicating the presence of CO molecules that do not promptly desorb within a few microseconds after the incident O atoms collide with the surface (there is no effusive background from CO in the pulsed beam source that could contribute to a slow background signal). The long tail in the TOF distribution corresponding to the lower-temperature surface can be fit well if it is assumed to be the sum of a MB component at 800 K and a convolution of a MB component with an exponential fall-off having a life-time of ~1500 μs (Figure 3.12). The success of this simple two-component fit suggests, but does not prove, that a fraction of the CO products on the lower-temperature surface are produced through a process that exhibits first order kinetics.

A secondary reaction product was CO_2, which was below detectable levels when the surface temperature was above 1100 K (Figure 3.13). Representative TOF and angular distributions for CO_2 scattering from the lower-temperature surface are shown in Figure 3.13. Similar to the CO data, the TOF distributions for CO_2 are characterized by a single, broad peak at long flight times, which could not be fit by a single MB distribution, again indicating that CO_2 might be produced through thermal and nonthermal reaction mechanisms. Unlike the scattering of CO, the TOF distributions returned to zero at long times, suggesting that the reaction occurred promptly after the incident beam pulse struck the surface. The angular distributions for both components have maxima toward the surface normal and deviate significantly from a $\cos\theta_f$ distribution.

3.4 Discussion

The temperature dependence of the reactive CO and CO_2 signals (Figure 3.3) exhibits non-Arrhenius behavior, where the rate of increase in the reactivity of hyperthermal O atoms with a vitreous carbon surface apparently slows and even becomes negative with increasing temperature. As the surface temperature increases from ~600 to

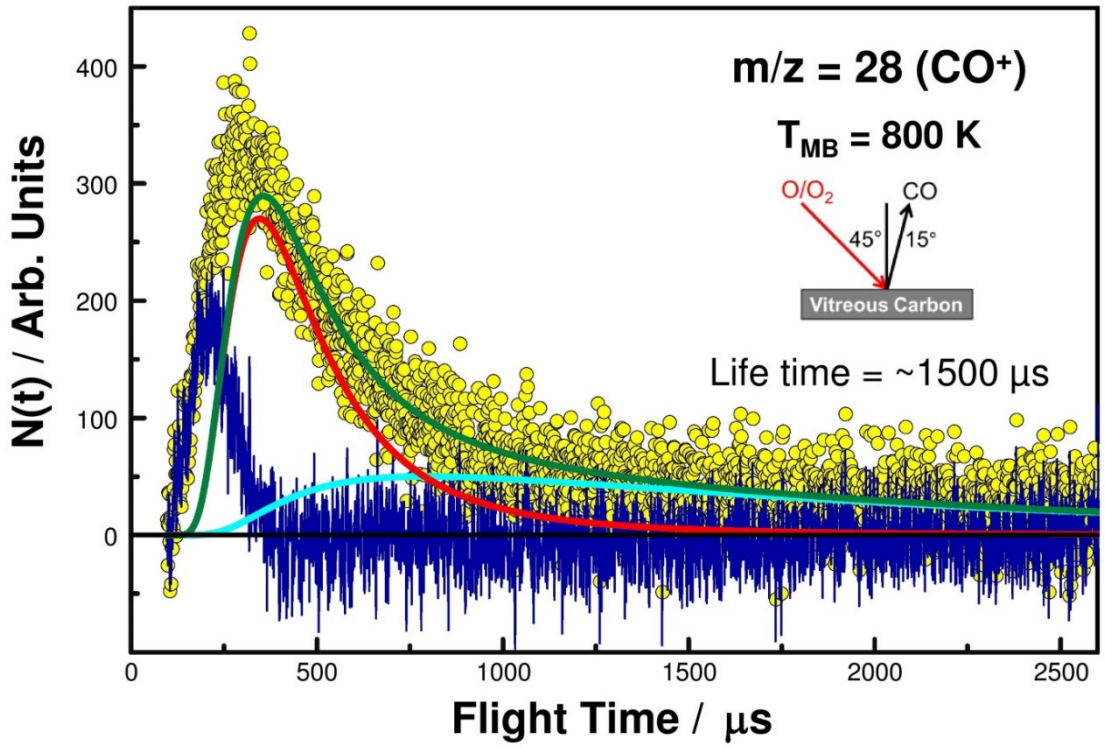


Figure 3.12. Representative TOF distribution for CO molecules scattering from a vitreous carbon surface at 800 K, following bombardment with the O/O_2 beam at θ_i = 45°. The slower portion of the TOF distribution has been fit well (green curve) by assuming it comes from the sum of a MB component at 800 K (red curve) and a convolution of a MB component at 800 K and a first-order (or pseudo-first-order) process that produces CO with a lifetime of ~1500 µs (light blue curve). The red curve corresponds to thermally desorbed CO that exits the surface promptly after O-atom bombardment, and the light blue curve represents thermally desorbed CO that exits the surface slowly after O-atom bombardment, possibly as a result of the Boudouard reaction. The dark blue curve is the difference between the total TOF distribution and the green curve; the blue curve is thus assumed to represent CO products that scatter through a nonthermal process.

~2100 K, the CO_2 signal drops quickly to zero above 1100 K, and the CO signal rises to a maximum at ~1400 K and then decreases. In addition, the CO flux shows a pronounced hysteresis where increasing surface temperatures lead to much higher CO flux than do decreasing temperatures (Figure 3.4c). The temperature dependence of the CO signal is similar to what was observed by Olander et al. in their studies of molecular oxygen reacting

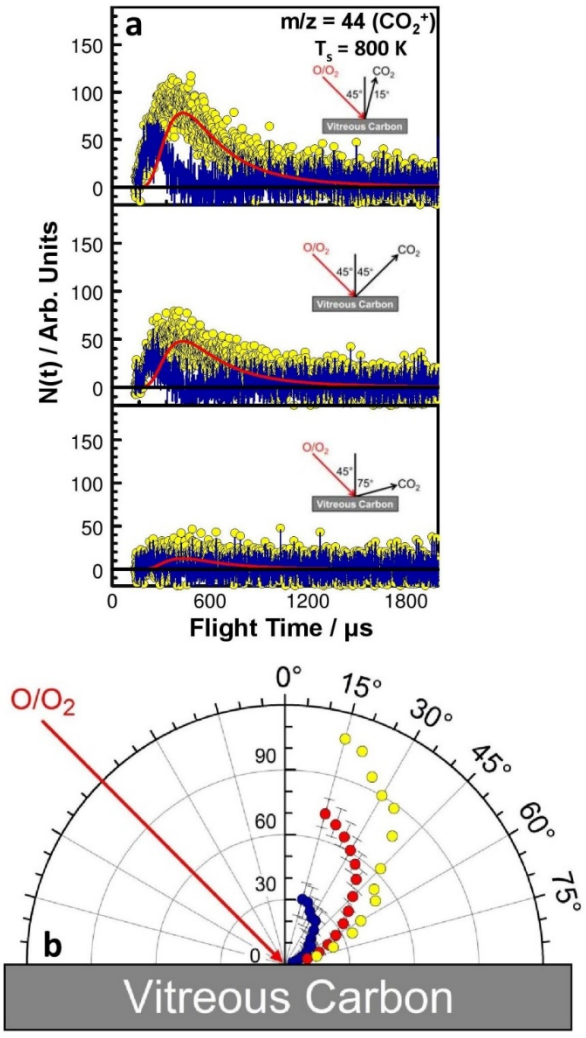


Figure 3.13. Representative TOF (a) and flux-integrated angular distributions (b) for CO_2 molecules scattering from a vitreous carbon surface at 800 K, following bombardment with the O/O_2 beam at θ_i = 45°. The corresponding final angles are indicated beside each TOF distribution. Total values for number density or flux, nonthermal scattering, and thermal desorption are represented by yellow, blue, and red colors, respectively.

with HOPG at high temperatures.[22] They suggested that there are more reactive sites on the HOPG surface at lower temperatures and that these sites are removed by annealing at higher temperatures. At first the reactivity increases with temperature, but when the temperature is elevated sufficiently the number of reactive sites decreases, which hinders the reaction rate. When the temperature is decreased from a high temperature, the number of reactive sites starts relatively low and does not recover until a much lower temperature has been reached. The earlier data did not probe the nature of the reactive sites. Following the general explanation of the hysteresis by Olander et al., we would conclude that adsorbed oxygen is closely linked with the reactive sites on a vitreous carbon surface that is bombarded by O atoms. We observed that the flux of TD O atoms increases significantly with surface temperature (Figures 3.3 and 3.8), indicating less sticking of O atoms on the surface. Hence, if surface-adsorbed O atoms are required for eventual CO production, then the CO product flux would be expected to be limited by the reduced sticking of O atoms on the surface. Indeed, we do observe that the CO product flux reaches a maximum at high temperatures where the sticking of O atoms to the surface is apparently low.

The observation of significant quantities of TD O atoms is a counterintuitive result, as O atoms would be expected to be very reactive with carbon, especially if they had time to come into thermal equilibrium with the surface. One possible explanation for the TD O atoms is that incident O atoms with hyperthermal energies penetrate into the surface before desorbing. Although data on the penetration of energetic atoms or ions into vitreous carbon do not exist, data obtained for HOPG may serve as an analog for understanding high-energy collisions with vitreous carbon. The threshold energies for Ne^+ and Ar^+ ions penetrating

into HOPG are reported to be 32.5 ± 2.5 eV and 43.5 ± 1.5 eV, respectively.[90] Given the masses of these two noble-gas ions, they are expected to have similar penetration thresholds as O and O_2. These threshold energies are significantly higher than the maximum translational energies of the O and O_2 in the incident beam, which are 5.7 eV (O) and 11.5 eV (O_2). Furthermore, it is unlikely that extreme temperatures would significantly change the values of these threshold energies. This supposition is reinforced by the fact that Ar atoms scatter only impulsively and that the Ar scattering dynamics remain essentially unchanged with surface temperature (Figure 3.7). It has been shown that atoms penetrating a surface have substantially different scattering dynamics than atoms that simply scatter impulsively from the surface.[91] Thus, we conclude that the thermal O atoms exiting the surface do not originate from O atoms that have penetrated the surface.

Instead of penetration, one might imagine that incident O atoms could become momentarily trapped in pores at the surface and lose most of their energy before desorbing. Although vitreous carbon comprises closed pores and is considered impenetrable to gases,[50-51] the porous structure of vitreous carbon may be exposed by removal of carbon in the form of CO and CO_2. Even after incident O atoms have reacted with all reactive sites, the residual rough, porous structure could conceivably lead to multiple collisions and enhanced trapping of O atoms at the surface. An increased surface temperature might be expected to increase the reactivity and lead to a more porous structure at the surface and therefore to more trapping of O atoms. However, the temperature dependence of the TD O-atom signal is reversible, so if a porous structure were revealed at high temperatures it should still persist at low temperatures and lead to the same mechanical trapping of O

atoms. The fact that the TOF signals at low and high surface temperatures are reproducible through several cycles of heating and cooling is therefore at odds with the idea that the opening of pores in the vitreous carbon could be the explanation for the thermal O-atom signal that grows with increasing surface temperature.

Thermal roughening of the surface would be a potential way to drive incident O atoms into thermal equilibrium with the surface that could explain both the increase in TD O atoms at higher temperatures and the reversibility in the TOF signals with temperature. It has been observed that modest increases in the temperature of a liquid surface bombarded by noble-gas atoms can lead to a higher fraction of thermally desorbing atoms.[92] However, the dependence of the Ar scattering dynamics on temperature discounts this possibility. The hyperthermal beam of Ar atoms (747 kJ mol^{-1}) was more energetic than the hyperthermal beam of O atoms (481 kJ mol^{-1}), so the colliding Ar atoms would need to lose more energy than the O atoms in order to come into thermal equilibrium with the surface; thus, a lower fraction of Ar atoms would be expected to scatter from the surface with thermal energies. Nevertheless, if thermal roughening were the explanation for the strong thermal O-atom signal at high temperatures, then the Ar TOF distributions should show at least a small TD component that increases with surface temperature, which they do not. The only apparent effect of thermal roughening on the Ar scattering data is in the width of the Ar TOF distributions, which does increase slightly with surface temperature. The temperature-dependent increase in the width of translational energy distributions for impulsive scattering has been observed previously.[93] The subtle increase in the width of the Ar TOF distributions with increasing surface temperature (Figure 3.6) is a thermal

roughening effect, but this effect is much too small to explain the thermal O-atom signal at high surface temperatures. Because the thermal desorption of O atoms is not an effect of mechanical surface roughening, then we conclude that it must be the result of the unique chemical interactions between incident O atoms and the vitreous carbon surface. The strength of those interactions relative to the Ar-surface interaction potential is no doubt the reason for the dramatically different scattering dynamics observed for the two atoms.

As suggested at the beginning of this section, the substantial increase in the TD flux of O atoms with temperature implies decreasing oxygen coverage as the surface temperature is increased (during stead-state O-atom bombardment). Thermal and nonthermal interaction pathways were apparent at all temperatures; however, the dominant scattering mechanism of the O atoms changed, for example, from IS at 800 K to TD at 1875 K, and the overall flux of O atoms increased significantly. The comparison of O and O_2 scattering dynamics also supports the conclusion of a reduced coverage at the higher temperature. The angular distributions for the IS O atoms were similar at 800 and 1875 K: both were peaked past the surface normal and had similar intensities and widths. The near invariance in the IS O angular distributions with temperature is in contrast to the nonthermal scattering of O_2, where the angular distribution from the 800 K surface is much broader than that from the 1875 K surface. The broader angular distribution at the lower temperature was attributed to an Eley-Rideal reaction, which provides an additional pathway to produce scattered O_2. The apparent absence of this reaction at the higher surface temperature is consistent with the conclusion that the increased flux of TD O atoms reflects a lower surface coverage of oxygen, as a reduced coverage would result in fewer O atoms

on the surface that are available to react with incident O atoms. While the observation of substantial TD O-atom flux at high temperatures is unequivocal, the mechanism through which O atoms adsorb or react on the surface and then desorb thermally remains curious and will require further study to understand.

Computational studies have shown that an Eley-Rideal reaction to produce O_2 is the primary reaction pathway on an HOPG surface during oxidation by O atoms.[9,20,72] In an earlier study in our laboratory on hyperthermal O-atom interactions with a 503 K HOPG surface, we attributed much of the O_2 signal to an Eley-Rideal reaction,[20] thus demonstrating consistency between the experimental and theoretical results. Recently, Morón et al. have challenged this assignment,[9] and we now agree that the earlier attribution of a significant fraction of the O_2 signal to an Eley-Rideal reaction was incorrect, because a detailed consideration of the data for the observed nonthermal O and O_2 reveals that the scattering dynamics for these two products were similar and are best interpreted as impulsive scattering from a smooth surface.[84] Thus, we no longer believe that our earlier data support the computational results that the Eley-Rideal reaction to produce O_2 is the dominant reaction pathway under continuous bombardment of an HOPG surface by hyperthermal O atoms. Furthermore, our new results clearly indicate that this reaction is only a minor reaction pathway when hyperthermal O atoms bombard a vitreous carbon surface under steady-state conditions at 800 K and that this reaction is essentially absent at 1875 K. The dominant components of the O_2 TOF distributions at both high and low temperature have nearly the same TOF distribution as the IS O atoms. In the abstraction of an O atom adsorbed on the surface by an impinging O atom, it has been shown that a large

fraction of the available energy is partitioned into internal modes (i.e., vibrational and rotational excitation),[9] which results in a lower final translational energy and a broader angular distribution than would be observed for an O_2 molecule that is scattered impulsively from a surface.[64] Accordingly, the peak at earliest times in the TOF distributions depicted in Figure 3.9a,d is assigned to IS O_2 that is not the result of a reactive process. When the surface was at 800 K, there was an additional nonthermal component at intermediate energies between the IS and TD components. This intermediate component reflects O_2 molecules that leave the surface with relatively low translational energies, which would be consistent with the high internal excitation that has been reported for an Eley-Rideal reaction.[9] In addition, the broadening of the angular distribution for nonthermal O_2 at 800 K (Figure 3.9c) suggests that the intermediate O_2 component has a maximum away from the surface normal yet below the specular angle, which is also consistent with an Eley-Rideal reaction.[9,11,75]

Unlike O-atom desorption, the flux of the TD O_2 shows a modest decrease with increasing surface temperature (Figure 3.9). O_2 is bound to the surface by a small barrier (0.1 eV),[56-58] indicative of physisorption, and has a very low sticking coefficient (10^{-14}), so it is expected to scatter without reacting.[59,64] Indeed, it appears that most of the O_2 scatters impulsively; however, there is still clear evidence of a relatively low flux of TD O_2 which must come either from a non-reactive process that leads to thermal desorption or from a reaction that produces O_2 that desorbs thermally. Larciprete et al. have shown that it is possible to produce thermal O_2 from the cyclic addition of O atoms in epoxide groups present on the surface.[8] If the TD O_2 were the result of such a reaction or from thermal

recombination of O atoms on the surface, then the flux of TD O_2 should decrease at increasing temperatures as the surface coverage of oxygen decreases, which is consistent with our data. It is thus possible that the TD O_2 signal that we observe is the result of recombination reactions involving O atoms on the surface. But we cannot rule out the possibility that some, or even all, of the TD O_2 signal that we observe is not the result of a reactive process but rather from O_2 that either physisorbs momentarily to the surface or loses sufficient energy to desorb thermally without physisorption.[94]

The decrease in surface oxygen coverage with temperature is inextricably linked with the ultimate decrease in the reaction probability of O atoms on the vitreous carbon surface at high temperatures. As discussed above, the Eley-Rideal reaction of incident O atoms with surface oxygen atoms to produce O_2 is essentially absent at a relatively high surface temperature of 1875 K. The Eley-Rideal reaction is nonthermal and should not depend on surface temperature; but as we do see this reaction disappear with increasing temperature, we must conclude that the surface oxygen coverage decreases with temperature. The flux of the main reaction product, CO, increases with surface temperature but then begins to decrease above ~1900 K (under steady-state conditions). The flux of the CO_2 reaction product drops quickly with increasing surface temperature and is below detectable levels above 1100 K. The reaction processes that lead to the main reaction product, CO, appear to be mostly thermal, based on the preponderance of slower products in the TOF distributions. Therefore, if Arrhenius behavior were applicable, the reaction probability to produce CO should increase with surface temperature. In fact, the CO flux does increase with surface temperature, but it reaches a maximum at 1900 K and then

begins to decrease. We surmise that the increasing reaction probability associated with increased temperature competes with the decreasing availability of surface O atoms as the temperature increases. The decrease and eventual disappearance of CO_2 with increasing surface temperature may be partially the result of the Boudouard reaction, $CO_2(g) + C(s) \rightarrow 2CO(g)$,[60] which is discussed below. But perhaps more important is the fact that the production of CO_2 requires more surface O atoms than does the production of CO; thus, the CO_2 yield would be expected to decrease with increasing temperature as the surface O atoms are depleted. The reduction in CO_2 yield could be enhanced if the increasing surface temperature leads to more rapid desorption of the CO product, because the formation of CO would be the required first step in the step-wise production of CO_2.

The Boudouard reaction may explain the long tail in the CO TOF distributions collected from the 800 K surface (see Figures 3.11 and 3.12). This long tail indicates that not all of the CO product formation occurred promptly after the beam pulse struck the surface. It is possible that a fraction of the nascent CO_2 goes on to react with the surface to form CO through the Boudouard reaction,[60] which is highly endothermic (ΔH = 172 kJ mol^{-1}) and becomes entropically favored at temperatures greater than 700 °C.[95] At 800 K, a small portion (~10%) of the CO_2 products formed through reactions between incoming O atoms and the oxidized surface could be converted to CO.[95] In addition, only the CO_2 products that remained on the surface long enough to react with a carbon site would be able to react and produce CO. Consequently, the fraction of CO produced through the Boudouard reaction would be expected to be minor fraction of the overall CO product. The long tail observed in the CO TOF distributions did indeed represent a minor fraction of the

CO product (Figure 3.11c), and such a tail was not evident in the CO TOF distributions at 1875 K or in the TOF distributions for CO_2 (Figure 3.13). As indicated in Figure 3.12, the long tail in the CO TOF distribution was fit well under the assumption that slow CO was produced through a first-order (or pseudo-first-order) process with a lifetime of ~1500 μs. The reaction rate of the Boudouard reaction at 800 K is not well known, but there is some evidence that this reaction is slow,[60,96] which would be consistent with the lifetime that we derived. The simultaneous observation of a long tail in the CO TOF distributions and absence of such a tail in the CO_2 TOF distributions is also consistent with the Boudouard reaction, as this reaction could lead to a slow CO product without affecting the observed scattering dynamics of unreacted CO_2 products. As the temperature of the surface increases, the fraction of CO_2 that would be reduced through the Boudouard reaction would be expected increase, giving rise to more CO with long apparent residence times on the surface. At higher surface temperatures, the thermal desorption of O atoms would limit the production of CO_2 and close the Boudouard channel for the secondary formation of CO, which is consistent with the absence of a long tail in the TOF distributions for CO at 1875 K. While our results suggest the intriguing possibility that the Boudouard reaction plays a role in the oxidation of carbon at elevated temperatures, further work would need to be done to confirm this tentative conclusion.

Computational studies have attempted to elucidate the reaction mechanisms for the gasification of carbon by O atoms. These studies have focused on HOPG as a model surface. It is expected that similar surface chemistry will take place on vitreous carbon, because vitreous carbon has a large aromatic ring network similar to that of HOPG.[49] The

first step in the production of CO and CO_2 is the adsorption of an oxygen atom to the surface. Some O atoms will react with carbon atoms on the surface to form semiquinone and lactone precursor sites.[20,61-62] Oxygen adatoms migrate across the surface, forming transient bonds with carbon atoms during their migration, and react at a semiquinone or lactone site to produce CO or CO_2.[20] Excess O atoms surrounding the reactive site lowers the endothermicity for reactions to produce both CO and CO_2, with more O atoms being required to lower the endothermicity for production of CO_2 to a given value.[21] Thus, these theoretical studies suggest that adsorbed O atoms are required for the production of CO and CO_2 and that more adsorbed O atoms are required to produce CO_2 than are required to produce CO. The competition between CO and CO_2 may be related to adsorbed O atoms in additional ways. The transient C-O bonds that are formed as an O atom migrates across the surface are weaker than the underlying C-C bond, making their breakage more favorable.[55] At high temperatures, a C-O bond may cleave and release the O atom back into the vacuum. A recent study suggests that this process may be aided by local O-atom collisions.[9] The consequence of C-O bond cleavage and escape of O atoms back into the gas phase is that O atoms desorb from a high-temperature surface before arriving at the precursor sites, which hinders the formation of CO and CO_2 produced through an indirect reaction mechanism. Again, because more O atoms are required for the formation of CO_2, any escape of O atoms before they can reach a reactive site will preferentially suppress the formation of CO_2 relative to that of CO. These theoretical results are consistent with our experimentally-derived deductions about the temperature-dependent reaction probabilities to form CO and CO_2, discussed above, and they offer some insight into the mechanism

through which O atoms desorb thermally with increasing likelihood as the surface temperature is increased. Neither the theoretical studies nor the experiments allow any conclusions to be drawn about the apparent nonthermal CO and CO_2. Direct, Eley-Rideal reactions are a possibility, as are several more complex mechanisms.

3.5 Conclusion

The dynamics of the interactions of O and O_2 with a vitreous carbon surface at high temperatures have been investigated with the use of a beam-surface scattering technique. Nonreactive O and O_2 and reactive O_2, CO, and CO_2 products were detected following bombardment of a vitreous carbon surface with a beam containing hyperthermal O and O_2. The dynamical behavior of these products was surveyed with a range of surface temperatures from 600 to 2100 K and investigated in detail at 800 and 1875 K. Nonreactive O and O_2 were observed to exit the surface through impulsive scattering and thermal desorption channels. The flux of O atoms that scattered from the surface with thermal energies increased dramatically with the temperature of the surface, while the flux of impulsively scattered O atoms remained essentially constant with temperature. Whereas the thermally scattered O atoms represented a small fraction of the products scattered at the lower temperatures, they were overwhelmingly dominant at high surface temperatures. Nonreactive O_2 exited the surface mostly through impulsive scattering at all temperatures, with only a small fraction accommodating to the surface temperature before desorbing thermally. The increase in thermally scattered O atoms reflects a decrease in oxygen coverage on the surface, which ultimately limits the reactivity of incident O atoms with the surface. The major reaction product was CO, and the probability to produce CO increased

with temperature to a maximum at ~1900 K (under steady-state bombardment conditions) and then decreased as the temperature was increased further. The reaction probability to produce CO_2 was comparable to that of CO at 600 K, but it dropped rapidly with increasing temperature and disappeared above 1100 K. Both the CO and CO_2 products were apparently formed through nonthermal and thermal mechanisms, but these products were most likely to exit the surface with translational energies characteristic of the surface temperature, implying that the underlying reaction mechanisms are mainly indirect. The direct (Eley-Rideal) reaction of incident O atoms with surface-adsorbed O atoms to produce O_2 was found to be a minor reaction pathway, in contradiction to the results of theoretical studies on HOPG. Evidence has been found for a secondary reaction of nascent CO_2 products with the carbon surface to produce CO, although the suggested Boudouard mechanism remains equivocal. The counterintuitive result that the reactivity of the surface decreases at high temperatures is a consequence of the desorption of O atoms at high surface temperatures, which diminishes the indirect reactions that produce CO and CO_2 and suppresses the overall reactivity of the surface.

Acknowledgments

This work has been supported by the Air Force Office of Scientific Research: FA9550-10-1-0563. V.J.M. is grateful for support from the Department of Defense (DoD) through the National Defense Science & Engineering Graduate Fellowship (NDSEG) Program.

CHAPTER FOUR

DYNAMICS OF GRAPHITE OXIDATION AT HIGH TEMPERATURE

Contribution of Authors and Co-Authors

Manuscript in Chapter 4

Author: Vanessa J. Murray

Contributions: Performed molecular beam scattering experiments and conducted data analysis. Prepared both the figures and the manuscript for publication.

Co-Author: Eric J. Smoll Jr.

Contributions: Provided crucial insight into data analysis and important feedback on data interpretation.

Co-Author: Timothy K. Minton

Contributions: Provided crucial insight regarding the experimental procedure and the interpretation of the collected data. Aided in the preparation of the manuscript and figures.

Manuscript Information Page

Vanessa J. Murray, Eric J. Smoll Jr., Timothy K Minton

Journal of Physical Chemistry C

Status of Manuscript:
____ Prepared for submission to a peer-reviewed journal
____ Officially submitted to a peer-review journal
__×__ Accepted by a peer-reviewed journal
____ Published in a peer-reviewed journal

Published online by the American Chemical Society
DOI: 10.1021/acs.jpcc.7b11772

Reproduced with permission from ACS – the American Chemical Society

DYNAMICS OF GRAPHITE OXIDATION AT HIGH TEMPERATURE

Vanessa J. Murray, Eric J. Smoll, Jr., Timothy K. Minton

Department of Chemistry and Biochemistry, Montana State University, 103 Chem/Biochem Bldg., Bozeman, MT, 59717

Abstract

Interactions of ground-state atomic and molecular oxygen, O(^3P) and O_2($^3\Sigma_g^-$), with a highly oriented pyrolytic carbon (HOPG) surface were investigated for a broad range of surface temperatures from 1100 K to approximately 2300 K. A molecular beam composed of 89% O atoms and 11% O_2, with average translational energies of 472.1 and 944.4 kJ mol^{-1}, respectively, was directed at the surface with an incidence angle, θ_i, of 45°. Angle- and velocity-resolved distributions were collected for non-reactively and reactively scattered products with the use of a rotatable mass spectrometer detector. Four scattered products were observed: O, O_2, CO, and CO_2. O atoms that exited the surface without reacting exhibited both impulsive scattering (IS) and thermal desorption (TD) components. The primary reaction product observed was carbon monoxide (CO). Carbon dioxide (CO_2) was observed only with surface temperatures below 1400 K, and O_2 was attributed to impulsive scattering of O_2 which was present in the incident beam. While there is evidence for either Eley-Rideal or hot atom reactions, CO and CO_2 were primarily formed by Langmuir-Hinshelwood (LH) reactions. However, the flux angular distributions of the LH products were significantly narrower than a cosine distribution, and the final energies were much higher than those predicted by a Maxwell-Boltzmann distribution characterized by

the surface temperature. These observations indicate that CO and CO_2 that were produced by LH reactions desorb from the surface over a barrier. The desorption barrier of CO was determined by using the principle of detailed balance (where the desorption and adsorption barriers are equal) and was found to increase from 121 ± 5 kJ mol^{-1} at 1100 K to 155 ± 7 kJ mol^{-1} at 1300 K. As the surface temperature increased, the flux of CO and CO_2 produced by LH mechanisms decreased. Simultaneously, the flux of O atoms that scattered via the TD channel increased, which reduced the surface oxygen coverage at higher temperatures. The combined effects of reduced O-atom surface coverage and increased desorption barriers for CO suppresses the reactivity of the surface at high temperatures.

4.1 Introduction

Hypersonic objects that fly through the Earth's atmosphere are subjected to high heat fluxes.[97] In order to survive such an extreme environment, a hypersonic vehicle requires a thermal protection system (TPS), which is often composed of carbon-based materials. The surface of a TPS can reach temperatures higher than 2000 K,[98] and partially dissociated air (O, O_2, N, and N_2) can react with the surface and lead to material ablation. The reaction mechanisms by which oxidation proceeds, such as Eley-Rideal (ER) or Langmuir-Hinshelwood (LH) mechanisms,[3] can greatly affect the heat flux to the surface. Additionally, scattered or desorbed products may react in the gas phase, which can be an important process for chemistry occurring in the shock layer in contact with the TPS.[12] A detailed understanding of the mechanisms by which surface oxidation proceeds at temperatures relevant to hypersonic flight would enable more accurate modeling of the heat flux to and mass loss from the surface and allow for more efficient TPS design.

Highly oriented pyrolytic graphite (HOPG) is a model carbon material for studying the oxidation of carbon-based TPSs, because its smooth and ordered surface allows for the precise study of fundamental reaction processes that lead to surface ablation. HOPG is a mosaic crystal composed of layered graphene crystallites, which can be tens of microns in length and which have their *c* axes oriented parallel to the surface normal of the overall crystal.[99] The individual graphene sheets are weakly bound together by van der Waals forces and are separated by 3.35 Å.[100] The surface of HOPG is slightly corrugated,[101-102] but molecular beam scattering experiments have shown that atoms and molecules interact with an atomically flat surface, presumably because the delocalized electrons of the topmost graphene layers present a surface that is effectively smooth.[20,84,102] The smooth surface simplifies the scattering dynamics and reduces the number of multiple-bounce collisions that occur after initial reactive and non-reactive interactions.

O_2 is only weakly reactive with HOPG and is expected to scatter inelastically from the surface with high probability. In order for O_2 to oxidize HOPG it must first dissociatively chemisorb on the surface, which can only occur when the O_2 binds at a defect site.[61-62,103] However, HOPG has a low defect density of 3-4 defects μm^{-2}, which suppresses the chemisorption of O_2.[63] Oxidation of HOPG by O_2 is also mitigated by the low sticking coefficient: 10^{-14} on a pristine surface held at 673 K and increasing to 10^{-7} on a surface with vacancy defects created by Ar^+ bombardment.[104] While O_2 can physisorb on a pristine HOPG surface, the molecule is only weakly bound (0.1 eV) and physisorption is not expected to occur at high surface temperatures.[56-58]

In contrast, O atoms readily react with HOPG. The oxidation of HOPG by O atoms begins with the formation of epoxy groups on the surface.[18] The adsorption of O on an HOPG surface is an activated process that has a barrier of 0.3 eV at room temperature.[68,105] The calculated barrier to O-atom diffusion on the surface ranges from 0.3 eV to 0.7 eV, depending on the level of theory used.[68,106] While 0.7 eV is a relatively high barrier, transition state theory predicts diffusion rates on the order of 100 s^{-1} at surface temperatures of 350 K (assuming a prefactor of 10^{13} s^{-1}), indicating that the O atoms are mobile on the surface even at relatively low surface temperatures.[8] Additionally, the diffusion barrier has been shown to decrease significantly with increasing surface temperature and decreasing O-atom surface coverage.[68,106] High resolution photoelectron spectroscopy studies of HOPG revealed that following the initial formation of epoxide groups on the surface, the surface becomes populated with ether and semi-quinone functional groups,[65] the latter of which are predicted to be the most favorable sites for reactions that produce CO and CO_2.[19] It has also been demonstrated computationally that excess oxygen around the reactive site lowers both the exothermicities and the barriers for the reactions that produce CO and CO_2.[19]

When HOPG with a surface temperature of 503 K was exposed to a beam of O atoms with a nominal translational energy of 500 kJ mol^{-1}, CO and CO_2 were formed via LH and ER reaction mechanisms.[20] The reactivity through the basal plane was faster than through the prism plane, which results in the formation of shallow, circular etch pits whose diameters increase with increasing O-atom fluence.[66] Experiments and simulations have shown that the O atoms react preferentially with carbon atoms at the edges of the etch pits

to form CO and CO_2, most likely through exothermic mechanisms in thermal equilibrium with the surface.[66,72] However, simulations have predicted that when HOPG is bombarded by high translational energy O atoms, the dominant reactive process is the recombination of O atoms to form O_2 by either ER or LH mechanisms.[20,72] While this process does not remove carbon from the surface, it could greatly affect the reactivity of HOPG by removing chemisorbed O, which is necessary for reactions that produce CO and CO_2. Moreover, both the ER and LH recombination of O atoms is exothermic and would probably increase the heat flux to the surface during hypersonic flight.[68]

The oxidation of carbon at surface temperatures relevant to hypersonic flight – i.e., greater than 1000 K – is not well understood. Rosner and Allendorf found that the mass loss of graphite filaments exposed to O and O_2 with thermal translational energies did not have an Arrhenius temperature dependence in the range of 1000 to 2000 K.[107] The rate of carbon removal was largest when the surface temperature was 1600 K, and increasing the surface temperature beyond this point resulted in a lower probability of carbon removal. For a similar temperature range, Olander et. al. measured the flux of CO produced when HOPG was exposed to O_2; this reaction also did not have an Arrhenius temperature dependence.[22] These observations were explained by invoking a two-site model for surface reactivity, which posited that at high temperatures one of the reactive sites was inactivated as the result of surface annealing, thus limiting the reactivity of the surface. More recently, a study probing the reactive and non-reactive scattering dynamics of high translational energy O atoms on vitreous carbon (an sp^2 carbon material without long range order) revealed that O atoms can desorb from the surface at high surface temperatures,[108]

indicating that the apparent non-Arrhenius temperature dependence of the surface reactivity was the result of the reduced surface coverage of O, which is a key reactant for the formation of CO and CO_2.

The work presented in this article is part of a larger effort aimed at understanding the effect of reagent species (such as O and O_2), incidence energy, and surface structure on the fundamental reaction mechanisms that govern the oxidation of carbon at high surface temperatures. Using beam-surface scattering techniques, we have collected angle- and velocity-resolved distributions for non-reactive and reactive species that exit an HOPG surface following bombardment by high translational energy O atoms. While the incidence energy employed in this experiment (~500 kJ mol^{-1}) is much higher than is typically applicable to hypersonic vehicles in an atmospheric re-entry environment (100 – 200 kJ mol^{-1}), it facilitates the identification of LH and ER surface reactions, as products formed via LH reactions with the surface will have different angular and velocity distributions than those resulting from ER mechanisms. The LH reaction dynamics characterized here occur in thermal equilibrium with the surface and should be the same as the LH reactions that are expected to dominate the gas-surface processes involving oxygen and carbon during atmospheric re-entry. Additionally, the high incidence energy of the molecular beam aids in the determination of the relative importance of LH and ER reactive processes to the oxidation of HOPG. The surface temperatures used covered a range of 1100 to 2300 K, with detailed investigations of the non-reactive and reactive scattering dynamics completed for surface temperatures of 1100, 1300, and 1900 K. The scattering dynamics have been used to infer the mechanisms of the high temperature oxidation of HOPG. The experiments

have revealed that the oxidation of HOPG at high temperatures is governed by the competition between the desorption of chemisorbed O atoms and reactions that produce CO and CO_2.

4.2 Experimental Methods

4.2A Experimental Design

The experimental procedure followed in this study has been described in detail in a previous publication.[108] The experiments were conducted with a crossed molecular beams apparatus reconfigured for beam-surface scattering.[73-75] The main scattering chamber was evacuated using only cryogenic pumps, with additional pumping provided by a liquid nitrogen panel that spanned the bottom of the chamber. The operating pressure during the experiment was 4×10^{-7} Torr. A pulsed molecular beam composed of high translational energy O and O_2 was directed at a radiatively heated HOPG surface at an incidence angle, θ_i, of 45°, as measured from the surface normal. Reactive and non-reactive products that exited the surface were detected at a variety of final angles, θ_f, located on the opposite side of the surface normal from the incident beam, by a mass spectrometer detector that rotated within the plane defined by the incident molecular beam axis and the surface normal. The detector, which consisted of an electron impact ionizer,[76] quadrupole mass filter, and a Daly type ion counter operated in pulse counting mode,[77] was triply differentially pumped so that the region containing the ionizer had a base pressure of $<10^{-11}$ Torr which did not increase during data collection. A multichannel scaler recorded the electrical pulses produced by the Daly detector that were correlated to ion impacts, yielding a trace that was proportional to the number density of the scattered products as a function of flight time

from the surface to the detector, $N(t)$, which were 34.4 cm apart. These number density distributions as a function of flight time are commonly referred to as time-of-flight (TOF) distributions and can be used to derive translational energy distributions, $P(E_T)$, of the scattered products with the use of a density-to-flux conversion that assumes a monoenergetic incident beam.[74,78] The average energies of the scattered products are determined from the $P(E_T)$ distributions. The $P(E_T)$ distribution obtained for each TOF distribution was integrated to obtain the total relative flux of the scattered products at a particular θ_f. Flux angular distributions were obtained by plotting the flux of the scattered products as a function of θ_f.

A laser detonation source, described in detail elsewhere,[80] was used to produce the molecular beam of high translational energy $O(^3P)$[81] and $O_2(\ ^3\Sigma_g^-)$.[82] The TOF distributions, corresponding $P(E_T)$ distributions, and relative fluxes of O and O_2 in the incident beam were determined by lowering the sample out of the beam path and directing the beam into the detector. The molecular beam, which was operated at a frequency of 2 Hz, was velocity selected with a synchronized chopper wheel that had three equally spaced 1.6 mm thick slots. The wheel rotated at a frequency of 300 Hz. The mean translational energy of O was 472.1 kJ mol^{-1} with an energy width (full width half maximum, FWHM) of 51.8 kJ mol^{-1}. The O_2 had a mean translational energy of 944.4 kJ mol^{-1} and a FWHM energy width of 118.8 kJ mol^{-1}. The mole fractions of O and O_2 in the beam were 89% and 11%, respectively.

A ZYA quality HOPG sample with dimensions of 25 mm × 7 mm × 1 mm with a mosaic spread of less than 0.4° was obtained from Momentive, Inc. The HOPG sample

was radiatively heated by a strip of vitreous carbon (Grade 22 SPI-Glas obtained from Structure Probe, Inc.) of equal size that was electrically isolated from the HOPG by two 2 mm × 2 mm × 0.675 mm thick sapphire spacers located at the ends of the sample. The sample assembly was fixed to the front of the sample mount with ceramic clamps, as described in our previous publication.[108] The temperature of the vitreous carbon strip used for the radiative heating was controlled by varying the current delivered. This method produced temperatures of the HOPG samples in the range of 1100 to 2300 K. The temperature of the HOPG sample was determined by measuring the temperature of the vitreous carbon using an optical pyrometer with a graphite filament. HOPG has a relatively high thermal conductance, and the sample was relatively thin, so the vitreous carbon and HOPG sample were assumed to be in thermal equilibrium. The HOPG surface might be at a slightly lower temperature than the vitreous carbon, but we expect that the difference in temperature is less than 20 K. Despite the relatively high operating pressure (4×10^{-7} Torr) of the scattering chamber, the surface of the HOPG sample was assumed to be free of contamination based on earlier results from our group on high translational energy Ar scattering on an HOPG surface, which demonstrated that the surface was clean even at the relatively low surface temperature of 503 K.[84]

4.2B Temperature Dependence of the Non-Reactive and Reactive Product Signals

The overall effect of temperature on the reactivity of the surface was first investigated for a fixed $\theta_i = \theta_f = 45°$. The surface temperature started at 1200 K and was increased in 100 K increments until a temperature of 2300 K was reached. TOF

distributions were collected for mass-to-charge ratios (*m/z*) of 16 (O^+), 32 (O_2^+), 28 (CO^+), and 44 (CO_2^+) for 500, 500, 1000, and 1000 beam pulses, respectively, for each temperature. Masses larger than *m/z* = 44 (CO_2^+) were not observed in our previous work on the oxidation of vitreous carbon and were consequently not investigated in this experiment. The number of beam pulses necessary to obtain a good signal-to-noise ratio resulted in a hold time of about 25 minutes at each surface temperature.

4.2C Temperature-Dependent Hysteresis in the Surface Reactivity

In previous studies, it was reported that the temperature dependence of the surface reactivity has a hysteresis.[22,108] Specifically, the reactivity of the surface was substantially higher when the surface temperature was increased from low to high than the reactivity when the surface temperature was subsequently decreased from high to low. This hysteresis was difficult to investigate in our experiments with HOPG, because it took several minutes for the surface temperature to stabilize when lowering the sample temperature, as the sample was not actively cooled by the mount. Consequently, we did not conduct a direct study of the temperature-dependent hysteresis of the surface reactivity in the same manner as previously employed for vitreous carbon.[22,108] Nevertheless, we conducted another experiment that is expected to provide information on the same temperature-dependent processes that led to the hysteresis. The sample was held in the beam at 1300 K for 30 minutes, and then the sample temperature was suddenly increased to 1800 K. TOF distributions for *m/z* = 16 (O^+), 28 (CO^+), and 32 (O_2^+) were collected sequentially for 500, 1000, and 500 beam pulses, respectively, until the signal for the *m/z* = 28 (CO^+) TOF distributions no longer changed with time. This measurement also

revealed the minimum amount of time necessary for the surface reactivity to reach a steady state.

4.2D Dynamical Behavior of Scattered or Desorbed Products

The dynamical behavior of reactive and non-reactive products was studied in detail for surface temperatures of 1100, 1300, and 1900 K and for $\theta_i = 45°$. TOF distributions were collected over the full range of accessible θ_f for m/z = 16 (O^+), 32 (O_2^+), 28 (CO^+), and 44 (CO_2^+). These distributions were collected after the reactivity of the surface had been determined to be at steady state. To compensate for long-term drift of the molecular beam source, θ_f was varied sequentially in 5° increments from 15° to 75° and then back down to 15°. This cycle was repeated until the summed TOF distributions for each θ_f showed a satisfactory signal-to-noise ratio. Analysis was thus conducted on the summed TOF distributions for each m/z at a given θ_f. For m/z = 16 (O^+) and 32 (O_2^+), TOF distributions were collected for a total of 750 beam pulses for a surface temperature of 1100 K and 1000 beam pulses for surface temperatures of 1300 and 1900 K. For m/z = 28 (CO^+), TOF distributions were collected for a total of 3000, 5000, and 8000 beam pulses for surface temperatures of 1100, 1300, and 1900 K, respectively. For m/z = 44 (CO_2^+), TOF distributions were collected for a total of 3000 and 4000 beam pulses for surface temperatures of 1100 and 1300 K, respectively. Prior to analysis, the summed TOF distributions for O and CO were corrected for the dissociative ionization of O_2 and CO_2, respectively. In the figures presented herein, the data have been normalized to account for the mass-dependent detection sensitivity associated with the transmission function of the quadrupole mass filter and the efficiency of the Daly detector. The normalization also

accounts for the differences in electron-impact ionization cross sections of the products and the number of beam pulses used to collect the TOF distributions. Thus, the relative fluxes of the four observed products are directly comparable.

4.3 Results and Analysis

4.3A Gas-Surface Interaction Mechanisms and their Scattering Signatures

The four products that exit the HOPG surface, O, O_2, CO, and CO_2, come from gas-surface interactions that result either in no net reaction (O, O_2) or in reaction (CO, CO_2). The non-reactive interactions are considered in terms of two limiting cases, impulsive scattering (IS) and thermal desorption (TD).[2,78] IS atoms or molecules undergo one or, perhaps, a few collisions with the surface and transfer little energy before exiting the surface on a time scale too short for thermal equilibrium to be attained. The IS products thus retain much of their initial kinetic energies and therefore appear at short flight times in the TOF distributions. In contrast, atoms or molecules that exchange a significant amount of energy with the surface through multiple collisions, physisorption, or chemisorption can come into thermal equilibrium with the surface before undergoing thermal desorption (TD). TD atoms or molecules have relatively low kinetic energies that are determined by the surface temperature, and they generally appear as a broad feature in a TOF distribution at relatively long flight times compared to IS products. The reactive process that is analogous to IS is an ER reaction, and the reactive process that is analogous to TD is a LH reaction. A third reactive process is a “hot atom” (HA) reaction, in which the incident reactive atom moves along the surface and reacts without coming into thermal equilibrium.[47] Thus, both ER and HA reactions involve nonthermal mechanisms, whereas

LH reactions occur in thermal equilibrium with the surface and are considered to proceed by thermal mechanisms. Non-reactive products that undergo TD and molecules produced by LH reactions desorb in thermal equilibrium with the surface. If the desorption process has no barrier above the adsorption potential energy well, then the TD and LH products will have a Maxwell-Boltzmann (MB) distribution of translational energies given by the surface temperature. On the other hand, if such a barrier exists, then the low energy products will be suppressed and the TD and LH products will have a translational energy distribution that has a higher average energy than predicted by a MB distribution at the surface temperature.[41] It is possible that products of ER or HA reactions could come into thermal equilibrium with the surface after they are formed and then desorb thermally, in which case these products would appear as TD products. However, given the weak interaction of CO and CO_2 with HOPG and the extreme smoothness of the surface, it is unlikely that nascent ER or HA CO or CO_2 products would undergo the multiple collisions that would be necessary to drive them into thermal equilibrium before desorbing.

4.3B Temperature Dependence of Non-Reactive and Reactive Products

The effect of the surface temperature on the measured TOF distributions of the scattered products is shown in Figure 4.1. A flight time of $t = 0$ corresponds to the nominal time at which the incident beam pulse collided with the surface. The O-atom TOF distributions shown in Figure 4.1a are bimodal; the first peak (flight time < 100 μs) corresponds to IS and the second peak corresponds to TD (flight time > 200 μs). The method used to separate the IS and TD components will be described in Section 4.3C. The TOF signal of TD O atoms increases with temperature and appears to level off above about

1700 K. This dependence is represented in terms of TD O-atom flux by the blue symbols in Figure 4.2. As may be seen, the TD O-atom flux increases with surface temperature until 1700 K. The TOF signal of IS O atoms also increases with surface temperature and reaches a plateau at ~1400 K (Figure 4.1a). The same trend is seen for the scattered O_2 shown in Figure 4.1b. For O_2, a TD component was not observed at any temperature. Figures 4.1c and 4.1d display the temperature dependence of the CO and CO_2 TOF distributions, respectively. Unlike the O-atom TOF distributions, the distributions for CO and CO_2 are not bimodal. As shown in Figure 4.2, the total flux of CO increases initially and reaches a maximum at 1300 K and then decreases to a constant flux at temperatures

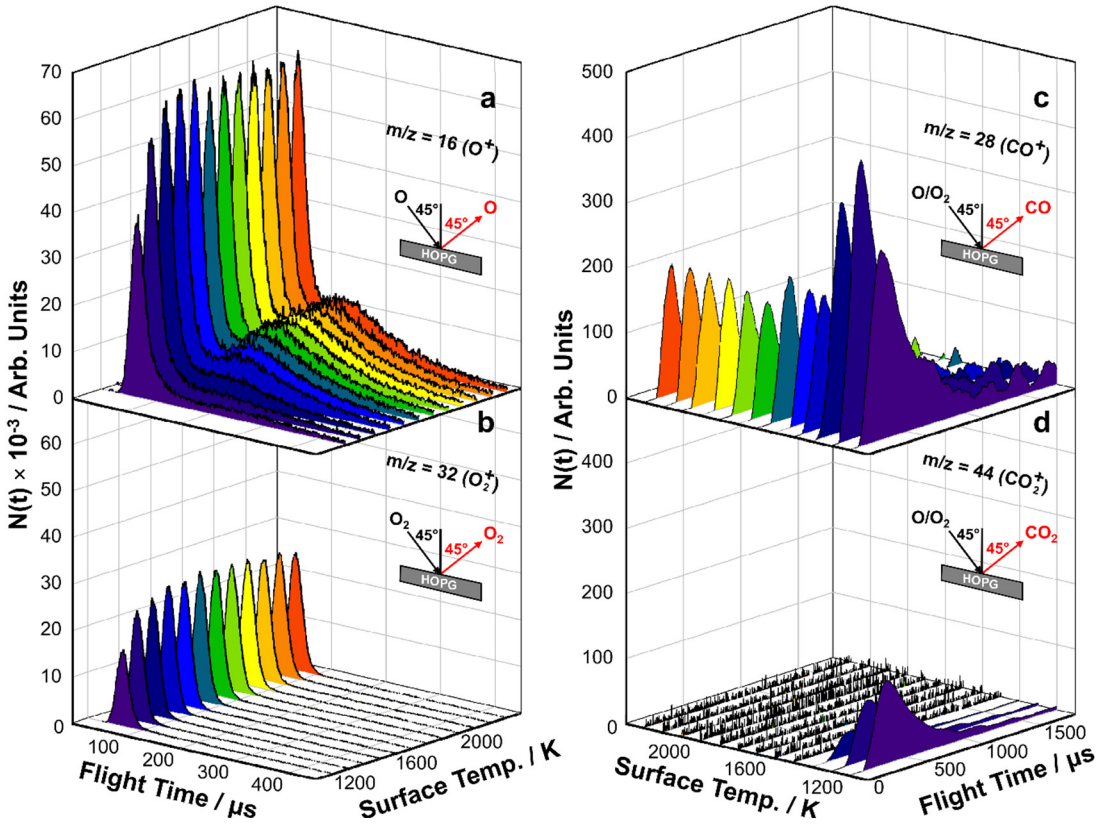


Figure 4.1. Time-of-flight (TOF) distributions, recorded following bombardment of the HOPG surface with the pulsed hyperthermal O/O_2 beam, for scattered (a) O, (b) O_2, (c) CO, and (d) CO_2, with surface temperatures from 1200 to 2300 K. Both the incidence angle, θ_i, and final angle of the scattered products, θ_f, were fixed at 45°.

above 1700 K (red symbols). In contrast, the total flux of CO_2 is at a maximum at 1200 K and decreases until it is below detectable limits at temperatures at 1500 K (green symbols) and above. CO_2 is a minor product compared to CO at all temperatures and has a maximum relative flux of less than half that of CO at the lowest surface temperature studied of 1200 K.

4.3C Time-Dependence of the Surface Reactivity

The time dependence of the total CO flux following a sudden increase in temperature from 1300 to 1800 K is shown in Figure 4.3. The flux of CO gradually decreased 42% in comparison to the flux obtained immediately after the temperature spike

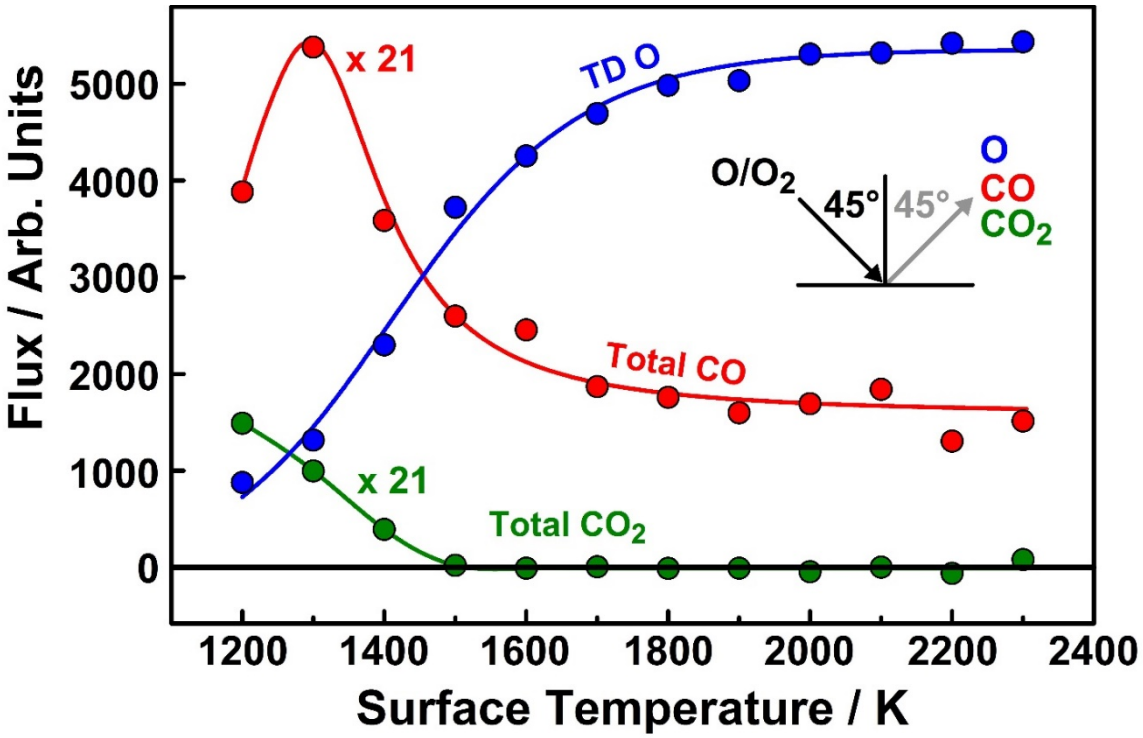


Figure 4.2. Temperature dependent flux of O, CO, and CO_2 exiting the HOPG surface for θ_f = 45°after the O/O_2 gas pulse collided with the surface with θ_i = 45°. Only the flux of the O atoms that desorb after coming into thermal equilibrium with the surface (TD O atoms) is shown. The total fluxes of CO and CO_2 are plotted and have been multiplied by a factor of 21. The solid lines are meant to guide the eye.

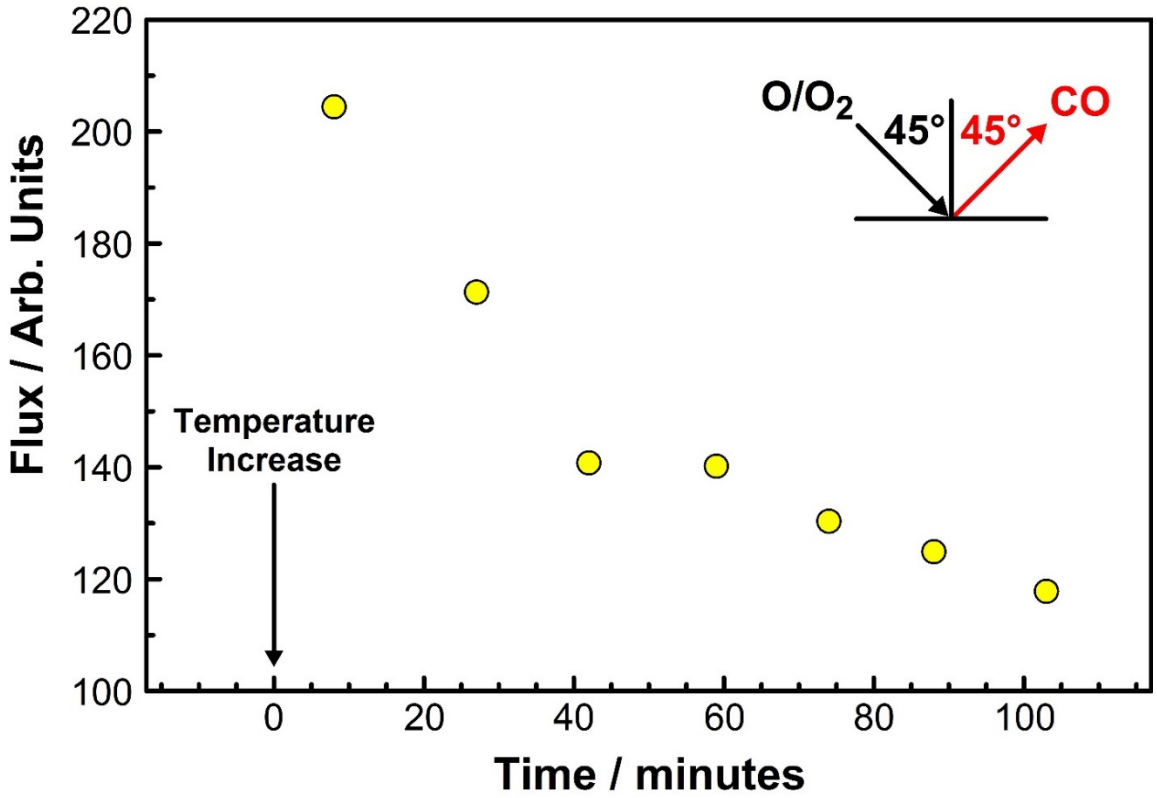


Figure 4.3. Time dependence of the scattered CO flux during bombardment by the O/O_2 molecular beam with $\theta_i = \theta_f = 45°$ after the surface temperature was increased suddenly from 1300 K to 1800 K.

over a time span of 100 minutes. The long time required to reach steady-state surface reactivity (>100 minutes) means that the temperature dependencies shown in Figures 4.1 and 4.2 were not collected at steady-state, because the hold time at each surface temperature was only 25 minutes. The values for CO and CO_2 flux in Figure 4.2 would be expected to decrease and the flux for O would be expected to increase (not shown) if the hold time at each temperature had been significantly longer. The detailed scattering dynamics data obtained with surface temperatures of 1100, 1300, and 1900 K were collected during continuous bombardment of the surface over a period of several days – long after the surface reactivity had reached a steady state at a given temperature.

4.3D Scattering Dynamics of O atoms

As mentioned above, the O-atom TOF distributions are bimodal at every combination of surface temperature and θ_f, indicating that O atoms exit the HOPG surface through both IS and TD channels. Representative TOF distributions for O atoms at surface temperatures of 1100, 1300, and 1900 K and θ_f = 15° and 65° are shown in Figure 4.4. The O atoms exit the surface predominantly through the IS channel. Accordingly, the y-axes for O atoms that exit at θ_f = 65° have been scaled such that the TD components can be clearly seen. The IS and TD components have frequently been separated by fitting the feature at long flight times with a MB distribution of energies (or flight times) characterized by the surface temperature and subtracting the fit from the total signal intensity, which yields the IS distribution.[39,78] However, for all three surface temperatures, the TD components in the O-atom TOF distributions cannot be described well by a MB

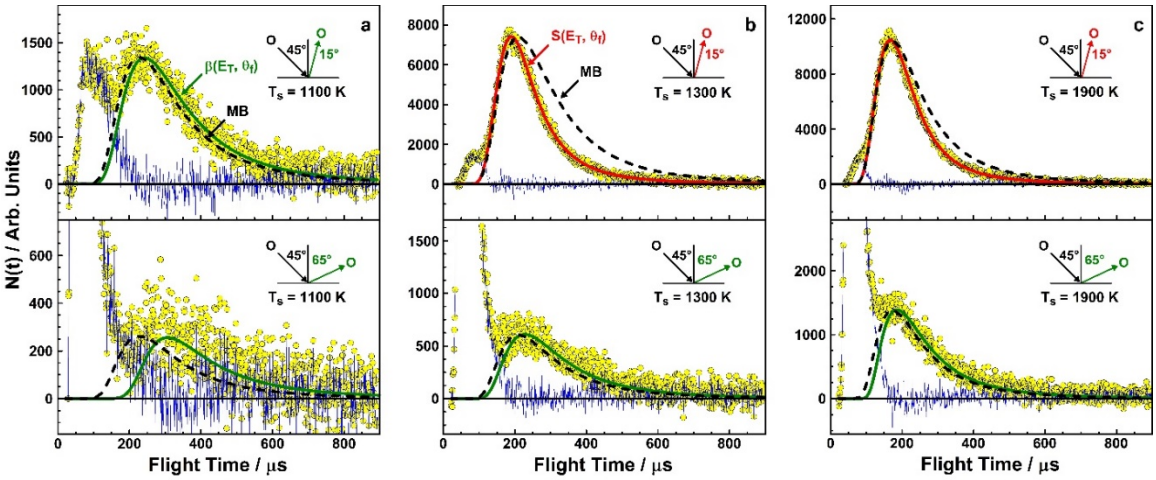


Figure 4.4. Representative TOF distributions for O atoms exiting the HOPG surface at θ_f = 15° and 65° following bombardment by the O/O_2 beam pulse at θ_i = 45°, for surface temperatures of (a) 1100 K, (b) 1300 K, and (c) 1900 K. The total signal is represented by the yellow circles. The dashed black lines represent MB distributions characterized by the surface temperature. The red and green lines represent the fit of the thermal desorption (TD) components using $S(E_T, \theta_f)$ and $\beta(E_T, \theta_f)$, respectively. The blue lines represent the impulsive scattering (IS) components.

distribution. For 1100 K and $\theta_f = 15°$, the arrival times of the TD component tend to be slightly longer than predicted by a MB distribution (black dashed line in Figure 4.4a, top panel). As θ_f increases, the arrival times of the TD O atoms become even longer (Figure 4.4a, bottom panel). We designate the products with flight times that appear to be longer, on average, than those predicted by a MB distribution of velocities at the surface temperature as TD_{slow}. These TD_{slow} atoms are calculated to have average translational energies less than $2RT_s$, which would be the average energy of products that desorb from the surface with a MB distribution of translational energies. This calculation is based on time zero ($t = 0$) being the time at which the beam pulse strikes the surface; however, products that desorb at later times may still have a MB distribution and yet appear to have a lower average energy than $2RT_s$ because the definition of $t = 0$ does not account for a residence time on the surface. At 1300 and 1900 K, a MB distribution overestimates the tail of the TD component in the O-atom TOF distribution when $\theta_f = 15°$ (Figures 4.4b and 4.4c, top panels). These O atoms, which we refer to as TD_{fast}, have arrival times shorter than predicted by a MB distribution characterized by the surface temperature, and they have average translational energies greater than $2RT_s$. The TD O-atom components shift to longer flight times and are well described by a MB distribution when θ_f is increased to 65° (Figures 4.4b and 4.4c, bottom panels).

The deviation of the TD_{fast} O-atom TOF distributions from a MB distribution at 1300 and 1900 K indicates that the O atoms desorb over a barrier, which results in final translational energies that are greater than $2RT_s$.[40] Therefore, the fitting procedure described by Michelsen and Auerbach, which is based on the principle of detailed balance,

has been used to analyze the data.[40] The angle-resolved $P(E_T)$ distributions were fit by multiplying a model function that describes the trapping or chemisorption probability, $D(E_T, \theta_f)$, by a flux-weighted MB distribution:

$$f(E_T, \theta_f) dE_T d\theta_f = E_T \exp\left(-\frac{E_T}{RT_s}\right) \cos(\theta_f)\, D(E_T, \theta_f) dE_T d\theta_f \qquad (4.1)$$

where E_T is the final translational energy (kJ mol^{-1}), T_s is the surface temperature (K), and R is the ideal gas constant (kJ mol^{-1} K^{-1}). When the O atoms are initially chemisorbed on the surface, $D(E_T, \theta_f)$ is assumed to have the functional form proposed by Harris for desorption over a barrier, $S(E_T, \theta_f)$:[41]

$$D(E_T, \theta_f) = S(E_T, \theta_f) = \frac{A}{2}\left[1 + \tanh\left(\frac{E_{eff} - E_0}{W}\right)\right] \qquad (4.2)$$

where E_0 represents the barrier for desorption, W is related to the range of desorption barriers arising from a variety of surface sites available for desorption, and A is a normalization factor (unitless). Eq 4.2 was used in our analysis because it has been used previously to describe desorption over a barrier. In fact, any sigmoidal function could substitute for eq 4.2 in the determination of the desorption barrier, E_0, by fitting to the TD_{fast} product TOF (or translational energy) distributions. The desorption barrier is determined from the "midpoint" of the rise of the sigmoidal curve and not does change significantly with functional form. On the other hand, the range of desorption barriers, proportional to W in eq 4.2, does depend on the exact functional form used for the sigmoidal function. Consequently, we will not draw any conclusions from the value of W, other than to point out qualitative changes in W with surface temperature. The functional form of eq 4.2 does not significantly affect the average final energy of the TD component, $\langle E_f \rangle_{TD}$, or the TD O-

atom flux that is derived. The $S(E_T, \theta_f)$ function depends on the kinetic energy and θ_f via the term E_{eff}, which is given by:

$$E_{eff} = E_T \cos^n \theta_f \tag{4.3}$$

where n is unitless and can have values from 0 to 2. When $n = 2$, only energy oriented normal to the surface is required to surmount the desorption barrier, which is one dimensional. Values of $n < 2$ can result when the potential energy surface is corrugated and barriers to desorption are multi-dimensional.[40] The parameters for $S(E_T, \theta_f)$ are adjusted until a satisfactory fit of the TD_{fast} component of the TOF distribution is obtained (red curves, Figure 4.4), and then the fit is subtracted from the total signal intensity (yellow symbols, Figure 4.4) to yield the IS component (blue curves, Figure 4.4).

As mentioned above, Figure 4.4a shows that the TD_{slow} O atoms that desorb from the 1100 K surface have an average final translational energy that is less than $2RT_s$, which can indicate a non-activated desorption process – i.e., there is no barrier to desorption.[39,42] In this case, the energy dependent trapping probability, $\beta(E_T, \theta_f)$, is substituted for $D(E_T, \theta_f)$ in eq 4.1 and is described by:[39]

$$\begin{aligned} D(E_T, \theta_f) &= \beta(E_T, \theta_f) \\ &= A\left[1 + \exp\left(\frac{E_{eff} - E_c}{X}\right)\right]^{-1} \end{aligned} \tag{4.4}$$

where E_{eff} is given by eq 4.3, A is a normalization constant (unitless), E_c is defined as the critical energy above which the trapping probability falls to zero, and X determines the shape of the curve. The fit resulting from this procedure is shown by the green curve in Figure 4.4a.

The data, a subset of which are presented in Figure 4.4, show that TD O atoms can scatter through two channels, TD_{slow} and TD_{fast}. At 1100 K, only the TD_{slow} O atoms are observed. At 1300 and 1900 K, it appears that both TD_{fast} and TD_{slow} O atoms are present. The $S(E_T, \theta_f)$ function was used to fit the TD_{fast} O-atom components of the TOF distributions, while the $\beta(E_T, \theta_f)$ function was used to fit the TD_{slow} O-atom components. Ideally, a set of TOF distributions covering the full angular range for a given surface temperature should be fit by one combination of parameters for $S(E_T, \theta_f)$ or $\beta(E_T, \theta_f)$.[39-40] However, one set of parameters for $S(E_T, \theta_f)$ or $\beta(E_T, \theta_f)$ that fits the TD components for all the O-atom TOF distributions in the range of $\theta_f = 15° - 75°$ could not be found for the three surface temperatures studied. Accordingly, we have fit the TOF distribution for each θ_f individually. Selected fitting parameters for $\theta_f = 15°$ and 65° are shown in Table 4.1. The error bars represent estimated 95% confidence intervals.

Figure 4.5 shows the calculated mean final translational energies of the TD O atoms (with $t = 0$ taken as the time at which the incident beam pulse struck the surface), for surface temperatures of 1100, 1300, and 1900K, that were obtained from the fitting procedure described above. Two aspects of this figure are striking. First, the TD_{slow} O atoms at 1100 K have $\langle E_f \rangle_{TD} < 2RT_s$ at every θ_f and $\langle E_f \rangle_{TD}$ has a downward trend with increasing θ_f. Final energies less than $2RT_s$ can originate from non-activated desorption processes but could also result if the atom resides on the surface for a period of time.[109] Second, for surface temperatures of 1300 and 1900 K, the TD_{fast} O atoms have $\langle E_f \rangle_{TD} > 2RT_s$ for $15° < \theta_f < 60°$; however, for $\theta_f > 60°$, $\langle E_f \rangle_{TD} < 2RT_s$, similar to the trend observed for TD_{slow} O atoms desorbing from the 1100 K surface.

Table 4.1. Selected fitting parameters for the energy dependent trapping coefficient, $\beta(E_T, \theta_f)$, and the energy dependent sticking probability, $S(E_T, \theta_f)$, for $\theta_f = 15°$ and 65°.

	$\theta_f = 15°$		$\theta_f = 65°$	
Surface Temperature	E_c / kJ mol^{-1}	X / *kJ mol^{-1}*	E_c / kJ mol^{-1}	X / *kJ mol^{-1}*
1100 K	39[a]	9.6[a]	4[a]	6.8[a]
	E_0 / kJ mol^{-1}	W / *kJ mol^{-1}*	E_c / kJ mol^{-1}	X / *kJ mol^{-1}*
1300 K	11.1 ± 0.3[b]	15.3 ± 0.7[b]	47[a]	145[a]
1900 K	5.7 ± 0.4[b]	16.8 ± 0.6[b]	20[a]	70[a]

[a] Obtained using $\beta(E_T, \theta_f)$, eq 4.4
[b] Obtained using $S(E_T, \theta_f)$, eq 4.2

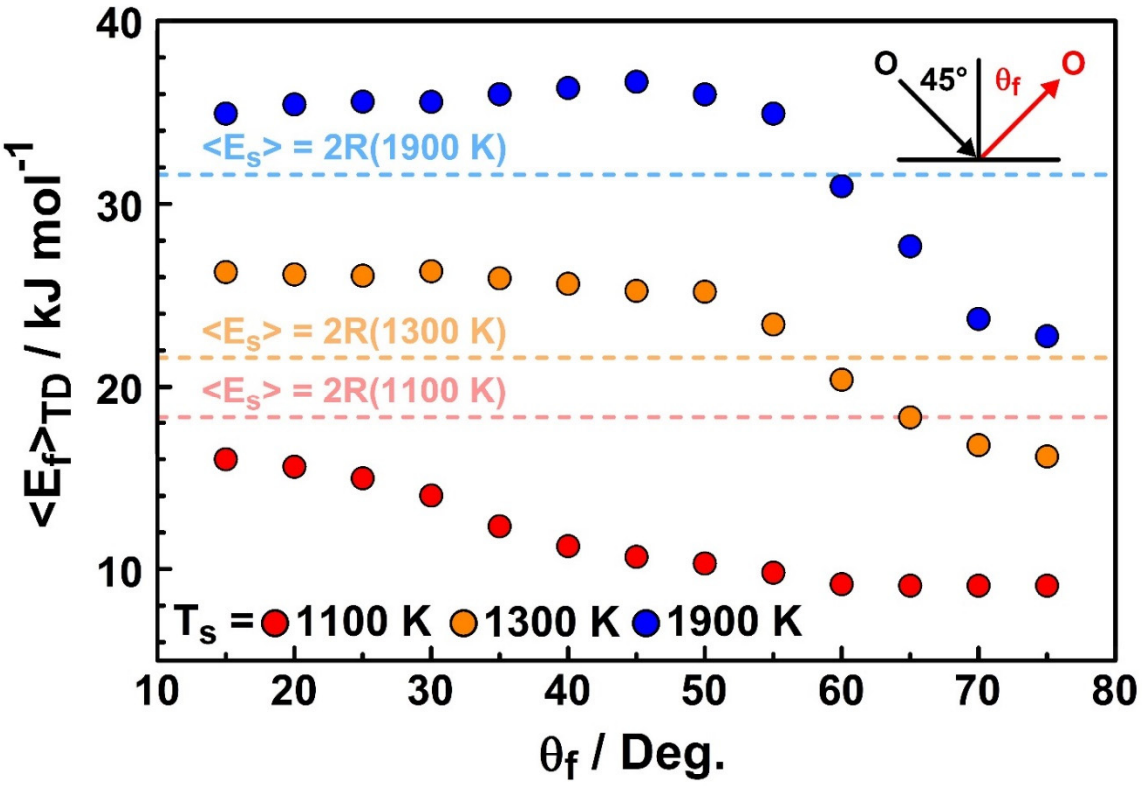


Figure 4.5. The calculated mean final translational energies, $\langle E_f \rangle_{TD}$, of the thermally desorbed (TD) O atoms as a function of θ_f with $\theta_i = 45°$, where $t = 0$ in the calculation is assumed to be the time at which the beam pulse struck the surface. The red, orange, and blue symbols represent the data for 1100, 1300, and 1900 K, respectively. The dashed lines designate the average translational energies if the products desorbed in a MB distribution at the indicated surface temperature.

Although O atoms may exit the surface through TD channels, the predominant scattering mechanism is IS. The flux angular distributions for IS and TD O atoms are presented separately for clarity in Figures 4.6a and 4.6b. The TD_{fast} and TD_{slow} components are not distinguished in Figure 4.6b. The angular distributions for IS O atoms at T_s = 1100, 1300, and 1900 K are lobular and directed beyond the specular angle, and these distributions can be fit with the functional form, $\cos^m(\theta_f - \theta_{max})$, where a larger value of m denotes a narrower angular distribution.[5] The value of θ_{max} was 56.5° at all three surface temperatures. The value of m was 46, 46, and 37, for 1100, 1300, and 1900 K, respectively. The FWHM of each angular distribution is 19.9°, 19.9°, and 22.2°, respectively. The angular distributions of the IS O atoms grow slightly broader as the surface temperature is increased, consistent with the findings of Hurst et al., which demonstrated that the thermal motions of the surface at high temperatures lead to an increase in the width of the angular distribution.[93] The total flux of IS O atoms, obtained

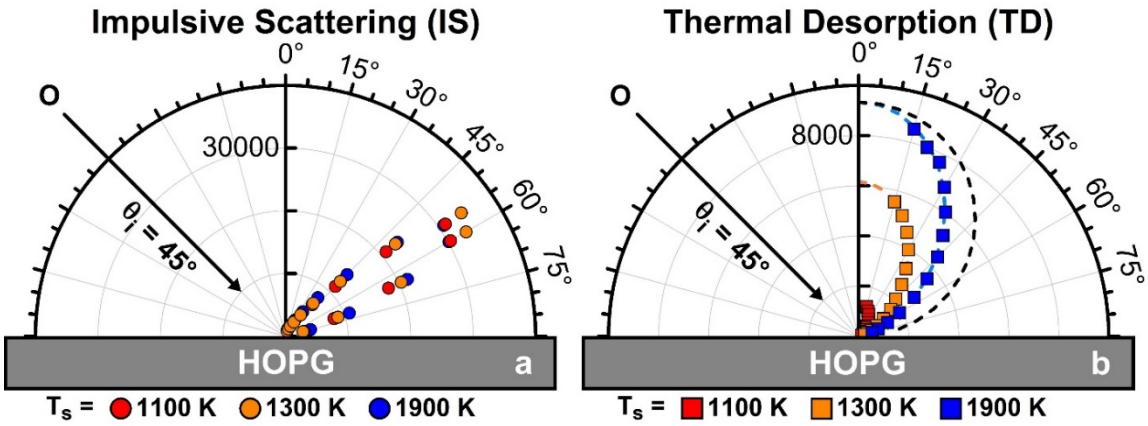


Figure 4.6. Flux angular distributions for (a) impulsively scattered (IS) and (b) thermally desorbed (TD) O atoms, for surface temperatures of 1100 K (red symbols), 1300 K (orange symbols), and 1900 K (blue symbols), following bombardment of the surface with the O/O_2 beam at θ_i = 45°. The dashed black line in (b) represents a cos(θ_f) distribution and is shown for comparison.

by integrating the angular distributions in Figure 4.6a, does not change substantially with surface temperature; the variation that is seen is likely the result of small changes in the incident beam flux. In contrast, the flux of TD O atoms (Figure 4.6b) increases nearly eight-fold from 1100 to 1900 K. All three TD angular distributions have maxima toward the surface normal and can be fit by a $\cos^m(\theta_f)$ distribution. For 1100 and 1300 K, the value of *m* that best fits the angular distributions is 3. The value of *m* decreases to 2.2 for the angular distribution obtained at 1900 K. These distributions are narrower than a $\cos(\theta_f)$ distribution, represented by the black dashed line in Figure 4.6b.

4.3E Scattering Dynamics of O_2

Figure 4.7 shows the flux angular distributions for O_2 scattering from the HOPG surface held at temperatures of 1100, 1300, and 1900 K. Unlike the O atoms, no TD signal was detected at any combination of θ_f and surface temperature. The O_2 angular distributions were also well described by a $\cos^m(\theta_f - \theta_{max})$ distribution. The values of *m* for 1100, 1300, and 1900 K were 75.2, 69.5, and 51.8, respectively, which corresponded to angular widths (FWHM) of 15.8°, 16.5° and 19.0°, respectively. For all three surface temperatures, θ_{max} was 56.5° at each temperature. The O_2 angular distributions are narrower than those obtained for the IS O atoms. As will be discussed below, these results indicate that O_2 is not produced from a reactive process, but is rather the result of impulsive scattering of O_2 that is in the incident beam. The total flux of O_2 scattering from the surface changed by less than 10% for the three surface temperatures measured. This variation is likely the result of small changes in the incident beam flux over the course of the experiment.

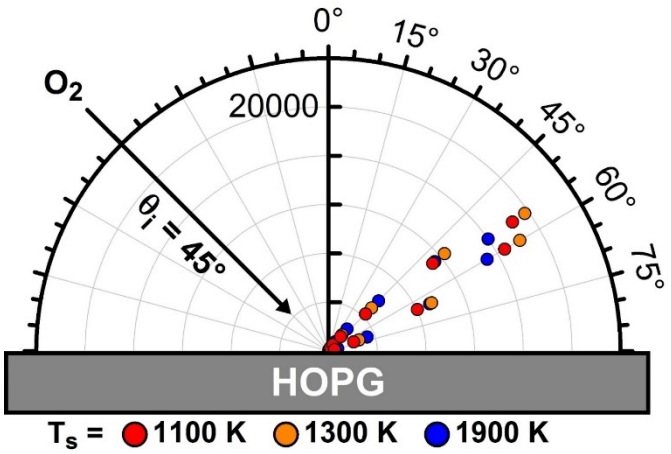


Figure 4.7. Flux angular distributions of scattered O_2 molecules from the HOPG surface held at temperatures of 1100 K (red symbols), 1300 K (orange symbols), and 1900 K (blue symbols). The O/O_2 molecular beam was directed at the surface with θ_i = 45°.

4.3F Scattering Dynamics of CO

The scattering dynamics of CO changed substantially with surface temperature. We will focus our attention first on the angular distributions of the total flux of CO scattering from the surface, which are represented by the yellow symbols in Figure 4.8. It is immediately apparent that the total CO flux is highest at the lowest surface temperature of 1100 K (Figure 4.8a). At first consideration, this result does not appear to be consistent with the trend shown in Figures 4.1 and 4.2, where the CO flux is at a maximum at 1300 K. However, as discussed in Section 3C, the angular distributions for CO were collected after the surface reactivity had reached a steady state, while the temperature dependence of the surface reactivity in Figures 4.1 and 4.2 were not. In fact, the flux of CO at 1300 K decreased steadily over a period of more than 100 minutes such that the flux of CO was lower than it was at 1100 K. The angular distributions of the total flux are clearly bimodal for surface temperatures of 1100 and 1300 K (yellow symbols, Figures 4.8a and 4.8b), with

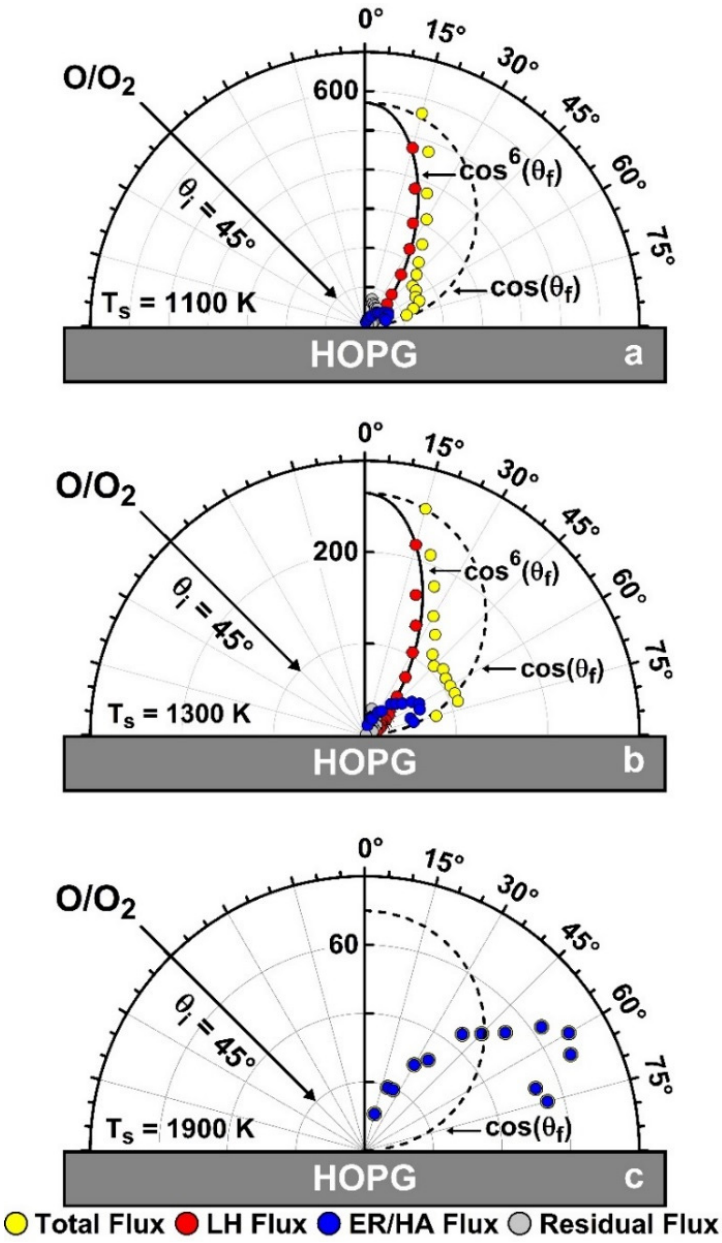


Figure 4.8. Flux angular distributions for CO molecules exiting the HOPG surface held at temperatures of (a) 1100 K, (b) 1300 K, and (c) 1900 K, following bombardment of the surface with the O/O_2 beam at $\theta_i = 45°$. The total flux is represented by the yellow symbols, which has been separated into thermal (LH) and nonthermal (ER/HA) components, represented by red and blue symbols, respectively. The flux not captured by the fitting method described in the text is denoted by the gray symbols (not clearly visible). The TD components in (a) and (b) have been fit by a $\cos^m(\theta_f)$ distribution, with the value of m indicated in the figures. The black dashed lines represent a $\cos(\theta_f)$ distribution and are shown for comparison.

a maximum flux toward the surface normal and a secondary maximum peaked beyond the specular angle. The bimodal angular distributions indicate that CO is formed by at least two reaction mechanisms. CO that scatters toward the surface normal is the product of a reaction that occurs in thermal equilibrium with the surface, commonly referred to as an LH mechanism.[3] In such a reaction, the incident O atom comes into thermal equilibrium with the surface before the reaction takes place and the CO product desorbs. The second reaction pathway has a lobular angular distribution, with a maximum far from the surface normal. This reaction likely occurs via an ER or HA reaction (both of which proceed directly through one or a few steps[3,47]), as will be demonstrated below. Despite the high incidence energy of the O atoms, CO is produced predominantly through LH mechanisms. However, as the surface temperature is increased from 1100 to 1300 K, the flux of CO produced via LH reactions decreases (Figures 4.8a and 4.8b, yellow symbols in the range of $15° < \theta_f < 50°$). When the surface temperature is 1900 K, evidence of CO produced by LH reactions is no longer observable, and the relatively low flux of CO exiting the surface has a lobular angular distribution with a maximum at $\theta_f \sim 60°$.

Representative TOF distributions for CO exiting the HOPG surface are shown in Figure 4.9. The experimental data are represented by the yellow symbols. While the total flux angular distributions indicate that CO is formed by two different mechanisms, the products of LH and ER/HA reactions are not easily distinguishable in the TOF distributions. At every θ_f, there is only one peak in the TOF distribution. Figure 4.10 shows the angular dependence of the total mean final energy, $\langle E_f \rangle_{\text{Total}}$, for CO exiting the HOPG surface at 1100, 1300, and 1900 K. For 1100 and 1300 K, the CO molecules that

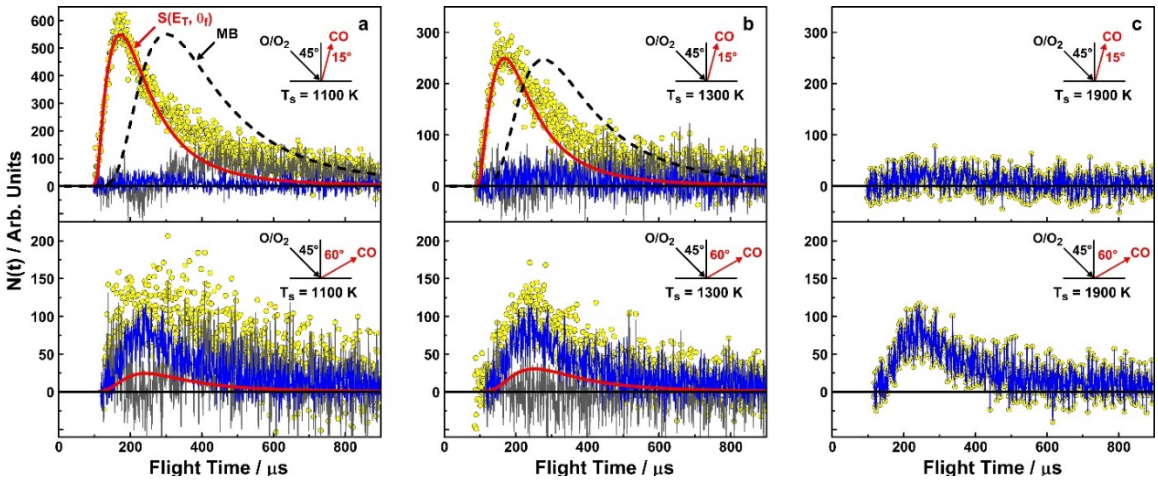


Figure 4.9. Representative TOF distributions for CO molecules exiting the HOPG surface held at temperatures of (a) 1100 K, (b) 1300 K, and (c) 1900 K, following bombardment with the O/O_2 beam pulse with $\theta_i = 45°$. $\theta_f = 15°$ for the top panels and 60° for the bottom panels. The experimental data are represented by yellow symbols. The blue curves represent CO that is produced via a ER/HA mechanism, while the red curves denote the fits to the TOF distributions of CO that originates from a thermal (LH) mechanism. The gray lines represent the residual signal not captured by the analysis procedure described in the text. The black dashed lines represent MB distributions characterized by the surface temperature and are shown for comparison.

exit toward the surface normal have $\langle E_f \rangle_{\text{Total}} > 2RT_s$, and $\langle E_f \rangle_{\text{Total}}$ decreases as θ_f increases to ~45°, after which it slowly increases but not substantially. For CO exiting the surface at 1900 K, the apparent $\langle E_f \rangle_{\text{Total}}$ is less than $2RT_s$ for every θ_f measured. Despite the high translational energy of the incident O atoms, the molecules formed by ER/HA and LH processes scatter from the surface with similar energies. Thus, attributing the products to one mechanism or the other requires careful consideration.

The angular distribution presented in Figure 4.8c suggests that the CO produced at high temperatures is formed by a single reaction. The distribution has a single lobe that is directed away from the surface normal, indicating that the scattered molecules have some memory of the incident trajectory of the O atoms which is a characteristic of either an ER or a HA reaction mechanism. As may be seen in Figure 4.2 (red symbols), the CO flux

does not change over the range of 1700 to 2300 K. The insensitivity of the CO flux to surface temperature over this 600 K range also suggests that the angular distribution in Figure 4.8c results from an ER or a HA reaction, as these reactions have been shown to be only weakly dependent on surface temperature.[110] Moreover, Figure 4.10 suggests that $\langle E_f \rangle_{\text{Total}}$ of CO for the angular range over which the component in Figure 4.8c is dominant, $50° < \theta_f < 75°$, does not change significantly when the surface temperature increases from 1100 K to 1900 K. If the CO that scatters in this range of θ_f were formed by a LH reaction (controlled by the surface temperature) that produced an angular distribution that was directed away from the surface normal, then $\langle E_f \rangle_{\text{Total}}$ would increase significantly over this

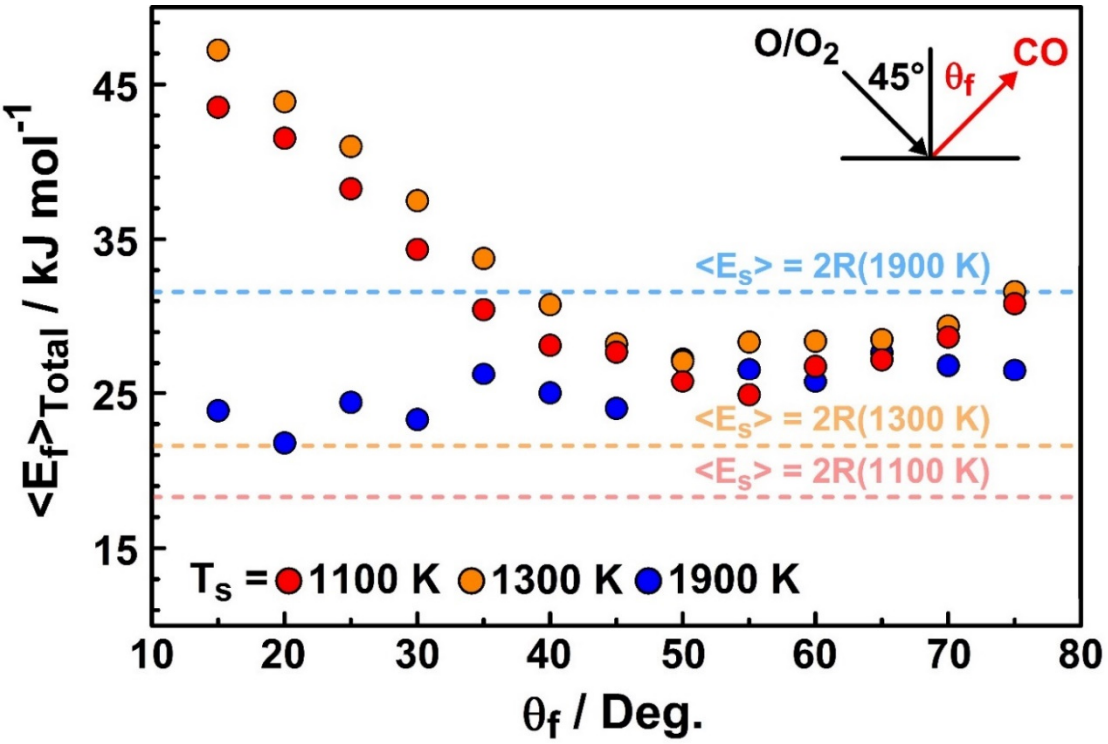


Figure 4.10. The calculated mean total final translational energies, $\langle E_f \rangle_{\text{Total}}$, of the desorbing CO as a function of θ_f with $\theta_i = 45°$, where $t = 0$ in the calculation is assumed to be the time at which the beam pulse struck the surface. The red, orange, and blue symbols represent the data for 1100, 1300, and 1900 K, respectively. The dashed lines designate the average translational energies if the products desorbed in a MB distribution at the indicated surface temperature.

800 K temperature range, which is clearly not observed in Figure 4.10. The observation of the lobular CO angular distribution that is directed away from the surface normal, as well as the insensitivity of the CO flux and $\langle E_f \rangle_{\text{Total}}$ (for $50° < \theta_f < 75°$) to surface temperature, lead us to conclude that the product whose angular distribution is shown in Figure 4.8c is the result of an ER or a HA surface reaction. We have thus assumed that the dynamics of this reaction remain constant over the temperature range of this study (1100 to 1900 K). For the analysis of the CO reaction dynamics, the TOF distributions obtained for CO at 1900 K have been extrapolated in order to analyze the TOF distributions collected at the much lower surface temperatures of 1100 and 1300 K, where signatures of ER/HA and LH CO reaction mechanisms cannot be clearly distinguished. For a given θ_f, the total TOF distribution obtained for CO when the surface temperature was 1900 K (examples in Figure 4.9c) was directly subtracted from the total TOF distributions for CO at 1100 and 1300 K (yellow symbols, Figures 4.9a and 4.9b). The TOF distributions resulting from this subtraction, which should only contain CO produced via LH mechanisms, were further analyzed as explained below.

For CO exiting the surface at temperatures of 1100 and 1300 K, the LH products (see results in Figure 4.10 for $\theta_f < 40°$) have $\langle E_f \rangle_{\text{Total}} > 2RT_s$, which indicates that molecules produced by LH reaction mechanisms desorb from the surface over a barrier. Therefore, the TOF distributions for CO with the ER/HA product subtracted were fit with eq 4.1, using eq 4.2 for $S(E_T, \theta_f)$. While a LH CO reaction involves several steps, the reaction occurs promptly after the O atom chemisorbs (within 200 - 500 femtoseconds).[20] The simple model represented by eq 4.2 is therefore suitable to fit the data because the reaction time is

extremely short on the time scale of the measured flight times in the experiment. The fits resulting from this procedure are denoted by the red curves in Figures 4.9a and 4.9b. The fits to the LH signals given by the simple model for desorption over a barrier account for 85% of the CO flux produced by LH reactions. The residuals not captured by the fits are represented by the gray lines apparent at long flight times in the TOF distributions in Figures 4.9a and 4.9b, while ER/HA CO TOF distributions are shown in blue. The results of applying the model to the analysis of the LH CO TOF data at a surface temperature of 1100 K are: E_0 = 121 ± 5 kJ mol^{-1}, W = 26.2 ± 0.3 kJ mol^{-1}, and n = 1. When the surface temperature was raised to 1300 K, E_0, W, and n are 155 ± 7 kJ mol^{-1}, 32.0 ± 0.6 kJ mol^{-1},

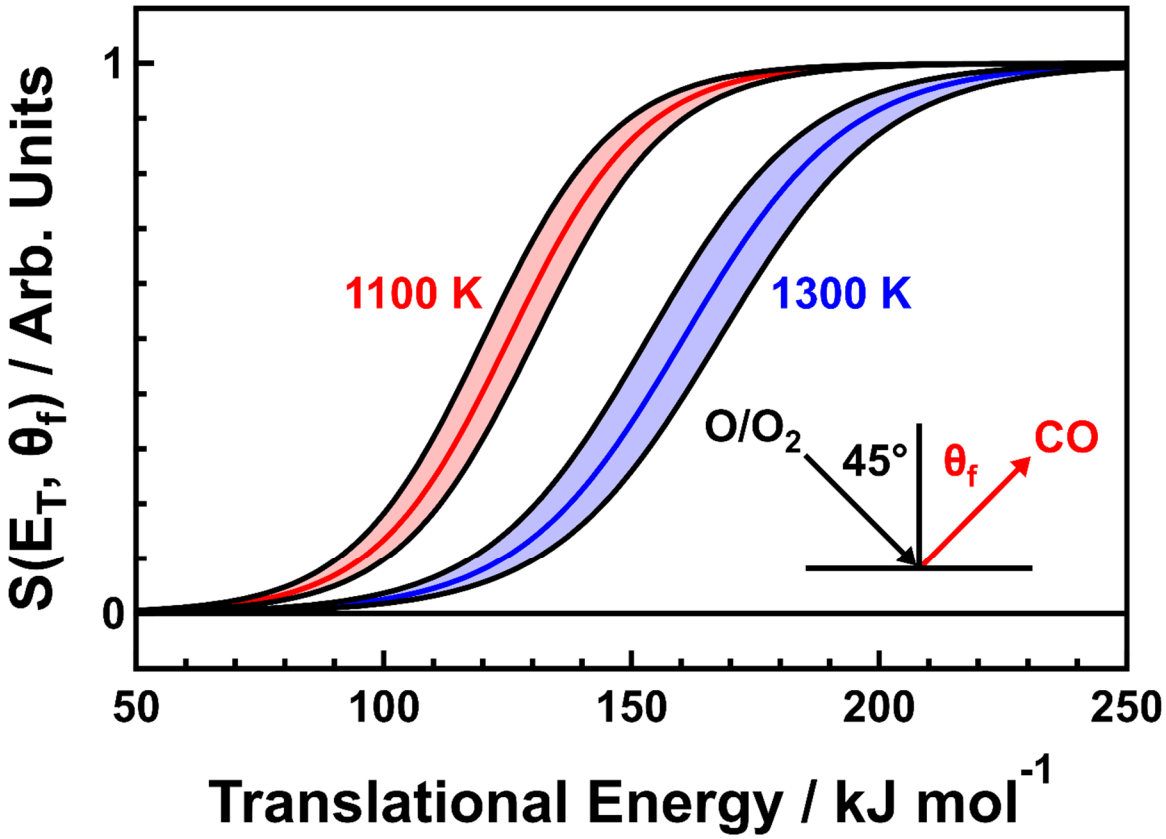


Figure 4.11. Energy dependent desorption functions, $S(E_T, \theta_f)$, for CO produced by thermal reaction mechanisms at surface temperatures of 1100 K (red curve) and 1300 K (blue curve). The colored sections represent an estimated 95% confidence interval.

and 1, respectively. A graphical representation of these results is seen in Figure 4.11, in which the $S(E_T, \theta_f)$ functions are plotted for CO desorbing from the HOPG surface held at 1100 and 1300 K. The desorption barriers reported correspond to the final step of the reaction process, where a C-C bond breaks and releases CO into the vacuum. The values of E_0 obtained from the fits are within the range and follow the trend of those obtained from DFT calculations which showed that E_0 increases when oxygen is removed from the surface (48 kJ mol^{-1} at high coverage and 179 kJ mol^{-1} at low coverage).[19] The value of n = 1 indicates that the molecule does not desorb over a simple, one-dimensional barrier, implying that energy directed both parallel and normal to the surface is required for the CO to overcome the desorption barrier. The angular distributions for the flux of CO produced by an LH mechanism at 1100 and 1300 K are denoted by the red symbols in Figures 4.8a and 4.8b. The angular distributions are narrower than $\cos(\theta_f)$ and can be described by a $\cos^6(\theta_f)$ distribution. It should be noted that specific CO vibrational states are not accounted for in the analysis because the experimental apparatus used for this study cannot provide information on the internal degrees of freedom of the desorbing molecules. However, because the surface temperature is high, up to 10% of the CO could be in vibrationally excited states at 1300 K. Thus, the reported energy barriers, E_0, are effective values for all CO scattering from the surface, and specific quantum states are not accounted for in the analysis.

4.3G Scattering Dynamics of CO_2

CO_2 is a minor reactive product that was observed only at low surface temperatures. Figures 4.12a and 4.12b show the flux angular distributions and the dependence of $\langle E_i \rangle_{\text{Total}}$

on θ_f for the CO_2 exiting the surface at 1100 and 1300 K. The angular distributions for CO_2 are bimodal, with one maximum toward the surface normal and a second maximum beyond the specular angle, indicating that this minor reactive product is also formed

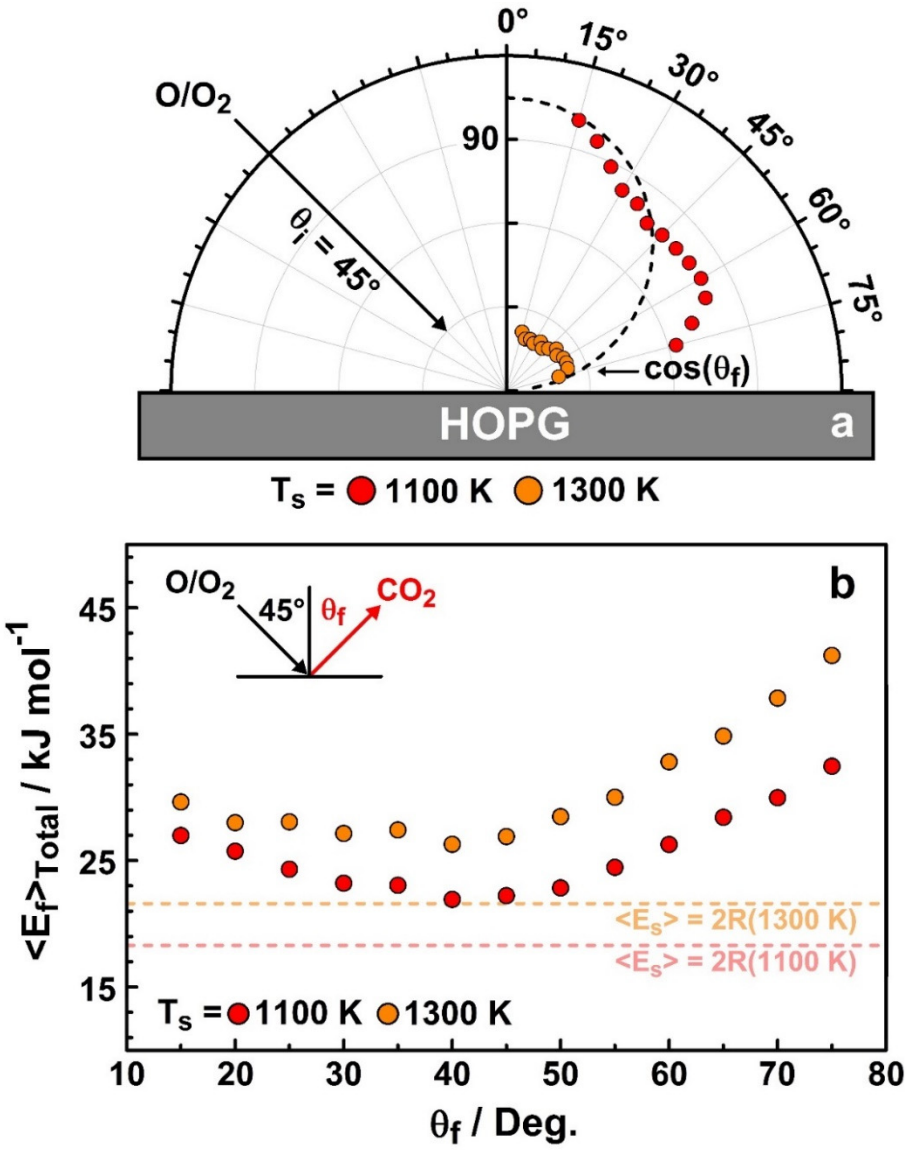


Figure 4.12. (a) Total flux angular distributions and (b) angular dependence of the average total final energies, $\langle E_f \rangle_{Total}$, for CO_2 molecules exiting an HOPG surface at 1100 K (red symbols) and 1300 K (orange symbols) following bombardment with the O/O_2 beam with $\theta_i = 45°$. The black dashed line in the top panel indicates a $\cos(\theta_f)$ distribution and is shown for comparison. The colored dashed lines in the bottom panel indicate the average energies of the products if they desorbed thermally from the surface at the temperatures denoted in the figure.

through LH and ER/HA mechanisms. In Figure 4.12b, $\langle E_f \rangle_{\text{Total}}$ is greater than $2RT_S$ for θ_f toward the surface normal, indicating that CO_2 formed by a LH reaction also must desorb from the surface over a barrier. Similar to CO, CO_2 that is produced by LH and ER/HA mechanisms cannot easily be distinguished in the TOF distributions, which have a single, broad peak (see Figure 4.1d). Although the disappearance of the LH CO component at higher temperatures provided a way to separate the ER/HA and LH components in the CO TOF distributions at lower temperatures, as described in the previous section, an analogous procedure to separate the two components in the CO_2 TOF distributions was not possible. First, signal for CO_2 at high temperatures, which would presumably be from ER/HA reactions, was nonexistent. Second, the reaction dynamics of the ER/HA mechanism that forms CO_2 has a temperature dependence, as is indicated by the increase in $\langle E_f \rangle_{\text{Total}}$ from 1100 to 1300 K, as seen in Figure 4.12b.

4.4 Discussion

Consistent with previous studies,[22,33,108] the reactions that produce CO and CO_2 have an apparent non-Arrhenius temperature dependence. The flux of CO initially increases with surface temperature and then decreases at temperatures above 1300 K. CO_2 has a maximum flux at 1100 K and the flux dwindles to zero at higher surface temperatures. Our earlier experiments on the oxidation of vitreous carbon showed that O atoms desorb with increasing probability as the surface temperature increases above 800 K, and we concluded that the reduction in reactivity is related to the diminished surface coverage of O atoms.[108] The oxidation of HOPG at high temperatures follows the same qualitative trend, suggesting that sp^2 allotropes of carbon oxidize by similar mechanisms regardless of

surface structure, although surface morphology undoubtedly influences the relative importance of the various mechanisms. The reduction in reactivity at high surface temperatures is particularly important for the design of TPSs, as the mass flux will decrease as the rate of CO and CO_2 producing reactions slows.[12] Additionally, O and CO ablation products can go on to react in the gas phase of the boundary layer that forms when a hypersonic vehicle travels through the atmosphere. Thus, the changing surface reactivity will greatly affect the chemistry occurring in the boundary layer as the surface temperature is increased.[12] Furthermore, considering that most of the reactions that form CO and CO_2 occur via LH mechanisms, decreased reactivity at elevated surface temperatures would decrease the heat flux to the surface, lowering the mass requirements for TPSs. While the earlier vitreous carbon study was pivotal in understanding the mechanism by which carbon reactivity is suppressed at high surface temperatures, the relatively rough surface made it difficult to distinguish LH and ER/HA reactive processes. The reactive and non-reactive scattering dynamics of high translational energy O atoms on HOPG lead to a better understanding of the relative importance of these processes to the oxidation of graphite at high temperatures.

4.4A Impulsive Scattering of O and O_2

Computational studies suggest that the dominant reactive process occurring when HOPG is bombarded by high energy O atoms is the abstraction of a chemisorbed O atom by a gas-phase O atom to produce O_2.[20,72] In Figure 4.1b, it appears that the O_2 signal increases with surface temperature, which falsely suggests that the rate of an O_2-forming reaction changes with temperature. From Figure 4.7, it can be understood that the apparent

change in flux in Figure 4.1b is caused by the slightly increasing width of angular distribution of the scattered O_2 molecules, presumably as a result of thermal vibrations of the surface at elevated temperatures.[93] An analogous phenomenon is undoubtedly the cause of the increase in the intensity of the IS O atoms with temperature, which is apparent in Figure 4.1a. Morón et al. calculated that O_2 produced via an ER mechanism has an angular distribution with a FWHM width of 23° and a maximum flux below the specular angle.[9] This result does not agree with the O_2 angular distributions observed in Figure 4.7, which have θ_{max} = 56.5° at all temperatures and FWHM widths that rise from 15.8° to 19° as the surface temperature increases from 1100 K to 1900 K. In fact, the O_2 angular distributions are even narrower than those obtained for IS O atoms, which have FWHM widths of 19.8° and 22.2° at 1100 and 1900 K, respectively. The observed scattering dynamics are indicative of impulsive scattering of O_2, which is present in the incident molecular beam, from a clean and well-ordered surface, which have been discussed in detail in an earlier publication.[102] If the surface were substantially roughened by either high temperature or severe surface oxidation, the angular distributions for IS species would be expected to be significantly broader. However, the TOF distributions for O_2 for every combination θ_f and surface temperature contain only a single well-defined peak and do not show evidence of a "shoulder" that would result from secondary collisions with the surface (see Figure 4.1b), further demonstrating that the surface is smooth and well-ordered. Multiple-collision events would yield IS molecules that have final energies between those of the primary IS scattering peak and those expected if the molecules had exited the surface through the TD channel. In addition, the lack of TD signals in the TOF distributions for O_2 indicates that

the cyclic recombination of epoxy groups, which is a LH reaction,[8] is not occurring. The absence of O_2 formed by reactions suggests that the O-atom surface coverage is low during the experiment.[9] The computational studies that predict the dominant reaction mechanism to be formation of O_2 by an ER reaction during bombardment of HOPG by 500 kJ mol^{-1} O atoms may be using a surface coverage of O that is higher than what our experimental conditions provided.

4.4B Thermal Desorption of O Atoms

The total flux and dynamical behavior of the IS O atoms was insensitive to the HOPG temperature; however, the dynamics of the TD O atoms exhibited a strong temperature dependence. The TD O atoms are unlikely to originate from O atoms that have penetrated the topmost graphene layer of the surface. Although the threshold energy for O atoms penetrating a graphene layer has not been measured, it has been obtained for Ne^+, which has a similar mass and size. The penetration threshold for Ne^+ is 32.5 ± 2.5 eV,[90] which is significantly higher than the maximum O-atom translational energy in the incident beam (560 kJ mol^{-1} or 5.8 eV). We inferred from our earlier study with vitreous carbon that the increasing flux of TD O atoms with higher surface temperatures was not the result of an increasing probability of gas-surface thermal equilibration brought about by a physical process such as thermal roughening[111] but rather an increasing probability of C-O bond cleavage that releases chemisorbed O atoms.[108] The implication of this conclusion is that the initial O-atom chemisorption probability is essentially constant with temperature. At low surface temperatures, the chemisorbed O atoms cannot desorb from the surface and either go on to react to form volatile CO and CO_2 or become permanently

trapped. At high surface temperatures, there is enough energy available from the surface that the C-O bond can dissociate, allowing the O atom to desorb into the vacuum and lowering the surface coverage of O. This interpretation of the earlier results is consistent with our current study on HOPG, which shows that the flux of IS O atoms hardly changes with surface temperature and therefore suggests that the sticking probability of O on HOPG depends only weakly on surface temperature, if at all. Thus, in analogy with the previous study with vitreous carbon, we conclude that the TD O-atom signal from HOPG originates from O atoms that have chemisorbed to the surface.

While the origin of the TD O atoms has a reasonable explanation, the scattering dynamics of the TD O atoms are more difficult to decipher. For a surface temperature of 1100 K, the TD O atoms exit the surface with energies that appear to be less than $2RT_s$. Final energies less than $2RT_s$ have been observed when atoms desorb from the surface in a barrierless (non-activated) process,[39,42] in which case the energy of the desorbing atoms increases with θ_f and their angular distribution is broader than $\cos(\theta_f)$. [39,42] It is clear from Figure 4.5 (red symbols) that while $\langle E_f \rangle_{TD} < 2RT_s$ for the TD_{slow} O atoms at 1100 K this value decreases with θ_f. Additionally, the angular distribution of these atoms is narrower than $\cos(\theta_f)$ (Figure 4.6b, red symbols), indicating that the O atoms desorb from the surface over a barrier (activated process).[40] Thus, for a surface temperature of 1100 K, the TD_{slow} O atoms exhibit dynamical traits that are indicative of both activated and non-activated desorption. In order to describe the observed trends shown by the red symbols in Figures 4.5 and 4.6b, an explanation beyond a simple, one-step desorption process is necessary.

It is possible that the dependence of $\langle E_f \rangle_{TD}$ on θ_f depicted by the red symbols in Figure 4.5 is the result of O atoms that chemisorbed on the surface and then intercalated under a graphene layer before desorbing. Graphite can be intercalated by a variety of atoms and molecules,[112] and intercalation methods are frequently used to produce graphite oxide, which is an important precursor in the production of graphene.[18] It has been demonstrated for graphene supported on a variety of metal substrates that the oxygen intercalation process is initiated at edge sites and defects.[113-114] This process can be reversed by annealing the surface at relatively low temperatures between 573 and 673 K.[114] Furthermore, DFT studies have shown that an O atom intercalated between 2 layers of graphene is more stable than an O atom bound to the surface.[115] Given these considerations, we propose that the TD_{slow} signal arises from O atoms that have intercalated between graphene layers.

In our experiment, intercalation could initiate at etch pits that form on the surface upon exposure to O atoms.[66] The fresh layers of graphene exposed when etch pits form can be readily populated by incoming O atoms. Considering that the O-atom diffusion coefficient on a graphite surface held at high surface temperatures is large,[106] it is possible that an O atom that lands in an etch pit on the surface could rapidly migrate underneath the top-most layers of graphite and become trapped for a period of time before eventually desorbing. The final desorption step would likely require surmounting a barrier, because O-atom adsorption is an activated process,[68,105] which would result in an angular distribution that is narrower than $\cos(\theta_f)$. This multistep process (adsorption/intercalation/de-intercalation/desorption) would result in $\langle E_f \rangle_{TD} < 2RT_s$ if the

O atoms had substantial residence times on the surface, because the desorption time would be decoupled from the time when the O-atom pulse collided with the surface, which is time zero (t = 0) for the analysis of the observed TOF distributions.[109] We estimate that the shortest detectable residence time in our experiment would be on the order tens of microseconds. In order to determine the true $\langle E_f \rangle_{TD}$ of the TD_{slow} O atoms on HOPG at 1100 K, the analysis would need to account for the residence time, which is currently unknown and cannot be unambiguously determined from this set of data. With further experimentation (beyond the scope of the current work) the residence time could be measured with an additional chopper wheel located between the surface and the detector.[109] Given the likelihood of a significant residence time for a fraction of the O atoms that eventually desorb, it is not appropriate to fit the data at 1100 K with eq 4.1 and 4.4, and the values of E_c and X obtained for the TD_{slow} O atoms at 1100, 1300, and 1900 K, listed in Table 4.1, do not have a straightforward interpretation. We only utilize the line shape resulting from the fit, which describes the TD_{slow} component in the TOF distributions well, and we consider only the product energy and the flux obtained from this analysis, which are underestimated as a result of the ambiguity introduced by the residence time.

As the surface temperature is increased, the C-O bonds for the O atoms that have chemisorbed to the surface have a higher probability of cleaving, allowing the O atoms to escape into the vacuum.[108] When the surface temperature is 1300 or 1900 K, $\langle E_f \rangle_{TD} > 2RT_s$ for the TD O atoms when $\theta_f < 60°$, but $\langle E_f \rangle_{TD} < 2RT_s$ when $\theta_f > 60°$, suggesting that two desorption channels are present: one that yields TD_{fast} O atoms and another that yields TD_{slow} O atoms. The O_2 TOF distributions indicate that secondary collisions for IS

products are not significant. Therefore, we do not expect a secondary IS component resulting from multiple-collision events to distort the TD_{fast} O-atom distributions and shift $\langle E_f \rangle_{TD}$ to higher values. The presumed TD_{fast} and TD_{slow} components are not distinguishable in the TOF (Figure 4.4) or $P(E_T)$ (not shown) distributions. In addition, we cannot estimate the residence time of the TD_{slow} O atoms or the desorption barrier for the O atoms at high temperatures, so we are unable to separate these two components with any confidence. Therefore, the translational energy barriers, E_0, obtained from the fitting procedure reported in Table 4.1 are effective barriers for the two processes combined and are difficult to interpret.

The values for the effective E_0 obtained at $\theta_f = 15°$ for TD O atoms desorbing from the HOPG surface held at 1300 and 1900 K are 11.1 ± 0.3 and 5.7 ± 0.7 kJ mol^{-1}, respectively, which suggests that the barrier to desorption decreases with surface temperature. In contrast, the values for W do not vary substantially over this temperature range (15.3 ± 0.7 kJ mol^{-1} at 1300 K and 16.8 ± 0.6 kJ mol^{-1} at 1900 K), suggesting that the nature of the sites from which the O atoms desorb does not change substantially with temperature. The angular distributions for the TD O atoms grow broader with temperature, from $\cos^3(\theta_f)$ at 1100 K and 1300 K to $\cos^{2.2}(\theta_f)$ at 1900 K (Figure 4.6b: red, orange, and blue symbols, respectively), also suggesting that E_0 decreases with increasing temperature. Simulations conducted for O-atom reactions with room temperature graphene have shown that the barrier to O-atom adsorption (which, according to the principal of detailed balance is equal to the desorption barrier) decreases when the O-atom surface coverage is reduced.[68] Our findings are consistent with these simulations, given our inference from

the temperature-dependent data that the surface coverage of O atoms must be decreasing as chemisorbed O atoms leave the surface at elevated surface temperatures. However, the overlap of the TD_{slow} and TD_{fast} O atoms signals does not allow us to conclude unequivocally that the barrier to O-atom desorption decreases with increasing surface temperature.

4.4C Effect of O-Atom Desorption on the LH CO and CO_2 Reactions

The desorption of O atoms at high surface temperatures coincides with a decrease in reactivity of the surface. DFT calculations revealed that a surface reactive site, typically composed of one or more lactone-ether groups, must be surrounded by a greater-than-stoichiometric number of O atoms in order for the reactions that produce CO and CO_2 to proceed.[19] The additional O atoms serve to lower both the exothermicity and the reaction barriers by saturating the dangling carbon bonds that form when the product exits the surface. With respect to our experiment, as the surface temperature increases the coverage of O presumably decreases, which decreases the reaction probability to form CO (or CO_2, at lower temperatures) and leads to an apparent non-Arrhenius temperature dependence in the product flux, as seen in Figures 4.1c, 4.1d, and 4.2. The reduced O-atom coverage at high temperatures also causes E_0 for CO produced by LH reactions to increase from 121 ± 5 kJ mol^{-1} at 1100 K to 155 ± 7 kJ mol^{-1} at 1300 K. As CO_2 formation requires more O atoms surrounding the reactive site in order for the reaction to be favorable,[19] this reaction is interrupted at a lower temperature than the CO reaction. Unfortunately, the data obtained for CO_2 in this study could not be used to determine a desorption barrier because the LH and ER/HA reaction products could not be separated.

A fraction of the CO products is detected with long flight times that could not be accounted for by the fitting procedure described in Section 3D (shown by the gray lines in Figure 4.9). Slow CO product desorption was also observed in our previous studies of the oxidation of vitreous carbon and HOPG.[20,108] In the vitreous carbon study, we proposed that the slow CO may be the result of the Boudouard reaction, where an initially formed CO_2 product undergoes a secondary reaction with the surface to produce CO.[108] However, our more considered hypothesis here is that O atoms can intercalate the graphene layers, so we now believe that it is more likely that the CO at long flight times originates from reactions with intercalated O atoms. Intercalation would result in CO that would appear to be leaving the surface slowly and could be responsible for the TD_{slow} O atoms described above.

4.4D ER/HA Reaction Mechanisms for CO and CO_2

While the majority of the CO products are produced by LH surface reactions, there is clear evidence for CO that is formed by either an ER or a HA mechanism, which persists even at high surface temperatures. The angular distribution for the ER/HA CO, represented by the blue symbols in Figure 4.8, has a maximum flux beyond the specular angle, which suggests that these products retain some memory of the incident O-atom trajectory. Both the flux and $\langle E_f \rangle_{Total}$ of the ER/HA CO did not change significantly with surface temperature. As discussed above, these characteristics are indicative of either an ER or a HA reaction mechanism,[3,47] both of which yield products that are translationally, vibrationally, and rotationally excited and have angular distributions that are peaked far from the surface normal.[10-11] In addition, the reaction rates of these mechanisms are

independent of surface temperature.[46] Products formed by ER and HA reactions are difficult to distinguish experimentally, and simulations are required to identify the two channels. However, experiments and theory have shown that molecules formed via an ER mechanism scatter from the surface with high translational energies, with angular distributions that have maxima below the specular angle.[11,116-118] This mechanism is more probable when the surface coverage of the abstracted adsorbate is high and the adsorbate is weakly bound to the surface.[10,45] Molecules formed via an HA mechanism have been shown by computation to have lower translational energies, because the incoming projectile enters a quasi-chemisorbed state before it reacts with the adsorbate.[10,47] The HA mechanism is favored over the ER mechanism when the surface coverage of the adsorbate is low and the adsorbate is bound tightly to the surface,[10,45] as is the case in our experiments with HOPG at high temperatures.

The angular distributions of the observed ER/HA CO are directed beyond the specular angle, while $\langle E_i \rangle_{\text{Total}}$ for the scattered molecules is low. O atoms with an average incident translational energy of 472 kJ mol^{-1} cannot abstract a carbon atom from a pristine graphite lattice because this process is 500 kJ mol^{-1} endothermic: each C-C bond in graphite has an energy of 524 kJ mol^{-1} while the C≡O bond formed has an energy of 1072 kJ mol^{-1}.[119] Therefore, unless all the ER/HA CO products come from the high-energy tail of the incident O-atom distribution, the carbon abstracted from the surface likely resides at a defect site, in which case the energy required to abstract a carbon atom would be reduced below the average O-atom incidence energy. The surface concentration of defects sites is presumably low, as indicated by the narrow angular distributions for O and O_2 that are

indicative of scattering from a smooth surface. As mentioned above, a low concentration of "abstractable" carbon atoms would be more favorable for HA reactions. It is interesting to note that $\langle E_f \rangle_{\text{Total}}$ for the CO produced by an ER/HA reaction is lower than $2RT_s$ (Figure 4.10, blue symbols). Although molecules produced via ER and HA mechanisms generally scatter from the surface with high translational energies, the reactions studied to date have focused on the abstraction of an adsorbate from a surface. In this study, the abstracted carbon atom is well coupled to a graphene layer, which might facilitate energy release to surface phonons. Such energy transfer has been shown to be important for the tug-of-war mechanism observed for the inelastic scattering of H from graphene, where the incident atom loses a large portion of its incident kinetic energy after it forms a short-lived chemical bond with a carbon atom and the available energy is transferred into the deformation of the graphene surface.[120] A significant fraction of the available energy might also be deposited into vibrational and rotational modes of CO. The detection method used in this experiment (mass spectrometry) only allows us to conclude unequivocally that very little of the available energy goes into translation of the CO product. Thus, further experiments and/or simulations would be necessary to determine how the available energy is partitioned when CO is produced by an ER/HA reaction.

CO_2 was also produced via an ER or a HA mechanism, as shown by the lobular angular distribution directed away from the surface normal (Figure 4.12a). In contrast to the ER/HA mechanism which produces CO, this reaction depends on surface temperature, as indicated by the decreasing flux and increasing $\langle E_f \rangle_{\text{Total}}$ of the scattered CO_2 with increasing surface temperature (Figures 4.12a and 4.12b). This temperature-dependent

behavior suggests that CO_2 that is formed by an ER/HA reaction proceeds through a precursor C-O group on the surface which subsequently reacts with an incoming O atom to produce CO_2. As O atoms begin to desorb from the surface at higher temperatures, this precursor is presumably no longer formed, and the ER/HA reaction can no longer proceed. Another possibility is that nascent CO, produced through an ER/HA reaction, could abstract an O atom that is chemisorbed close to the initial reaction site. However, this process is not consistent with the observation that the flux of ER/HA CO does not change with surface temperature, as such a two-step mechanism involving CO would result in an increasing flux of ER/HA CO with increasing temperature as the ER/HA CO_2 disappears.

4.5 Conclusion

Beam-surface scattering experiments have been used to study the non-reactive and reactive gas-surface interactions of high translational energy O and O_2 with an HOPG surface held at temperatures in the range of 1100 K to 2300 K. Several important observations regarding the interplay between reactive and non-reactive processes have been made. O atoms with an average translational energy of 472 kJ mol^{-1} were found to scatter from the surface without reacting through both impulsive scattering (IS) and thermal desorption (TD) channels. Two different TD pathways were observed, one which produced O atoms with apparent average final translational energies that were less than $2RT_s$ (TD_{slow}) and another which yielded O atoms with average final energies that were greater than $2RT_s$ (TD_{fast}). It was proposed that the TD_{slow} O atoms originated from a complex process that involves an O atom resident on the surface for a period of time, which causes the final energies to appear less than $2RT_s$. The TD_{fast} O atoms desorbed from the

surface over a barrier, the height of which may decrease as surface temperature is increased. While the flux of the IS O atoms did not change with surface temperature, the flux of all TD O atoms increased dramatically as the surface temperature increased. As a result, the surface coverage of O atoms decreased, which limited the formation of CO and CO_2 at high temperatures. The dominant reactive product was CO, which was formed by Langmuir-Hinshelwood (LH) and Eley-Rideal (ER) or hot-atom (HA) mechanisms, the relative fluxes of which strongly depended on surface temperature. The flux of CO produced by LH mechanisms was dominant at low temperatures. CO was produced by LH mechanisms that involved desorption from the surface over a barrier, which increased from 121 ± 5 kJ mol^{-1} at 1100 K to 155 ± 7 kJ mol^{-1} at 1300 K. These desorption barriers correspond to the final step of the CO reaction, which would be the breaking of the bond between a surface C atom and the C atom of the CO. CO products that scattered from the surface at 1900 K were produced only by ER/HA mechanisms. CO_2 was formed through LH and ER/HA mechanisms, the fluxes of which decreased below detectable limits as the surface temperature was increased above 1300 K. O_2 was only observed to scatter through IS processes. The O_2 originated in the incident beam, which contained 11 percent O_2, and not from a reaction between an incident O atom and a chemisorbed O atom. These experiments reveal how the surface temperature governs the complex reactive and non-reactive processes occurring on the HOPG surface. At high temperatures, the incident O atoms desorb promptly from the surface, which in turn hinders the reactions that produce CO and CO_2 and thus protects the surface from further oxidation. Given that similar non-Arrhenius behavior has been observed for several graphitic surfaces, it seems that this process is

relevant to the oxidation of sp^2 bonded carbon regardless of the surface structure. The competition between O-atom desorption and CO/CO_2 formation is critical to the design of TPSs. For example, as the reactivity of the surface decreases at elevated temperatures, the heat flux to the surface and mass flux away from the surface will decrease. Furthermore, the gas-surface reactions have an impact on the heat and mass flux through the contribution of their products to the gas-phase chemistry occurring in the boundary layer in contact with the TPS. This study is another step in advancing our fundamental understanding of boundary layer chemistry for ablating TPSs and may therefore help to reduce the uncertainty in computational fluid dynamics models of the critical flow processes important in hypersonic flight.

Acknowledgements

This work has been supported by the Air Force Office of Scientific Research: FA 9550-17-0057. V.J.M. is grateful for support from the Department of Defense (DoD) through the National Defense Science & Engineering Graduate Fellowship (NDSEG) Program. The authors thank Philip J. Woodburn and Brooks C. Marshall for their assistance with data collection.

CHAPTER FIVE

GAS-SURFACE SCATTERING DYNAMICS APPLIED TO CONCENTRATION OF GASES FOR MASS SPECTROMETRY IN TENUOUS ATMOSPHERES

Contribution of Authors and Co-Authors

Manuscript in Chapter 5

Author: Vanessa J. Murray

Contributions: Performed molecular beam scattering experiments and conducted data analysis. Prepared both the figures and the manuscript for publication.

Co-Author: Marcin D. Pilinksi

Contributions: Performed SPARCS simulations and provided draft text for the manuscript.

Co-Author: Eric J. Smoll Jr.

Contributions: Provided crucial input regarding the analysis of the experimental data.

Co-Author: Min Qian

Contributions: Assisted with the molecular beam scattering experiments.

Co-Author: Timothy K. Minton

Contributions: Provided crucial insight regarding the experimental procedure and the data analysis. Aided in the preparation of the manuscript and figures.

Co-Author: Stojan M. Madzunkov

Contributions: Introduced us to the initial concept that motivated the experiments.

Co-Author: Murray R. Darrach

Contributions: Introduced us to the initial concept that motivated the experiments.

Manuscript Information Page

Vanessa J. Murray, Marcin D. Pilinski, Eric J. Smoll, Jr., Min Qian, Timothy K. Minton, Stojan M. Madzunkov, and Murray R. Darrach

Journal of Physical Chemistry C

Status of Manuscript:
_____ Prepared for submission to a peer-reviewed journal
_____ Officially submitted to a peer-review journal
_____ Accepted by a peer-reviewed journal
__×__ Published in a peer-reviewed journal

Published by the American Chemical Society
In Volume 121, Issue 14, pp 7903 - 7922 (2017)

Reproduced with permission from ACS – the American Chemical Society

GAS-SURFACE SCATTERING DYNAMICS APPLIED TO CONCENTRATION OF GASES FOR MASS SPECTROMETRY IN TENUOUS ATMOSPHERES

Vanessa J. Murray,[a] Marcin D. Pilinski,[b] Eric J. Smoll, Jr.,[a] Min Qian,[a] Timothy K. Minton,[a,*] Stojan M. Madzunkov,[c] and Murray R. Darrach[c]

[a] *Department of Chemistry and Biochemistry, Montana State University, 103 Chem/Biochem Bldg., Bozeman, MT, 59717*

[b] *Atmospheric and Space Technology Research Associates (ASTRA), 5777 Central Ave., Suite 221, Boulder, CO, 80301*

[c] *Jet Propulsion Laboratory, California Institute of Technology, 4800 Oak Grove Dr., Pasadena, CA, 91109*

Abstract

A concept for a passive neutral gas concentrator that facilitates the analysis of rarefied atmospheres using mass spectrometry on spacecraft has been developed. The efficiency of the concentrator depends strongly on gas-surface scattering dynamics between the incoming gas molecules and the concentrator surface. We have conducted beam-surface scattering experiments using hyperthermal beams containing atomic and molecular oxygen with speeds of approximately 5,500 m s^{-1}, with angular and velocity resolution of the inelastically scattered O and O_2, on gold thin-film, SiO_2, and highly oriented pyrolytic graphite (HOPG) surfaces, which were chosen as candidate concentrator surfaces. The results show clearly that atoms and molecules scattering from HOPG have the narrowest and most super-specular angular distributions with the least energy transferred to the surface. A test particle model, referred to as the Statistical Program for Aerodynamic and Radiation Pressure Coefficient Simulation, utilized the experimental

results to model gas concentration in three-dimensional cone and annular-ring geometries constructed of the representative materials chosen for study. The modeling results indicate that a cone concentrator with a 10° half-angle opening yields the highest concentration factors. In addition, a cone constructed of HOPG yields a concentration factor that is an order of magnitude higher than what can be achieved using gold or SiO_2 surfaces.

5.1 Introduction

Mass spectrometry is an accurate method for identifying the composition of planetary atmospheres and has been used extensively on robotic missions to planetary bodies across the solar system.[25-27] For flyby or probe missions, mass spectrometers (MSs) are designed for short sampling times of the low pressure atmosphere of a planetary body. Analytes of interest include life-signature organic molecules at number densities ranging from 10^{10} down to 10^{3} molecules cm^{-3}. Direct measurement of these extremely rarefied atmospheric constituents is very difficult in the environment of the spacecraft's outgassing particles. In order to increase the relative abundances of analytes with respect to the background, suitable gas-concentration approaches are required.

The new-generation MSs on board atmospheric entry probes are expected to provide a detailed survey of an atmosphere's chemical and isotopic composition at increased temporal and spatial resolutions. The main design challenges of such an instrument are: (a) the amount of atmosphere sampled has to provide sufficient signal to overcome the background, (b) the neutral molecules and atoms in the sampled atmosphere must remain unaffected by the sampling method, and (c) the transmission of atmospheric constituents through the instrument must be relatively fast so as not to distort the time

response of the instrument and compromise the spatial information of the data. In addressing these challenges, the design of the MS inlet which collects the neutral gas analytes must be carefully considered. The MS inlet collects the neutral gas and provides a conduit for it to enter the ion source. The MS ion source, generally a beam of electrons, ionizes the neutral atoms or molecules according to their ionization cross sections. Next, the ionized analytes enter the mass filter, which separates the ionized analytes according to their mass-to-charge ratio, *m/z*. Finally, a detector converts the filtered ion current into an electrical signal which ultimately may be related to the flux of incident atoms or molecules at that *m/z* ratio which entered the inlet. This paper focuses on the gas-surface scattering dynamics and the design informed by these dynamics; the design, and testing of a gas-concentrating inlet for future mass spectrometers will be the subject of a future study.

Previous MS instruments flown on spacecraft were equipped with either open ion source inlets or closed ion source inlets. Open ion source inlets, or simply open-source inlets, expose the ionization region in the MS ion source directly to the incoming gas, usually through a series of collimating knife-edge apertures. The open-source inlet approach has the benefit of minimizing gas-surface interactions in the instrument, which reduces the probability of surface reactions that may complicate the data analysis. Drawbacks of this technique are that the fluxes of neutral molecules passing through the ionization region are low and that several assumptions must be made about the collimated velocity distribution.

Closed-sourced inlets are also used to study tenuous atmospheres. This method relies on an accommodation chamber, such as the one used for the NASA/ESA Cassini

probe mission.[25] Generally, the accommodation chamber is a spherical cavity fed by a large circular opening facing the approximate direction of spacecraft motion. The incoming neutral analytes are passed to the MS ionization region by a transfer tube with a smaller cross section that is offset from the entrance aperture.[26] The high relative velocity between the spacecraft and the ambient atmosphere, which often reaches hypersonic speeds, allows the buildup of pressure inside the accommodation chamber which in turn improves the detection efficiency of the instrument. Analytes are introduced into the accommodation chamber as a directional beam having an unknown free-stream temperature and leave the cavity after experiencing many surface collisions as a thermalized ensemble at the temperature of the chamber walls. Three drawbacks of this method are: (1) the collisions of analytes with the walls of the accommodation chamber can be sufficiently energetic to cause chemical changes, rendering their identification questionable, (2) adsorption on the walls can lead to reactions on their surfaces, the products of which later desorb into the analyzer, and (3) the gas concentration can be limited as a result of analytes escaping the accommodation chamber through the relatively large intake opening.[121] The last drawback may be addressed by reducing the ratio of the inlet to exit aperture areas. However, this approach will lead to a larger cavity and longer transmission times through the instrument if the incoming flux is to be maintained. Transmission times through the Cassini MS instrument were already large for non-volatile species, leading to an instrument step-response on the order of several minutes for H_2O. This step response was often a large fraction of the total duration of a Cassini atmospheric flyby. Another feature of the closed-source inlet used on the Cassini mission was that the location of the transfer tube allowed

analytes to reach the transfer tube directly from the entrance aperture, which introduced a non-symmetric dependence of the inlet response to its orientation in the free-stream. This effect complicated the data analysis associated with this MS by adding extra parameters to the model describing the instrument response.[122] The closed source inlet must have both low transmission times (achieved by a smaller accommodation chamber) and an instrument response that can be modeled with as few input variables as possible.

Here we propose a modification of the closed-source method that prevents a substantial loss of collected analytes through the intake opening and minimizes the effect of analyte-surface interactions while maintaining fast transmission times and high signal-to-background levels. We have designed several configurations of a neutral gas concentrator that allows for the accumulation of atmospheric analytes in an accommodation chamber that is attached to a MS. The concentrator has an atmospheric intake opening that is much larger than its exit to the accommodation chamber and acts as a unidirectional valve allowing pressure buildup in the accommodation chamber. The accommodation chamber in turn has a large opening toward the MS ionization and analysis regions. This design should achieve a large signal-to-background ratio while maintaining a low transmission time. The efficiency of the concentrator is enabled by the specific gas-surface interactions of the incoming molecules that favor direct, inelastic scattering that is focused toward, or beyond, the specular angle. This scattering behavior was tailored into the design by carefully choosing the material used to construct the concentrator surface. The final material selection was informed by molecular beam scattering experiments performed on several candidate surfaces.

Molecular beam experiments provide detailed information about the interactions between an impinging molecule and a surface and therefore aid in the optimization of gas concentrator design. The concentrator surface should promote impulsive scattering over trapping and thermal desorption (trapping desorption) so the maximum number of molecules pass through the concentrator and into the accommodation chamber. In addition, a chemically inert surface is required to minimize gas adsorption or surface reactions, as the formation of an adsorbed layer or a change in surface morphology would alter the scattering dynamics of the incident molecules.[123-124] Beam–surface scattering experiments facilitate the identification of desirable concentrator surfaces through measurements of the translational energy and angular distributions of the scattered species. The widths of the angular distributions and the energy transfers during the collisions are greatly affected by both surface roughness and the corrugation of the potential energy surface (PES) between the incoming molecule and the surface.[4,125] Rough or disordered surfaces with root mean square (RMS) roughnesses greater than a few nanometers produce broad angular distributions and promote energy loss resulting from multiple collisions with the surface.[126] Conversely, a smooth or well-ordered surface promotes scattering over a narrow angular range toward the specular direction with little energy transfer to the surface.[125,127] Indeed, it was shown that the inelastic scattering of N_2 can be a very sensitive probe of the extent of surface roughening during etching.[128]

In order to guide the design of the concentrator for the MS inlet, we have studied the scattering dynamics of a molecular beam containing high velocity O atoms from prospective concentrator surfaces. Atomic oxygen has been shown to be a highly reactive

species in a number of planetary atmospheres including Venus, Earth, and many of the icy moons of Jupiter and Saturn. In the case of low Earth orbit, O atoms cause significant oxidation and erosion of the surfaces of materials that are commonly used on the exterior of spacecraft.[129-131] Thus, surfaces that are deemed to be appropriate for use with O atoms will likely be appropriate for other potentially reactive compounds found in planetary atmospheres, such as water. A laser-detonation source[132] that produces a beam of hyperthermal O and O_2 was therefore chosen for our initial studies of gas-surface interactions on candidate concentrator surfaces, which need to be unreactive and remain smooth even when bombarded by reactive species at high relative velocities of several kilometers per second.

Gold is a chemically inert, noncatalytic surface that is a promising candidate as a concentrator material. Smooth thin films of gold can easily be produced on a variety of different substrates and geometries via a variety of different deposition techniques. Most chemical constituents, including water and organic molecules such as acetone, methanol, formic acid, and formaldehyde, have low adsorption energies on gold and adsorb/desorb reversibly without decomposing.[133-136] Furthermore, gold is the only transition metal that does not have a stable oxide; Au_2O_3 is metastable and decomposes quickly at temperatures above 423 K.[137-138] For the application of a concentrator, if the gold oxidizes, the oxide can be removed by heating the surface for several minutes.

Very smooth wafers of silicon are regularly produced for the semiconductor industry and might also make suitable concentrator surfaces. While unsaturated hydrocarbons, water, and ammonia have been shown to decompose on a bare Si(100)

surface, a silicon surface can be protected from contamination by oxidizing it with atomic oxygen, which produces a thin layer of SiO_2 with an alpha-quartz orientation that retains the initial surface roughness of the original silicon surface.[139-141] In an effort to develop a concentrator of O atoms for accelerated testing of materials for low Earth orbital applications, Tagawa et al. evaluated several cone-shaped test concentrators constructed from Pyrex glass, which has similar chemical properties as SiO_2. The glass cones were used to concentrate a beam of hyperthermal atomic oxygen, and concentration factors between 3 and 4 were achieved.[142-143]

A highly oriented pyrolytic graphite (HOPG) surface is nearly perfectly ordered and atomically flat, and it has been shown in previous work in our laboratory that energetic atoms scattering from HOPG have remarkably narrow angular distributions that are peaked in the super-specular direction.[144] HOPG has been shown to be unreactive with O_2 at low temperatures and can only react through dissociative chemisorption at defect sites at higher temperatures. As such, HOPG is another promising choice as a concentrator material. HOPG has a low defect density of 3-4 μm^{-2}, which retards the reactivity of the surface.[21,145-147] O atoms are more reactive with HOPG than O_2; however, the reactivity is sufficiently low that the dynamics of the scattered O atoms are not distorted.[148]

We have conducted a series of experiments that investigated the scattering dynamics of hyperthermal molecular beams containing O and O_2 from the surfaces of the three prospective concentrator materials described above: a gold thin film, SiO_2, and HOPG. The experimental results have been used in Monte Carlo test particle simulations to study the efficacy of cone-shaped and annular-ring concentrators that are constructed of

the three proposed materials. We have found that concentration factors may exceed 100 for a cone that is composed of HOPG.

5.2 Methods

5.2A Experimental Methods

The experiments were performed with the use of a crossed molecular beams apparatus configured for beam-surface scattering experiments coupled to a hyperthermal, laser-detonation beam source (Figure 5.1).[126,132,149] Briefly, a pulsed molecular beam, with a repetition rate of 2 Hz, was directed at planar surfaces of Au, SiO_2, or HOPG. Inelastically scattered O and O_2 were monitored with a MS detector that rotated about an axis that passed through the surface of the sample within the plane determined by the incident beam and the surface normal. The MS detector consisted of an electron-impact ionizer,[150] a quadrupole mass filter, and a Daly-type ion counting system operating in pulse counting mode.[151] The amplified ion pulses produced by the detector were recorded by a

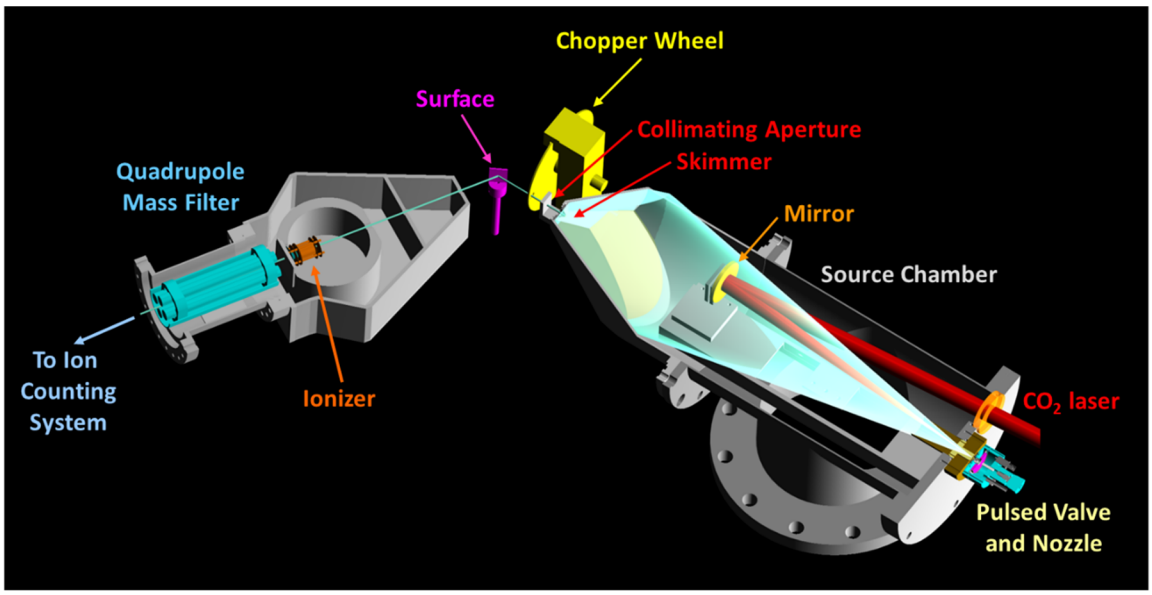


Figure 5.1. Schematic diagram of the experimental apparatus.

multichannel scaler. After accounting for the ion flight time from the electron impact ionizer to the ion counter, as well as additional experimental offsets,[132] we obtained relative number density distributions of the detected species as a function of arrival time at the electron impact ionizer, $N(t)$. These distributions are commonly referred to as time-of-flight (TOF) distributions. The mass spectrometer detector was triply differentially pumped so that the region containing the electron-impact ionizer had a base pressure of less than 10^{-11} Torr and did not rise during data collection even though the operating pressure of the main chamber was 4×10^{-7} Torr.

Two hyperthermal beams were produced with the laser-detonation source for this study: one containing a mixture of O and O_2 and the other composed solely of Ar. The beam was collimated by a 2.0 mm skimmer and a 0.7 mm aperture located 77 cm and 80 cm, respectively, away from the beam origin at the apex of the conical source nozzle. The aperture ensured that the spot illuminated on the sample by the beam was smaller than 2.8 mm, even at the most grazing incidence angles, so that the entire beam spot could be viewed by the detector which had a total viewing range of slightly more than 3 mm × 3 mm. A synchronized chopper wheel with three equally spaced 1.6 mm wide slots, spinning at 300 Hz, was used to select a narrow velocity distribution from the collimated molecular beam pulse.[132] TOF distributions and component fluxes of the incident molecular beams were determined by lowering the sample out of the beam path and directing the beam into the detector, 132.2 cm away from the beam origin. Probability distributions for velocity and translational energy, $P(V_{in})$ and $P(E_{in})$, respectively, for the beam were derived from the TOF distributions with a density-to-flux conversion.[35,152] Atomic and molecular oxygen

produced in the beam are in their ground electronic states, O(^3P) and O_2 ($^3\Sigma_g^-$).[153-154] TOF distributions for *m/z* = 16 (O^+) were corrected for the dissociative ionization of *m/z* = 32 (O_2^+) in the electron impact ionizer. The flux of each component in the molecular beam was obtained by integrating the respective $P(E_{in})$ distribution. The velocity-selected molecular beam was directed at a sample located 99.2 cm away from the beam origin. The experimental conditions for each surface are shown in Table 5.1.

Table 5.1. Experimental conditions for each sample.

Surface	*Surface Roughness (Å)*	*Incident Species*	*Incident Velocity (m s^{-1})*	*Incident Energy (kJ mol^{-1})*	*O atom %*	*Surface Temperature (K)*
Au	4.23 ± 0.17	O	5440.32	236.87	43.2	773
		O_2	5440.32	474.31		
SiO_2	0.94 ± 0.06	O	7845.09	495.55	83.7	675
		O_2	7421.83	889.49		
HOPG	3.25 ± 1.01	O	5568.36	248.15	44.8	673, 873
		O_2	5568.36	496.81		
		Ar	4836.78	468.78	--	873

Each sample was heated using a resistance-based cylindrical cartridge heater that was inserted into a hole in a copper plate which was in contact with the back of the sample. The temperature of the sample, denoted as T_w because it coincides with the wall conditions of the concentrators described below, was monitored using a type K thermocouple fixed to the back of the copper plate with a screw. Since each of the materials investigated was thermally conductive and relatively thin, the sample and the copper plate were assumed to be in thermal equilibrium. The mount was fastened to a manipulator that could be lowered in and out of the beam path as well as rotated to vary the incidence angle, θ_{in}, of the molecular beam. TOF distributions for scattered products were detected with the rotatable

MS, located 34.4 cm from the surface, for a variety of final angles (θ_{out}) corresponding to θ_{in} of 60° or 70°. All θ_{in} and θ_{out} angles are referenced to the surface normal, with positive θ_{out} angles being on the opposite side of the surface normal from the incoming molecular beam. To compensate for long term drift of the hyperthermal molecular beam during data collection, θ_{out} was varied sequentially from highest to lowest and then lowest to highest repeatedly until a satisfactory signal-to-noise ratio was achieved. The TOF distributions collected for each m/z ratio and θ_{out} were summed before data analysis, and the distributions collected at m/z = 16 (O^+) were corrected for the dissociative ionization of O_2 and for the difference in detection sensitivities of O and O_2 in the MS.

Prior to the experiments, each sample was analyzed using a VEECO Dimension 3100 atomic force microscope (AFM) (Digital Instruments, Santa Barbara, CA, USA) operated in tapping mode in atmosphere. Etched silicon cantilevers with a resonant frequency of approximately 280 kHz were used to analyze the samples. The HOPG surface was prepared for analysis by lifting off several layers of graphene with adhesive tape; the Au and Si(100) were analyzed without any additional sample preparation; the native oxide was not removed from the Si(100) sample for the AFM measurements. The scan rate for the Si(100) and HOPG samples was 1.3 Hz; a lower scan rate of 0.25 Hz was used for the Au sample. Three separate 10 μm × 10 μm areas were scanned on each sample, and the RMS roughness was calculated for each location. The average RMS roughness was calculated from the three measurements taken for each sample. The AFM images of the pristine gold thin film, Si(100), and HOPG surfaces are shown in Figure 5.2. The RMS roughnesses for each sample are reported in Table 5.1.

An Au thin film was prepared using a TSC E-Beam evaporator with a base pressure of 8.7×10^{-7} Torr. A 10 nm thick titanium adhesion layer was deposited at a rate of 1 Å s^{-1} on a 1.3 cm × 1.3 cm x× 0.006 cm piece of prime grade, unannealed silicon (Ted Pella, Inc), followed by deposition of 30 nm of gold at a rate of 1 Å s^{-1}. The resulting thin film had an RMS roughness of 4.23 ± 0.17 Å. The sample was placed into the molecular beam machine with no additional preparation. The O/O_2 beam had an average velocity of 5440.3 m s^{-1} with a velocity width (full width at half maximum, FWHM) of 260.7 m s^{-1} and was composed of 43.2% O atoms, with the balance being O_2. Angular distributions for *m/z* =

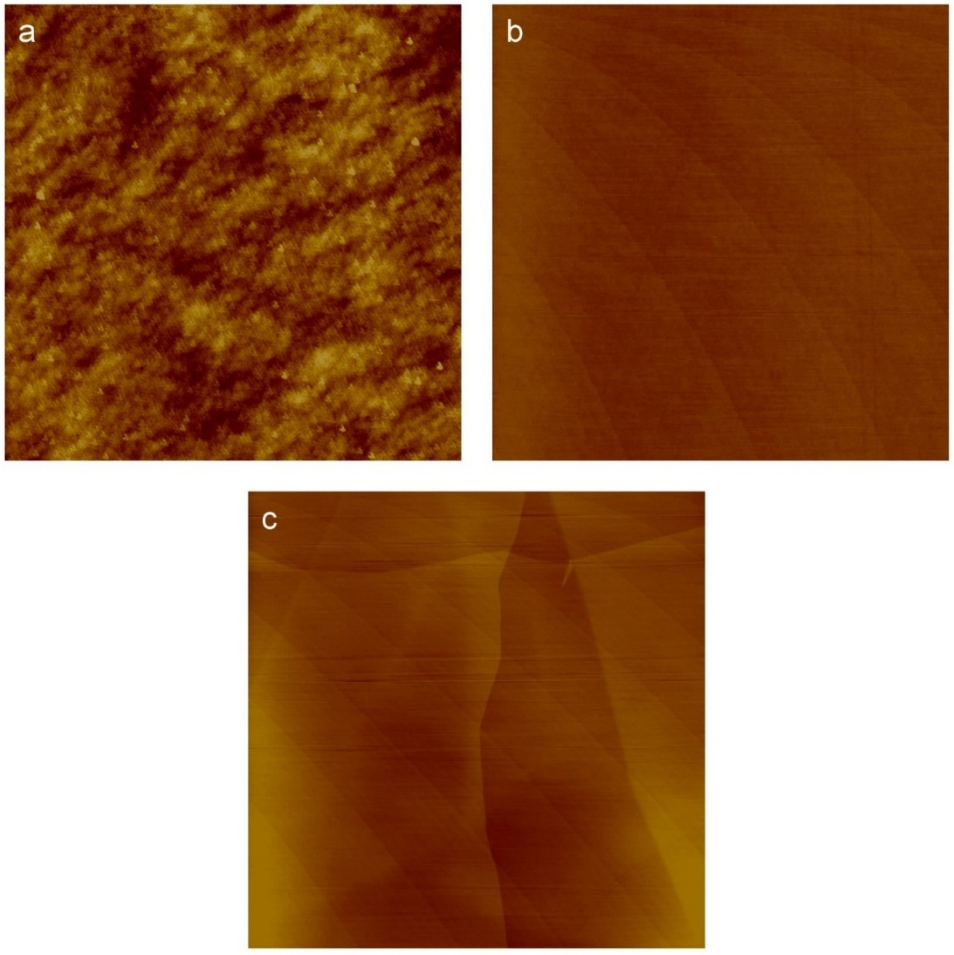


Figure 5.2. AFM images (10 μm × 10 μm) for surface of pristine (a) Au, (b) Si(100), and (c) HOPG. The *z* scale for all three images is 5 nm.

16 (O^+) and m/z = 32 (O_2^+) were collected with T_w = 773 K for θ_{in} = 60° and θ_{out} in the range of 30° to 70°. The apparatus used for this experiment cannot reach ultra-high vacuum (UHV) pressures, 10^{-9} Torr or lower, and lacks an ion sputtering device; thus, a clean surface cannot be maintained at low temperatures. Efforts were therefore made to ensure the cleanest vacuum possible by using only cryogenic pumps and a liquid nitrogen cooled panel to maintain a clean high vacuum environment in the scattering chamber, and the surface was maintained at a high temperature to prevent residual organic contamination from adsorbing onto the surface. Moreover, the surface was continuously bathed in O atoms, which is a commonly used method for removing organic contamination from metal surfaces. We determined that the Au surface was mostly free of contamination by monitoring the reaction products of O atoms with adsorbed organic contamination, m/z = 17 (OH^+) and m/z = 18 (H_2O^+), as a function of surface temperature. At T_w > 750 K, the OH and H_2O signals were <<1% of those for inelastically scattered O and O_2, indicating that the surface was essentially free of contamination.

A 12 mm × 12 mm × 0.65 mm thick piece of prime grade, boron doped Si(100) (Ted Pella, Inc.) with an initial RMS surface roughness of 0.94 ± 0.06 Å, was prepared *ex situ* by removing the native oxide using hydrofluoric acid as prescribed by the method described by Minton et. al.[36] Organic contamination and residual fluorine were removed by rinsing the sample with deionized water after treating the surface with hydrofluoric acid. The sample was placed in the molecular beam machine and the chamber was evacuated immediately after the cleaning procedure was finished. It has been shown that a layer of polycrystalline alpha quartz forms when Si(100) is exposed to hyperthermal O atoms and

the roughness of the oxide layer formed deviates only slightly from the initial surface roughness.[140-141] For this experiment, it can be assumed that the O atoms and O_2 are scattering from a thin SiO_2 layer with an alpha quartz orientation that has a similar surface roughness as that of the pristine Si(100) surface. The surface temperature, T_w, was maintained at 673 K to prevent residual organic contamination in the vacuum chamber from adsorbing the sample. The synchronized chopper wheel was not used for the SiO_2 experiment. Consequently, the O/O_2 beam had a higher velocity of 8745.1 m s^{-1} with a FWHM of 1094.1 m s^{-1}. The beam was composed of 83.7% O atoms with the balance being O_2. Angular distributions for m/z = 16 (O^+) and m/z = 32 (O_2^+) were collected for θ_{in} = 70° and θ_{out} = -20° to 85°.

A 25 mm × 7 mm × 1 mm piece of HOPG (ZYA Grade, Momentive Ceramics) was prepared by lifting off several layers of graphene using tape, leaving a pristine surface with an RMS roughness of 3.25 ± 1.01 Å. The O/O_2 beam used for the beam-surface scattering experiments with HOPG had an average velocity of 5568.4 m s^{-1} with a FWHM of 269 m s^{-1} and was 44.8% O atoms with the balance being O_2. Angular distributions for m/z =16 (O^+) and m/z = 32 (O_2^+) were collected for T_w = 673 K for θ_{in} = 60° and 70° and θ_{out} = 0° to 85°. Angular distributions were also collected with T_w = 873 K to confirm that the surface was clean at the lower T_w. A beam of hyperthermal Ar was also directed at the HOPG surface to investigate if exposure to the O-atom beam affected the surface morphology of the sample. The Ar beam had an average velocity of 4836.78 m s^{-1} with a FWHM of 221.25 m s^{-1}. The incident velocity was chosen so that the incidence energy, E_{in}, of the Ar matched that of the O_2. The angular distribution of the recoiling Ar atoms was

measured for θ_{in} = 60° and θ_{out} = 0° to 85° for T_w = 873 K on the portions of the surface that were exposed and unexposed to the O-atom beam. Angular distributions for the HOPG surface that was unexposed to O atoms were collected by lowering the sample mount 2.5 mm from the position that was used for scattering studies with the O/O_2 beam.

5.2B Computational Methods

A test particle model called the Statistical Program for Aerodynamic and Radiation Pressure Coefficient Simulation (SPARCS) used the experimental data for scattering from a planar surface to calculate flow through a representative three-dimensional concentrator geometry.[155] The model considers particle-surface collisions in the absence of gas-phase collisions. The neglect of gas-phase collisions is consistent with the single-collision conditions of the beam-surface scattering experiments and the extremely low pressures where a concentrator would be used in a tenuous atmosphere. SPARCS first initializes the velocities of particles at one of the six flow boundaries enclosing the surface geometry. Particle position coordinates on each boundary are randomly selected from a uniform probability distribution, and the flux through each boundary is scaled to the theoretical effusion $\dot{N}$ across that boundary as given by the following equation:

$$\dot{N} = n \frac{\exp\left(-s^2 \cos^2\theta\right) + \sqrt{\pi} s \cos\theta \left(1 + \operatorname{erf}\left(s\cos\theta\right)\right)}{2\sqrt{m\pi / \left(2k_b T_{fs}\right)}}, \qquad (5.1)$$

where n is the number density (m^{-3}) and θ is the angle of the free-stream bulk velocity with respect to the axis of revolution of the concentrator (degrees). We will refer to this angle throughout the paper as the angle of attack with respect to the free stream or simply the

"angle of attack". Continuing with eq 5.1, m is the mass of the particle (kg), k_b is the Boltzmann constant (J K^{-1}), T_{fs} is the free-stream temperature (K) upstream of the inlet and erf is the error function. The speed ratio, s, is defined as

$$s = U\sqrt{m/\left(2k_bT_{fs}\right)}, \tag{5.2}$$

where U is the magnitude of the free-stream bulk velocity (m s^{-1}). Note that s can be thought of as the ratio of the bulk to thermal velocities in the free stream.

Next, the incoming velocities are selected by sampling from a drifting Maxwellian distribution at temperature T_{fs} and bulk velocity V_{in} (m s^{-1}). Ray tracing is then performed from the initial position of the particle to surface elements of the geometry, and a scattered velocity is selected at each impact location based on the desired scattering model. Surface elements are represented by a geometric mesh file that can be generated by a number of computer aided design software packages.

The surface scattering model is chosen randomly for each detected impact based on a pre-specified probably of occurrence for various simplified scattering types. The two broad categories of simplified scattering types considered by SPARCS in this study are diffuse and quasi-specular (QS) scattering. The probability of diffuse scattering is set to $(1 - f_{qs})$ where f_{qs} is the probability of QS scattering. QS scattering can be taken to mean either (a) sub-specular scattering, where the maximum in the angular distribution of scattered flux is directed closer to the surface normal direction than the specular angle, (b) specular scattering, where the angular distribution is focused around the specular angle and the most probable θ_{out} is equal to θ_{in}, or (c) super-specular scattering, where the angular distribution

is directed farther from the surface normal than the specular angle. The super-specular model presented here is sometimes referred to as the hard cube model.[156]

In describing the velocity distribution of the scattered particles, we focus our discussion on three empirical scattering models: the sub-specular or Schamberg model,[157] the super-specular model,[156] and the diffuse or cosine scattering model.[158] We do not consider other well-known models, such as the Cercignani-Lampis-Lord model (CLL) and Nocilla drifting-Maxwellian model.[159-160] However, the models included here are sufficient to approximate all the experimental surface scattering results observed in this investigation.

The sub-specular scattering angle, based on the model by Schamberg, is defined by

$$\sin\theta_{out} = \sin^{\upsilon}\theta_{in}\,, \tag{5.3}$$

where the incidence angle, θ_{in}, is the angle between the incoming particle velocity and the surface normal vector; the outgoing angle, θ_{out}, is the direction between the scattered molecule velocity and the surface normal vector, and the exponent υ is set to a value from 1 (specular scattering) to infinity (scattering in the direction of the surface normal).[157] The exponent, υ, has the effect of biasing the most-probable scattering angle towards the surface normal ($\hat{n}$). θ_{in} is defined as

$$\theta_{in} = \operatorname{acos}\left(-\hat{n}\cdot\hat{v}_{in}\right), \tag{5.4}$$

where $\hat{n}$ is the surface normal vector and $\hat{v}_{in}$ is the unit vector in the direction of the incident velocity. For the sub-specular case, θ_{out} in eq 5.3 is defined as

$$\theta_{out} = \operatorname{asin}\left(\sin^{\upsilon}\theta_{in}\right)\,. \tag{5.5}$$

In the case of super-specular scattering, θ_{out} is

$$\theta_{out} = \left| \cot^{-1}\left(\left(\frac{1-\mu}{1+\mu} + \frac{\mu}{1+\mu} a \frac{1}{\cos^2(\theta_{in})} \right) \cot(\theta_{in}) \right) \right| , \qquad (5.6)$$

where μ is the ratio of incident to surface molecular mass and a is equal to the ratio of half of the thermal energy of the surface to incident kinetic energy of the incoming particles: $\langle k_b T_w / E_{in} \rangle$.[161] The sub-specular or super-specular unit vector represents the most probable angle and is computed in eq 7: [162]

$$\hat{v}_{out} = \frac{\sin\theta_{out}}{\sin\theta_{in}} \hat{v}_{in} + \left(\frac{\sin\theta_{out}}{\sin\theta_{in}} \cos\theta_{in} + \cos\theta_{out} \right) \hat{n} \qquad 0 \le \theta_{out} , \qquad \theta_{in} < \pi/2 \ . \qquad (5.7)$$

The velocity vector of each scattered particle is randomly chosen from a half-Maxwellian distribution which is centered on $\hat{v}_{out}$ in eq 5.7 and limited to lie inside a cone with a half-angle ϕ_o. In the case of diffuse scattering, also referred to as cosine scattering, ϕ_o is 90°; when ϕ_o is equal to 0°, all particles scattering at that location have the same direction, $\hat{v}_{out}$. Figure 5.3 is a visual representation of the scattering models discussed above and shows a two-dimensional cross section of the angular distributions generated in SPARCS, taken from a plane containing both the incident and outgoing velocity vectors. The surface is represented by a grey rectangle; the blue line is the incident velocity vector; the green dashed line is the specular direction; the dashed red circle represents the diffuse (cosine) model; and the black dots represent the angular distributions of the scattered particles. The panels in Figure 5.3 illustrate (a) diffuse scattering, (b) sub-specular scattering, (c) super-specular scattering, and (d) a blended model of 80% diffuse and 20% sub-specular scattering (f_{qs} = 0.20).

The magnitude of the scattered velocity of the particle is dependent on the instantaneous accommodation coefficient, α_k, which is defined for each particle-surface interaction as:[163]

$$\alpha_k = \frac{T_{in} - T_{out}}{T_{in} - T_w}. \tag{5.8}$$

T_{out} is the kinetic temperature of the outgoing particles, T_w is the surface temperature (assumed to be 300 K), and the incident kinetic temperature, T_{in}, is defined according to

$$T_{in} = \frac{mV_{in}^{\ 2}}{3k_b}. \tag{5.9}$$

Next, T_{out} at the surface is defined in terms of the most probable scattered velocity,

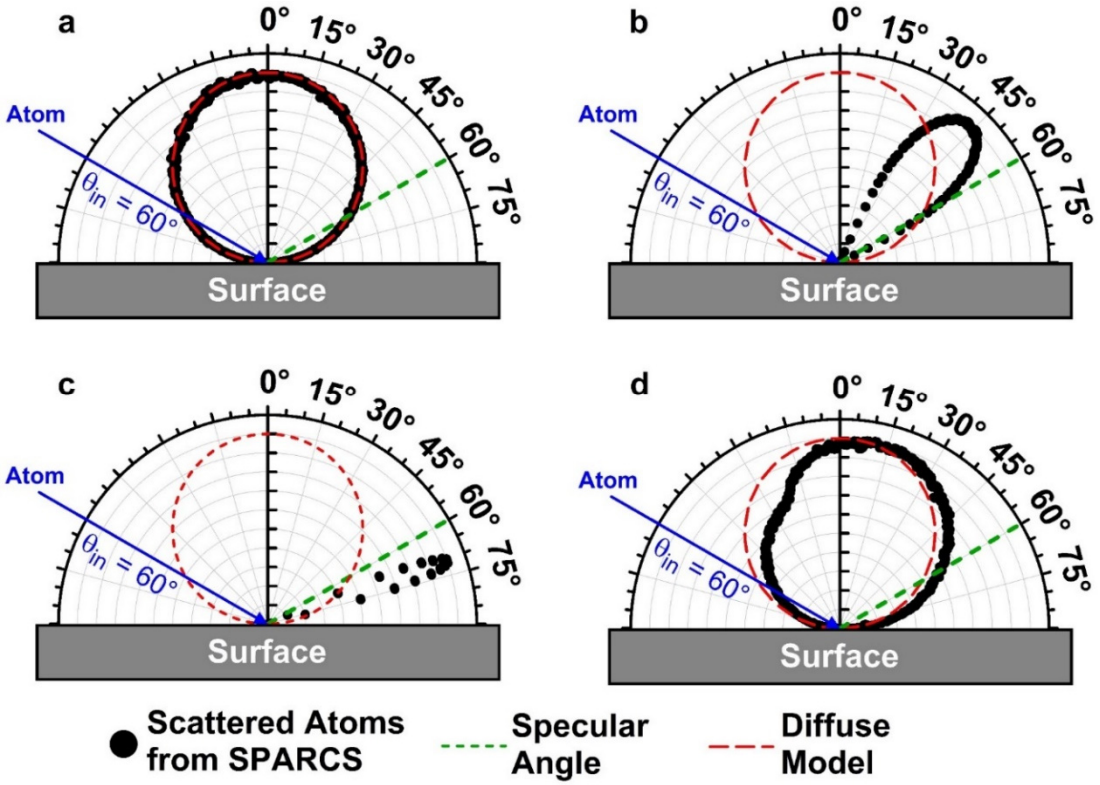


Figure 5.3. Scattering models represented in SPARCS: (a) diffuse (cosine), (b) sub-specular (υ = 2.215, ϕ_o = 20°), (c) μ = 0.25, a = 0.0195, ϕ_o = 5° (super-specular), and (d) blended diffuse and QS.

$$T_{out} = \frac{m}{3k_b} V_{in}^{\ 2} (1 - \alpha_k) + \alpha_k T_w \,. \tag{5.10}$$

Written in terms of the most probable scattered velocity, eq 5.10 becomes:

$$V_{out} = V_{in} \left[\frac{2}{3} \left(1 + \alpha_k \left(\frac{3k_b T_w}{m V_{in}^{\ 2}} - 1 \right) \right) \right]^{1/2} . \tag{5.11}$$

Once a scattered velocity has been selected for any given particle, it becomes the new incident velocity for that particle, and the ray tracing and scattering processes are repeated until the particle leaves the computational volume. SPARCS simulates the simultaneous propagation of hundreds of thousands of particles through and around an arbitrary geometry. Figure 5.4 illustrates the trajectories of three particles propagating

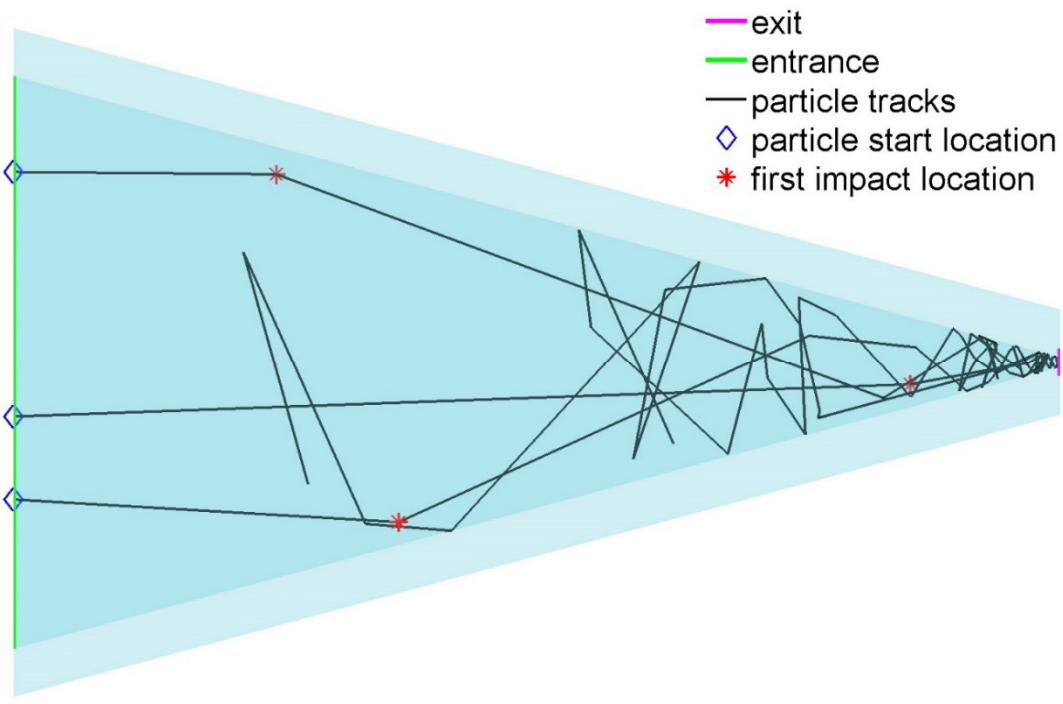


Figure 5.4. Example geometry showing particles propagating toward the exit of a cone concentrator. The trajectories for three particles are shown (black lines) propagating from the entrance (green circle) to the exit (pink circle). The first impact with the concentrator wall is denoted by a red asterisk.

through the interior of a conical concentrator and exiting into the attached spherical accommodation chamber. The exit aperture of the concentrator is located in the exit plane shown in magenta at the right-hand side of the geometry. Particle tracking for internal flows, exemplified here, involves tabulating (a) all the generated free-stream molecules that have entered the inlet (shown by the green line in Figure 5.4) and (b) the subset of these that have left through the geometry exit (represented by the magenta line in Figure 5.4). The latter includes those particles that may have traveled through the geometry without interacting with any surfaces. The number of scattering events undergone by each group of particles is also tracked.

The performance of any given concentrator geometry is parametrized by the concentration factor, C_a, which is defined as the ratio of the simulated flux through the exit aperture of the concentrator to the effusive flux though an aperture of the same size exposed directly to the free-stream (eq 5.1):

$$C_a = \frac{\dot{N}_{b,SPARCS}}{\dot{N}}$$

$$\dot{N}_{b,SPARCS} = \frac{N_{b,SPARCS}}{A_b dt_{SPARCS}} \quad , \tag{5.12}$$

$$dt_{SPARCS} = \left. \frac{N_{fs}}{\dot{N} A_{fs}} \right|_{fs \text{ boundary}}$$

where $N_{b,SPARCS}$ is the number of particles passing through the exit aperture, A_b is the area of the exit aperture (m^2), dt_{SPARCS} is the simulated timestep, N_{fs} is the number of particles generated at a flow boundary, $\dot{N}$ is the effusive flux computed by eq 5.1, and A_{fs} is the area of the flow boundary (m^2). All modeling presented in this paper, unless otherwise noted, was performed with a free stream speed and temperature of 5,000 ms^{-1} and 100 K,

respectively, and the particles were O atoms. The angle of attack is zero unless otherwise stated.

As Figure 5.4 illustrates, O atoms may undergo significant numbers of collisions when propagating towards the exit of a conical concentrator inlet. In most of the simulations, it is assumed that the empirically determined scattering model for any given O atom does not change from one atom-surface collision event to the next. However, as the experimental measurements indicate that a small but finite amount of energy transfer occurs during each gas-surface interaction, one might expect the angular distribution for a given atom to change as it loses more energy with each successive surface impact. To evaluate the effect of this phenomenon, a simple model for angular distribution broadening was implemented in SPARCS. The change in angular distribution with consecutive collisions was based on an ad-hoc relationship between the overall energy accommodation, α, and the scattering parameters $\langle k_b T / E_{in} \rangle$ and ϕ_o. This simple relationship reflects the propensity of atom-surface interactions with higher levels of energy-loss to produce broader angular distributions. The overall accommodation coefficient, α, is computed using eq 5.8 where the T_{in} is set to T_{fs}, $T_{in} = mV_{fs}^{\,2} / 3k_b$, rather than T_{in} specified by eq 5.9. Meanwhile, T_{out} is computed normally using α_k in eq 5.10. The overall accommodation coefficient, α, is a measure of total energy loss resulting from multiple surface interactions whereas α_k specifies the energy loss during a single bounce.

A set of SPARCS simulations was initiated for the 15° half-angle cone and annular ring geometries at 0° angle of attack and the same free-stream properties as described earlier. As before, a constant α_k was assumed throughout the simulation; $\langle k_b T / E_{in} \rangle$ and ϕ_o

for each subsequent collision were modified according to a continuously updated value of α for each particle. Specifically, the width of the QS distributions was modified to be $\phi_{o,out} = \phi_o(1-\alpha) + \alpha \cdot 85^\circ$ leading to an almost entirely diffuse (±85° wide) angular distribution when α = 1. The thermal to kinetic energy ratio for each particle (*a* in eq 5.6) was likewise modified arbitrarily by α to be:

$$\langle k_b T / E_{in} \rangle_{out} = a_{out} = k_b T_w \left((1-\alpha) 0.5 m V_{in}^2 \right)^{-1} \tag{5.13}$$

5.3 Results

5.3A Experimental Results

The experimental work focused on the scattering dynamics of inelastically scattered O and O_2 from three surfaces: a thin film of Au deposited on a silicon substrate, an SiO_2 surface on a Si(100) substrate, and HOPG. The TOF distributions of the O and O_2 scattering from the Au and SiO_2 surfaces were bimodal (Figures 5.5 and 5.6), with a broad peak at long times and a relatively narrow peak at short times. In contrast, the O and O_2 recoiling from HOPG exhibited only a single, sharp component, which appears at short times in the TOF distributions (Figure 5.7). Inelastic scattering of gases from surfaces can be interpreted in terms of two limiting cases of processes that occur in non-reactive gas-surface scattering: impulsive scattering (IS) and thermal desorption (TD).[2,164] Impulsively scattered atoms or molecules collide with the surface once, and sometimes 2-5 times,[38] before scattering from the surface and lose only a fraction of their incident kinetic energy during the collisions. They arrive at the detector quickly due to their high post-collisional translational energies and are manifested in the TOF distributions by a narrow peak at short

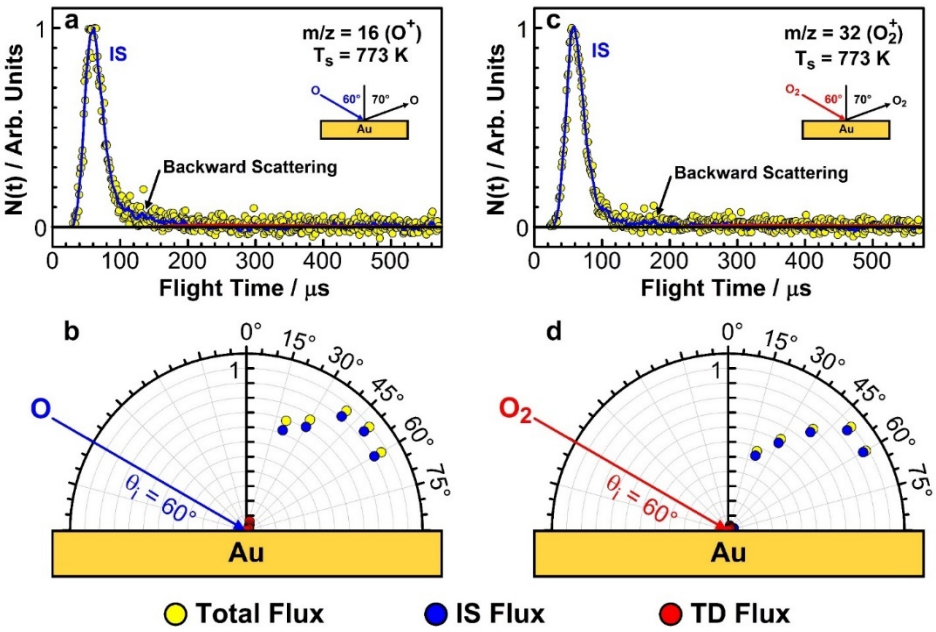


Figure 5.5. Representative TOF distributions (a, c) and flux-integrated angular distributions (b, d) for O (left) and O_2 (right) scattering from an Au surface, with θ_{in} = 60°, T_w = 773 K, and E_{in} = 236.87 kJ mol^{-1} and 474.31 kJ mol^{-1} for O and O_2, respectively.

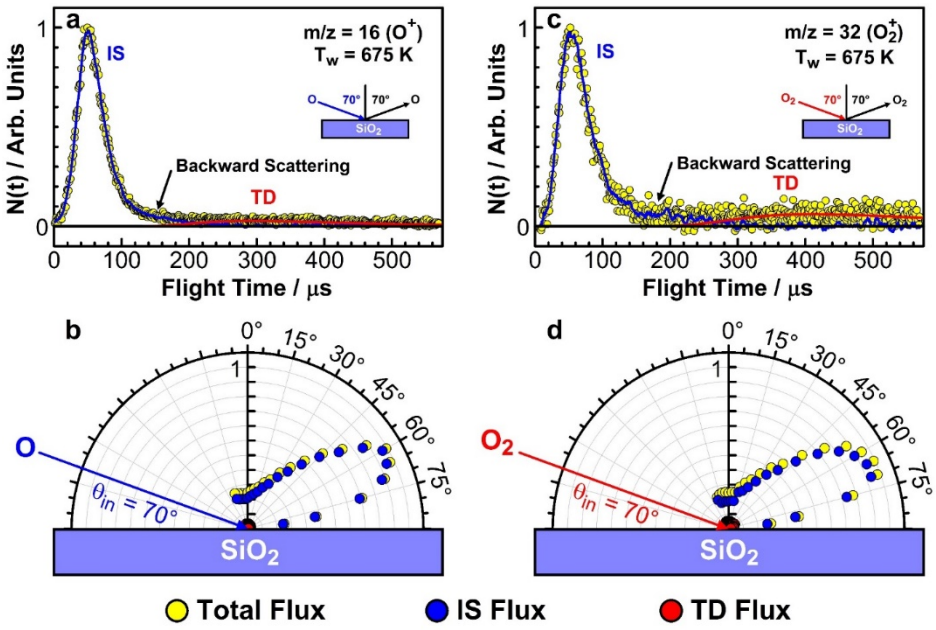


Figure 5.6. Representative TOF distributions (a, c) and flux-integrated angular distributions (b, d) for O (left) and O_2 (right) scattering from the oxidized silicon surface, with θ_{in} = 60°, T_w = 675 K, and E_{in} = 495.55 kJ mol^{-1} and 889.49 kJ mol^{-1} for O and O_2, respectively.

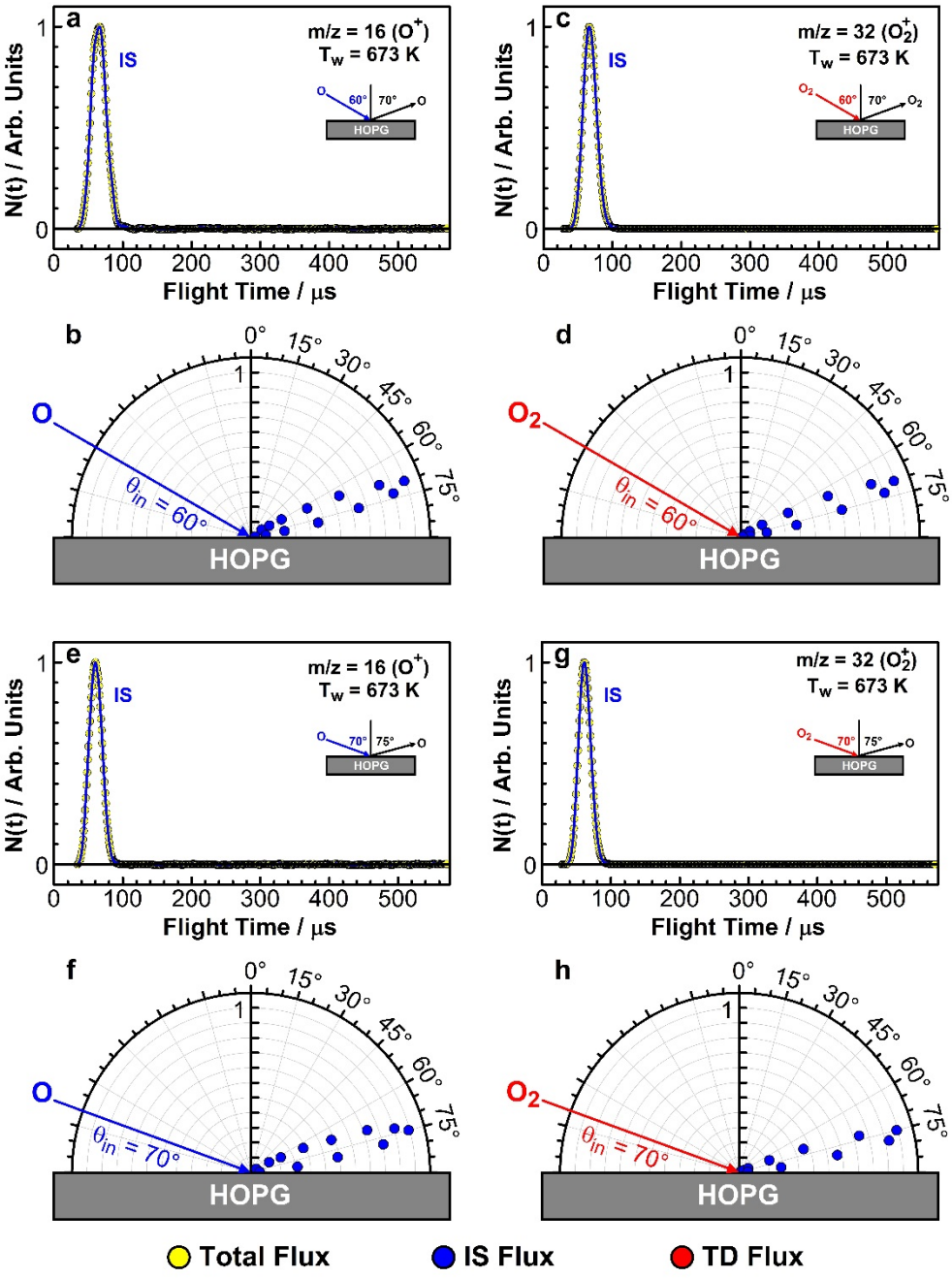


Figure 5.7. Representative TOF distributions (a, c, e, g) and flux-integrated angular distributions (b, d, f, h) for O (left) and O_2 (right) scattering from an HOPG surface, with $\theta_{in} = 60°$ (top), $\theta_{in} = 70°$ (bottom), $T_w = 673$ K, and $E_{in} = 248.15$ kJ mol^{-1} and 496.81 kJ mol^{-1} for O and O_2, respectively.

times. The flux angular distribution of impulsively scattered species has a maximum oriented toward, or beyond, the specular angle. Conversely, atoms or molecules that undergo TD lose virtually all of their incident translational energy and memory of their initial trajectories when they strike the surface. The atoms or molecules spend sufficient time interacting with the surface to achieve thermal equilibrium before desorbing into the vacuum with a velocity distribution that is typically described by a Maxwell-Boltzmann (MB) distribution characterized by the temperature of the surface. Species that undergo thermal desorption arrive at the detector slowly because of their low velocities and can be distinguished as a broad peak at long times in the TOF distributions. The flux angular distribution of TD species has a maximum along the surface normal. The IS and TD components of the TOF distributions can be separated by fitting a MB distribution of translational energies, $P(E_{out})$, converted to a number density distribution as a function of flight time, $N(t)$, that is scaled to match the TD component of the TOF distributions. The TOF distribution of the IS component is obtained by taking the difference between the overall TOF distribution and the calculated, best-fit MB distribution. The average energy of the IS component is determined by using a forward convolution procedure which takes into account the different arrival times of the atoms and molecules at the surface due to the spread in the incident energy distribution, $P(E_{in})$, of the beam.[36,152] Angular distributions of scattered flux for each component can be derived from the TOF distributions collected at a variety of θ_{out} for a given θ_{in}. In this study, atoms and molecules colliding with the surface generally tended to scatter impulsively with little energy transfer to the surface. Only a small fraction of the incident atoms came into thermal equilibrium with the surface,

with the Au and SiO_2 surfaces facilitating thermal accommodation more so than HOPG. For each surface, the final energies, E_{out}, of the scattered atoms and molecules increased with larger final angles, a phenomenon that is indicative of structural scattering.[6] This behavior is frequently observed when the incidence energy of the impinging species is high, allowing for penetration of the potential energy surface (PES) and interaction with individual ion cores of the atoms at the surface. This indicates that the experiments probe the corrugation of the PES of the interaction between the incident atom or molecule and the surface.[44]

Figure 5.5 displays representative TOF and angular distributions of O and O_2 scattering from the Au surface. For the TOF distributions shown in Figures 5.5a and 5.5c, the yellow circles represent the total scattering signal, while the blue and red lines denote the IS and TD components, respectively. For the angular distributions shown in Figures 5.5b and 5.5d, the yellow circles represent the total scattered flux, while the blue and red circles indicate the IS and TD flux, respectively. Each set of data has been normalized to the maximum observed value. The convention used for Figure 5.5 is applied to all the figures displaying similar experimental results (Figures 5.6, 5.7, 5.10, and 5.11). IS was the primary scattering mechanism for both O and O_2, with only ~4% of O and O_2 coming into thermal equilibrium with the surface. The TD scattering component becomes more apparent at long times and has a maximum along the surface normal (not visible with the scales used in Figure 5.5). After the initial IS peak, there appears to be a small shoulder that arrives at the detector at intermediate times between the IS and TD component (~120-150 μs). This feature likely arises from O and O_2 that are scattered backward in the center-

of-mass (c.m.) frame of the incoming atom or molecule and the surface, meaning they scatter back toward the beam rather than forward toward the specular angle.[35,152] The angular distributions for both O and O_2 scattering from the Au (Figures 5.5b and 5.5d) are very broad, with a FWHM greater than 55° and a maximum flux at the sub-specular angle of $\theta_{out} = 50°$. It appears that the angular distribution for O_2 is narrower than that of the O atoms, which can be attributed to the higher incidence energy, E_{in}, of O_2.[6] No signal could be measured at θ_{out} greater than 70° because of a geometric constraint associated with the sample mount that was removed for the experiments involving SiO_2 and HOPG. The angular distributions for O and O_2 compare well with the angular distribution of Ar from Au(111) observed by Saltzburg et. al, indicating that the surface deposited by e-beam evaporation used in this experiment was well ordered and clean.[123] E_{out} for O and O_2 that scatter from the Au surface increases with θ_{out}, as seen in Figure 5.8. These results are displayed as a ratio of E_{out}/E_{in}, so the results for the two species can be easily compared. In this ratio, E_{out} and E_{in} represent average values of the outgoing and incidence translational energies, respectively. Values of E_{out}/E_{in} range from 0.6 at $\theta_{out} = 20°$ to 0.89 at $\theta_{out} = 60°$. The low energy transfer at $\theta_{in} = \theta_{out} = 60°$ confirms that the surface is clean. If the surface were contaminated, O and O_2 would lose considerably more energy while colliding with the Au.

Figure 5.6 shows representative TOF distributions and flux angular distributions of O and O_2 scattering from the SiO_2 surface. The majority of the O and O_2 scattered impulsively from the surface, as can be seen in the TOF distributions in Figures 5.6a and 5.6c. Only 5% of O and 9% of the O_2 came into thermal equilibrium with the surface. As

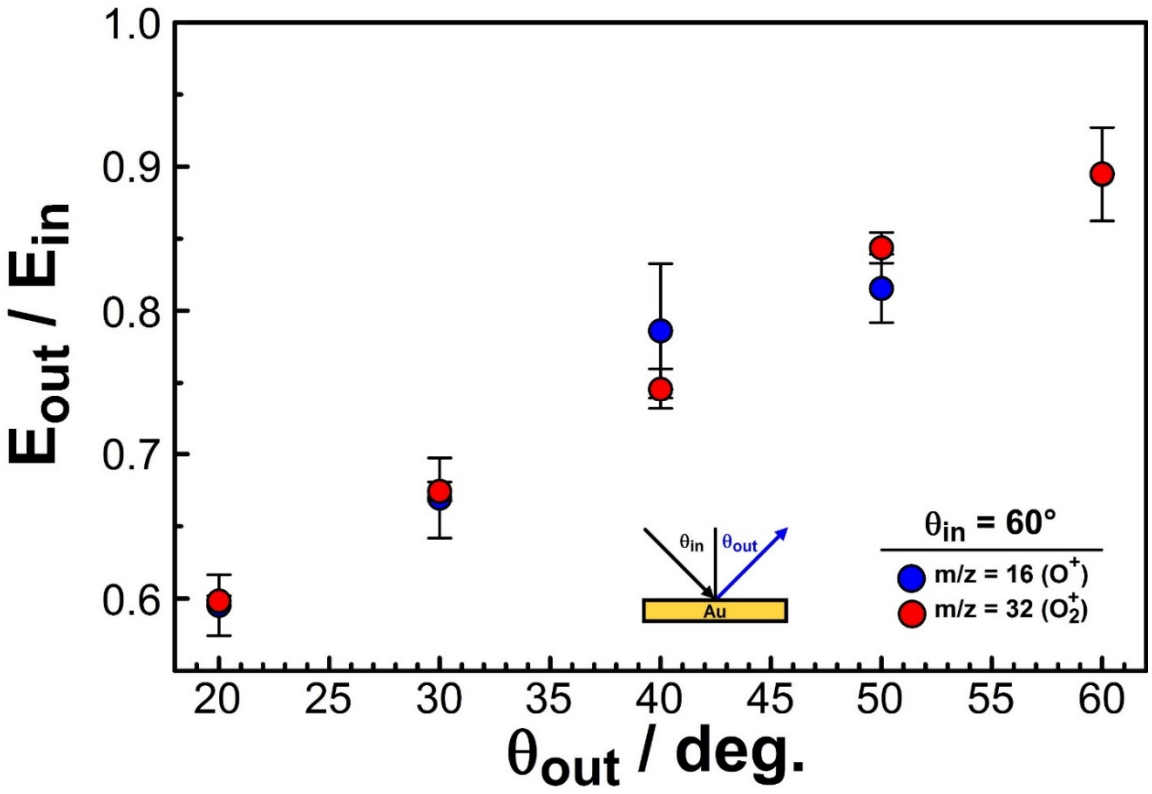


Figure 5.8. Ratio of final to incidence energy of inelastically scattered O and O_2 as a function of θ_{out} following collision with the gold surface, with θ_{in} = 60°, T_w = 773 K, and E_{in} = 236.87 kJ mol^{-1} and 474.31 kJ mol^{-1} for O and O_2, respectively.

was the case with the Au surface, a fraction of the incident O and O_2 scatters backward in the c.m. frame, as indicated by the shoulder in the IS peak of the TOF distribution at long times (~200 μs). This backward component is also evident as a rise in intensity in the angular distributions of O and O_2 when the θ_{out} angles are increasingly negative (Figures 5.6b and 5.6d). The forward scattered O and O_2 have lobular angular distributions centered near θ_{out} = 65°, which is 5° degrees lower than the specular angle, with a FWHM of 40° for O and 38° for O_2. The relatively broad energy distribution of the incident molecular beam used for the experiment with SiO_2 significantly complicates the calculation of E_{out}. Consequently, E_{out} for the O and O_2 recoiling from the SiO_2 surface could not obtained.

The scattering dynamics of O and O_2 from HOPG were remarkably different from the results for either the Au or SiO_2 surfaces. Figure 5.7 shows representative TOF distributions and angular distributions for scattered O and O_2 for θ_{in} = 60° and 70° and T_w = 673 K. As can be seen in Figures 5.7a, 5.7c, 5.7e, and 5.7g, there is only one sharp peak in the TOF distributions, which results from IS of O and O_2. There is no trace of TD and no indication that any of the incident atoms and molecules are scattered backward in the c.m. frame. The angular distributions for O and O_2, shown in Figures 5.7b, 5.7d, 5.7f, and 5.7h, all have a maximum flux in the super-specular direction for both θ_{in} = 60° and 70°: the O-atom angular distributions have maxima at θ_{out} = 69° for θ_{in} = 60° and θ_{out} = 70.5° for θ_{in} = 70°, and the O_2 angular distributions have maxima at θ_{out} = 73.5° for θ_{in} = 60° and θ_{out} = 75.8° for θ_{in} = 70°. Most of the scattered O and O_2 exit the surface between θ_{out} = 60° and 80°, and the scattered flux is zero at the extrema of the angular distributions, confirming the absence of TD and backward scattering in the c.m. frame. The angular distributions of the atoms and molecules scattering from the HOPG surface at T_w = 673 K are extremely narrow, with a FWHM for θ_{in} = 60° of 13.2° for O and 10.5° for O_2. The angular distribution for O_2 is narrower because the incidence energy of O_2 is twice as high as that of O. The width of the angular distributions decreased slightly with increasing θ_{in}, with a FWHM for θ_{in} =70° of 13.2° and 9.55° for O and O_2, respectively. The O and O_2 lost little translational energy when colliding with the surface, as can be seen in Figure 5.9. The blue and red filled symbols indicate O and O_2, respectively, while the circles and triangles represent data for θ_{in} = 60° and θ_{in} = 70°, respectively. The normalized energy ratios, E_{out}/E_{in}, for O and O_2 are nearly identical, diverging only at the highest and lowest

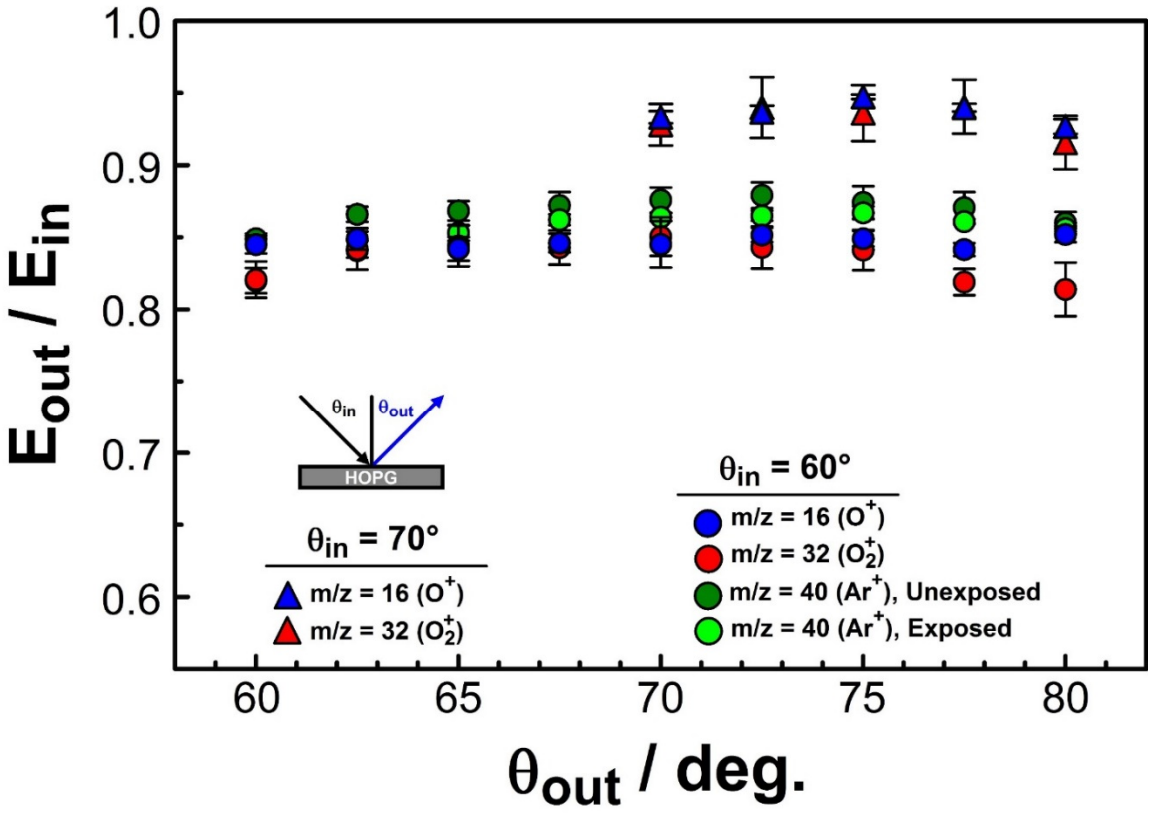


Figure 5.9. Ratio of final to incidence energy of inelastically scattered O (blue symbols) and O_2 (red symbols) as a function of θ_{out} following collision with the HOPG surface, with θ_{in} = 60° (circles), θ_{in} = 70° (triangles), T_w = 675 K, and E_{in} = 248.15 kJ mol^{-1} and 496.81 kJ mol^{-1} for O and O_2, respectively. The dark and light green circles denote Ar scattering from HOPG surfaces that were unexposed and exposed to O atoms, respectively, with E_{in} = 468.78 kJ mol^{-1} and T_w = 875 K.

final angles. E_{out}/E_{in} is approximately 0.85 between θ_{out} = 60° and θ_{out} = 80° for θ_{in} = 60°. This ratio increases to 0.95 when θ_{in} = 70°. The widths of the TOF and angular distributions increased when T_w was increased to 875 K (Figures 5.10a, 5.10b, 5.10c, 5.10d). The angular widths (FWHM) for O and O_2 were 17.0° and 12.1° respectively, for θ_{in} = 60°. If the surface were contaminated when T_w = 673 K, the widths of the TOF and angular distributions for O and O_2 would be expected to decrease as the surface temperature was increased, because adsorbed molecules would desorb at the higher temperature, leaving a

pristine carbon surface that would yield a narrow angular distribution. Instead, as shown in Figure 5.10 the angular distributions for O and O_2 grew broader at the higher temperature instead of narrower, which may be explained by increased thermal motion at the surface,[1] thus indicating that the surface was already clean when T_w = 673 K.

To test if exposure to the O-atom beam altered the surface morphology of the HOPG, a beam of hyperthermal Ar was directed at portions of the HOPG surface that were unexposed and exposed to O atoms, with T_w = 873 K. Ar is a nonreactive noble gas that has weak attractive forces with the carbon surface in comparison to O, allowing the collision dynamics to be simplified to hard-sphere interactions. Thus, any differences between the unexposed and exposed surfaces can be inferred to be a result of surface roughening caused by surface ablation resulting from exposure to the O-atom beam. The results for the Ar scattering are shown in Figure 5.11; both the TOF and angular distributions have been normalized to the maximum observed value for Ar scattering from HOPG that was unexposed to the O-atom beam. The TOF distributions in Figures 5.11a and 5.11c indicate that Ar scatters impulsively from the surface regardless of whether the surface is unexposed or exposed to O atoms. Figures 5.11b and 5.11d display the angular distributions of Ar recoiling from the exposed and unexposed surfaces, which have the same shape, indicating that the surface morphology did not change substantially when exposed to the O-atom beam. The angular distributions of the scattered Ar are similar to the O_2 angular distribution, with a FWHM of 11.6° and 11.7° for the unexposed and exposed surfaces, respectively, for T_w = 875K. The flux of Ar scattering from the portion of the sample that had been exposed to O atoms was 15% lower than that of the HOPG

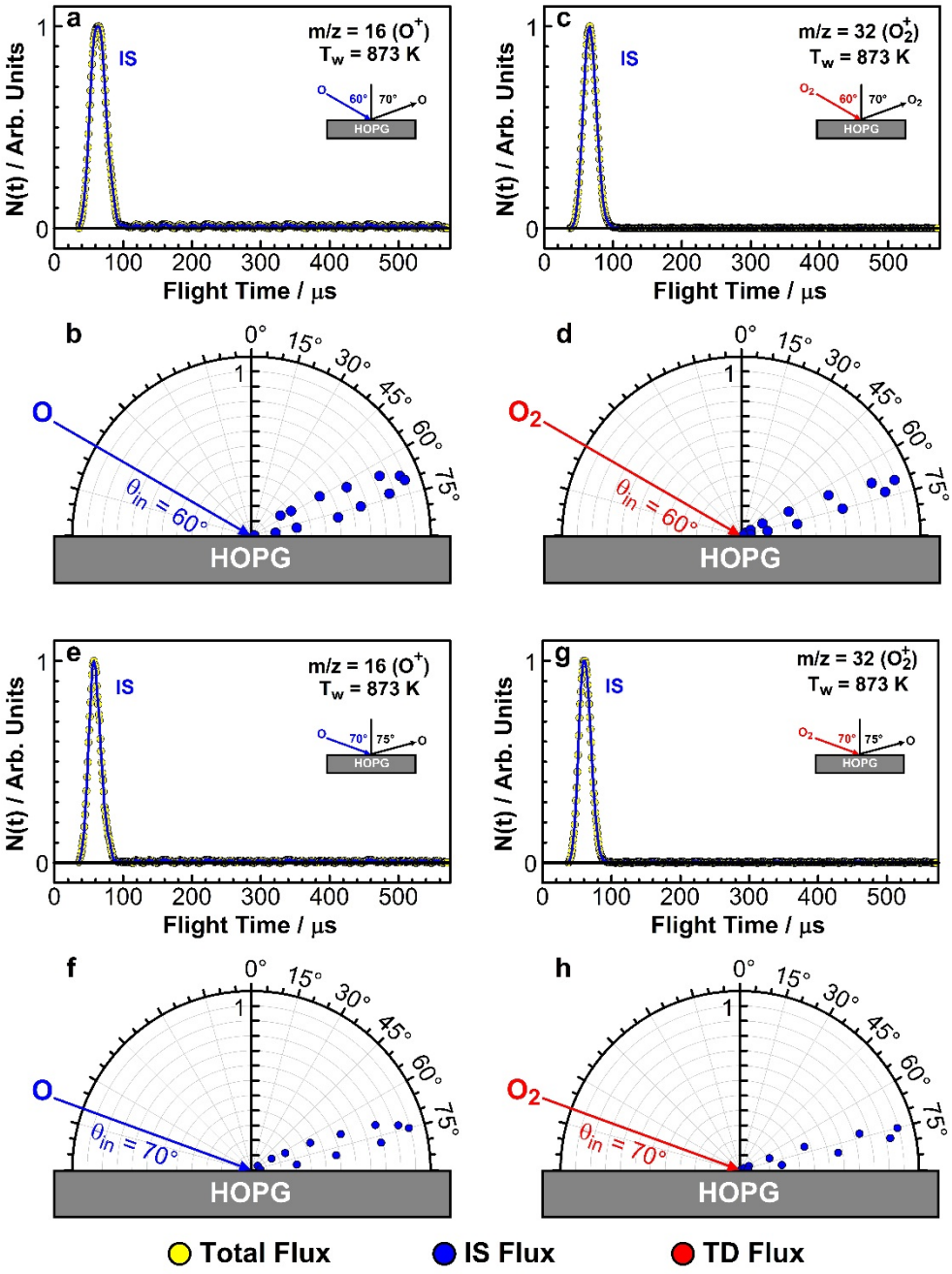


Figure 5.10. Representative TOF distributions (a, c, e, g) and flux-integrated angular distributions (b, d, f, h) for O (left) and O_2 (right) scattering from an HOPG surface, with θ_{in} = 60° (top), θ_{in} = 70° (bottom), T_w = 873 K, and E_{in} = 248.15 kJ mol^{-1} and 496.81 kJ mol^{-1} for O and O_2, respectively.

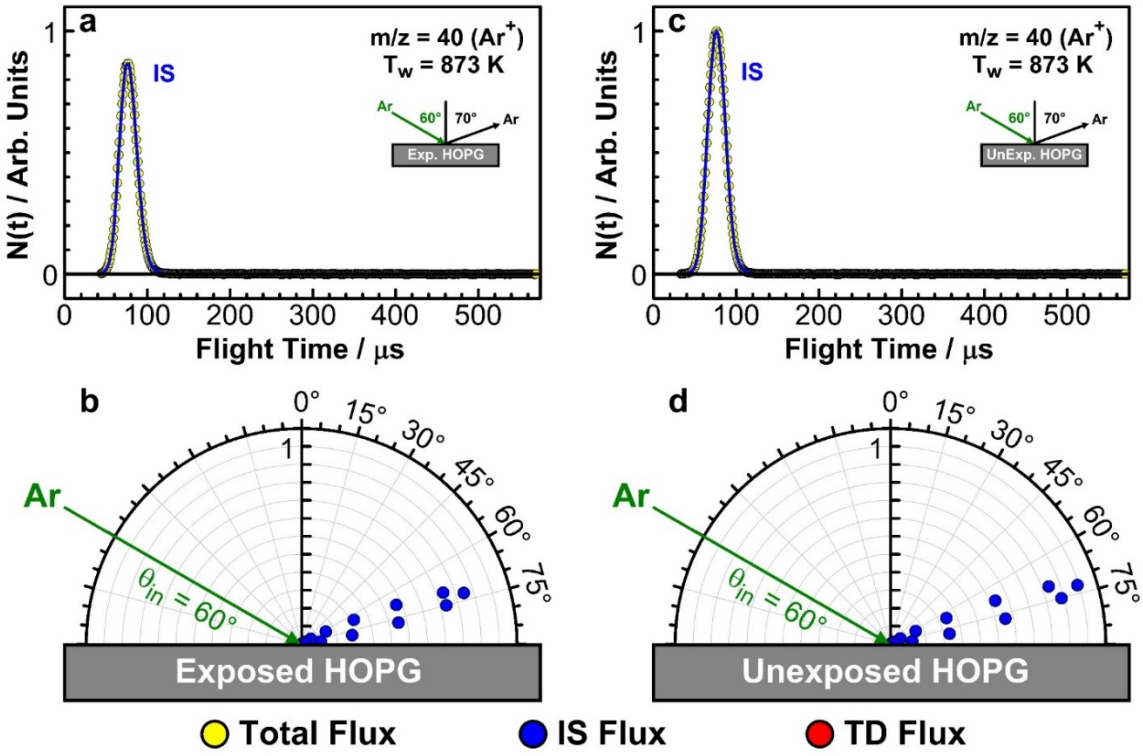


Figure 5.11. Representative TOF distributions (a, c) and flux-integrated angular distributions (b, d) for Ar scattering from the HOPG surface exposed (left) and unexposed (right) to O atoms, with θ_{in} = 60°, T_w = 873 K, and E_{in} = 468.78 kJ mol^{-1}.

surface that was unexposed to O atoms. The deviation in the scattered flux between the unexposed and exposed HOPG was likely the result of an increase in scattering of Ar out of the plane defined by the incident molecular beam and the surface normal, which was caused by changes in surface morphology resulting from reactions with the incoming O atoms. Figure 5.9 shows the behavior of the E_{out}/E_{in} of the Ar scattered from the unexposed and exposed surfaces, represented by the light and dark green circles, respectively. Ar retains 87% of its incidence energy when θ_{in} = 60° when it collides with either the unexposed or the exposed HOPG surfaces.

5.3B Computational Results

The simulated concentrator geometries are solids of revolution. Two types of concentrators are presented in this paper: (1) a simple cone with opening half-angles of 10° and 15° and (2) an annular ring concentrator composed of nested concentric rings whose spacing and opening angle is chosen specifically for the angular scattering distributions measured in the laboratory. Figure 5.12a illustrates the 15° half-angle cone that is 11 cm long with a 7.2 cm outer diameter (OD). The diameter of the exit aperture is 1.12 mm. Figure 5.12b shows the front view of the annular ring concentrator with three support structures emanating radially from the center ring out to the perimeter with the exit aperture visible in the center and a cross-sectional view of the annular-ring concentrator with the entrance on the left and the exit plane on the right. The distance from entrance plane to exit plane is 3.6 cm, and the outer diameter is 4.7 cm, as defined by the leading edge of the outermost ring. The exit aperture diameter, 1.12 mm, is the same as that used in the model

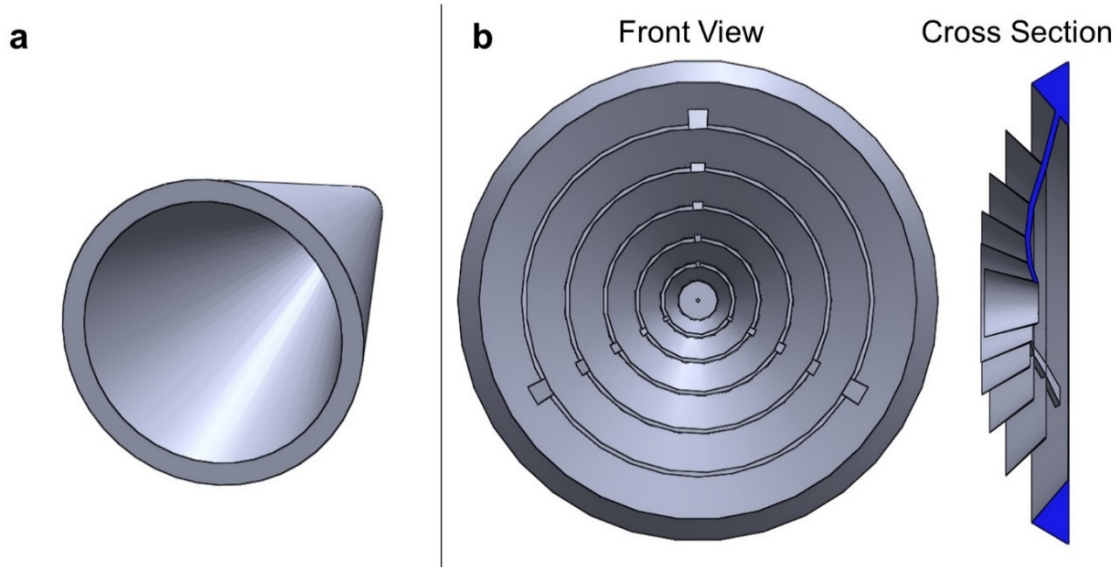


Figure 5.12. Geometries for the concentrators: (a) cone-shaped concentrator with a 15° half-angle opening and (b) an example of an annular ring concentrator.

cone geometries. The annular design pursued here was made from rings that each have straight cross sections. Incoming atoms collided only once with a surface before exiting the annular ring concentrator. This is in contrast to the curved cross sections described by Tagawa et al., which were optimized for a single super-specular scattering model at all impact locations along the surface and which utilized the entire curved surface to direct molecules to the exit aperture.[142-143] The use of a straight design is driven by the need to account for a realistic range of scattering models. Scattering model parameters may vary from particle to particle due to a variety of molecular masses entering the instrument, changes in the scattering model as a function of θ_{in}, as well as a variety of θ_{in} which may be present in a warmer gas such as a thermospheric region (Earth, Venus, Titan, etc.) or in a non-equilibrium exosphere (Europa, Enceladus, etc.). In the curved concentrator, deviations of the scattered angular distributions from the distributions assumed while designing the concentrator will cause a significant decrease in C_a because the atoms fail to reach the exit aperture. The optimal scattering region in a straight design will shift along the cross section of each ring depending on the exact θ_{out}. Thus, the design pictured in Figure 5.12b provides a level of robustness necessary to focus particles of various masses, θ_{in}, θ_{out}, and free-stream properties.

Figure 5.13 shows the SPARCS simulated angular distributions of O atoms scattering from Au, SiO_2, and HOPG planar surfaces (black dotted curves). The experimental data, shown as yellow circles, were used to determine the SPARCS scattering model parameters. The location of the specular angle in each case is denoted by the green dotted line. Figure 5.13a shows that scattering from Au is sub-specular with a large diffuse

Table 5.2. SPARCS scattering parameters based on experimental results.

Case	ν	μ	$<k_bT/E_{in}>$	f_{qs}	ϕ_o
(a) O on Au	1.05	-	0.0195	20%	35°
(b) O on Si (SiO_2)	2.20	-	0.0195	55%	25°
(c) O on HOPG	-	0.253	0.0195	95%	5°

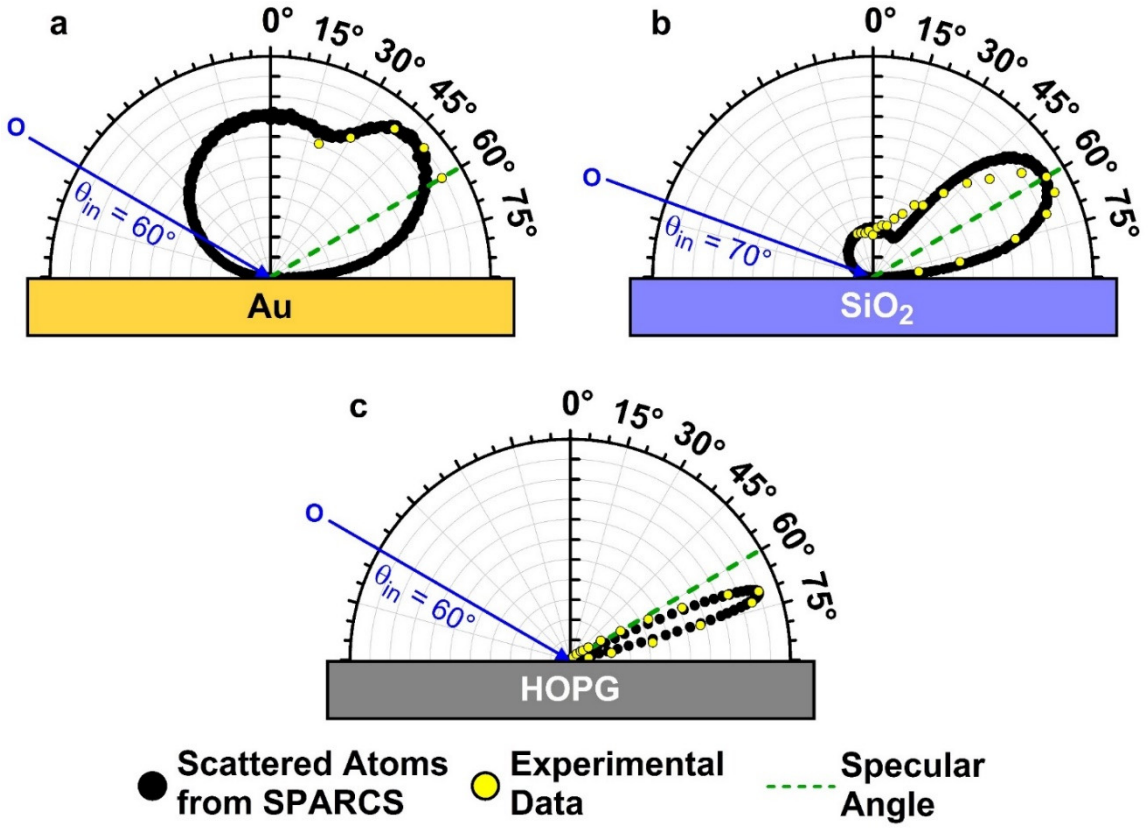


Figure 5.13. Beam-surface scattering data (red circles) compared with modeled scattering distributions (black dots) for O atoms on (a) Au, (b) SiO_2, and (c) HOPG.

component. Figure 5.13b shows that scattering from SiO_2 is also sub-specular with a smaller diffuse component. Figure 5.13c shows that the scattering distribution from an HOPG surface is super-specular with a very narrow lobe (small ϕ_0 values). The fitting parameters for each case are included in Table 5.2. Note that the scattering distributions shown in Figures 5.5, 5.6, 5.7, 5.10, 5.11, and 5.13 are the in plane sections of 3D scattering distributions having out of plane components. The scattering models in SPARCS represent 3D velocity distributions as discussed in Section 5.2B. The scattering models were tuned such that the 2D in- plane cross sections of the modeled scattering matched the 2-D scattering plane results observed in the laboratory.

Figure 5.14 illustrates the trajectories of three incident O atoms as they pass through the inlet geometry of a cone-type concentrator and exit through the critical aperture on the right. The cone surfaces were modeled to correspond to scattering of O atoms on Au (Figure 5.14a), SiO_2 (Figure 5.14b), and HOPG (Figure 5.14c). The broader (or diffuse) the angular distributions (Au), the more the impact locations for the scattering O atoms are distributed throughout the length of the concentrator geometry. When the atoms scatter in a narrow angular distribution peaked in a super-specular direction (HOPG), the atom-impact locations cluster toward the exit of the concentrator. This indicates that for narrower angular distributions (HOPG), the concentrator can be made shorter than in cases with broad scattering lobes (Au and SiO_2).

We have run SPARCS simulations for 10° and 15° half-angle cones and an annular ring concentrator comprised of six rings, made of Au, SiO_2, and HOPG. Each annular ring concentrator was optimized for the surface scattering properties corresponding to Au, SiO_2,

and HOPG. All concentrators were simulated using a 0° angle of attack to a hyperthermal flow, i.e., the concentrator axis of symmetry was aligned with the free-stream velocity and the entrance aperture was pointing into the direction of the incoming particles. The incident velocity was 5,000 m s^{-1} and T_{fs} = 100 K. Table 5.3 shows the C_a for each of the nine concentrators. The values in parentheses indicate the percentage of impacts that reached the exit after a single surface collision. Note that for all concentrator geometries, HOPG resulted in values for C_a that are an order of magnitude higher than those for Au and SiO_2. The narrow, super-specular scattering dynamics on HOPG result in very efficient propagation of O atoms toward the exit with little backscatter and flow propagation back toward the entrance and thus yield a higher C_a. The 10° half-angle cone has the highest overall C_a, resulting from less scattering back through the entrance aperture than the 15° half-angle cone. The annular 6-ring geometry has the lowest C_a of the three geometries

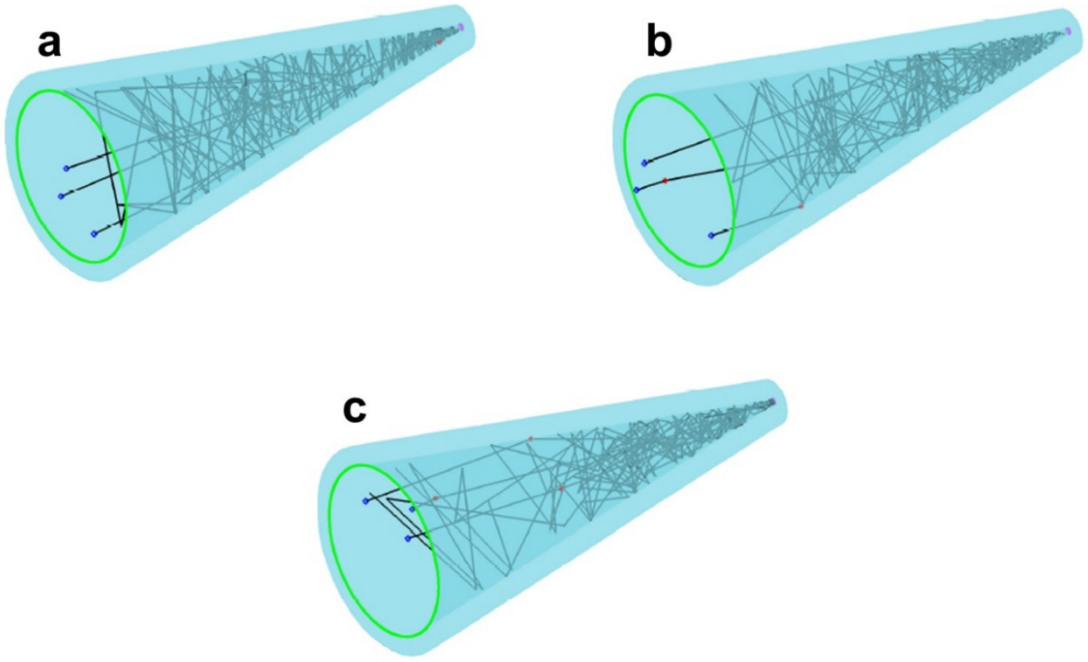


Figure 5.14. Three O-atom trajectories through a 10° half-angle cone constructed from (a) Au, (b) SiO_2, and (c) HOPG.

tested, regardless of the surface used to model the concentrator. The percentage of particles scattering only once before reaching the exit aperture for the annular ring concentrator is significantly higher than for the cone geometries. This is because the annular ring concentrator is specifically designed to direct O atoms directly into the exit aperture from each ring location. This property can have some desirable features in the design of future concentrators, as will be discussed later.

Table 5.3. C_a and percentage of primary impacts at 0° angle of attack.

Concentrator Geometry	HOPG	Si	Au
10° cone	366.0 (2%)	10.5 (34%)	8.6 (28%)
15° cone	116.8 (8%)	9.9 (10%)	8.7 (10%)
6-ring Annular Concentrator	62.8 (100%)	4.9 (84%)	3.7 (76%)

To further evaluate the results in Table 5.3, the angle of attack of the free-stream particles was varied from 0° to 20° for the three HOPG concentrators. Such angles of attack could result from changes in the spacecraft attitude or from deviations of the bulk flow velocity from the spacecraft ram direction caused by winds and other components of motion, such as atmospheric co-rotation or surface sputtering, in the planetary atmosphere. Figure 5.15 illustrates the effect of the angle of attack on C_a, which was normalized to the value of C_a at 0° for the three concentrator geometries constructed of HOPG. For an angle of attack of 20°, the normalized C_a for all geometries decreases to between 0.01 and 0.23 of the maximum value. Somewhat surprisingly, the 10° half-angle HOPG cone is more robust to changes in angle of attack than the 15° half-angle HOPG cone. This is not the case for 10° and 15° half-angle cones using Au and SiO_2 surfaces (not shown). In the Au and SiO_2 cones, collimation of the flow dominates the angle-dependence of C_a, and

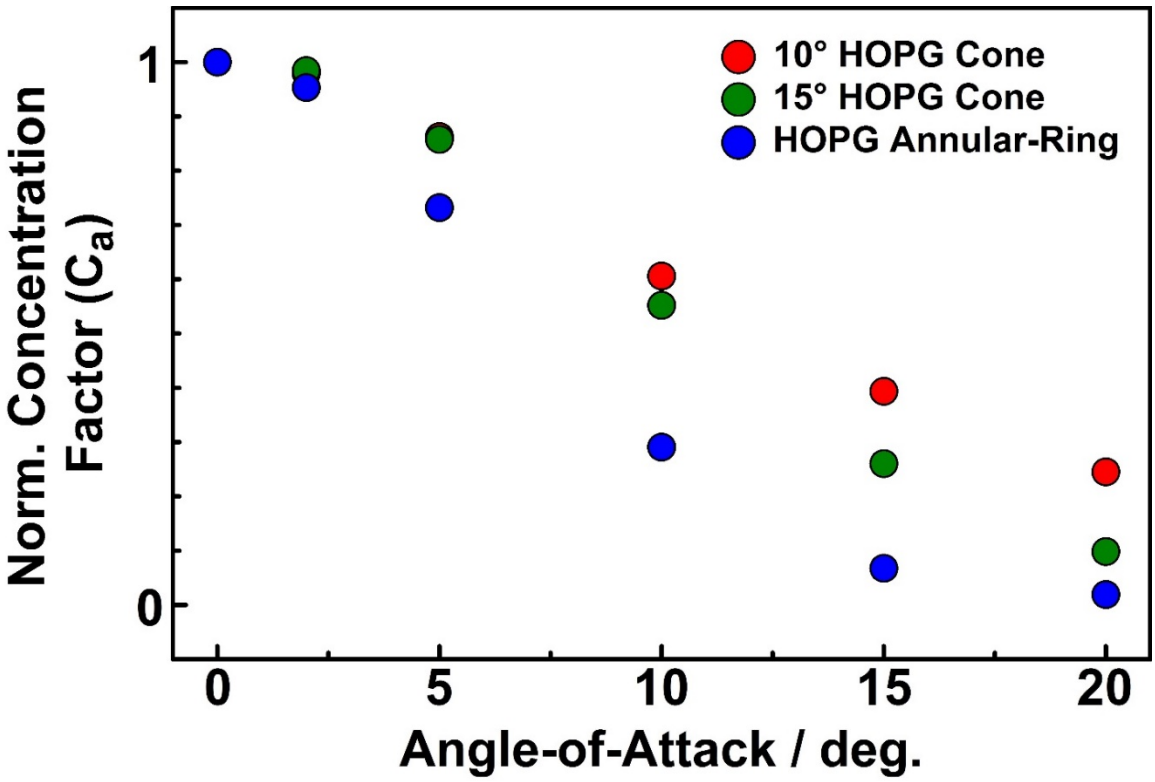


Figure 5.15. C_a as a function of angle of attack, normalized to the value of C_a at an angle-of-attack of 0°.

narrower cone half-angles lead to C_a values that are more sensitive to the incidence angle of the free-stream velocity. A narrower SiO_2 or Au cone at larger angles of attack provides a low conductance conduit for the entering free molecular flow and reduces the overall flux of O atoms propagating into the geometry. The tendency for a smaller cone angle to limit conductance is mitigated in the case of HOPG by the higher probability of forward-propagation through a cone geometry when opposing walls of the geometry are closer to parallel. For the annular ring design, flow-shadowing of the surfaces by the concentric rings themselves significantly impedes flow to the rings at angles of attack of the concentrator axis of symmetry with respect to the free stream velocity beyond 5°.

The scattering experiments performed for this study probe single atom-surface interactions. It was assumed that the scattering dynamics for any O atom propagating inside the geometry remain constant with each atom-surface interaction, as the details of secondary, tertiary, etc. collisions could not be probed in the experiment. Simulations were carried out to test the validity of this assumption by allowing the instantaneous accommodation coefficient (α_k) to decrease with each successive surface collision. Simulations were run with seven values of the α_k ranging from 0 to 1, and the effect on C_a was recorded for each case. The results are shown in Figure 5.16. When $\alpha_k = 0$, the O atoms maintain their free-stream kinetic energies as they propagate from entrance to exit apertures of the concentrator geometries and the scattering dynamics remain constant. These cases

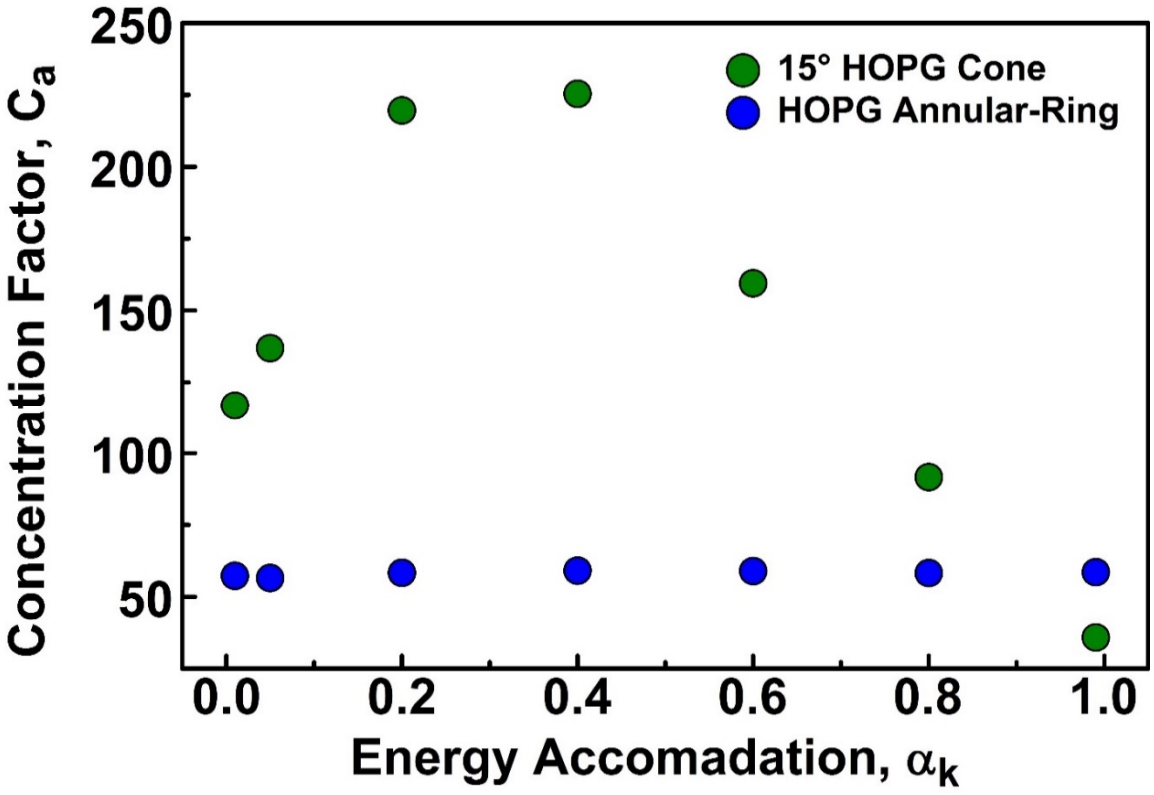


Figure 5.16. Effect of energy accommodation for an HOPG cone with a half-angle of 15° and an HOPG annular ring concentrator.

correspond to the results in Table 5.3 for the HOPG 15° half-angle cone and annular ring concentrator. As α_k is increased, successive atom-surface interactions result in increasingly broad angular distributions. In the case of the 15° half-angle cone, small values of α_k actually increase the C_a. At values of α_k between 0.2 and 0.4, the C_a increases by a factor of two. This increase in C_a is diminished at α_k above 0.5 as the atoms scatter with broader angular distributions throughout the geometry of the cone and causes the propagation of flow in the concentrator to approach the Au and SiO_2 concentrators in Table 5.3. The C_a of the annular ring concentrator does not change as α_k increases because it was designed such that the O atoms collided only once with the surface before exiting the geometry. Note that the results in Figure 5.16 depend on the assumed broadening of the angular distributions with successive surface impacts. The effect of successive collisions on the angular distributions of the scattered atoms is beyond the scope of this paper and will be investigated in future experiments.

5.4 Discussion

Most space borne MS inlets used for aeronomy have either an open-source or a closed-source inlet. In the former, molecules are collimated to restrict the velocity distribution to a population which may be reasonably modeled, and the collimated beam is then directed through the ionization region and into the analyzer. In a closed-source inlet, an accommodation chamber is used to capture and thermalize the incoming molecules while building up the atmospheric pressure to increase signal-to-noise. The molecules exiting the accommodation chamber into the ionization region have a velocity distribution which can be modeled as thermally desorbing molecules at the chamber temperature. This

approach inherently involves many gas-surface interactions that may result in a modification of the analytes prior to ionization. The closed-source approach can also introduce undesirable response times in the instrument, as non-volatile species (particularly water) may take seconds to minutes to travel from instrument entrance to accommodation chamber exit via a long series of collisions and adsorption/desorption events.[122] The open-source approach has the benefit of minimizing gas-surface interactions in the instrument, which leads to reduced surface reactions that may complicate the data analysis. However, the flux of neutral molecules passing through the ionization region in an open source is low and assumptions must be made about the collimated velocity distribution of the incoming atoms and molecules. It is desirable to understand the velocity distribution into the ionization region such that an ionization efficiency can be computed for each molecular species.

What is needed for many planetary science applications with high flyby speeds and low atmospheric densities is an inlet which can concentrate atmospheric species into the instrument to increase the signal-to-background ratio while at the same time maintaining low transmission times from the atmosphere to the analyzer. Additional desirable properties include axial symmetry of the instrument response to the angle-of-attack (i.e., no azimuthal dependence) and low or negligible surface reactivity. The concentrators described in this paper meet these criteria by using an inert surface that has a high propensity for super-specular scattering. Such concentrators can be used to direct gas into an accommodation chamber that can be designed to be much smaller than what has been used in the classic closed-source approach, reducing the overall transmission time through

the instrument. The result is a technique that significantly improves the signal levels of the closed-source approach while reducing transmission times and minimizing surface reactions.

For an efficient concentrator, the surface must promote impulsive scattering, and the angular distributions of the scattered atoms and molecules must be narrow and peaked near, or beyond, the specular angle. The results of the molecular beam experiments clearly indicate that HOPG is the best material for a concentrator. While the Au surface did not promote significant energy transfer or thermal accommodation of the incoming O and O_2, the broad angular distributions shown in Figure 5.5 (FWHM = 55° for both species) yielded low concentration factors for all three modeled concentrator geometries (Table 5.3). The SiO_2 surface was considerably smoother than the Au surface and yielded angular distributions that were narrower, with a FWHM of 40° and 38° for O and O_2, respectively (Figure 5.6). It should be pointed out that the incident molecular beam used for the SiO_2 experiment had a higher incident energy for both O and O_2 (495.55 kJ mol^{-1} and 889.49 kJ mol^{-1}, respectively) than was used for the Au and HOPG experiments (~240 kJ mol^{-1} and ~480 kJ mol^{-1}, respectively). It is well known that angular distributions for IS species become narrower and the maximum θ_{out} moves farther from the surface normal as the E_{in} of the incoming particles increases.[6] We believe that the experiments on the SiO_2 surface represent a best case scenario as far as its use in a concentrator is concerned: lowering the E_{in} would broaden the distributions of the scattered O and O_2, lower the maximum θ_{out}, and increase the fraction of atoms and molecules that trap at the surface, all of which would result in an even lower C_a for any concentrator constructed from SiO_2. In contrast to the

relatively broad angular distributions from Au and SiO_2, the angular distributions of scattered O, O_2, and Ar from HOPG are extremely narrow (Figures 5.7, 5.10, and 5.11). Indeed, they are among the narrowest angular distributions that have been observed for gas-surface scattering; the only reported distributions that are narrower come from Ar, NO, and CO scattering from a hydrogen covered Ru(100) surface.[125,127] Moreover, the HOPG surface is associated with low energy transfer, with O, O_2, and Ar retaining over 85% of their incident kinetic energy when $\theta_{in} = 60°$, corresponding to $\alpha \sim 0.15$ (Figure 5.9). When θ_{in} is increased to 70°, the scattered atoms and molecules retain 95% ($\alpha \sim 0.05$) of their incidence kinetic energy. The low energy transfer that occurs on HOPG is ideal for a concentrator; the incident gas particles can undergo multiple collisions before thermally accommodating to the surface and have a higher probability of reaching the exit of the concentrator, as will be discussed later.

It is tempting to attribute the difference in the widths of the angular distributions of the scattered O and O_2 to deviations in roughness for the three surfaces studied. The effect of surface roughness on the scattering dynamics is clearly demonstrated by the scattering of Ar from vitreous carbon and HOPG.[126,144] Both of these surfaces are composed of sp^2 bonded carbon; however, the surface of vitreous carbon is rougher. The width of the angular distributions for the recoiling Ar increase from a FWHM of 6° for HOPG (E_{in} = 800 kJ mol^{-1}, $\theta_{in} = 45°$, $T_w = 503$ K) to ~50° for vitreous carbon (E_{in} =747 kJ mol^{-1}, θ_{in} = 45°, $T_w = 800$ K).[126,144] Considering that Ar is scattering from sp^2 bonded carbon in both systems, the increase in the width of the angular distribution can be attributed largely to the difference in surface morphology. For this study, the SiO_2 surface has the lowest RMS

roughness over a 10 μm × 10 μm area (0.94 ± 0.04 Å), whereas the HOPG and Au surfaces have average RMS roughnesses of 3.25 ± 1.01 Å and 4.23 ± 0.17 Å, respectively, over the same area. Based on the surface roughness, the SiO_2 surface should have the narrowest angular distribution. However, the widths of the angular distributions did not scale with the roughness of the surface. The angular distributions for O and O_2 scattering from SiO_2 were four times wider than those from HOPG, despite the facts that the SiO_2 was smoother than the HOPG surface and the E_{in} of the molecular beam for the SiO_2 experiment was twice as high. While the Au and HOPG surfaces have similar roughnesses within the error of the measurement, the angular distribution for O and O_2 scattering from Au were five times wider than the distributions of O and O_2 scattering from HOPG. However, the apparent roughness of HOPG is mainly the result of step edges in the graphene planes. Over a smaller area of 1 × 1 μm, the RMS roughness of HOPG is 0.055 Å, which is similar to the roughness of the SiO_2 surface over the same area (RMS roughness of 0.051 Å). Even if the SiO_2 and HOPG surfaces had similar roughnesses, the much broader angular distributions observed from SiO_2 compared to HOPG suggest that other factors besides roughness must contribute to the width of the angular distributions from these different surfaces.

The corrugation of the PES between the incident atom or molecule and the surface also affects the width of the angular distributions. This was demonstrated in a study by Butler et al. that investigated the interaction of NO with bare Ru(0001) and hydrogen covered Ru(0001)-(1x1)H.[125] The FWHM of the angular distributions of NO decreased from 27° to 8° (for θ_{in} = 60° and T_w = 575 K) when a Ru(0001) surface went from bare to

hydrogen covered. The adsorbed hydrogen served to smooth the PES; consequently, the incoming NO experienced a "flatter" surface that yielded a narrower angular distribution. The effect of the PES on the scattering dynamics of He, Ne, and Kr were also demonstrated in prior experiments conducted on the (111) faces of gold, silver, and nickel.[4] The gold surface yielded the broadest angular distributions for all the scattered noble gases, while the nickel surface produced the narrowest angular distributions. These results indicate that the corrugation of the PESs for the gold-He, Ne, Kr systems were relatively high and the PESs for the nickel systems had lower corrugations. The corrugation of the PES is affected in part by the lattice constant of the surface.[165] For metals with small lattice constant, such as nickel, the lattice constants are sufficiently small that the conducting electrons are distributed uniformly along the surface; the PES has little corrugation and the surface appears smooth to the incident atom or molecule. For metals with large lattice constants, such as gold, the electrons in the conduction band are not distributed uniformly between the atoms, yielding a corrugated PES. Returning to the data from the present study, it can be inferred from the angular distributions of scattered O, O_2, and Ar that the PES for HOPG interacting with the incoming species is only slightly corrugated. Conversely, the interaction potential for the Au-O and Au-O_2 systems must be highly corrugated, as is indicated by the broad angular distributions observed. Semiconductor surfaces, including Si(100), have been shown to have even higher surface corrugations than those of metals because the valence electrons are not delocalized and cannot smooth out the corrugation of the PES.[165] The surface corrugation is expected to be even more pronounced for the insulating SiO_2 surface because the electrons are tightly bound in covalent bonds. As a

result of the highly corrugated interaction potential between the incident species and the surface, the scattering dynamics on perfectly smooth Au and SiO_2 will be less favorable for a gas concentrator than those from an HOPG surface.

The observed scattering dynamics with highly reactive O atoms indicate that HOPG has the characteristics of an excellent concentrator material, but there are additional reasons to consider its use. Organic contamination is a critical materials issue for any concentrator device, and an HOPG concentrator could be kept clean in flight relatively easily. Great pains are usually undertaken to remove adsorbed carbon and organic residue to ensure the cleanliness of gold during experiments: the experimental apparatuses are maintained at UHV pressures and the surface is repeatedly treated with 3 kV Ar ion sputtering and dosed with an oxygen plasma to remove any contamination on the surface. In space flight, these treatment options are not available and it would be impractical to maintain the surface at high temperatures to prevent adsorption of incoming molecules on the surface, as was done in the experiment. In contrast, organic contaminants can be removed from an HOPG surface by heating it to 673 K for a few seconds and then the UHV conditions present the space environments where it would be used would ensure that the surface would stay clean almost indefinitely.

The experimental O-atom scattering results were used to constrain the angular distributions of an O atom propagating through concentrator geometries in a series of test particle Monte Carlo simulations that show overall C_a between approximately 60 and 370 for concentrators that utilize HOPG surfaces at a 5,000 m s^{-1} free-stream velocity. These concentration factors are far greater than those possible with a concentrator using Au or

SiO_2 surfaces. Two basic geometries were evaluated in the simulations. The first is a cone-shaped concentrator having opening half-angles of 10° and 15°. The second is an annular ring concentrator optimized to the preferential scattering direction from the surface. The annular ring concentrator was found to have lower modeled C_a values than the cone-shaped device, but it has the property that the majority of molecules entering the accommodation chamber would have undergone only a single reflection with the concentrator geometry. The dependence of C_a on angle of attack of an HOPG concentrator was also investigated (Figure 5.16). The results indicated the reduction of C_a below a 5° angle of attack. All concentrators evaluated had C_a values above unity below a 20° angle of attack. The concentrator designs presented do not attenuate the flow as long as the angle of attack is within ± 20°.

It is instructive to compare the results presented here to previous examinations of O-atom concentrators. In a study by Tagawa et al., several concentrator designs constructed from Pyrex were tested with a hyperthermal O-atom beam and the results were compared with a model of the flow through the concentrator.[142-143] In modeling the flow through the Pyrex concentrators, Tagawa et al. based the scattering model on previous results of F-atom scattering from fluorinated Si(100), assuming that the results of O-atom scattering on rough Pyrex were basically identical to the F-atom scattering results, with the exception that the angular distributions were treated as being infinitesimally narrow.[36] Tagawa et al. tested a cone-type geometry as part of their investigation, which allows us to compare their results with our experimentally constrained model. The cone in the Tagawa et al. study was 10 cm long but had a larger exit aperture (5 mm diameter) than the concentrators considered

in our study (1.12 mm diameter). Consequently, a cone from the Tagawa et al. investigation scaled to the same exit aperture diameter as the cones investigated in this study has a shorter length, with a value of 2.8 cm. The experimental C_a of the Pyrex cone at 11.3° (10 cm length but 2.8 cm equivalent length at the exit aperture size considered here, 1.12 mm) was measured by Tagawa et al. to be 3.4. In comparison, the 10° half-angle (11 cm long) HOPG and SiO_2 cones presented here have modeled C_a factors of 366 and 10.5, respectively. If these cones were 2.8 cm long, the C_a factors would decrease to 230 and 6.6 for HOPG and SiO_2, respectively. Since the cone half-angle tested by Tagawa is slightly larger than the cone in our model (11.3° half-angle vs. 10° half-angle), we would expect a further reduction in the C_a for our concentrators. While the estimated C_a for the SiO_2 concentrator developed in this paper, which should be similar to the Pyrex cone, is higher than the concentration factor of 3.4 measured by Tagawa et al., it is significantly closer than the simulated prediction of 25 made in that paper. Tagawa et al. concluded that O-atom recombination was preventing the measurement of the vast majority of concentrated oxygen. Lowering the original flux of O atoms into one of their concentrators by a factor of 14 resulted in a measured C_a of 5.2 for the cone which agrees reasonably well with our modeling prediction for the SiO_2 10° half-angle cone. It should be noted that the surfaces considered by Tagawa et al. were significantly rougher (RMS roughness of ~ 210 Å) than the SiO_2 investigated here (RMS roughness of 0.94 Å) and that this could contribute to the difference in the modeled C_a and their experimental measurements. The discrepancy could also be explained in our model by a change in angular distributions and/or the

accommodation coefficients with increased O-atom flux to the inlet surfaces. Such a change has been proposed previously by Moe et al. [166] as well as Pilinski et al.[167]

Given the relatively good agreement between our model and previous concentrator results, we conclude that the discrepancy between the results of Tagawa et al. and their prediction of a C_a of 25 can be explained by a more realistic aerodynamic and scattering model. Applying our model and the experimental SiO_2 scattering results to the Pyrex cone funnel examined by Tagawa et al. leads to a modeled C_a of 6.6, which compares well with the value of C_a = 5.2 measured by Tagawa et al. The remaining part of the discrepancy between our experimentally calibrated modeling results could also be due to high O-atom flux levels in the experiment, which might lead to gas-phase collisions that could inhibit passage through the concentrator or promote O-atom recombination. In addition, a high incident flux would likely lead to enhanced oxygen surface coverage and O-atom recombination on the surface. As Tagawa et al. could not measure the levels of O_2 exiting the concentrator, we do not know how O-atom recombination and O atoms adsorbed on the surface may have affected the measured C_a. However, the peak O-atom flux reported by Tagawa et al. was 1.2 x 10^{23} atoms m^{-2} s^{-1} which, at ~8000 m s^{-1} corresponds to mean free-paths of 1-2 mm. It is entirely possible that gas-phase collisions and O-atom recombination were occurring inside their concentrator volume at these high pressures. Given that there were many other times during the experimental data collection that the mean-free path would have been larger (lower pressure), it is not clear to what extent this could have affected their concentration results. It is also important to note that a similar decrease of funnel efficiency from the theoretical expectation was reported for the

aluminum funnels in the Effects of Space Environment on Materials Experiment (ESEM) experiment flown on the space Shuttle.[143,168] We expect that the mean free paths during that experiment at 290 km altitude above the Earth's surface (peak flux of ~5×10^{18} atoms m^{-2} s^{-1}) would be ~180 m in the free-stream. Certainly, since the Space Shuttle Orbiter was well within the free-molecular flow regime at this altitude,[169] the mean free paths would never be expected to fall below the characteristic length of the spacecraft, i.e., 37 m. It is unlikely that the local mean-free path inside those funnels dropped much below 10 m because the highest theoretical C_a for the ESEM funnels was 16. Nevertheless, the C_a obtained for the ESEM experiments were, like the Tagawa et al. results, similarly low.[142,168] This is consistent with the assumption that the aluminum concentrator surfaces used in the ESEM experiments produce angular distributions similar to those obtained for Au and SiO_2 in our experiments and would yield correspondingly low C_a.

O-atom recombination on instrument surfaces has been documented many times in the history of space-borne instrumentation.[170] However, our present study has found that the dynamics of O and O_2 scattering on HOPG are nearly identical, indicating that any O_2 observed scattering from the surface originated from O_2 in the incident beam. The angular distributions for O_2 are slightly narrower than those for O atoms, and both species have nearly identical energy transfers with the surface. It has been shown that the angular distribution for O_2 produced by an Eley-Rideal abstraction of an surface-adsorbed O atom by an incident O atom would result in a broad angular distribution of O_2 that has a peak flux below the specular angle.[64] Furthermore, the O_2 produced through this abstraction mechanism would have a significantly lower translational energy than was observed in the

experiment, because much of the available energy would be channeled into internal modes instead of translation. Additionally, the absence of TD in the TOF spectra for O_2 indicate that there is no O-atom recombination that is produced through a Langmuir-Hinshelwood reaction. The experiments show that O-atom recombination on HOPG is negligible, and a concentrator using HOPG surfaces would not experience reduced efficiency due to O-atom recombination on the surface.

In the cases presented so far, the energy transfer and angular distributions of the scattered atoms were assumed to be unaffected by multiple collisions throughout the simulation, an assumption that needs to be verified through further testing. This assumption was examined by using SPARCS to investigate the effect of broadening of the angular distribution with subsequent bounces following the first atom-surface collision on the overall concentration factor. The underlying assumption was that the angular distributions of the scattered atoms might become broader with each successive atom-surface interaction inside the concentrator. To model this effect, we related the angular distributions of each O atom to its overall energy loss and simulated test cases under varying α_k assumptions. This procedure introduced a relationship between the overall energy accommodation coefficient, α, and the resulting angular distributions on successive bounces. The results indicated a non-monotonic behavior of C_a with α_k. In fact, as α_k was increased from zero, C_a for a 15° cone was seen to increase by more than a factor of two. When α_k was greater than 0.4, C_a began to decrease, and at values of α_k above 0.7, C_a became lower than that of the $\alpha_k = 0$ case. The non-monotonic nature of C_a with the gradual broadening of the angular distribution can be explained by considering how O atoms with static angular distributions

exit the concentrator geometry through the entrance aperture. In the super-specular (HOPG) and sub-specular (Au and SiO_2) cases, the most probable outgoing angle moves closer to the surface normal with each successive collision inside a conical geometry. Eventually, the most probable outgoing angle moves toward the surface normal which points away from the exit aperture, and the atoms begins progressing back toward the entrance of the concentrator. In the case where the parameters of the angular distributions are static, once this "reversal" point is reached, the O atom is certain to leave the instrument through the entrance aperture before it can be ionized and analyzed. The effect is particularly dramatic with the narrow angular distributions observed for scattering from HOPG. This "reversal" behavior explains why the HOPG cone collects most of its atoms from the area closest to the exit aperture and why atoms captured farther away from the exit are likely to be rejected. However, if the angular distribution becomes more diffuse as the bouncing atom reverses direction, the probability of the atom being lost is lowered from nearly 100% to nearly 50% if the "reversal" point is just at the concentrator exit. This phenomenon explains why the modeled C_a for the 15° half-angle cone increases as the angular distribution becomes gradually more diffuse with successive bounces. As expected, the annular ring concentrator is immune to this effect, because the vast majority of exiting O atoms have undergone only a single collision in the geometry and that first impact is based on the empirically determined angular distributions. Therefore, one can expect that data analysis of signals measured by an instrument employing an annular-ring concentrator is much less sensitive to how atoms accommodate along their propagation path. This decreased sensitivity to α_k would lead to a decrease in experimental uncertainty

because the final velocities of the atoms exiting the annular ring concentrator could easily be modeled using the existing experimental data. For the cone geometry, the uncertainty must be constrained experimentally by examining how the observed C_a for concentrator geometry compares with the modeled cases. Further testing will be needed to confirm assumptions about angular distributions and energy accommodation inside the concentrator. The results of the test and modeling presented here as well as those planned in the future, will form the basis of a detailed and accurate model of the concentrator that is based on experimental results performed in flight-like conditions. This model will in turn form the basis of flight data analysis for future MS instruments equipped with a concentrator inlet.

5.5 Conclusions

The scattering dynamics of hyperthermal O and O_2 from Au, SiO_2, and HOPG have been investigated using a beam-surface scattering technique in order to identify a surface that would be suitable for a gas concentrator inlet in front of a mass spectrometer detector for species in tenuous atmospheres. Flux angular distributions for each surface were derived from TOF distributions that were collected for $\theta_{in} = 60°$ and $\theta_{in} = 70°$. O and O_2 were found to scatter impulsively from both the Au and SiO_2 samples with only a small fraction of the incident atoms and molecules coming into thermal equilibrium with these surfaces; a fraction of O and O_2 were found to scatter backward in the c.m. frame. The resulting angular distributions for both O and O_2 from Au and SiO_2 were peaked below the specular angle and were broad. Conversely, the O and O_2 recoiling from the HOPG surface lost little energy during the collision and scattered from the surface with narrow angular

distributions that had maxima beyond the specular angle; thermal desorption and backward scattering of O and O_2 from the HOPG surface were not observed. The dynamics of hyperthermal Ar scattering from surfaces of HOPG that were both unexposed and exposed to O atoms revealed that modification of the surface by the incident O and O_2 was minimal.

The scattering dynamics on HOPG were the most favorable for a concentrator. By applying the results of the laboratory investigation to a free-molecular flow model of cone-shaped and annular-ring inlet geometries, we found that values of C_a in excess of 100 are possible with the use of HOPG surfaces. The concentrator geometries evaluated are robust to scattering-model variability as well as to a broader set of free-stream conditions than designs evaluated in previous studies. For an HOPG cone-type inlet, the C_a was calculated to be 117 for a 15° half-angle cone and 366 for a 10° half-angle cone. For the HOPG annular-ring inlet, the C_a was 66. For all inlet geometries, the C_a calculated from the observed HOPG surface scattering results were approximately an order of magnitude higher than those calculated from the Au or SiO_2 surface scattering results. We found that the scattering dynamics associated with successive atom-surface bounces can significantly increase or decrease C_a. An HOPG concentrator based on the geometries presented could be used to increase the signal-to-background ratios in future space-borne mass spectrometers.

Acknowledgements

This work was supported by the Jet Propulsion Laboratory (JPL), California Institute of Technology, under contract with the National Aeronautics and Space Administration (NASA), with subcontracts to Dr. Marcin Pilinski (#1519790) and Prof.

Timothy K. Minton (#1518872). Vanessa J. Murray is grateful for support awarded by DoD, Air Force Office of Scientific Research, National Defense Science and Engineering Graduate (NDSEG) Fellowship, 32 (Code of Federal Regulations) CFR 168a. AFM data were collected at the Image and Chemical Analysis Laboratory (ICAL) at Montana State University.

CHAPTER SIX

SCATTERING DYNAMICS OF N_2 FROM HIGHLY ORIENTED PYROLYTIC GRAPHITE

Contribution of Authors and Co-Authors

Manuscript in Chapter 6

Author: Neil A. Mehta

Contributions: Performed molecular dynamics simulations. Prepared both the figures and the computational sections of manuscript for publication.

Author: Vanessa J. Murray

Contributions: Performed molecular beam scattering experiments, data analysis, and prepared both the figures and the experimental sections of manuscript for publication.

Co-Author: Chenbiao Xu

Contributions: Aided with the molecular beam scattering experiments.

Co-Author: Deborah A. Levin

Contributions: Provided crucial insight regarding the molecular dynamics simulations. Aided in the preparation of the manuscript and figures.

Co-Author: Timothy K. Minton

Contributions: Provided crucial insight regarding the experimental procedure and the data analysis. Aided in the preparation of the manuscript and figures.

Manuscript Information Page

Neil A. Mehta, Vanessa J. Murray, Chenbiao Xu, Deborah A. Levin, and Timothy K. Minton

Journal of Physical Chemistry C

Status of Manuscript:
_____ Prepared for submission to a peer-reviewed journal
_____ Officially submitted to a peer-review journal
__×__ Accepted by a peer-reviewed journal
_____ Published in a peer-reviewed journal

Published online by the American Chemical Society
DOI: 10.1021/acs.jpcc.7b11721

Reproduced with permission from ACS – the American Chemical Society

Note: Note: Chapter 6 has been adapted from an article titled "Non-Reactive Scattering of N_2 from Layered Graphene using Molecular Beam Experiments and Molecular Dynamics". This article was written with Neil Mehta and Prof. Debbie Levin from the University of Illinois, Urbana-Champagne. Only the work completed for the experimental portion of the study has been presented in Chapter 6. The introduction was re-written to put the study in the context of the field of gas-surface scattering and the abstract was updated to represent the subject matter of Chapter 6. The contributions from Neil A. Mehta and Deborah A. Levin, which detailed the molecular dynamics simulations, have not been included in Chapter 6.

SCATTERING DYNAMICS OF N_2 FROM HIGHLY ORIENTED PYROLYTIC GRAPHITE

Vanessa J. Murray, Chenbiao Xu, and Timothy K. Minton

Department of Chemistry and Biochemistry, Montana State University, 103 Chem/Biochem Bldg., Bozeman, MT, 59717

Abstract

The inelastic scattering dynamics of N_2 colliding with a highly oriented pyrolytic graphite (HOPG) surface have been studied for incidence energies of 30.3 and 67.9 kJ mol^{-1} with incidence angles of θ_i = 30°, 45°, and 70°. Although the angular distributions grew narrower as the incidence energy was increased, the energy transfer dynamics were largely insensitive to E_i. The exception was for θ_i = 70°, where the ratio of incidence energy to final energy (E_f / E_i) increased when E_i was increased from 30.3 to 67.9 kJ mol^{-1}. While the experimental results indicate molecules scatter via an impulsive scattering mechanism, which is often considered to proceed through a single gas-surface collision, molecular dynamics simulations have revealed that the molecules can scatter by three distinct scattering trajectories. The dominant scattering channel proceeds through a single collision. The remaining two mechanisms involve the molecule suffering multiple collisions with the surface before it either scatters into the vacuum or becomes trapped; both of these trajectories have been interpreted as a quasitrapping mechanism where the incidence energy of the molecule was not fully accommodated. The probability of the multi-collision scattering mechanisms increased as the θ_i became more grazing.

Furthermore, the probability of multi-collision scattering events decreased with increasing E_i.

6.1 Introduction

Carbon-based thermal protection systems (TPSs) are often used to protect space vehicles during atmospheric re-entry. Non-reactive gas-surface collisions of relatively inert gases, such as N_2, can proceed through an impulsive scattering channel, where the molecule retains most of its incidence energy, or it can transfer a large portion of its energy to the surface during the collision and become trapped.[2] The relative probabilities of impulsive scattering (IS) and trapping desorption (TD) will thus greatly affect the heat transfer to the surface. Furthermore, it is important to understand the TD dynamics on a TPS because this step can precede chemisorption,[171] which is necessary for Langmuir-Hinshelwood chemical reactions.[3] In order to characterize the nonreactive scattering events on a model air-carbon system, we have conducted a combined experiment/theory study of the post-collision angular and translational energy distributions for N_2, with average incidence energies of 30.3 and 67.9 kJ mol^{-1}, that scatter from a highly oriented pyrolytic graphite (HOPG) surface. The surface temperature was 673 K, which was high enough to ensure cleanliness of the surface for the duration of the experiment while being sufficiently low enough that non-reactive scattering dynamics could be studied without complication arising from reactive processes.

Inelastic scattering from smooth surfaces has been the subject of extensive study.[1,172-174] For many gas surface systems, molecules that scatter impulsively from the surface are focused in a lobe centered at or beyond the specular angle. The width of the angular

distribution of scattered product flux initially grows narrower as the incidence energy, E_i, is increased. However, the width begins to increase above a threshold energy as the molecules begin to sample the surface corrugation. The observed trend of the angular widths indicates that the scattering dynamics are qualitatively different at high and low E_i.

The energy transfer dynamics add further insight into the gas-surface interactions at low and high incidence energies, referred to as the thermal and structural regimes.[6] For the thermal scattering regime, the incident molecule experiences a smooth surface during the collision because the turning point far from the surface. This allows for the conservation of parallel momentum during the collision. The energy of the scattered molecule decreases with final angle, θ_f, which is measured from the surface normal. Rigorous parallel momentum conservation (PMC) requires that the ratio of initial to final translation energy (E_f / E_i) follows the trend $\sin^2(\theta_f)$ / $\sin^2(\theta_i)$,[175] where θ_i is the incidence angle which is located on the opposite side of the surface normal from θ_f. For structural regime, the molecule experiences a corrugated interaction with the ion cores that constitute the surface. Consequently, parallel momentum is not conserved during the collision and the E_f / E_i ratio increases with θ_f. The seminal works by Rettner, Barker, and Bethune showed that the transition from the thermal scattering regime to the structural scattering regime occurs smoothly as the E_i is increased, and the dependence of E_f / E_i on θ_f had zero slope when the incidence energy was 2 eV for the Xe/Pt(111) system.[6] Subsequent work has shown that the energy at which this transition occurs is heavily dependent on the system being studied.[172]

The energy transfer is governed in part by the potential energy surface on which the collision occurs. A deep well in the interaction potential between the incoming molecule and the surface will accelerate the molecule towards the surface, leading to a harder collision and more energy transferred to the surface.[172] If the potential well is shallow, the molecule will retain more of its incidence energy during the collision. This effect has been well demonstrated by the scattering of hyperthermal Ar and Xe from HOPG.[144,176] While the angular distributions for the two systems were similar (though not identical), the angular dependencies of E_f / E_i were drastically different. The scattering dynamics of Ar with an incidence energy in the range of 2 - 14 eV indicate that the scattering occurs in the structural regime (E_f / E_i increases with θ_f) and the results were well described by a binary collision model. In contrast, the scattering dynamics for Xe with E_i = 3.6 eV indicated that parallel momentum was conserved during the collisions and the interactions occur in the thermal regime. The origin of these drastically different results lies in the differences in the potential energy surfaces for the two systems. The potential well for Xe + HOPG is twice as deep as that of Ar + HOPG (0.86 kJ mol^{-1} versus 0.47 kJ mol^{-1}); thus, the Xe transferred more energy during collisions with the surface.

Collisions of N_2 with highly oriented pyrolytic graphite (HOPG) have recently become the focus of several studies, including the study presented in this chapter, to probe the effects of the gas-surface interaction potential on non-reactive gas-surface scattering dynamics. The impulsive scattering of N_2 from HOPG was studied by Oh et. al for incidence energies in the range of 26 – 60 kJ mol^{-1} and surface temperatures of 150 – 400 K.[177] The experimental configuration constrained the data collection such that the $\theta_i + \theta_f$ =

90°. The results of this study suggested that the molecules scattered after a single collision with the surface. Majumander et. al. investigated this system using molecular dynamics simulations.[43] In contrast with the report by Oh et al., but in agreement with our preliminary simulations,[178] this study found that the molecules scattered via three distinct mechanisms: single collisions events, multiple-collision events, and multiple-collision without escape events. The branching between the three mechanisms depends strongly on the θ_i and E_i of the N_2 molecules. The multiple-collision with and without escape events were described in terms of quasi-trapping caused by the high surface temperature of the HOPG.

At the opposite extreme of impulsive scattering is thermal desorption, where an atom or molecule dissipates enough energy during the collision to come into thermal equilibrium with the surface before eventually desorbing back into the vacuum. Molecules that undergo conventional thermal desorption exit the surface with a Maxwell-Boltzmann distribution of energies determined by the surface temperature and have an angular distribution that follows the Knudsen cosine law.[42] The momentum oriented both normal and parallel to the surface must be fully accommodated for the molecule to undergo trapping desorption. However, accommodation of the parallel momentum occurs more slowly than accommodation of the normal momentum on a smooth surface. This difference in momentum accommodation time scales has important consequences for the thermal desorption dynamics when the surface temperature is high and the residence time of the incoming molecule is low, because the molecule can exit the surface before the parallel momentum has been fully accommodated. This phenomenon has been referred to as quasi-trapping and is probable when the surface is smooth and the surface temperature is high

(>80 K).[42] As a result of the incomplete accommodation of the parallel momentum, quasi-trapped molecules retain some memory of their incident trajectory. Consequently, the angular distributions of the quasi-trapped molecules that exit the surface are asymmetric about the surface normal and the post-collision translational energies cannot be described by a Maxwell-Boltzmann (MB) distribution characterized by the surface temperature. The distinction between impulsively scattered and quasi-trapped molecules is difficult to determine experimentally because of the similar time scales over which these processes occur.

The objective of the study presented in Chapter 6 is investigate the scattering dynamics of N_2 from a HOPG surface. The work presented below has been conducted as part of a collaboration with Neil A. Mehta and Professor Deborah A. Levin at the Univeristy of Illinois, Urbana-Champaign where MD simulations of N_2 colliding with layered graphene have been compared with the results of molecular beam-surface scattering experiments of N_2 on HOPG. The experimental results indicate that the molecules scatter impulsively from the surface. There is no evidence that N_2 scatters from the surface via a thermal desorption mechanism. However, the MD simulations reveal that multiple-collision events are significant, and their probability increases as θ_i is increased and the normal momentum decreases. As the incidence energy is increased, the probability for multiple-collision events decreases. The MD results are reflected in the experimental findings, which show that the angular and translational energy distributions are most sensitive to the incidence energy of the N_2 when the incidence angle is 70°, where multiple-collision events are the most probable. The results of these experiments indicate that even if the molecules suffer

multiple collisions with the surface, they retain a significant portion of their incidence parallel momentum. Thus, the molecules can exit the surface before becoming trapped. This would reduce the probability of gas-surface reactions between the incoming N_2 and the HOPG surface. Additionally, the incomplete thermal accommodation would improve the efficiency of a neutral gas concentrator described in Chapter 5 because the angular distributions of the scattered molecule remain lobular despite suffering multiple collisions with the surface.

6.2 Experimental Methods

The experiments were performed with a crossed molecular beams apparatus configured for beam-surface scattering.[179] A beam containing N_2 seeded in He was directed at a highly oriented pyrolytic graphite (HOPG) surface, and inelastically scattered products were detected with a mass spectrometer that rotated about the same axis as the surface, within the plane defined by the incident beam and surface normal. The mass spectrometer detector consisted of a Brink-type ionizer,[150] a quadrupole mass filter, and a Daly-type ion counter operated in pulsed counting mode.[151] The detector was triply differentially pumped such that the region containing the ionizer had a base pressure of $<10^{-11}$ Torr and increased only slightly while collecting data even though the scattering chamber had a pressure of 2.0×10^{-6} Torr. The increased pressure in the detector was caused by the accumulation of the He carrier gas used with the N_2 beam, which could not be effectively pumped by the ion pumps used for the detector. The N_2 background did not increase during data collection. The signal of the continuously scattered products was modulated using a 17.8 cm diameter chopper wheel that was mounted on the front of the

detector 30.2 cm away from the ionizer. This chopper wheel had three equally spaced 1.6 mm wide slots and spun with a frequency of 300 Hz. N_2 molecules recoiling from the surface were detected over a range of final angles, θ_f, with incidence angles of $\theta_i = 30°$, 45° and 70°. A multichannel scaler was used to record the number density as a function of arrival time at the ionizer for $m/z = 28$ (N_2^+). These distributions are commonly referred to as time-of-flight (TOF) distributions. To compensate for long-term drift in the experiment, the TOF distributions were recorded by incrementing θ_f from high to low and then the reverse. Two TOF spectra were thus collected for each θ_f, and these were summed and corrected for ion flight time and electronic offsets before being analyzed.

The supersonic molecular beams of N_2 were prepared by expanding a gas mixture with a backing pressure of 250 Torr through a 0.150 mm diameter pin hole. The beam was collimated by a 0.56 mm diameter skimmer placed 5.8 mm downstream of the nozzle and a 0.44 mm wide × 1.3 mm high slit located 44.7 mm from the nozzle in the scattering chamber. For $\theta_i = 70°$, the molecular beam illuminated a 2.8 mm × 1.3 mm spot on the surface, which was located 96.1 mm from the nozzle. A mixture of 10% N_2 (99.999%) seeded in He (99.9999%) with a nozzle temperature of 296 K yielded a molecular beam with a translational energy of 30.3 kJ mol^{-1}. A higher energy molecular beam was prepared by expanding the same mixture through the same nozzle with a temperature of 683 K. The resulting molecular beam had a nominal translation energy of 67.9 kJ mol^{-1}.

The supersonic molecular beams were directed at the surface of ZYA-quality highly oriented pyrolytic graphite (HOPG) obtained from Momentive Inc., with dimensions of 12 mm × 12 mm × 2 mm. The HOPG was prepared in air by removing a few layers of

graphene from the sample with a piece of tape shortly before being placed in the vacuum chamber and pumped down to a high vacuum of ~2×10^{-7} Torr. The HOPG sample pressed against a stainless steel frame with a copper backing plate that housed a cylindrical resistive heater. The sample assembly was attached to a manipulator that could translate the sample into and out of the beam path as well as rotate to alter the θ_i of the molecular beam. The stainless steel mount had a 10 mm × 10 mm viewing window; the edges of the sample mount around the viewing window were very thin, in order to allow incident and scattered species to enter and leave the sample without colliding with the stainless steel frame. The power supplied to the resistive heater could be altered to adjust the temperature of the sample, which was measured using a type K thermocouple attached to the copper backing plate. The sample was maintained at a temperature of 677 K for the duration of the experiment and assumed to be free of contamination based on earlier results on the interaction of Ar with HOPG, which exhibited scattering dynamics that were indicative of a clean surface even at the relatively low temperature of 503 K.[144]

6.3 Results

The TOF distributions, *N(t)*, are used to derive the translational energy distributions, P(E_T), of the recoiling N_2 molecules. The P(E_T) are proportional to t^2 *N(t)*, where *t* is the flight time from the chopper wheel to the detector, such that the translational energy, E_T is equal to,

$$E_T = \frac{1}{2} m \left(\frac{d}{t}\right)^2 . \tag{6.1}$$

The chopper wheel slit was found to have a negligible effect on the width of the TOF distributions and its effect was not considered during the analysis. The P(E_T) distributions are proportional to flux and the angular flux distributions are produced by integrating these distributions at each θ_f. The experimental results are summarized in Figures 6.1 through 6.3.

Figure 6.1 displays representative TOF distributions for both the incident molecular beams and the N_2 scattering from the surface for θ_i = 70° and E_i =30.3 and 67.9 kJ mol^{-1}. Each TOF distribution has been normalized its maximum intensity. Both the molecular beam and the scattered TOF distributions where modulated by a chopper wheel located in the same position on the detector; the detector was aligned with the beam axis to collect TOF distributions of the incident N_2 molecules. Thus, the flight times if the incident and scattered N_2 can be directly compared. The gray lines indicate the average arrival times of the respective incident beams at the detector. For every θ_f, the TOF distributions have only a single component. If any molecules had come into thermal equilibrium with the surface before scattering, their outgoing energies could be well described by a Maxwell-Boltzmann (MB) distribution characterized by the surface temperature,[2] which is represented by the green, dashed lines in Figure 6.1. The MB distribution would have peak arrival times between 300 and 400 μs. If the MB distribution were scaled to fit the data, there would be a negligible amount of overlap with the scattered TOF distributions. The absence of signal at large flight times thus indicates that few molecules come into thermal equilibrium with the surface and that essentially all the N_2 molecules scatter from the surface impulsively. When θ_f is close to the surface normal, the TOF distributions are

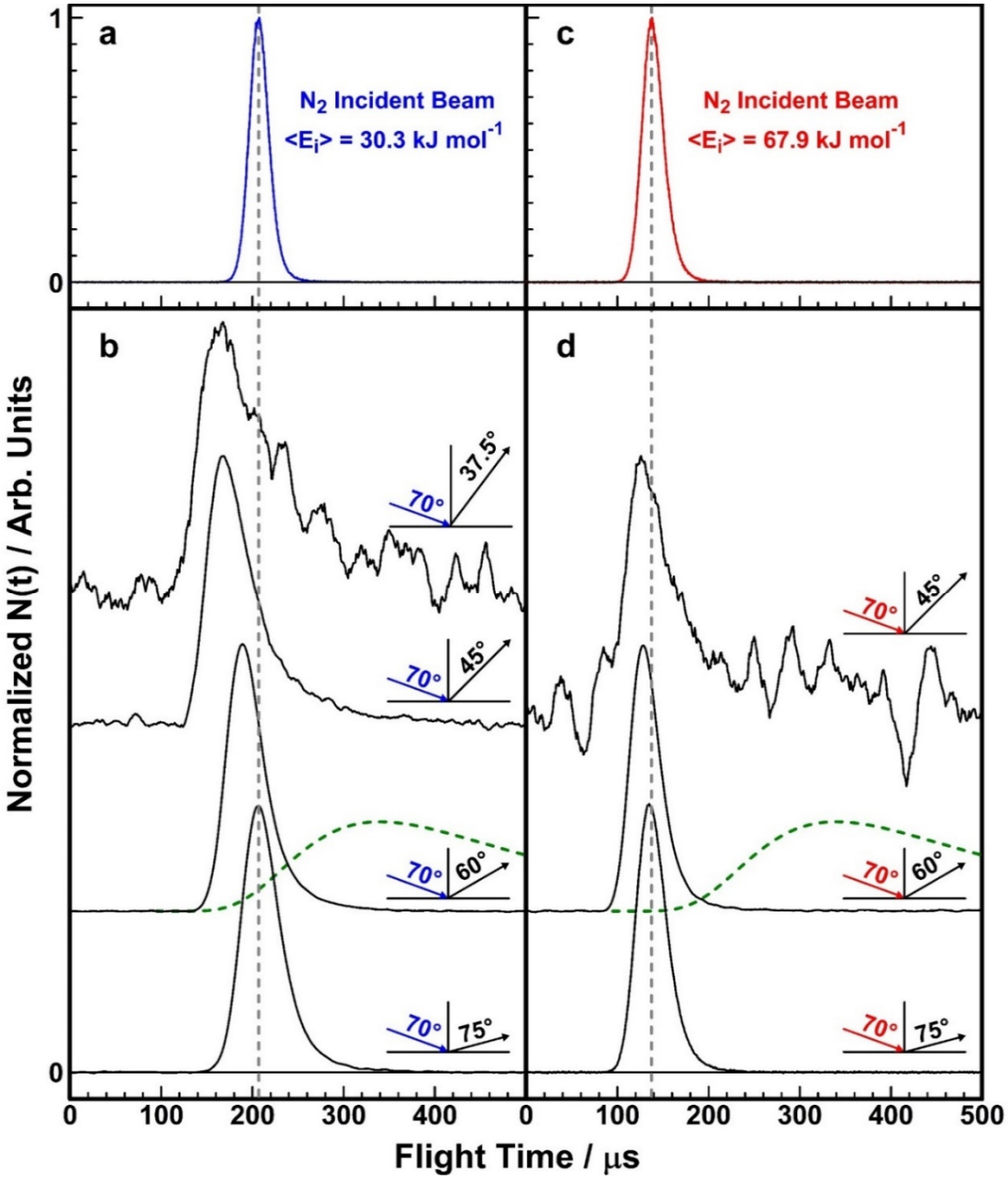


Figure 6.1. Representative TOF distributions for the incident molecular beam (a, c) and the scattered N_2 (b, d) for E_i = 30.3 kJ mol^{-1} (left panel) and E_i = 67.9 kJ mol^{-1} (right panel), with T_s = 677 K and θ_i = 70°. Each distribution has been normalized to its maximum value. The θ_f for the scattered distributions (b, d) are indicated by the diagram next to each curve. The gray dashed line indicates the average arrival time of the incident beam at the detector. The green dashed lines indicate the predicted arrival times of molecules that desorb in thermal equilibrium with the surface.

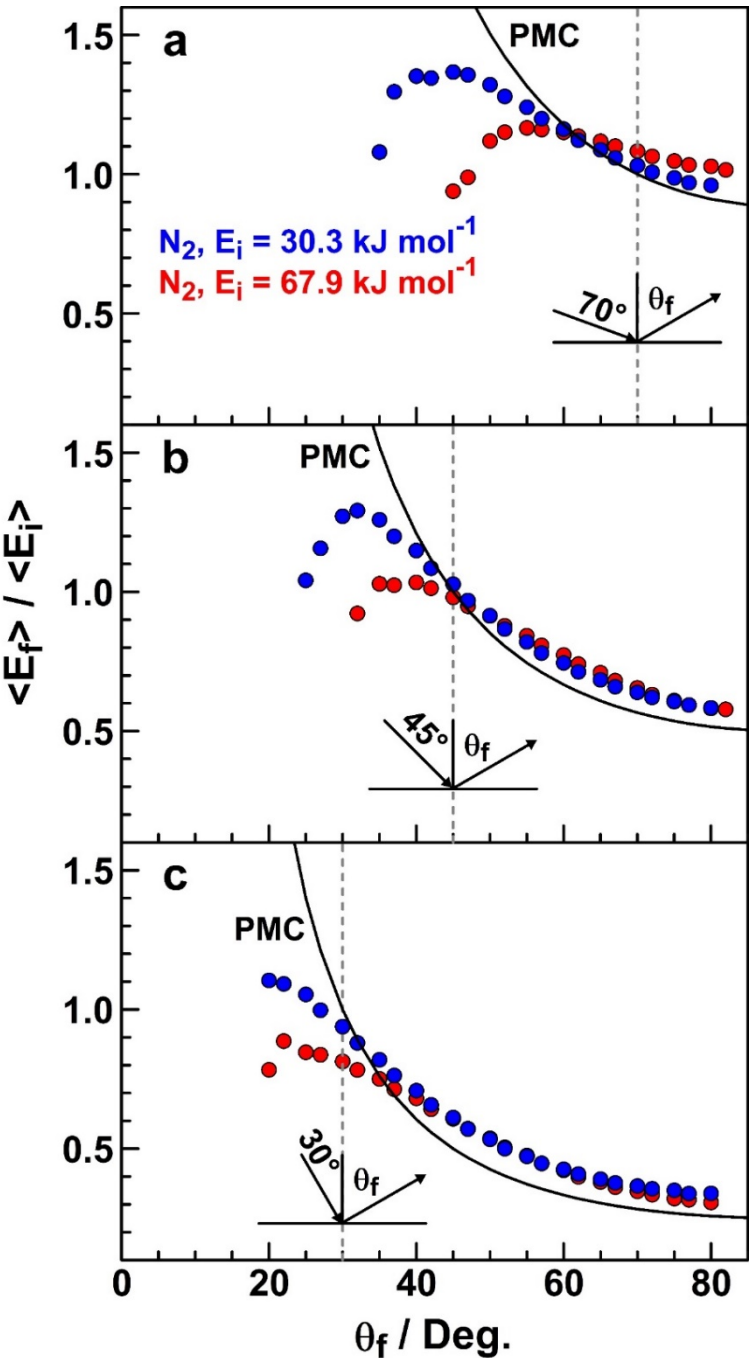


Figure 6.2. The ratio of $\langle E_f \rangle$ to $\langle E_i \rangle$ of the scattered N_2 molecules as function of θ_f for θ_i = (a) 70°, (b) 45°, and (c) 30°, with E_i = 30.3 kJ mol^{-1} (blue symbols), E_i = 67.9 kJ mol^{-1} (red symbols), and T_s = 677 K. The black line in each panel indicates the energy ratio resulting if the parallel momentum of the incident N_2 molecule is conserved during the collision (see text). The dashed gray lines indicate the specular angles ($\theta_f = \theta_i$).

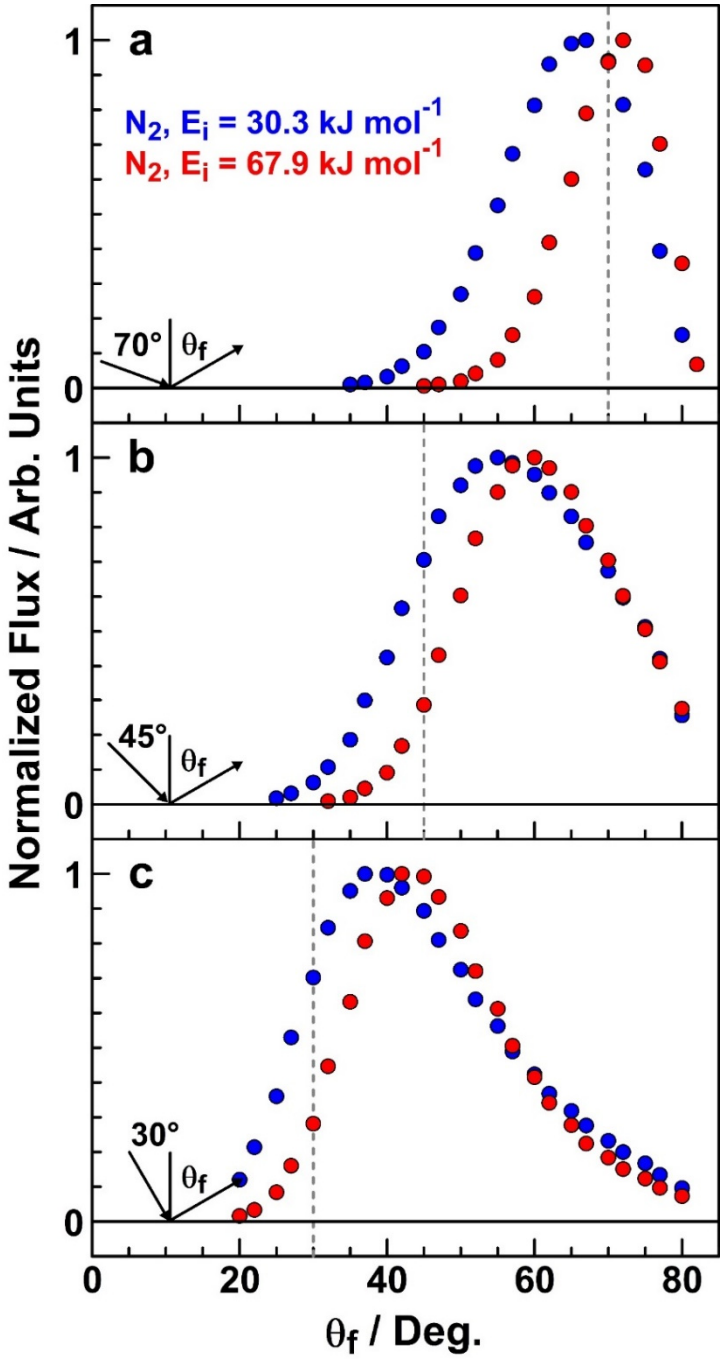


Figure 6.3. Flux angular distributions for N_2 molecules scattering from the HOPG surface for θ_i = (a) 70°, (b) 45°, and (c) 30°, with E_i = 30.3 kJ mol^{-1} (blue symbols), E_i = 67.9 kJ mol^{-1} (red symbols), and T_s = 677 K. The distributions have been normalized to their respective maxima. The dashed gray lines indicate the specular angles ($\theta_f = \theta_i$).

broad and arrive at the detector before the incident beam. The TOF distributions for grazing θ_f become narrower and shift to longer times. This behavior is characteristic of molecules scattering in the "thermal regime," and indicates that the molecules tend to retain their incident parallel momentum after scattering from the surface.[6] When the E_i of the molecular beam is increased to 67.9 kJ mol^{-1}, the corresponding TOF distributions shift to smaller flight times, but the qualitative scattering dynamics remain unchanged.

Figure 6.2 depicts the ratio of average incidence and final energies, $\langle E_f \rangle / \langle E_i \rangle$, where $\langle E_i \rangle$ is the average energy of the N_2 molecules in the incident beam, for both the lower (blue symbols) and higher (red symbols) incidence energies for θ_i = 70°, 45°, and 30°. The dashed lines indicate the specular angle ($\theta_i = \theta_f$), and the solid black curves correspond to the energy ratio obtained if the momentum parallel to the surface of the incident N_2 molecule is conserved during the collision. Parallel momentum conservation (PMC) requires that $\langle E_f \rangle / \langle E_i \rangle = \sin^2(\theta_i)/\sin^2(\theta_f)$. The energy ratios exceed the PMC values at grazing θ_f. At low θ_f, the energy ratio increases with θ_f before decreasing and following the general shape of the PMC prediction. The energy ratios in the low θ_f regime were very sensitive to the E_i. In contrast, for θ_f greater than 40°, the energy ratio is invariant with respect to E_i for θ_i = 30° and 45°. However, for θ_i = 70°, the energy ratios for E_i = 67.9 kJ mol^{-1} are greater than those obtained from the energy ratios of E_i = 30.3 kJ mol^{-1}. It appears that the scattering dynamics for θ_i = 70° are sensitive to the E_i of the incoming molecular beam.

Figure 6.3 presents angular distributions of scattered N_2 flux, corresponding to E_i = 30.3 and 67.9 kJ mol^{-1} (blue and red symbols, respectively) and θ_i = 70°, 45°, and 30°.

The angular distributions have been normalized to their maximum intensities for ease of comparison; the gray dashed lines indicate the specular angle for each distribution. For E_i = 30.3 kJ mol^{-1}, the angular distributions have a maximum flux past the specular angle for θ_i = 30° and 45°. For θ_i = 70°, the maximum flux of the angular distribution occurs slightly below the specular angle. The distributions are relatively narrow, indicating that N_2 molecules scattered from a flat surface. However, the angular distributions are asymmetric about the maximum final angle, with a tail trailing off to lower θ_f. When E_i is increased to 67.9 kJ mol^{-1}, the angular distributions grow narrower, the angle at which the maximum flux occurs shifts to higher θ_f, and the distributions become more symmetric. Table 6.1 shows the angular widths of the peak (full width half maximum, FWHM), the θ_f at which the maximum flux occurs (θ_{max}), and the amount that these values changed (Relative Change) for angular distributions collected at both E_i. The values in Table 6.1 show that the angular distributions for θ_i = 70° are the most sensitive to E_i.

Table 6.1. Characteristics of the angular distributions displayed in Figure 6.3

	θ_i	E_i = 30.3 kJ mol^{-1}	E_i = 67.9 kJ mol^{-1}	Relative Change
θ_{max}	70°	67°	72°	0.15
	45°	55°	60°	0.09
	30°	39°	43°	0.10
	θ_i	E_i = 30.3 kJ mol^{-1}	E_i = 67.9 kJ mol^{-1}	Relative Change
FWHM	70°	21.6°	15.5°	0.28
	45°	34°	26.7°	0.21
	30°	30°	24°	0.20

6.4 Discussion

By comparing the experimental measurements of the angular distributions and recoil energies of the scattered N_2 with MD simulations conducted by the UIUC group, we hope to gain a better understanding of the potential energy surface and energy transfer mechanisms that govern the scattering dynamics of as N_2 molecule colliding with an HOPG surface. The energy transfer for this system may be complicated because the incident molecule is more massive than the individual C atoms composing the surface. Additionally, the low incidence energy combined with the relatively high surface temperature can have consequences on the partitioning between impulsive scattering and trapping desorption.

The angular dependencies of the ratio, $\langle E_f \rangle / \langle E_i \rangle$, shown in Figure 6.2, generally follow the shape of the PMC curve, indicating that the incident parallel momentum of the N_2 molecules is conserved during the collision. Moreover, this result indicates that a large fraction of the molecules suffer only a single collision with the surface before scattering. Considering that the parallel momentum of the molecules is basically conserved during the collision, it is the accommodation of the normal momentum that determines the scattering dynamics. If the molecules lose normal momentum during the collision, they will exit the surface toward the specular angle, yielding an energy ratio that less than one. If the molecules scatter toward the surface normal, the surface has transferred energy to the molecules, resulting in an energy ratio greater than one. As more normal momentum is transferred to the surface, the molecule's trajectory will move farther way from the surface normal. The angular distributions in Figure 6.2 indicate that a large portion of the incident

momentum normal to the surface is transferred to the surface while the momentum parallel to the surface is conserved, resulting in a maximum flux beyond the specular angle.

The angular dependencies of the energy ratios indicate that the molecules are scattering in the thermal regime.[6] During a collision, the N_2 molecule is sufficiently far from the surface when it reverses its direction that it does not experience any surface corrugation from the individual carbon atoms on the surface. Therefore, the N_2 molecule "feels" a smooth surface when it scatters. The scattered molecules retain a large fraction of their E_i, which indicates that each molecule is encountering a relatively large mass on the surface during the collision. Indeed, it has been shown that an N_2 molecule interacts with as many as 13 carbon atoms during a collision.[180]

The $\langle E_f \rangle / \langle E_i \rangle$ energy ratios are consistently higher than the PMC predictions for every θ_i and E_i. This has also been observed for Xe scattering from an HOPG surface, particularly at low incidence energies and θ_i.[176] The deviation from the PMC prediction was attributed to deformation of the flat carbon surface as the collision, a phenomenon known as dynamic corrugation. Considering the similarity of the results of this study with the previous work for Xe scattering from HOPG, a similar mechanism could be governing the energy transfer dynamics of N_2 scattering from HOPG. Clearly, the energy transfer mechanisms of this system are complicated and cannot be described by simple models.

As was mentioned previously, the high surface temperature employed in the experiments could have interesting consequences on the scattering dynamics because the definition of trapping becomes ambiguous at high surface temperatures. As surface temperature increases, the different time scales of accommodation for normal and parallel

momentum become increasingly important.[42] Incident momentum normal to the surface is accommodated significantly faster than momentum parallel to the surface. At high surface temperatures, the residence time of a colliding particle on a surface is short, and the particle can exit the surface before the parallel momentum is fully dissipated. This scattering mechanism has been referred to as "quasitrapping" and is characterized by lobular angular distributions that are asymmetric about the surface normal and final energies that increase with θ_f. This mechanism could be of particular importance for this system because (1) the HOPG surface is smooth and facilitates the conservation of parallel momentum and (2) the surface temperature is high.

The experimental results are consistent with a simple mechanism of molecules scattering impulsively from the surface after a single collision, whereas the simulations reveal that a large fraction of the molecules may undergo multiple bounces on the surface before scattering into the vacuum. As will be discussed later, such a multiple-bounce scattering pathway can be considered as quasitrapping. When a molecule collides many times with the surface, each collision, or bounce, presumably increases the energy transfer to the surface. Thus, N_2 molecules that scatter after multiple bounces would be expected to have a lower $\langle E_f \rangle$ and a broader angular distribution than molecules that scatter from the surface after a single collision. While the simulations suggest that multiple-bounce scattering events occur frequently in this system (Figure 8), evidence of this mechanism is difficult to identify in the individual experimental TOF distributions (Figure 1). Although the distributions at low θ_f are broad, there is no temporal distinction (or obvious inflection point) in the TOF distributions that would imply distinctly different single- and multiple-

collision scattering dynamics. Additionally, there is no resolved structure in the angular distributions (Figure 3) that would allow an experimental conclusion about distinct single- and multiple-collision scattering events. The initial rise in the $\langle E_f \rangle / \langle E_i \rangle$ ratios with θ_f, shown in Figure 2, could originate from molecules that undergo multiple collisions with the surface. However, the $\langle E_f \rangle / \langle E_i \rangle$ ratios for $\theta_i = 30°$ and 45° are relatively insensitive to $\langle E_i \rangle$ at large θ_f. By contrast, the $\langle E_f \rangle / \langle E_i \rangle$ ratios for $\theta_i = 70°$ increase with $\langle E_i \rangle$ at larger θ_f. The simulations show that the fraction of molecules that scatter after multiple collisions increases with θ_i and for $\theta_i = 70°$ and $E_i = 30.3$ kJ mol^{-1}, more than half of the N_2 molecules undergo more than one collision with the surface before scattering. As E_i increases, the fraction of molecules that experience multiple collisions with the surface (or quasitrap) decreases and more N_2 molecules scatter after a single collision. This prediction from the simulations would imply that $\langle E_f \rangle / \langle E_i \rangle$ should increase when E_i increases. Thus, existence of quasitrapping and its angular and energy dependencies could explain why the $\langle E_f \rangle / \langle E_i \rangle$ ratios for $\theta_i = 70°$ increase more than those for $\theta_i = 30°$ and 45° when E_i is increased. The lack of clear evidence of quasitrapping in the experimental TOF and angular distributions is likely just a consequence of the limited experimental resolution. This hypothesis has been corroborated by the simulations conducted by Majumander et. al. and our collaborators at UIUC.[43,178,181]

6.5 Conclusion

The interaction of N_2 with HOPG has been studied for $E_i = 30.3$ and 67.9 kJ mol^{-1} for $\theta_i = 70°$, 45°, and 30° using beam surface scattering techniques. The experimental results revealed that N_2 molecules scattered from an HOPG surface in lobular angular

distributions, the widths of which decreased when the E_i was increased. There was no evidence of molecules that scattered from the surface via the trapping desorption mechanism. However, for E_i = 30.3 kJ mol^{-1} the observed dynamical behavior of the scattered molecules suggested that some of the molecules were partially accommodated (or "quasitrapped") to the surface. The extent of quasi-trapping was greatest at the largest incidence angle studied (θ_i = 70°), where the energy oriented along the surface normal was lowest. The results presented in this chapter have been compared to molecular dynamics simulations in a conducted by our collaborators at the UIUC, which is the subject of the journal article titled "Non-Reactive Scattering of N_2 from Layered Graphene using Molecular Beam Experiments and Molecular Dynamics" which was submitted to the Journal of Physical Chemistry C and is currently under review.

Acknowledgments

This work was supported by the Jet Propulsion Laboratory (JPL), California Institute of Technology, under contract with the NASA.

CHAPTER SEVEN

SCATTERING DYNAMICS OF NITROMETHANE AND METHYL FORMATE ON HOPG

Contribution of Authors and Co-Authors

Manuscript in Chapter 7

Author: Vanessa J. Murray

Contributions: Performed molecular beam scattering experiments and conducted data analysis. Prepared both the figures and the experimental sections of manuscript for publication.

Co-Author: Chenbiao Xu

Contributions: Aided with the molecular beam scattering experiments.

Co-Author: Savio Poovathingal

Contributions: Performed ReaxFF calculation for the nitromethane and methyl formate potential energy surfaces.

Co-Author: Timothy K. Minton

Contributions: Provided crucial insight regarding the experimental procedure and the data analysis. Aided in the preparation of the manuscript and figures.

Manuscript Information Page

Vanessa J. Murray, Chenbiao Xu, Savio Poovatthingal, and Timothy K. Minton

Journal of Physical Chemistry C

Status of Manuscript:
__×__ Prepared for submission to a peer-reviewed journal
_____ Officially submitted to a peer-review journal
_____ Accepted by a peer-reviewed journal
_____ Published in a peer-reviewed journal

SCATTERING DYNAMICS OF NITROMETHANE AND METHYL FORMATE ON HOPG

Vanessa J. Murray, Chenbiao Xu, Savio Poovathingal, and Timothy K. Minton

Department of Chemistry and Biochemistry, Montana State University, 103 Chem/Biochem Bldg., Bozeman, MT, 59717

Abstract

The gas-surface scattering dynamics of nitromethane (NM) and methyl formate (MF) on a highly oriented pyrolytic graphite (HOPG) surface have been investigated to evaluate the efficacy of a gas concentrator. Molecular beams of NM and MF with incidence energies of 106.5 and 98.8 kJ mol^{-1}, respectively, were directed at the surface with incidence angles, θ_i, of 70°, 45°, and 30°. A rotatable mass spectrometer was used to collect angle- and velocity-resolved time-of-flight distributions for the molecules exiting the surface. The distributions for the parent ions and dominant fragments were identical, indicating that NM and MF fragmented in the electron bombardment ionizer and not while colliding with the surface. The scattering dynamics indicated that the parallel energy of the molecules was conserved during the surface collision. The total angular distributions and final energies for NM and MF were identical when θ_i = 70°. For θ_i = 45° and 30°, the MF angular distributions were shifted to slightly larger final angles, θ_f, than the NM distributions. The molecules scattered from the surface through impulsive scattering (IS) and quasitrapping (QT) pathways. The IS molecules scatter directly with relatively little energy transfer to the surface. The QT molecules exhibit more energy accommodation on

the surface, but they do not come into thermal equilibrium before they leave the surface. Both IS and QT molecules scatter in a lobular angular distribution peaked far from the surface normal and thus retain some memory of the incident beam conditions. This study shows that at incidence energies around 100 kJ mol^{-1}, the molecules will not dissociate when they collide with the surface of a gas concentrator constructed of HOPG. While the observed scattering dynamics suggest that such a concentrator could perform well for a variety of molecular species, accurate concentration factors are ultimately molecule-specific and are determined by the details of the molecule-surface interaction potential.

7.1 Introduction

A passive neutral gas concentrator has recently been proposed for the analysis of highly rarified atmospheres using mass spectrometry.[102] The device consists of a conical inlet with a large entrance and small exit. The exit leads to an accommodation chamber with a large opening that is connected to a mass spectrometer. Molecules that enter the concentrator scatter on its surface. The details of the scattering dynamics will determine the number of molecules that ultimately enter the accommodation chamber and pass into the mass spectrometer. Collisions that lead to specular, or super-specular, angular distributions will result in a higher number of molecules that enter the accommodation chamber, thus yielding a higher concentration factor. This concentrator is envisioned for use in flyby or probe missions and may travel through tenuous atmospheres with velocities of 1500 – 2500 m s^{-1}.

The initial design of the concentrator was guided by the results of beam-surface scattering experiments which identified highly oriented pyrolytic graphite (HOPG) as the

most suitable surface for a concentrator because atoms and molecules scattered from this surface with narrow and well defined angular distributions. Additionally, HOPG is fairly inert to chemical attack, so gas-surface reactions will not complicate the identification of atmospheric species by a mass spectrometer. The initial experiments focused on the scattering of atoms and diatomic molecules, namely O, O_2, and Ar, from an HOPG surface. However, for the concentrator to be a viable option for the study of tenuous atmospheres, which may contain complex organic molecules, the fate of polyatomic molecules that collide with an HOPG surface at high collision energies must be understood.

When a polyatomic molecule collides with a surface, its incidence translational energy can be transferred into internal modes of the scattered molecule as well as into the surface and the final translational energy of the molecule. The details of the energy transfer different molecules will affect the impulsive scattering dynamics, which may lead to a molecule-dependent concentration factor. Additionally, the trapping probability may be enhanced as the impinging molecules become more complex, because there are more internal degrees of freedom into which energy can be dissipated.[29,182] An increased trapping probability of large molecules would decrease the efficiency of the concentrator. The angle of impact on concentrator surfaces is also expected to influence the efficiency of the concentrator, as the amount of internal excitation has been found to depend on the incidence energy oriented normal to the surface.[28,31] Furthermore, it has been shown that the fragmentation pattern of the trapped molecules changes drastically as the surface temperature is increased, presumably because the internal modes of the molecule are accommodated to the temperature of the surface.[183] The internal excitation of the molecule

can also lead to shattering. The probability of shattering depends on the incidence energy of the molecule and increases as the θ_i deccreases.[31-32,184] Shattering of molecules could lead to incorrect identification of the atmospheric constituents.

The purpose of this study is to assess the sensitivity of the scattering dynamics to the molecular structure. If the scattering dynamics of molecules with a similar mass but a different structure are dissimilar, it could lead to a molecule-dependent concentration factor that would need to be accounted for when analyzing data obtained during flyby missions. To this end, we have studied the scattering dynamics of nitromethane (NM) and methyl formate (MF) on an HOPG surface held a temperature of 677 K using beam-surface scattering techniques. MF and NM were chosen as analogs for life-signature organic molecules in part because it is easy to entrain these species in a molecular beam. In addition, these two molecules have masses that differ by only one amu and may be readily prepared with similar incidence energies. However, MF has more degrees of freedom and thus may accommodate more energy into internal modes than NM. Additionally, differences in the molecule-surface interaction potentials arising from the nitro group in NM and ester group in MF could lead to different scattering dynamics. The results indicate that the scattering dynamics for NM and MF are different only when the incidence energy oriented normal to the surface is high.

7.2 Experimental Methods

The experiments were performed with the use of a crossed molecular beam apparatus reconfigured for beam-surface scattering, shown in Figure 7.1. The details of the experiment have been provided in a previous publication and only the important parameters

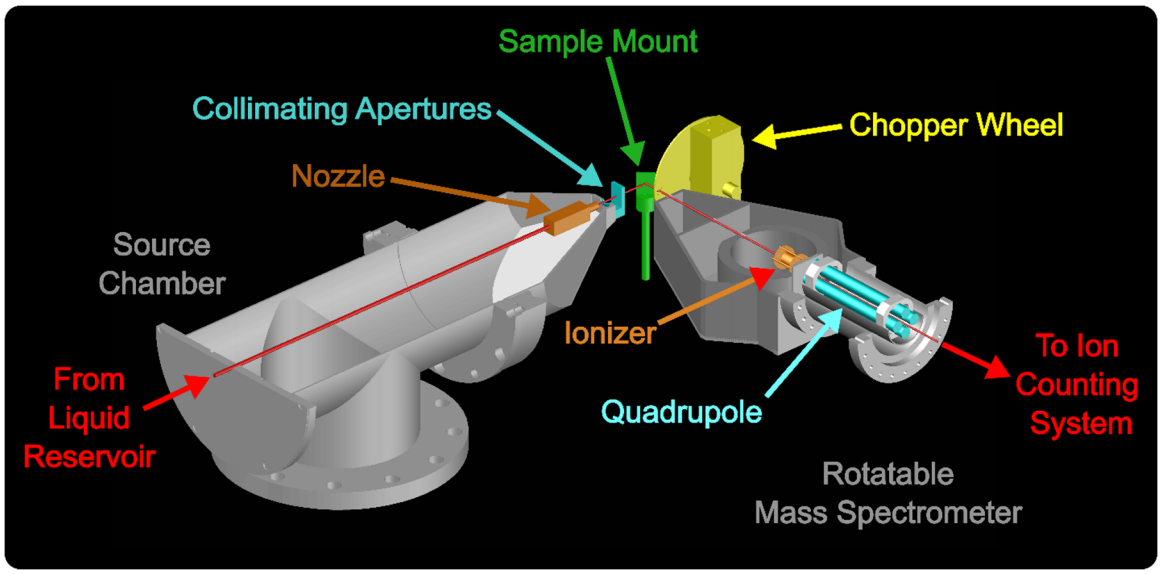


Figure 7.1. Schematic of the molecular beam machine utilized for the experiment.

will be described here.[181] The molecular beams of NM and MF were directed at a piece of ZYA quality HOPG that was mounted on a manipulator that could be rotated to change the incidence angle, θ_i. In order to ensure that the surface was clean for the duration of the experiment, the sample was held at a surface temperature, T_s, of 677 K.[144] A rotatable mass spectrometer that consisted of an electron bombardment ionizer,[150] quadrupole mass filter, and a Daly type ion counter operated in pulsed counting mode[151] was used to monitor the scattered products. The continuous beams and scattered products were modulated with a chopper wheel rotating at a frequency of 300 Hz that was mounted on the detector, 30.4 cm from the ionizer. Distributions of the scattered products were monitored for the parent masses of NM and MF, m / z = 61 and 60, respectively, and the dominant mass fragments formed in the electron bombardment ionizer (E_{electron} = 160 eV), m / z = 30 and 31 for NM and MF, respectively. No additional mass fragments were observed scattering from the surface, indicating the absence of surface reactions. The scattered molecules were detected

for a range of final angles, θ_f, for θ_i = 30°, 45°, and 70°. The number density of the scattered products as a function of arrival time, $N(t)$, at the ionizer was recorded by a multichannel scaler with a 1 μs dwell time. These distributions are commonly referred to as time-of-flight (TOF) distributions. The TOF distributions were corrected for the ion flight time through the mass filter and electronic offsets prior to data analysis.

The continuous, supersonic molecular beams were produced by bubbling 250 Torr of He (99.9999 %) through a reservoir containing either nitromethane, NM, (98.5 %, Sigma Aldrich) or methyl formate, MF, (98.5 %, Sigma Aldrich). The NM reservoir was held at -15 °C using an ethanol bath, resulting in a vapor pressure of 2.8 Torr. The MF reservoir was held at -56 °C using a n-octane slush bath, resulting in a vapor pressure of 6.2 Torr. The gas mixture was expanded through a 0.150 mm platinum pinhole that was fixed in a copper nozzle assembly which was held at a temperature of 200 °C to prevent the formation of dimers in the beam. The beam was initially collimated using a skimmer and slit. The velocity of the NM beam was 1865 m s^{-1}, corresponding to a translational energy of 106.5 kJ mol^{-1} with a ΔE/E of 0.3. The MF had a velocity of 1810 m s^{-1}, corresponding to a translational energy of 98.6 kJ mol^{-1} with a ΔE/E of 0.3.

7.3 Results and Analysis

7.3A Scattering Dynamics of the Total Flux

Figure 7.2 displays representative TOF distributions for the NM parent (m / z = 61, yellow symbols) and the dominant fragment (m / z = 30, black line) for θ_i = 45° and θ_f = 15°, 40°, and 60°. The salient features represented in the TOF distributions of Figure 7.2 are present in the TOF distributions measured for all three θ_i. The TOF distributions for

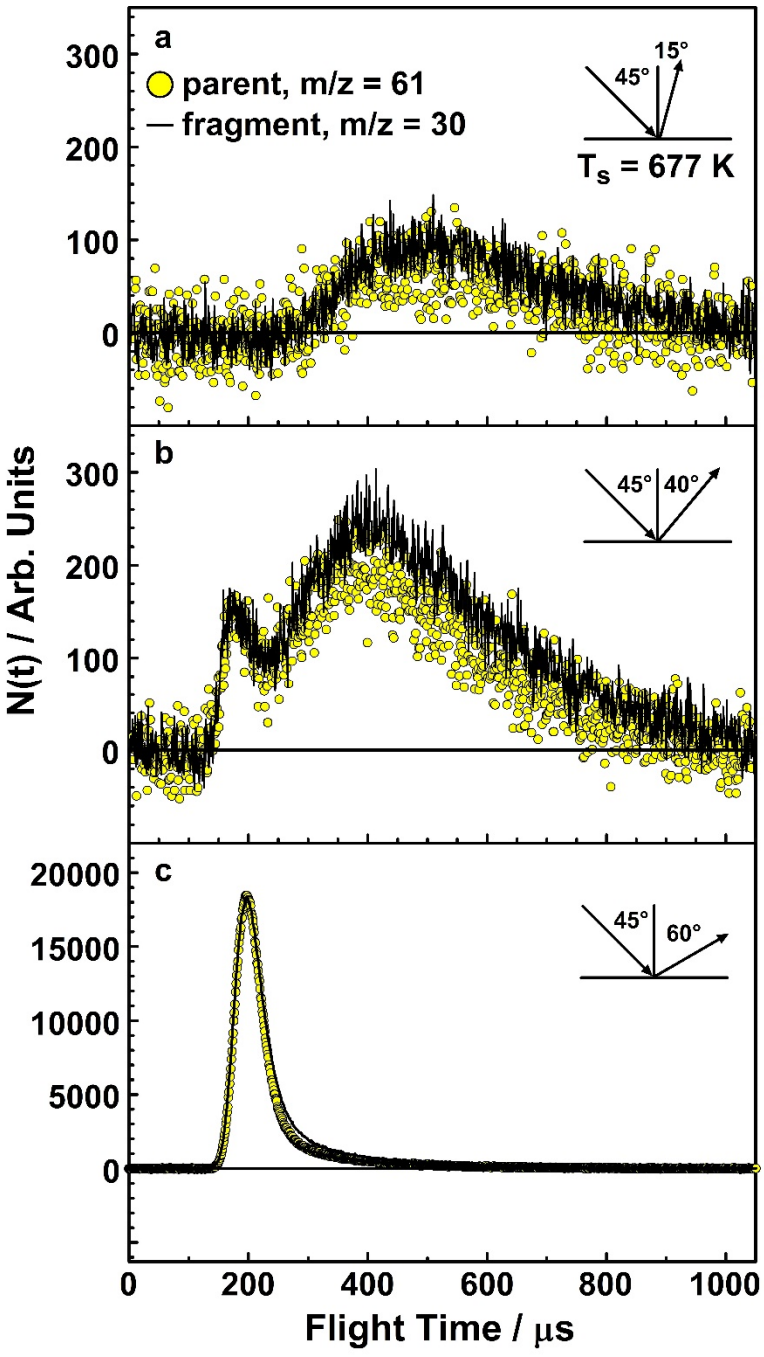


Figure 7.2. Representative TOF distributions for NM parent (m / z = 61, yellow symbols) and the dominant fragment (m / z = 30, black lines) observed for θ_i = 45° and θ_f = (a) 15°, (b) 40°, and (c) 60°.

MF closely resemble the NM distributions and have not been displayed. The signal for the fragment is higher than that of the parent molecule at long flight times. This is an artifact of the detection method utilized in the experiment, which originates from a count-rate-dependent detection sensitivity. The count rate for the fragment ion was twice as high as the count rate for the parent ion and has been normalized to the value for $m / z = 61$ for ease of comparison in Figure 7.2. However, the shape of the TOF distributions for the parent and the fragment are identical, and they exhibit the same angular distributions and energy transfer dynamics. This indicates that the molecules are not shattering when colliding with the surface, and thus the fragment must be formed by dissociative ionization in the electron bombardment ionizer. Because the signal-to-noise ratio for the parent is sufficiently high, we will focus our attention on the scattering dynamics detected for the parent molecules for NM and MF for the remainder of this chapter.

7.3B Scattering Dynamics of the Total Flux

For small values of θ_f, the TOFs exhibit a single component at long flight times which grows in intensity and shifts to shorter flight times as θ_f increases (Figure 7.2a). As will be discussed later, this is indicative of a trapping mechanism where the molecule does not fully accommodate to the surface and will be referred to as the quasitrapping (QT) component. At intermediate θ_f, the TOF distributions are bimodal (Figure 7.2b), and this QT component can be clearly distinguished. In addition to the QT component apparent at long flight times, a peak appears at short flight times. This component corresponds to impulsive scattering (IS), where the molecule suffers one, or maybe a few, collisions with the surface before scattering into the vacuum.[38,43,181] The IS component shifts to longer

flight times as θ_f is increased, indicating that the collisions are occurring in the thermal scattering regime and parallel momentum of the incident molecule is conserved during the collision.[6] The procedure for separating the two components will be presented in Section 7.3C.

The total flux, *I(molecule)*, of the scattered NM and MF has been calculated from the TOF distributions by integrating the quotient of the $N(t)$ of the scattered molecules and the flight time (t) from the HOPG surface to the electron bombardment ionizer:

$$I(molecule) = \int \frac{N(t)}{t} dt. \tag{7.1}$$

Angular distributions of *I(molecule)* as a function of θ_f for NM (blue symbols) and MF (red symbols) for θ_i = 70°, 45°, and 30° are shown in the left column Figure 7.3. These angular distributions have been normalized to their maximum flux so their shapes can be easily compared. The angular distributions for θ_i = 70° are nearly identical (Figure 7.3a) and have a maximum flux at a final angle of θ_f^{max} = 72.5°. For θ_i = 45°, the angular distributions for the two molecules deviate slightly, with θ_f^{max} = 70° for NM and θ_f^{max} = 72.5° for MF. The deviation become larger when θ_i = 30°. The maximum flux in the angular distribution occurs at θ_f^{max} = 60° and 55°.

The average translation energy of the scattered molecules was determined from translational energy distributions, $P(E_T)$, that were derived from the measured TOF distributions using the relationship $P(E_T) \propto t^2 N(t)$. The translational energy, E_T, is equal to,

$$\frac{1}{2} m \left(\frac{d}{t}\right)^2, \tag{7.2}$$

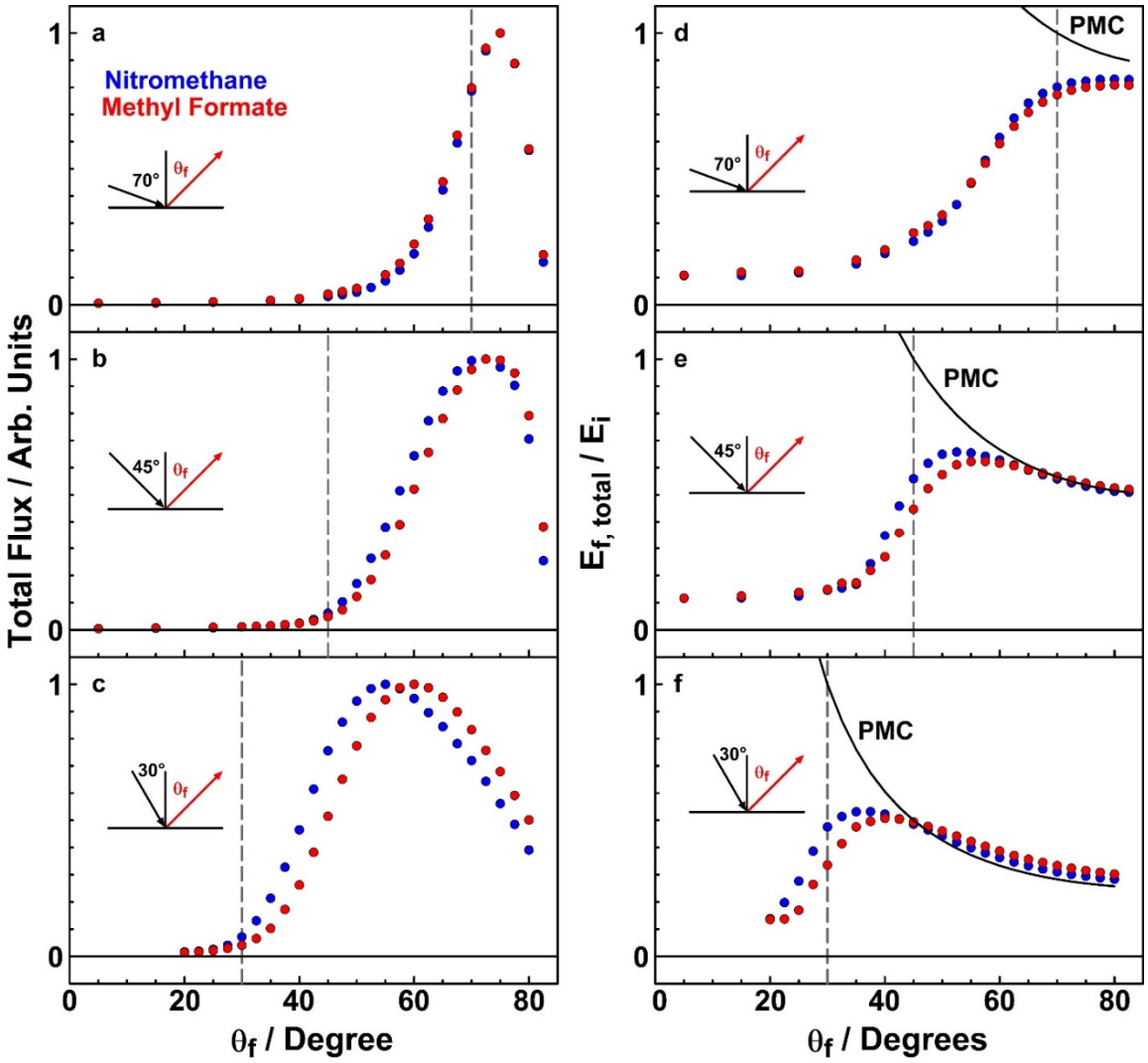


Figure 7.3. Angular distributions (a – c) and E_f / E_i (d – f) for the total scattered flux of NM (blue symbols) and MF (red symbols) for θ_i = 70°, 45°, and 30°. The gray, dashed lines indicate the specular angle ($\theta_i = \theta_f$). The black lines in panels d – f indicate the values of E_f / E_i obtained when the parallel momentum is conserved.

where d is the flight length from the chopper wheel to the ionizer and m is the mass of the scattered molecule. The ratio of final energy, E_f, to incidence energy, E_i, for the scattered molecules is shown in Figure 7.3d – f. For $\theta_i = 70°$, E_f / E_i for NM and MF are nearly identical. For $\theta_i = 45°$, the E_f / E_i values deviate at low θ_f because the angular distribution for NM is shifted to lower θ_f in comparison to MF; however, at grazing θ_f, the energy ratios are indistinguishable. For $\theta_i = 30°$, the energy ratios also deviate at low θ_f. However, at high θ_f, the E_f / E_i values for MF are higher than those obtained for NM, indicating that NM loses more energy when colliding with the surface.

Evidence of the IS and QT scattering mechanisms can be clearly identified in the E_f / E_i trends for all three θ_i. At low θ_f, the energy ratio increases with θ_f. This trend has been reported for the QT mechanism,[42] but is also characteristic of molecules scattering in the structural regime.[6,172] As θ_f increases, the flux of IS molecules increases and the E_f / E_i begins to decrease with θ_f. For $\theta_i = 30°$ and 45°, the energy ratios at grazing θ_f follow the prediction of the hard cube model,[156] which assumes that parallel momentum is conserved during the collision. For strict parallel momentum conservation, $E_f / E_i = \sin^2(\theta_f) / \sin^2(\theta_i)$. At $\theta_i = 70°$, the E_f / E_i ratios deviate substantially from the hard cube model. It has been shown that multiple-bounce scattering and trapping are most probable at grazing θ_i, where (for a given incidence energy) the normal momentum and thus the normal energy, $E_n = E_i \cos^2(\theta_f)$, are the lowest.[43,181] Multiple-bounce collisions would increase the energy transfer from the molecule to the surface and yield E_f / E_i ratios that fall below the hard cube predictions.

When the molecule collides with the surface, some of the E_i can be dissipated into internal modes.[28,30] The fragmentation patterns of molecules have been shown to increase as the internal energy of the molecule increases,[185] which will alter the relative intensity of fragments produced in the electron bombardment ionizer.[186-187] While our detection method is only sensitive to the translational energy of the scattered molecules, by comparing the fragmentation pattern of the molecules in the beam to that of the molecules scattering from the surface, we can broadly assess whether the NM and MF become internally excited while colliding with the surface. The ratio of the total flux of the parent molecule and the dominant fragment, *I(parent)* / *I(fragment)*, is shown in Figure 7.4 for NM (red bars) and MF (blue bars). The *I(parent)* / *I(fragment)* for the incident molecular beam is 0.63 and 0.41 for NM and MF, respectively. For the scattered molecules, the *I(parent)* / *I(fragment*) is ~11% and ~13% lower for NM and MF, respectively, when compared to the beam. This modest change in the fragmentation patter indicates that the internal modes are not significantly excited when the NM and MF collide with the surface. It has been shown that the internal excitation of the molecule depends on the E_n of the incident molecule.[28] This dependence suggests that the vibrational excitation should be highest, and *I(parent)* / *I(fragment)* the lowest, when $\theta_i = 30°$, which is not evident in Figure 7.4. The internal excitation of the scattered molecules is only weakly dependent on θ_i for this system. Even for $\theta_i = 30°$ and $E_i \approx 100$ kJ mol^{-1}, the molecules are not substantially excited.

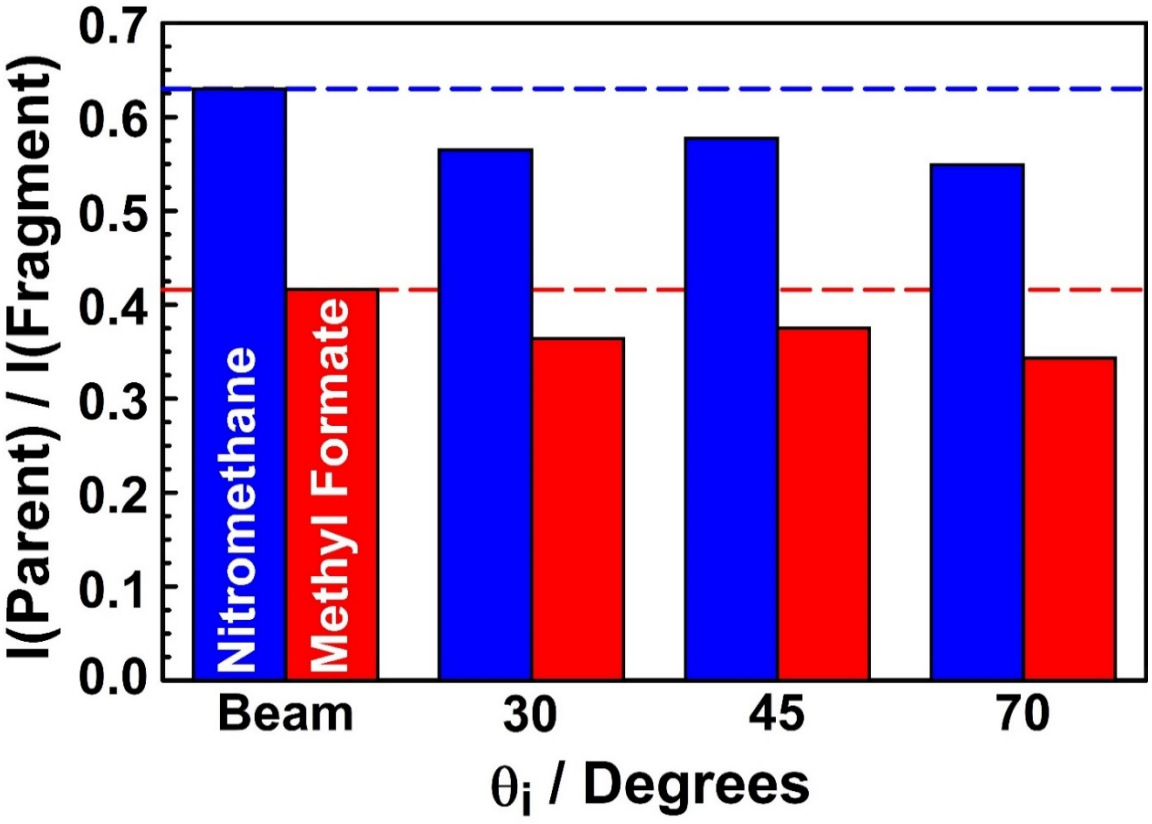


Figure 7.4. Ratio of the total flux of the parent molecule, *I*(parent), and the flux of the dominant fragment, *I*(fragment), for the molecules in the incident beam and those scattering from the surface with θ_i = 30°, 45°, and 70°, for NM (blue) and MF (red). The dashed blue and red lines indicate the value of *I(parent)/I(fragment)* measured for the NM and MF, respectively, in the incident beam.

7.3C Separation of IS and QT Components

As was mentioned previously, there are two distinct scattering mechanisms observable in the TOF distributions for the scattered NM and MF. We can separate the components in the TOF distributions by fitting the IS peak with a shifted flux-weighted Maxwell-Boltzmann (MB) distribution[39]

$$P(v_{IS}) = v^3 \exp\left(\frac{(v-v_{pk})^2}{a}\right), \tag{7.3}$$

where v is the velocity (m s^{-1}), v_{pk} is the most probable velocity of the scattered molecules (m s^{-1}), and a determines the width of the distribution (m^2 s^{-2}). Using the relationship $P(v_{IS}) \propto t\,N(t)$ and $v \propto 1/t$, the eq 7.3 can be expressed as a function of flight time, t (μs):

$$N(t_{IS}) \propto \frac{1}{t^4} \exp\left(\frac{\left(\frac{1}{t} - \frac{1}{t_{pk}}\right)^2}{a}\right) \tag{7.4}$$

where t_{pk} is the most probable flight time of the scattered molecules (μs) and a determines the width of the distribution (μs^{-2}). A sample fit of the TOF distributions is shown in Figure 7.5. The QT molecules cannot be described by a MB distribution characterized by T_s. As demonstrated in Figures 7.2 and 7.3, the slow component shifts to shorter flight times as θ_f is increased. It is unclear what functional form best describes this component and how the distribution will change with θ_f. Thus, we refrain from fitting the slow component in the TOF distributions. The QT component (green line) is obtained by subtracting the IS fit (blue line) from the total $N(t)$ (yellow symbols).

Figure 7.6 displays the angular distributions for the IS (right) and QT (left) components for NM and MF. The angular distributions have been normalized to their maximum fluxes to allow for easy comparison of their shapes. The angular distributions of the IS component look very similar to the total angular distribution shown in Figure 7.2. IS is the dominant scattering mechanism for scattering, as is shown in Figure 7.7, which displays the fractions of the molecules that recoil via the IS and QT mechanisms. It is apparent that as the θ_i is increased, the IS fraction decreases while the QT fraction increases. This is consistent with several studies that show that the trapping fraction increases as θ_i increases because only

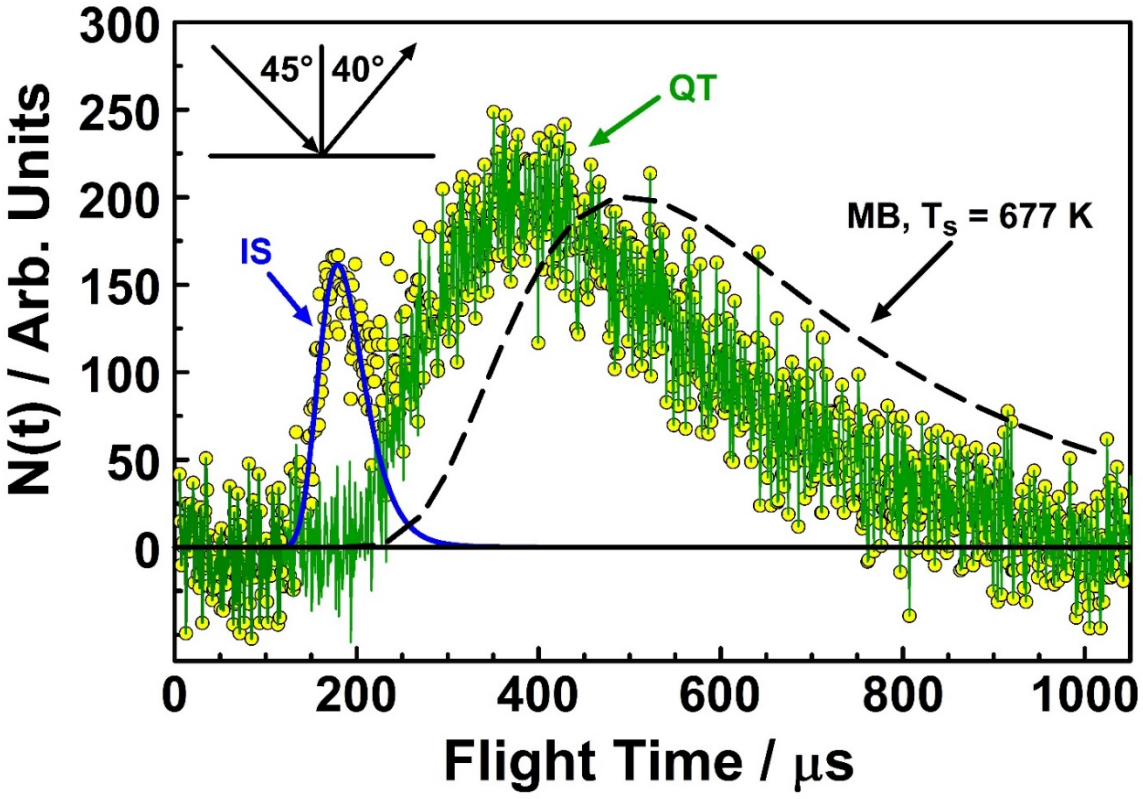


Figure 7.5. Example of the procedure used to fit time-of-flight distributions, illustrated with a representative time-of-flight distribution for NM collected with $\theta_i = 45°$ and $\theta_f = 40°$. The blue curve is a shifted MB distribution that is used to fit the IS component. The green curve is obtained by subtracting this fit from the experimental data (yellow symbols) and is designated as QT. The black, dashed line represents a MB distribution for $T_s = 677$ K and is shown for comparison.

E_n must be accommodated for the molecule to trap on the surface.[39,188-190] Figure 7.8 presents *I(parent) / I(fragment)* for the IS and QT components. The ratio for the IS component is higher than that for the QT component, suggesting that the molecules that have scattered via the QT mechanism have a warmer internal energy distribution.

The angular distribution for the IS MF have a higher θ_f^{max} than the NM distributions for $\theta_i = 45°$ and 30°. By contrast, there is very little difference between the MF and NM QT angular distributions (Figure 7.7). Interestingly, the QT angular distributions are also lobular, though broader than the IS distributions, and also have a maximum flux beyond

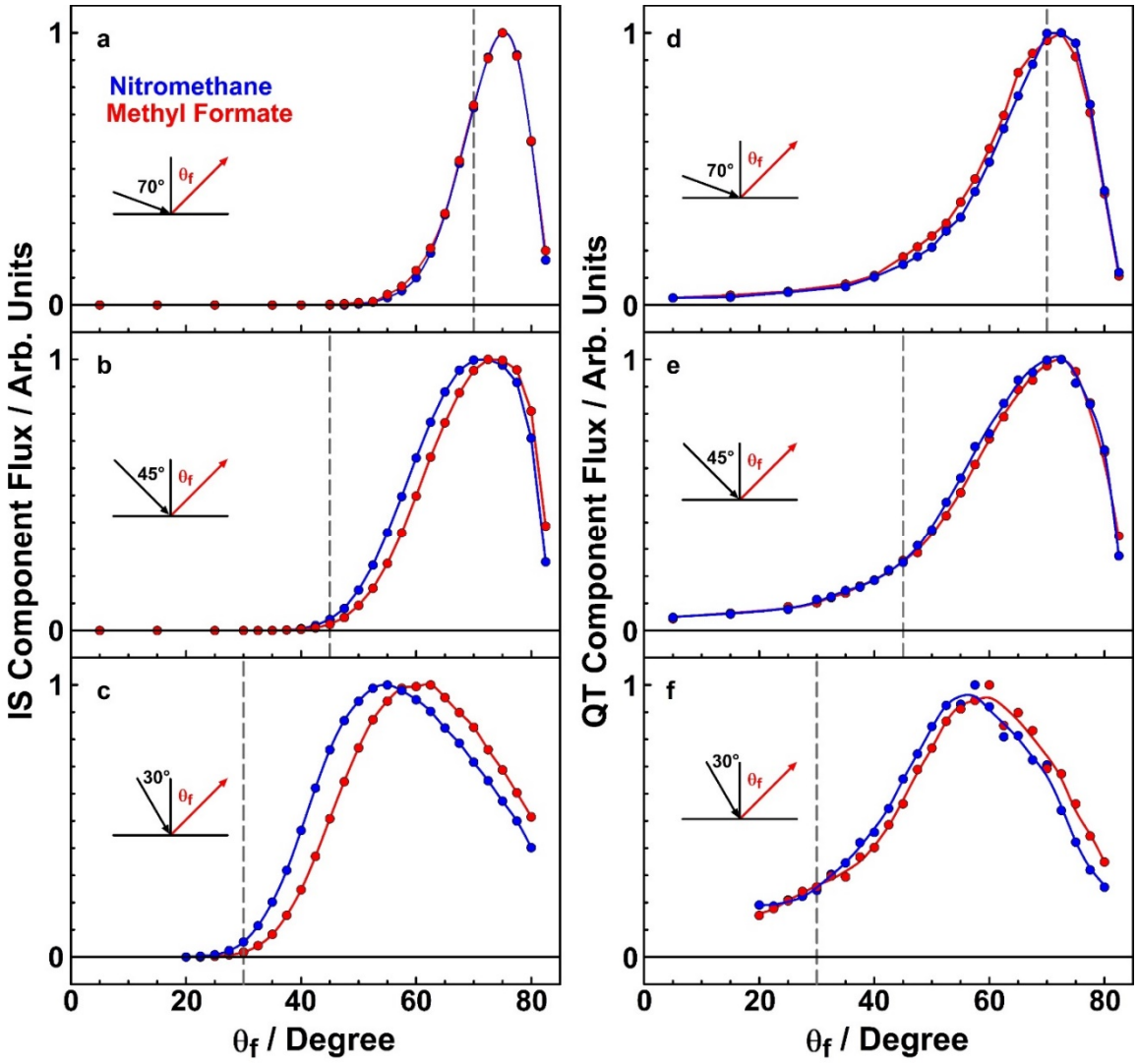


Figure 7.6. Angular distributions for the IS (a – c) and QT (d – f) components of NM (blue symbols) and MF (red symbols) for $\theta_i = 70°$, 45°, and 30°. The gray, dashed lines indicate the specular angle ($\theta_i = \theta_f$). The experimental data points are connected with lines to help guide the eye.

the specular angle. This is consistent with MD simulations of N_2 scattering from HOPG, which demonstrated that the QT molecules have lobular angular distributions and the molecules conserve a fraction of their incidence parallel momentum during the collision.[43]

The E_f / E_i ratios for the IS (circles) and QT (squares) components for NM (blue symbols) and MF (red symbols) are shown in Figure 7.9. The E_f / E_i ratios for the molecules scattering through the IS channel qualitatively follow the trend predicted by the hard cube model. However, for θ_i = 70°, the energy ratios for the IS molecules fall below the hard cube model predictions and it appears that MF loses more energy when colliding with the surface than does NM. When the θ_i is lowered, the energy ratios for both NM and MF

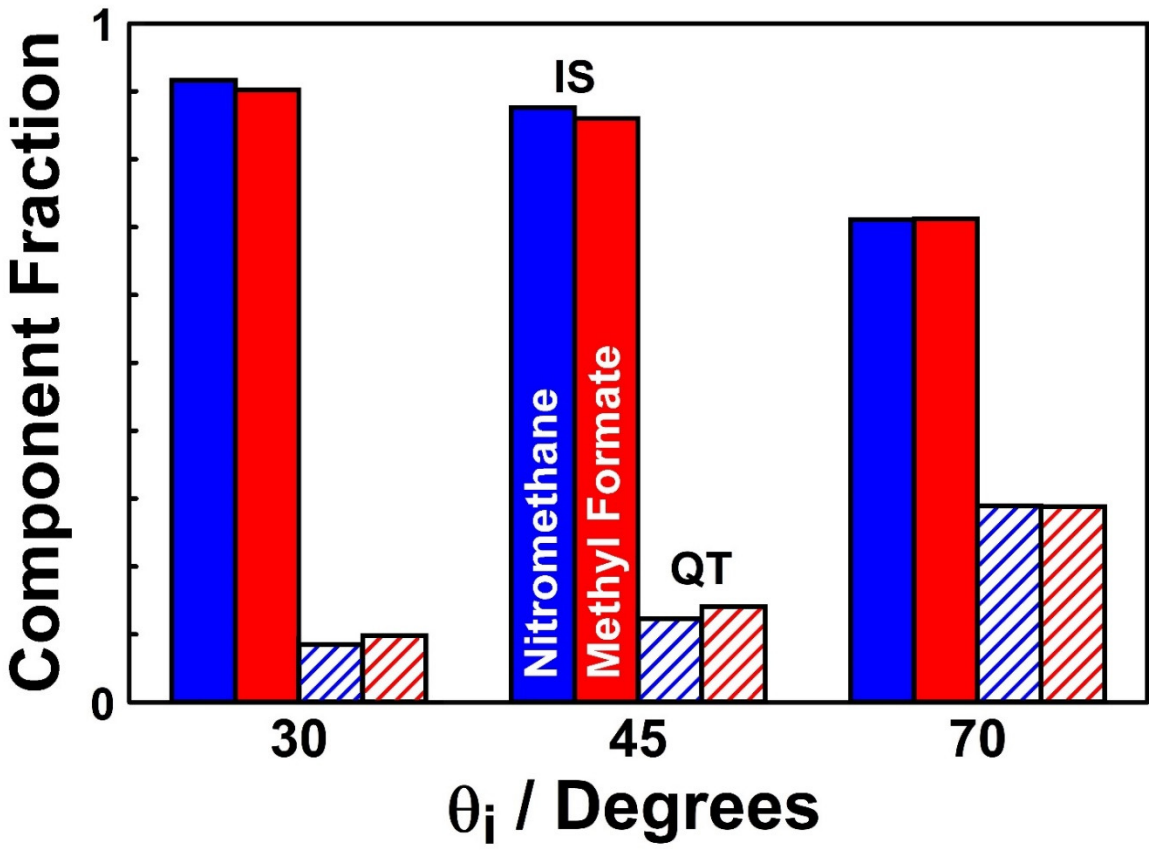


Figure 7.7. Fraction of NM (blue) and MF (red) molecules scattering via the IS (solid bars) and QT (hashed bars) pathways.

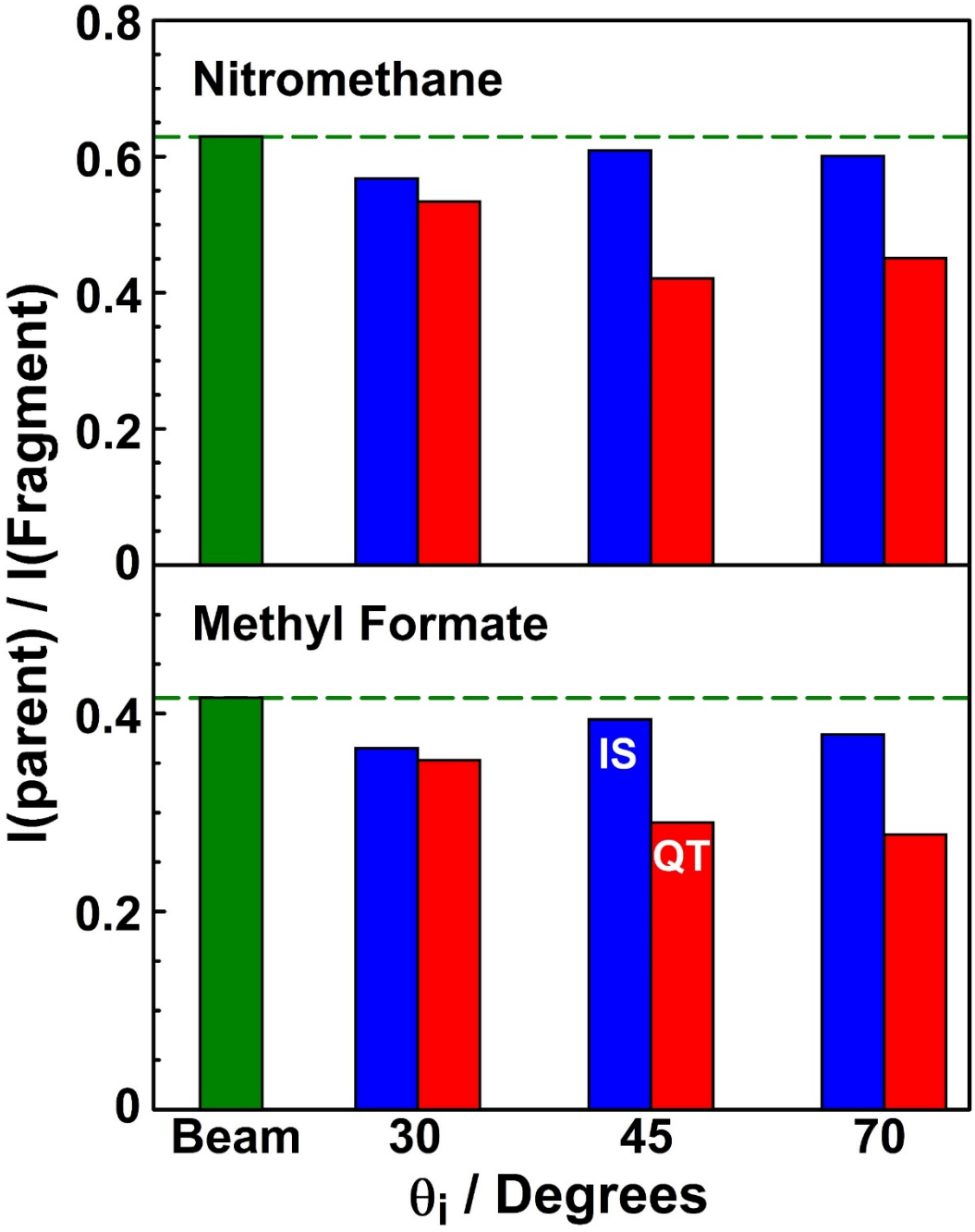


Figure 7.8. Ratio of the total flux of the parent molecule, *I*(parent), to the flux of the dominant fragment, *I*(fragment), for the molecules in the incident beam (green bar) and the molecules that scatter through IS (blue bars) and QT (red bars), when θ_i = 30°, 45°, and 70°, for NM (top panel) and MF (bottom panel). The green lines indicate the values of *I(parent)/I(fragment)* measured for the incident beams of NM and MF.

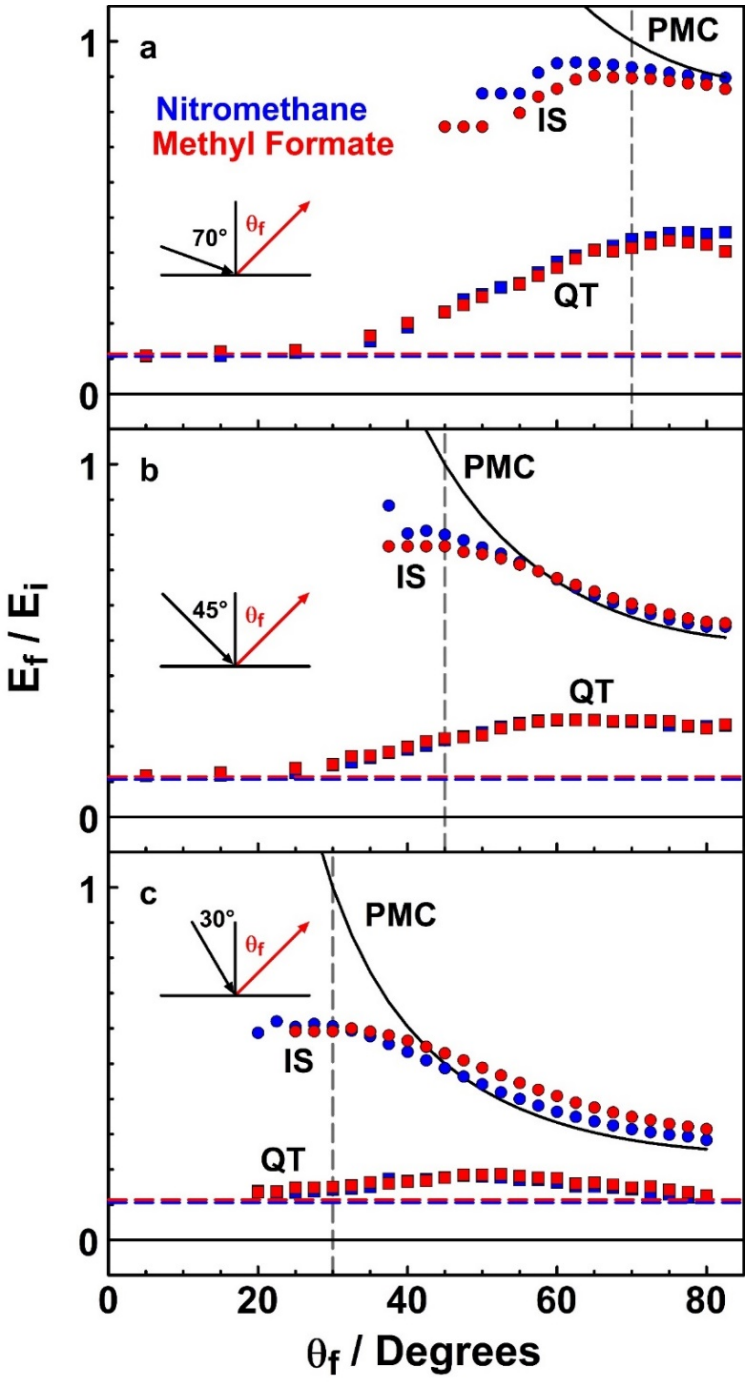


Figure 7.9. Angular dependence of E_f / E_i for the IS (circles) and QT (squares) components of NM (blue symbols) and MF (red symbols) scattering from the surface with θ_i = 70°, 45°, and 30°. The dashed blue and red lines represent the energy of the surface ($2RT_s$) as a fraction of the E_i for NM (blue) and MF (red).

exceed the value predicted by the hard cube model. The deviation is higher for θ_i = 30° than for θ_i = 45°. This behavior has been observed for Xe scattering from HOPG.[176] This deviation could indicate that E_i is high enough that the scattering dynamics are transitioning from the thermal scattering regime to the structural scattering regime.[6] Alternatively, the molecules could be gaining energy from the trampoline motions that are excited when the molecules strike the surface.[176] For both θ_i = 30° and 45°, the E_f / E_i ratios for MF are greater than for NM, indicating that NM loses more energy when colliding with the surface. By contrast, the E_f / E_i ratios for the molecules scattering via the QT mechanism are nearly identical and increase as θ_i increases, consistent with the assumption that the parallel momentum of the molecules, which increases as θ_i increases, is retained during the molecule-surface interaction.

7.4 Discussion

The energy transfer observed for NM and MF presented in Figures 7.3 and 7.9 follow the prediction of the hard cube model, indicating that the parallel momentum of the scattered molecules is conserved during the surface impact.[156] Thus, the fate of the collision is determined by the accommodation of energy oriented normal to the surface. Extensive work by Hase has shown that shattering is most probable as θ_i approaches the surface normal, because more E_n is available to transfer to internal modes of the molecule.[31] If too much energy is partitioned into internal modes, the molecule can dissociate, which would result in different scattering dynamics for the parent molecule and the dominant mass fragment. As can be seen in Figure 7.2, the scattering dynamics of the two constituents are identical, which indicates that the fragment is formed in the electron bombardment ionizer,

not from a collision with the surface. This is not necessarily a surprising result. The C – NO_2 bond of NM, which is the weakest bond in the two molecules studied, has a bond energy of 254.4 kJ mol^{-1}.[191] Thus, even if $\theta_i = 0°$ and all of the E_i was partitioned into the C – NO_2 bond (a scenario that is physically unreasonable because intramolecular vibrational redistribution is fast in molecules), there would not be enough energy available to lead to bond dissociation for the E_i utilized in this study.

The ion fragmentation pattern in the mass spectrometer is dependent on the internal excitation of the parent molecule. Thus, we can qualitatively assess the degree of internal excitation by analyzing the *I(parent)* / *I(fragment*). Kay has shown that vibrational excitation of NH_3 is dependent on the E_n of the molecule.[28] Therefore, for a given E_i, the amount of internal excitation would decrease as the θ_i is increased. From Figure 7.4, *I(parent)* / *I(fragment*) is lower for the scattered molecules than for the molecular beam. It is likely that some excitation of internal modes occurred during the collision. However, we can infer that the internal energy distribution of the scattered molecules does not increases substantially because *I(parent)* / *I(fragment*) changes by only by ~10%. This result agrees with previous studies which found the internal excitation of molecules colliding with the HOPG to be inefficient.[186-187] This would suppress the shattering probability even if the E_i was sufficiently high to lead to bond dissociation.

It is peculiar that the *I(parent)* / *I(fragment*) is lower for $\theta_i = 70°$, which is contrary to the results from Kay and Hase that demonstrate that internal excitation is greatest for normal θ_i.[28,184] MD simulations of N_2 scattering from HOPG reported that the probability of QT, where the molecule presumably experiences multiple collisions with the surface,

increases with θ_i. Considering that the molecule transfers energy each time it collides with the surface, E_f / E_i would be expected to fall below that of the hard cube model predictions for $\theta_i = 70°$ (Figures 7.3 and 7.9). Additionally, multiple collisions could lead to accommodation of the internal modes to the temperature of the surface, which would lead to the slightly higher cracking probability shown for $\theta_i = 70°$ in Figures 7.4 and 7.8.

The angular distributions and energy transfer show that the scattering dynamics depend on E_n. From Figures 7.3 and 7.9, the MF angular distributions are peaked at a larger θ_f than NM for $\theta_i = 45°$ and 30°. A possible explanation for this result is that MF transfers more E_n when colliding with the surface, possibly to internal modes. The energy transfer to internal modes could be higher for MF because it has more degrees of freedom into which E_i can be dissipated. However, the E_f / E_i for $\theta_i = 45°$ and 30° indicates that MF retains more energy than NM, which suggests that NM has a stronger interaction with the HOPG than MF. Hence, the NM suffers a harder collision with the surface, transfers more energy, and scatters toward lower θ_f (Figures 7.3 and 7.7). This hypothesis is supported by molecular dynamics simulations that calculated the potential energy surface between NM or MF with HOPG (Figure 7.10). The molecular dynamics simulations were performed using Large-scale Atomic/Molecular Massively Parallel Simulator (LAMMPS)[192] with the ReaxxFF forcefield for inter-atomic force computations.[193-194] A single layer of graphene was used as the model surface. To minimize any edge-effects, the size of the surface was 45 × 45 Å. The simulated box is periodic in all three directions with a supercell dimension of 30 Å in the z direction on either side of the graphene surface. The graphene surface is located at $z = 0$ Å. The surface was minimized with box relaxation to allow the surface to

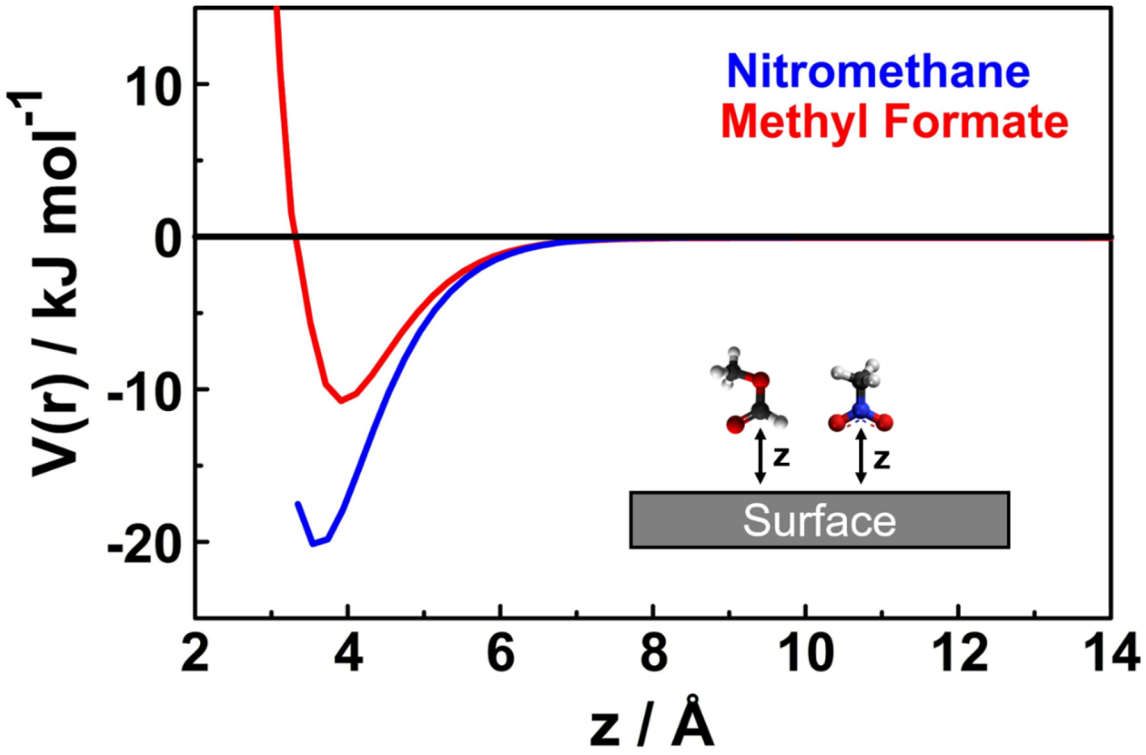


Figure 7.10. Potential energy curves for NM (blue) and MF (red) with single layer graphene. For NM, z is the distance from the N atom of the nitro group to the surface. For MF, *z* is the distance from the C atom of the ester group and the surface. (The calculation was performed by Dr. Savio Poovathingal.)

expand. The two gas molecules were then placed with the center of mass at 16 Å and a further minimization was performed for the entire system. The gas molecules were then moved towards the surface in steps of 0.1 Å; an energy minimization is performed after every step. The potential energy was monitored as the molecule was moved toward the surface which provides the estimate for the well-depth. The alignment of the gas molecules was fixed such that the nitro-group of nitromethane and the ester group of methyl formate were oriented toward the surface. The calculations show that the NM potential well is twice as deep as the MF potential (Figure 7.10), which leads NM to transfer more energy when colliding with the surface. However, for $\theta_i = 70°$, the E_f / E_i for MF is lower than for NM, which seems to be in contradiction with the well depths shown in Figure 7.10. Recently,

MD simulations have shown that for grazing θ_i, the shallower potential well did not affect the angular distribution, but resulted in more energy transfer to the surface,[181] which could explain why E_f / E_i of the IS MF for $\theta_i = 70°$ is lower than that of NM while the angular distributions are identical.

A striking feature of the data presented in this study is the presence of the QT peak in the TOF distributions. This component is the cause of the initial rise in the E_f / E_i plots for all three θ_i shown in Figure 7.2. The energy transfer observed in Figure 7.2 is reminiscent of the data obtained for O_2 scattering from Ag(111).[172] It was determined that the angular dependence of E_f / E_i for the O_2 + Ag(111) system was indicative of a mixture of scattering from the structural and thermal regimes. The potential energy surface of the O_2 + Ag(111) system has physisorption well separated from a chemisorption well by a barrier. Molecules that scatter from the repulsive wall of the physisorption well, which is located far from the surface, experience a smooth surface and display energy transfer dynamics that can be described by the hard cube model. When the molecule scatters from the repulsive wall of the chemisorption well, which is located closer to the surface, the molecule experiences a corrugated interaction potential which leads to scattering dynamics indicative of the structural regime. The probability of surmounting the barrier separating the chemisorption and physisorption well and scattering from the repulsive wall of the chemisorption well increases as the E_n of the incident molecule increases. Therefore, for a given E_i, the probability of structural scattering increases as θ_i approaches the surface normal. This is contrary to the trend observed in the current study, where the probability of QT scattering increases with θ_i. Furthermore, while the interaction of NM with HOPG has not been

studied extensively, TPD experiments have shown that MF can only physisorb on the surface and has a desorption energy of 35 kJ mol^{-1}.[195] Additionally, the reaxFF potentials shown in Figure 7.10 contain only a single well. Therefore, the molecule + HOPG potential is not expected to have a dual potential well that would lead to the type of energy transfer observed for the O_2 + Ag(111) system. While the scattering dynamics for the QT component are reminiscent of structural regime scattering because the E_f / E_i ratios increase with θ_f (Figure 7.9) and the angular distributions are lobular (Figure 7.6 d – f), the dependence of the QT fraction on θ_i (Figure 7.7) indicates that the QT component originates from a trapping mechanism where the E_i of the molecules fails to fully accommodate to the surface.

The dynamical behavior of the QT molecules arises because the surface is smooth, which allows for the retention of momentum oriented parallel to the surface. It has been shown for the scattering of Ar from Pt(111) that the normal momentum is rapidly equilibrated to the surface during impact (t_{eq} < 1 ps).[42] Conversely, the parallel momentum is dissipated on a much longer time scale (t_{eq} > 100 ps). Accordingly, when the surface temperature is high, the residence time of the atom on the surface is too short and it desorbs before its parallel momentum is fully dissipated. As a result, the scattered atoms retain memory of their incidence conditions. This mechanism was referred to as "quasitrapping" and was shown to yield an angular distribution focused away from the surface normal and a final energy that is greater than the energy of the surface ($2RT_s$).[42-43] Using a desorption energy of 35 kJ mol^{-1} and a prefactor on the order 10^{14} s^{-1},[195] the residence time of MF on the surface is 10 fs when T_s = 677 K. The NM and MF retain a large portion of their

incidence parallel momentum even though their normal momentum has been accommodated, and the QT molecules scatter from the surface with a lobular angular distribution with E_f / E_i > $2RT_s$. The effect of the incomplete parallel momentum accommodation can be seen in Figure 7.9. The E_f / E_i ratio of the QT component increases with θ_i and is highest when θ_i = 70°, where the parallel momentum is the highest, and the ratio decreases as θ_i is reduced to 45° and 30°. The QT scattering mechanism was observed, though not discussed in detailed, for the scattering of a molecular beam of dimethyl methylphosphonate (DMMP) from multilayer graphene.[183] At low temperature (250 K), the molecules fully accommodated to the surface energy and scattered with a cosine distribution and E_f equal to the energy of the surface ($2RT_s$). When the surface temperature was increased to 600 K, the peak of the angular distributions for the trapped molecules shifted from the surface normal and had $E_f > 2RT_s$.

For the scattering of DMMP from multilayer graphene, *I(parent)* / *I(fragment*) for the trapped molecules exiting the surface at $\theta_f \approx 0°$ approached zero as the surface temperature was increased to 600 K. This was not caused by the thermal decomposition of DMMP on the surface, which did not occur until the surface temperature greater than 900 K, but rather the fragmentation pattern of the trapped molecules changed as their internal energy distribution warmed. Thus, it would be expected that *I(parent)* / *I(fragment*) for the QT molecules, which partially equilibrate to the surface temperature, would be lower than for the molecules that scatter by the IS channel. This is demonstrated in Figure 7.9, which shows that *I(parent)* / *I(fragment*) for the IS molecules is higher than for the QT molecules, because the QT molecules are at least partially accommodated to the surface (T_s = 677 K),

whose temperature is hotter than the temperature of the incident beam (T_n = 473 K). In Figure 7.9, *I(parent)* / *I(fragment*) for the QT molecules is lower for θ_i = 70° and 45° than for θ_i = 30°. This suggests that the internal energy distributions of the QT molecules at the more grazing θ_i are warmer, likely because they have suffered more collisions with the surface, as discussed previously. However, these molecules are still not fully accommodated with the surface and the internal energy distributions of the scattered molecules are not expected to reflect desorption after thermal equilibrium with the surface. Thus, *I(parent)* / *I(fragment*) is higher than would be expected if the molecules had fully equilibrated with the surface.

7.5 Conclusions

Using beam-surface scattering techniques, we have investigated the scattering dynamics of NM and MF with E_i = 106.5 and 98.8 kJ mol^{-1}, respectively, on a HOPG surface held at T_s = 677 K. For θ_i = 70°, 45, and 30 the scattering dynamics indicated that the molecules did not shatter when colliding with the surface. For grazing incidence angles (θ_i = 70°), the total angular distributions of NM and MF were nearly identical. For θ_i = 45° and 30°, the scattering dynamics deviate slightly from each other. The angular distributions for MF were peaked farther from the surface normal than those for NM, presumably because NM has a stronger interaction potential with HOPG.

While most of the molecules scattered from the surface via an impulsive scattering mechanism, a portion of the molecules trapped at the surface. However, because the surface is smooth and the surface temperature is high, the parallel momentum of the trapped molecules was not fully accommodated. The molecules were thus quasitrapped (QT) and

retained some memory of their incident conditions. Consequently, the QT molecules scattered with a lobular angular distribution and E_f scaled with the momentum oriented parallel to the surface.

These results provide important information that can guide the design of a gas-concentrator designed for the analysis of tenuous atmospheres. The observed scattering dynamics indicate that if θ_i is sufficiently grazing, the scattering dynamics of different molecules with similar masses will be nearly indistinguishable even if the potential energy surface is different. Therefore, the concentration factor will be independent of the molecule that scatters from the surface. This facilitates the determination of the relative intensities of the different constituents in tenuous atmospheres. Furthermore, even if the molecules trap on the surface, they will scatter with a lobular angular distribution, which will improve the efficiency of the proposed gas concentrator.

Acknowledgements

This work was supported by the Jet Propulsion Laboratory (JPL), California Institute of Technology, under contract with the NASA. The authors would like to thank Dr. Min Qian for her help with preliminary data collection.

CHAPTER EIGHT

CONCLUDING REMARKS

The experiments presented in this dissertation have studied the gas-surface interactions that occur when atomic and molecular species collide with sp^2 hybridized carbon surfaces. Using molecular beam-surface scattering techniques, a wealth of new insight into the fundamental dynamics of reactive and non-reactive processes that occur at elevated surface temperatures and incidence energies have been obtained. These studies shed light on the reactive and non-reactive processes that can occur in extreme environments, where the gas-surface collision energy is high and/or the surface temperature is high.

The research described herein was conducted with a crossed molecular beams machine reconfigured for beam-surface scattering that could be outfitted with two different molecular beam sources. A laser-detonation source was used to generate a pulsed beam of high translational energy O(^3P) and O_2 ($^3\Sigma_g^-$) or Ar. A continuous, supersonic source was used to generate low translational energy molecular beams of N_2, methyl formate, and nitromethane seeded in He. Angular- and velocity-resolved distributions of products that scattered from the surface were collected with a rotatable quadrupole mass spectrometer. By analyzing the measured angular and translational energy distributions, we have been able to determine the general mechanisms for both reactive and non-reactive scattering processes occurring on model carbon surfaces.

The interaction of O atoms with vitreous carbon and HOPG with surface temperatures of 600 – 2300 K was presented in Chapters 3 and 4, respectively. The vitreous carbon study demonstrated that the oxidation of the surface is governed by the adsorption and desorption of O atoms. At low surface temperature, O atoms were observed to scatter mainly via the impulsive scattering (IS) channel. At high temperature, the dominant scattering mechanism for O atoms switched to trapping desorption (TD). The inelastic scattering dynamics of Ar from vitreous carbon were insensitive to the surface temperature, demonstrating that the change in O-atom scattering dynamics was not due to a change in surface structure that drives more O atoms into thermal equilibrium with the surface. Instead, at high surface temperature, there is enough energy available from the surface to cleave the C-O surface bonds and the O atoms can desorb before they undergo reactions to form CO and CO_2. The O-atom desorption leads to a decrease in O-atom surface coverage

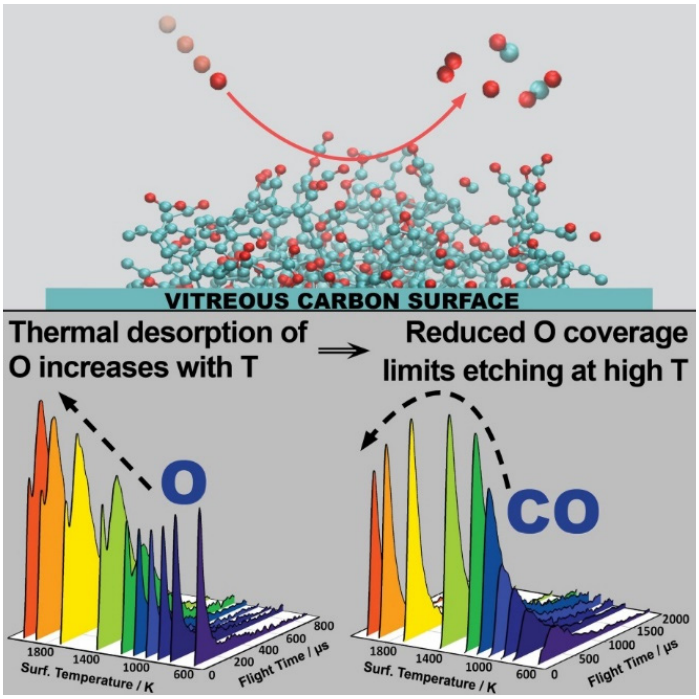


Figure 8.1. Summary of the results for the oxidation of vitreous carbon by $O(^3P)$

which is in the origin of the non-Arrhenius temperature dependence observed for the reactive products (Figure 8.1).

The oxidation of HOPG by O atoms, presented in Chapter 4, leads to a better understanding of both the reactive and non-reactive scattering dynamics observed in the vitreous carbon system (Figure 8.2). It was suggested that at low surface temperature, O atoms adsorb to and possibly intercalate under the top most layer of graphene, where they concomitantly undergo and catalyze Langmuir-Hinshelwood (LH) reactions. CO and CO_2 were produced mainly by LH reactions, which occur in thermal equilibrium with the

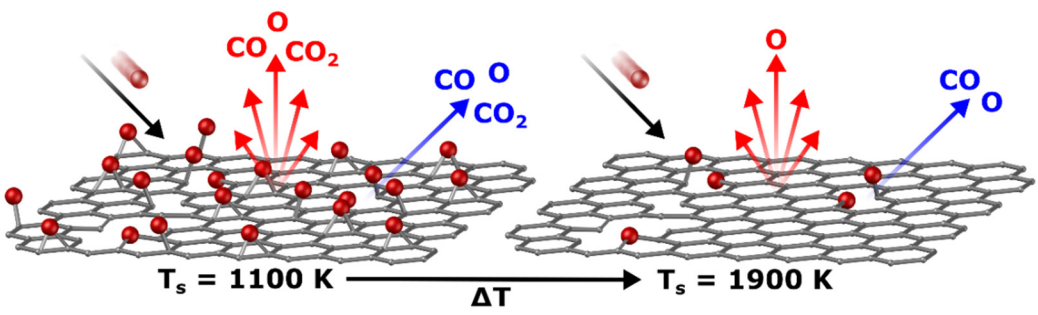


Figure 8.2. Summary of the results for the oxidation of HOPG by O(^3P)

surface. A small portion of the CO and CO_2 were produced by abstraction reactions that proceeded through either an Eley-Rideal (ER) or hot atom (HA) mechanism. The results from this study were used to determine the desorption barrier for the CO exiting the surface, which increased from 121 ± 5 kJ mol^{-1} at a surface temperature of 1100 K to 155 ± 7 kJ mol^{-1} at 1300 K. The reaction barriers increased as a result of the decreasing O-atom surface coverage at high temperature, which also suppressed the LH reactions forming CO and CO_2. The experiments presented in Chapters 3 and 4 reveal how the surface temperature governs the complex reactive and non-reactive processes occurring on sp^2 hybridized

carbon surfaces. The oxidation of vitreous carbon and HOPG seem to proceed by similar mechanisms, suggesting that the reaction dynamics are determined by the bonding environment rather than the surface structure. Thus, these results may be relevant to the oxidation sp^2 bonded allotropes of carbon.

In another study presented, the results of beam-surface scattering experiments were used to optimize the design of a gas concentrator proposed for the characterization of tenuous atmospheres by mass spectrometry. This study demonstrated that the surface roughness alone does not determine the scattering dynamics (Figure 8.3). The potential energy between the incoming atoms and molecules and the surface can drastically affect the translational energy and angular distributions of the scattered products. While both the SiO_2 and HOPG surfaces had similar RMS surface roughnesses, the O + HOPG potential energy surface is considerably smoother than the O + SiO_2 potential. As a result, the angular distributions for O atoms scattering from HOPG were the narrowest out of the three surfaces investigated. Thus, a concentrator constructed from HOPG yielded was predicted

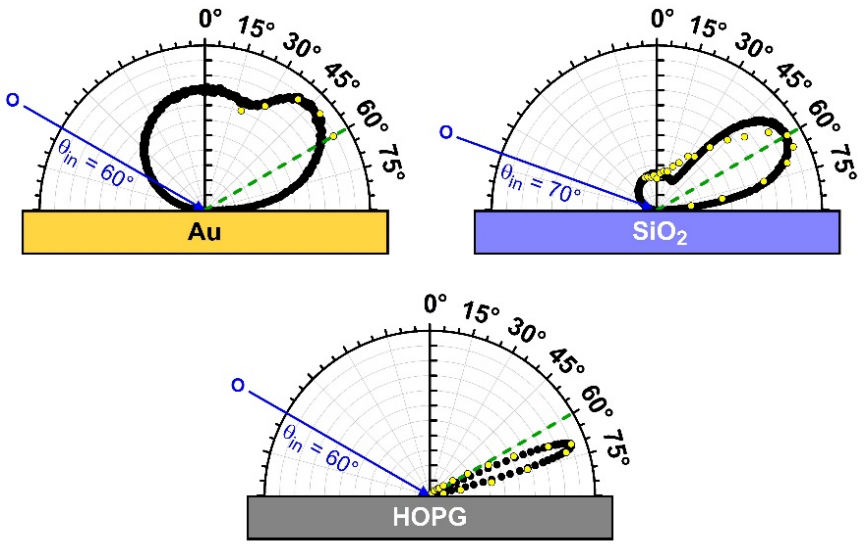


Figure 8.3. Summary of the results presented in Chapter 6.

to yield a concentration factor that is an order of magnitude larger than those for Au or SiO_2.

The nonreactive scattering dynamics of N_2, nitromethane, and methyl formate scattering from an HOPG surface were also studied (Figure 8.4). These experiments demonstrate that the trapping dynamics become ambiguous a high surface temperature as a result of the incomplete accommodation of momentum oriented parallel to the surface. Thus, the trapped molecules retain memory of their incidence conditions and scatter from the surface with a lobular angular distribution. As complete thermal accommodation often precedes chemisorption and subsequent surface reaction, incomplete accommodation will suppress the reactivity of the incoming molecules with the HOPG surface. The scattering dynamics presented in Chapter 7 indicate that nitromethane and methyl formate do not shatter when colliding with the HOPG surface. These molecules scatter with a well-defined lobular angular distribution that is directed passed the specular angle, further supporting the proposed use of an HOPG concentrator as a general method to concentrate molecules of all sizes. The concentration factor will be molecule independent as long as the incidence angle with the concentrator surface is grazing. These experiments can inform the design

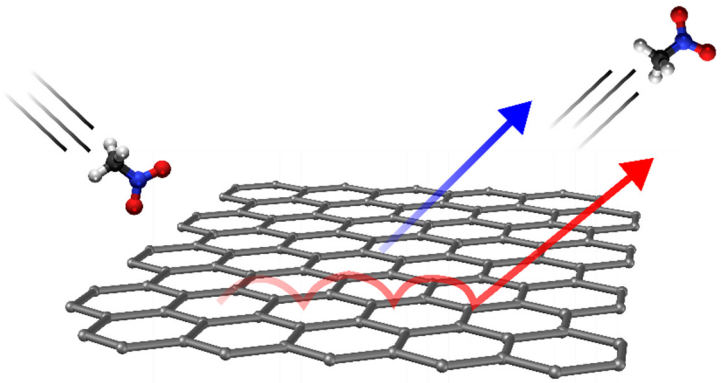


Figure 8.4. Summary of the results presented in Chapters 6 and 7.

and simulations of gas concentrators that have been proposed for the identification of constituents in tenuous atmospheres.

The work presented in this dissertation demonstrates the depth of understanding of reactive and non-reactive gas-surface interactions obtainable from molecular beam scattering experiments. These studies not only have improved the fundamental understanding of the chemistry occurring on sp^2 hybridized carbon surfaces, but have been used by our collaborators to investigate engineering applications.[12,23-24] The results presented in Chapters 3 and 4 have been used to construct a computational fluid dynamics model used to calculate the mass flux from and heat flux to carbon surfaces during hypersonic flight through the Earth's atmosphere. The gas-surface scattering dynamics presented in Chapters 5 – 7 have informed the design of a gas concentration apparatus that has been proposed to facilitate the study of rarefied atmospheres.

APPENDIX

DERIVATION OF THE SOFT SPHERE MODEL

Note: The derivation of the Soft Sphere Model presented in this section was published in Faraday Discussions.

Alexander, W. A.; Zhang, J.; Murray, V. J.; Nathanson, G. M.; Minton, T. K. Kinematics and Dynamics of Atomic-Beam Scattering on Liquid and Self-Assembled Monolayer Surfaces. **2012,** *157*, 355-374.

Appendix: Derivation of the Soft Sphere Model

The kinematic model is based on a treatment of hard-sphere scattering (often referred to as the "Baule formula"), in which a gas-phase, hard-sphere projectile, with an incidence translational energy of E_i, undergoes an elastic collision with a hard sphere on the surface in the c.m. frame.[44] This model can be extended by assuming that the collision may be inelastic in the center-of-mass (c.m.) frame, which assumes that the c.m. collision energy is partitioned into total translational energy, E_T, and total internal excitation, E_{int}, of the two recoiling spheres. Because the spheres may acquire internal excitation, the extended model describes "soft-sphere" scattering. Figure A.1 provides a diagram of the model, where m_1 and m_2 are the masses of the incident and surface spheres, respectively, and v_0 is the incidence velocity of m_1. The surface mass is assumed to be at rest initially in the laboratory frame. After the collision, m_1 scatters away from the surface with velocity, v_1, and m_2 recoils into the surface with velocity, v_2. χ is the angle through which the incident sphere is deflected from its initial direction, and θ_2 is the angle between the recoil direction of m_2 and the initial direction

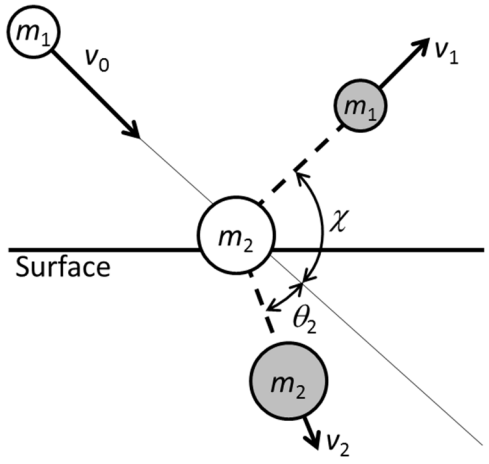


Figure A.1. Sphere-sphere scattering model of gas-surface collisions.

of m_1. It is assumed that the collision will impart instantaneous translational and internal energy to m_2, which will determine the final translational and internal (if applicable) energy of m_1, but soon after the collision the energy associated with m_2 will be dissipated throughout the surface modes.

The derivation of an expression for fractional energy transfer comes from considerations of conservation of momentum and energy. Conservation of momentum in the initial direction of m_1 requires

$$m_1 v_0 = m_1 v_1 \cos\chi + m_2 v_2 \cos\theta_2 , \tag{A.1}$$

and conservation of momentum perpendicular to the initial direction of m_1 requires

$$m_1 v_1 \sin\chi = m_2 v_2 \sin\theta_2 . \tag{A.2}$$

Assuming the initial energy of the surface is negligible compared to the translational energy of m_1, conservation of energy requires

$$\frac{1}{2} m_1 v_0^2 = \frac{1}{2} m_1 v_1^2 + \frac{1}{2} m_2 v_2^2 + E_{\text{int}} . \tag{A.3}$$

Using eqs A.2 and A.3, an expression for the ratio of the squares of the final and initial velocities of m_1 may be obtained,

$$\frac{v_1^2}{v_0^2} = \frac{1 - \frac{E_{\text{int}}}{E_{\text{i}}}}{1 + \mu \frac{\sin^2\chi}{\sin^2\theta_2}} , \tag{A.4}$$

where μ is the mass ratio, m_1/m_2. Eqs A.1 and A.2 allow the derivation of an expression for the ratio, $\sin^2\chi/\sin^2\theta_2$,

$$\frac{\sin^2\chi}{\sin^2\theta_2} = 1 + \frac{v_0^2}{v_1^2} - 2\frac{v_0}{v_1}\cos\chi , \tag{A.5}$$

which may be used in eq A.4 to find the ratio of the squares of the final and initial velocities of m_1. This ratio is related to the fractional energy transfer through

$$\frac{\Delta E}{E_\mathrm{i}} = \frac{E_\mathrm{i} - E_{\mathrm{f},1}}{E_\mathrm{i}} = 1 - \frac{v_1^2}{v_0^2}\ , \tag{A.6}$$

where $E_{\mathrm{f},1}$ is the final translational energy of m_1. Eqs A.4, A.5, and A.6 may manipulated into the form,

$$\frac{\Delta E}{E_\mathrm{i}} = \frac{2\mu}{(\mu+1)^2}\left[1 + \mu\sin^2\chi + \frac{E_\mathrm{int}}{E_\mathrm{i}}\left(\frac{\mu+1}{2\mu}\right) - \cos\chi\sqrt{1 - \mu^2\sin^2\chi - \frac{E_\mathrm{int}}{E_\mathrm{i}}(\mu+1)}\right]. \tag{A.7}$$

The terms involving E_int become zero in the limit of hard-sphere scattering. This function has two parameters, μ and E_int, which may be found by optimizing a fit of this functional form to a plot of $\Delta E/E_\mathrm{i}$ vs. χ.

This kinematic model may be viewed in velocity space with the use of a Newton diagram,[45] which relates the laboratory and c.m. reference frames. Figure A.2 shows an example of a Newton diagram for direct inelastic scattering of O atoms from squalane, with an average incidence energy of 504 kJ mol^{-1} and an incidence angle of 60º. Assuming that the thermal velocity of the tethered surface mass (m_2 in the derivation above) is negligible compared with the velocity of the incident atom (m_1 in the derivation above), the c.m. moves in the laboratory frame in the same direction as the incident atom. The surface mass is fixed in the laboratory frame, so the relative velocity, v_rel, between the incident atom and the surface is the velocity of the incident atom, which, in a beam-surface scattering experiment, is the measured beam velocity. There is no *a priori* knowledge of the velocity of the c.m., because the effective surface

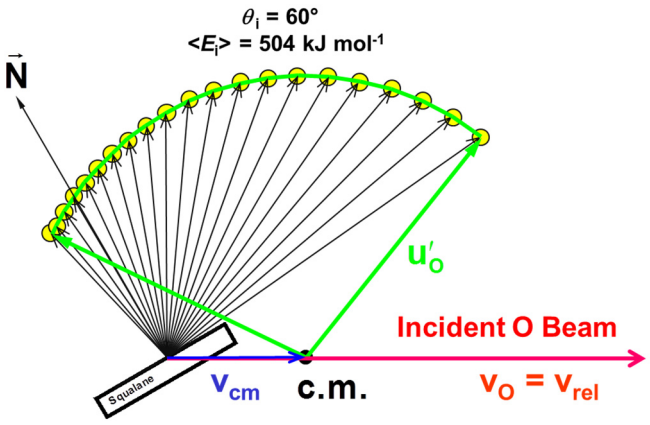


Figure A.2. Newton diagram for impulsive scattering of hyperthermal O atoms on a squalane surface, with $\langle E_i \rangle$ = 504 kJ mol^{-1} and θ_i = 60°.

mass is unknown. The kinematic model predicts, however, that vectors corresponding to the final velocities of the scattered atoms should lie on a point on the relative velocity vector and that this point is the tip of the velocity vector of the c.m. in the laboratory reference frame, v_{cm}.

The effective surface mass ($m_s = m_2$) follows directly from v_{cm} because the mass of the incident atom (m_1) and its velocity (v_0) are known:

$$m_2 = m_1 \left(\frac{v_0}{v_{cm}} - 1 \right). \tag{A.8}$$

Indeed, the data show that the average final velocities of scattered O atoms at various in-plane scattering angles lie on a circle whose center is on the relative velocity vector. After the effective surface mass has been determined, the collision energy in the c.m. frame can be calculated as follows:

$$E_{coll,cm} = \frac{1}{2} \mu_r v_{rel}^2 , \tag{A.9}$$

where μ_r is the reduced mass of the incident atom and the surface collision partner.

The total energy that goes into translation of the scattered product and the recoiling surface collision partner in the c.m. frame is

$$E_{\mathrm{T}} = \frac{1}{2}\mu_r' v_{\mathrm{rel}}'^2 = \frac{1}{2}(m_1' + m_2')\frac{m_1}{m_2}u_1'^2. \tag{A.10}$$

where the primes refer to post-collision quantities, and u_1' is the velocity of the scattered product in the c.m. frame. Note that this model applies to both inelastic and reactive scattering. In the latter case, the product masses would be different from the incident and effective surface masses. Implicit in the kinematic analysis is the assumption that the average final velocity, u_1', and the total translational energy release, E_{T}, are independent of the scattering angle. This assumption is supported by the near perfect fit of a circular arc to the average final velocities over a c.m. angular range of 97º, as seen in Figure A.2. The difference between the c.m. collision energy and the total energy in translation yields the product internal excitation, $E_{\mathrm{int}} = E_{\mathrm{coll,cm}} - E_{\mathrm{T}}$. Thus, when cast in the form of a Newton diagram, the kinematic model allows for the straightforward determination of the effective surface mass, the c.m. collision energy, the c.m. translational energy release, and the total internal excitation of the products. The mass ratio, μ, and the internal energy, E_{int}, from an analysis of the final velocities of scattered products should match these same quantities when they are derived from a fit of a plot of $\Delta E/E_{\mathrm{i}}$ vs. χ. In our experiments, we do find agreement between the mass ratios and internal energies determined by the two different methods.

REFERENCES CITED

[1] Hurst, J. E.; Wharton, L.; Janda, K. C.; Auerbach, D. J. Direct Inelastic Scattering Ar from Pt(111). *J. Chem. Phys.* **1983,** *78*, 1559-1581.

[2] Hurst, J. E.; Becker, C. A.; Cowin, J. P.; Janda, K. C.; Wharton, L.; Auerbach, D. J. Observation of Direct Inelastic Scattering in the Presence of Trapping-Desorption Scattering: Xe on Pt(111). *Phys. Rev. Lett.* **1979,** *43*, 1175-1177.

[3] Kleyn, A. W. Molecular Beams and Chemical Dynamics at Surfaces. *Chem. Soc. Rev.* **2003,** *32*, 87-95.

[4] Weinberg, W. H.; Merrill, R. P. Scattering of Helium, Neon, Argon, Krypton, Xenon, and Deuterium from a Tungsten(110) Surface Characterized by LEED. *J. Chem. Phys.* **1972,** *56*, 2881-2891.

[5] Butler, D. A.; Berenbak, B.; Stolte, S.; Kleyn, A. W. Elastic Scattering in a Reactive Environment: NO on Ru(0001)-(1 x 1)H. *Phys. Rev. Lett.* **1997,** *78*, 4653-4656.

[6] Rettner, C. T.; Barker, J. A.; Bethune, D. S. Angular and Velocity Distributions Characteristic of the Transition Between the Thermal and Structure Regimes of Gas-Surface Scattering. *Phys. Rev. Lett.* **1991,** *67*, 2183-2186.

[7] Devi, G. R.; Rao, K. R. Carbon-Carbon Composites: An Overview. *Def. Sci. J.* **1993,** *43*, 369-383.

[8] Larciprete, R.; Fabris, S.; Sun, T.; Lacovig, P.; Baraldi, A.; Lizzit, S. Dual Path Mechanism in the Thermal Reduction of Graphene Oxide. *J. Am. Chem. Soc.* **2011,** *133*, 17315-17321.

[9] Morón, V.; Martin-Gondre, L.; Gamallo, P.; Sayós, R. Quasiclassical Trajectory Dynamics Study of Atomic Oxygen Collisions on an O-Preadsorbed Graphite (0001) Surface with a New Analytical Potential Energy Surface. *J. Phys. Chem. C* **2012,** *116*, 13092-13103.

[10] Pétuya, R.; Larrégaray, P.; Crespos, C.; Aurel, P.; Busnengo, H. F.; Martínez, A. E. Scattering of Atomic Hydrogen Off a H-Covered W(110) Surface: Hot-Atom versus Eley–Rideal Abstraction Dynamics. *J. Chem. Phys. C* **2015,** *119*, 3171-3179.

[11] Zaharia, T.; Kleyn, A. W.; Gleeson, M. A. Eley-Rideal Reactions with N Atoms at Ru(0001): Formation of NO and N_2. *Phys. Rev. Lett.* **2014,** *113*, 053201.

[12] Poovathingal, S.; Schwartzentruber, T. E.; Murray, V. J.; Minton, T. K. Molecular Simulation of Carbon Ablation Using Beam Experiments and Resolved Microstructure. *AIAA J.* **2016,** *54*, 999-1010.

[13] Paredes, J. I.; Martínez-Alonso, A.; Tascón, J. M. D. Multiscale Imaging and Tip-Scratch Studies Reveal Insight into the Plasma Oxidation of Graphite. *Langmuir* **2007,** *23*, 8932-8943.

[14] Drits, V. A.; Tchoubar, C.; Klimanek, P. X-Ray Diffraction by Disordered Lamellar Structures: Theory and Applications to Microdivided Silicates and Carbons. *Cryst. Res. Technol.* **1991,** *26*, 956.

[15] Jenkins, G. M.; Kawamura, K., *Polymeric Carbon-Carbon Fibre, Glass and Char* Cambridge University Press: Cambridge ; New York, 1976.

[16] Arnold, G. S.; Peplinski, D. R. Reaction of Atomic Oxygen with Vitreous Carbon - Laboratory and STS-5 Data Comparisons. *AIAA J.* **1985,** *23*, 976-977.

[17] Park, C. Effects of Atomic Oxygen on Graphite Ablation. *AIAA J.* **1976,** *14*, 1640-1642.

[18] Larciprete, R.; Lacovig, P.; Gardonio, S.; Baraldi, A.; Lizzit, S. Atomic Oxygen on Graphite: Chemical Characterization and Thermal Reduction. *J. Phys. Chem. C* **2012,** *116*, 9900-9908.

[19] Sun, T.; Fabris, S.; Baroni, S. Surface Precursors and Reaction Mechanisms for the Thermal Reduction of Graphene Basal Surfaces Oxidized by Atomic Oxygen. *J. Phys. Chem. C* **2011,** *115*, 4730-4737.

[20] Paci, J. T.; Upadhyaya, H. P.; Zhang, J.; Schatz, G. C.; Minton, T. K. Theoretical and Experimental Studies of the Reactions between Hyperthermal O(^{3}P) and Graphite: Graphene-Based Direct Dynamics and Beam-Surface Scattering Approaches. *J. Phys. Chem. A* **2009,** *113*, 4677-4685.

[21] Rosner, D. E.; Allendor.Hd Comparative Studies of Attack of Pyrolytic and Isotropic Graphite by Atomic and Molecular Oxygen. *AIAA J.* **1968,** *6*, 650-654.

[22] Olander, D. R.; Schwarz, J. A.; Siekhaus, W.; Jones, R. Reactions of Modulated Molecular-Beams with Pyrolytic-Graphite: 1. Oxidation of Basal Plane. *J. Chem. Phys.* **1972,** *57*, 408-420.

[23] Borner, A.; Swaminathan Gopalan, K.; Stephani, K. A.; Murray, V.; Poovathingal, S. J.; Minton, T.; Panerai, F.; Mansour, N. N., DSMC Analysis of Molecular Beam Experiments on Light-Weight Carbon Preform Ablators. In *47th AIAA Thermophysics Conference*, American Institute of Aeronautics and Astronautics: 2017.

[24] Poovathingal, S.; Schwartzentruber, T. E.; Murray, V. J.; Minton, T. K.; Candler, G. V. Finite-Rate Oxidation Model for Carbon Surfaces from Molecular Beam Experiments. *AIAA J.* **2017,** *55*, 1644-1658.

[25] Waite, J. H.; Lewis, W. S.; Kasprzak, W. T.; Anicich, V. G.; Block, B. P.; Cravens, T. E.; Fletcher, G. G.; Ip, W.-H.; Luhmann, J. G.; Mcnutt, R. L.; Niemann, H. B.; Parejko, J. K.; Richards, J. E.; Thorpe, R. L.; Walter, E. M.; Yelle, R. V. The Cassini Ion and Neutral Mass Spectrometer (INMS) Investigation. *Space Sci. Rev.* **2004,** *114*, 113-231.

[26] Mahaffy, P. R.; Benna, M.; King, T.; Harpold, D. N.; Arvey, R.; Barciniak, M.; Bendt, M.; Carrigan, D.; Errigo, T.; Holmes, V.; Johnson, C. S.; Kellogg, J.; Kimvilakani, P.; Lefavor, M.; Hengemihle, J.; Jaeger, F.; Lyness, E.; Maurer, J.; Melak, A.; Noreiga, F.; Noriega, M.; Patel, K.; Prats, B.; Raaen, E.; Tan, F.; Weidner, E.; Gundersen, C.; Battel, S.; Block, B. P.; Arnett, K.; Miller, R.; Cooper, C.; Edmonson, C.; Nolan, J. T. The Neutral Gas and Ion Mass Spectrometer on the Mars Atmosphere and Volatile Evolution Mission. *Space Sci. Rev.* **2015,** *195*, 49-73.

[27] Fenselau, C.; Caprioli, R.; Nier, A. O.; Hanson, W. B.; Seiff, A.; McElroy, M. B.; Spencer, N. W.; Duckett, R. J.; Knight, T. C. D.; Cook, W. S.; Biemann, K.; Oro, J.; Toulmin, P.; Orgel, L. E.; Nier, A. O.; Anderson, D. M.; Simmonds, P. G.; Flory, D.; Diaz, A. V.; Rushneck, D. R.; Biller, J. A.; Owen, T.; Biemann, K. Mass Spectrometry in the Exploration of Mars. *J. Mass. Spectrom.* **2003,** *38*, 1-10.

[28] Kay, B. D.; Raymond, T. D.; Coltrin, M. E. Observation of Direct Multiquantum Vibrational Excitation in Gas-Surface Scattering: NH_3 on Au(111). *Phys. Rev. Lett.* **1987,** *59*, 2792-2794.

[29] Kruger, B. C.; Park, G. B.; Meyer, S.; Wagner, R. J. V.; Wodtke, A. M.; Schafer, T. Trapping-Desorption and Direct-Scattering of Formaldehyde at Au(111). *Phys. Chem. Chem. Phys.* **2017,** *19*, 19896-19903.

[30] Meroueh, S. O.; Wang, Y.; Hase, W. L. Direct Dynamics Simulations of Collision- and Surface-Induced Dissociation of N-Protonated Glycine. Shattering Fragmentation. *J. Phys. Chem. A* **2002,** *106*, 9983-9992.

[31] Park, K.; Song, K.; Hase, W. L. An Ab Initio Direct Dynamics Simulation of Protonated Glycine Surface-Induced Dissociation. *Int. J. Mass Spec.* **2007,** *265*, 326-336.

[32] Wang, Y.; Hase, W. L.; Song, K. Direct Dynamics Study of N-Protonated Diglycine Surface-Induced Dissociation. Influence of Collision Energy. *J. Am. Soc. Mass Spectrom.* **2003,** *14*, 1402-1412.

[33] Rosner, D. E.; Allendorf, H. D. High Temperature Oxidation of Carbon by Atomic Oxygen. *Carbon* **1965,** *3*, 153-156.

[34] Bonn, M.; Kleyn, A. W.; Kroes, G. J. Real Time Chemical Dynamics at Surfaces. *Surf. Sci.* **2002,** *500*, 475-499.

[35] Zhang, J.; Garton, D. J.; Minton, T. K. Reactive and Inelastic Scattering Dynamics of Hyperthermal Oxygen Atoms on a Saturated Hydrocarbon Surface. *J. Chem. Phys.* **2002,** *117*, 6239-6251.

[36] Minton, T. K.; Giapis, K. P.; Moore, T. Inelastic Scattering Dynamics of Hyperthermal Fluorine Atoms on a Fluorinated Silicon Surface. *J. Phys. Chem. A* **1997,** *101*, 6549-6555.

[37] Lahaye, R. J. W. E.; Kang, H. Energy Exchange in Structure scattering: a Molecular Dynamics Study for Cs+ from Pt(111). *Surf. Sci.* **2001,** *490*, 327-335.

[38] Alexander, W. A.; Zhang, J.; Murray, V. J.; Nathanson, G. M.; Minton, T. K. Kinematics and Dynamics of Atomic-Beam Scattering on Liquid and Self-Assembled Monolayer Surfaces. *Faraday Discuss.* **2012,** *157*, 355-374.

[39] Rettner, C. T.; Schweizer, E. K.; Mullins, C. B. Desorption and Trapping of Argon at a 2H-W(100) Surface and a Test of the Applicability of Detailed Balance to a Nonequilibrium System. *J. Chem. Phys.* **1989,** *90*, 3800-3813.

[40] Michelsen, H. A.; Auerbach, D. J. A Critical Examination of Data on the Dissociative Adsorption and Associative Desorption of Hydrogen at Copper Surfaces. *J. Chem. Phys.* **1991,** *94*, 7502-7520.

[41] Harris, J. On Vibrationally-Assisted Dissociation of H_2 at Metal Surfaces. *Surf. Sci.* **1989,** *221*, 335-345.

[42] Head□Gordon, M.; Tully, J. C.; Rettner, C. T.; Mullins, C. B.; Auerbach, D. J. On the Nature of Trapping and Desorption at High Surface Temperatures. Theory and Experiments for the Ar–Pt(111) System. *J. Chem. Phys.* **1991,** *94*, 1516-1527.

[43] Majumder, M.; Bhandari, H. N.; Pratihar, S.; Hase, W. L. Chemical Dynamics Simulation of Low Energy N_2 Collisions with Graphite. *J. Phys. Chem. C* **2018,** *122*, 612-623.

[44] Barker, J. A.; Auerbach, D. J. Gas-Surface Interactions and Dynamics; Thermal energy Atomic and Molecular Beam Studies. *Surf. Sci. Rep.* **1984,** *4*, 1-99.

[45] Zecho, T.; Güttler, A.; Sha, X.; Lemoine, D.; Jackson, B.; Küppers, J. Abstraction of D Chemisorbed on Graphite (0001) with Gaseous H Atoms. *Chem. Phys. Lett.* **2002,** *366*, 188-195.

[46] Quintas-Sánchez, E.; Larrégaray, P.; Crespos, C.; Martin-Gondre, L.; Rubayo-Soneira, J.; Rayez, J.-C. Dynamical Reaction Pathways in Eley-Rideal Recombination of Nitrogen from W(100). *J. Chem. Phys.* **2012,** *137*, 064709.

[47] Harris, J.; Kasemo, B. On Precursor Mechanisms for Surface Reactions. *Surf. Sci.* **1981,** *105*, L281-L287.

[48] Harris, P. J. F. Fullerene-Related Structure of Commercial Glassy Carbons. *Philos. Mag.* **2004,** *84*, 3159-3167.

[49] Parker, S. F.; Imberti, S.; Callear, S. K.; Albers, P. W. Structural and Spectroscopic Studies of a Commercial Glassy Carbon. *Chem. Phys.* **2013,** *427*, 44-48.

[50] Lewis, J. C.; Redfern, B.; Cowlard, F. C. Vitreous Carbon as a Crucible Material for Semiconductors. *Solid State Electron.* **1963,** *6*, 251-254.

[51] Cowlard, F. C.; Lewis, J. C. Vitreous Carbon - A New Form of Carbon. *J Mater. Sci.* **1967,** *2*, 507-512.

[52] Rothwell, W. S. Small□Angle X□Ray Scattering from Glassy Carbon. *J. Appl. Phys.* **1968,** *39*, 1840-1845.

[53] Pérez-Mendoza, M.; Domingo-García, M.; López-Garzón, F. J. Modifications Produced by O_2 and CO_2 Plasma Treatments on a Glassy Carbon: Comparison with Molecular Gases. *Carbon* **1999,** *37*, 1463-1474.

[54] Kelemen, S. R.; Freund, H. XPS Characterization of Glassy-Carbon Surfaces Oxidized by O_2, CO_2, and HNO_3. *Energy Fuels* **1988,** *2*, 111-118.

[55] Pan, Z.; Yang, R. T. Strongly Bonded Oxygen in Graphite: Detection by High-Temperature TPD and Characterization. *Ind. Eng. Chem. Res.* **1992,** *31*, 2675-2680.

[56] Sorescu, D. C.; Jordan, K. D.; Avouris, P. Theoretical Study of Oxygen Adsorption on Graphite and the (8,0) Single-walled Carbon Nanotube. *J. Phys. Chem. B* **2001,** *105*, 11227-11232.

[57] Janiak, C.; Hoffmann, R.; Sjovall, P.; Kasemo, B. The Potassium Promoter Function in the Oxidation of Graphite: an Experimental and Theoretical Study. *Langmuir* **1993,** *9*, 3427-3440.

[58] Xu, Y.-J.; Li, J.-Q. The Interaction of Molecular Oxygen with Active Sites of Graphite: a Theoretical Study. *Chem. Phys. Lett.* **2004,** *400*, 406-412.

[59] Zhu, Y.; McBride, J. D.; Hansen, T. A.; Beebe, T. P. Controlled Production of Molecule Corrals Using Cesium Ion Bombardment: A TOF−SIMS, XPS, and STM Study. *J. Phys. Chem. B* **2001,** *105*, 2010-2018.

[60] Walker, P. L.; Rusinko, J. R.; Austin, L. G., Gas Reactions of Carbon. In *Advan. Catal. Relat. Subj.*, Eley, D. D.; Selwood, P. W.; Weisz, P. B., Eds. Academic Press: NY, 1959; Vol. XI, pp 133-221.

[61] Chen, N.; Yang, R. T. *Ab Initio* Molecular Orbital Study of the Unified Mechanism and Pathways for Gas−Carbon Reactions. *J. Phys. Chem. A* **1998,** *102*, 6348-6356.

[62] Montoya, A.; Mondragón, F.; Truong, T. N. Formation of CO Precursors During Char Gasification with O_2, CO_2 and H_2O. *Fuel Proc. Technol.* **2002,** *77–78*, 125-130.

[63] Chu, X.; Schmidt, L. D. Reactions of NO, O_2, H_2O, and CO_2 with the Basal Plane of Graphite. *Surf. Sci.* **1992,** *268*, 325-332.

[64] Morón, V.; Martin-Gondre, L.; Gamallo, P.; Sayos, R. Dynamics of the Oxygen Molecules Scattered from the Graphite (0001) Surface and Comparison with Experimental Data. *J. Phys. Chem. C* **2012,** *116*, 21482-21488.

[65] Kinoshita, H.; Umeno, M.; Tagawa, M.; Ohmae, N. Hyperthermal Atomic Oxygen Beam-Induced Etching of HOPG (0001) Studied by X-Ray Photoelectron Spectroscopy and Scanning Tunneling Microscopy. *Surf. Sci.* **1999,** *440*, 49-59.

[66] Nicholson, K. T.; Minton, T. K.; Sibener, S. J. Spatially Anisotropic Etching of Graphite by Hyperthermal Atomic Oxygen. *J. Phys. Chem. B* **2005,** *109*, 8476-8480.

[67] Nicholson, K. T.; Minton, T. K.; Sibener, S. J. Temperature-Dependent Morphological Evolution of HOPG Graphite Upon Exposure to Hyperthermal O(^{3}P) Atoms. *Prog. Org. Coat.* **2003,** *47*, 443-447.

[68] Morón, V.; Gamallo, P.; Sayós, R. DFT and Kinetics Study of O/O_2 Mixtures Reacting Over a Graphite (0001) Basal Surface. *Theor. Chem. Acc.* **2011,** *128*, 683-694.

[69] Lamoen, D.; Persson, B. N. J. Adsorption of Potassium and Oxygen on Graphite: A Theoretical Study. *J. Chem. Phys.* **1998,** *108*, 3332-3341.

[70] Incze, A.; Pasturel, A.; Chatillon, C. Oxidation of Graphite by Atomic Oxygen: a First-Principles Approach. *Surf. Sci.* **2003,** *537*, 55-63.

[71] Paci, J. T.; Belytschko, T.; Schatz, G. C. Computational Studies of the Structure, Behavior upon Heating, and Mechanical Properties of Graphite Oxide. *J. Phys. Chem. C* **2007,** *111*, 18099-18111.

[72] Poovathingal, S.; Schwartzentruber, T. E.; Srinivasan, S. G.; van Duin, A. C. T. Large Scale Computational Chemistry Modeling of the Oxidation of Highly Oriented Pyrolytic Graphite. *J. Phys. Chem. A* **2013,** *117*, 2692-2703.

[73] Lee, Y. T.; McDonald, J. D.; LeBreton, P. R.; Herschbach, D. R. Molecular Beam Reactive Scattering Apparatus with Electron Bombardment Detector. *Rev. Sci. Instrum.* **1969,** *40*, 1402-1408.

[74] Zhang, J.; Garton, D. J.; Minton, T. K. Reactive and Inelastic Scattering Dynamics of Hyperthermal Oxygen Atoms on a Saturated Hydrocarbon Surface. **2002,** *117*, 6239-6251.

[75] Zhang, J.; Upadhyaya, H. P.; Brunsvold, A. L.; Minton, T. K. Hyperthermal Reactions of O and O_2 with a Hydrocarbon Surface: Direct C−C Bond Breakage by O and H-Atom Abstraction by O_2. *J. Phys. Chem. B* **2006,** *110*, 12500-12511.

[76] Brink, G. O. Electron Bombardment Molecular Beam Detector. *Rev. Sci. Instrum.* **1966,** *37*, 857-860.

[77] Daly, N. R. Scintillation Type Mass Spectrometer Ion Detector. **1960,** *31*, 264-267.

[78] Minton, T. K.; Giapis, K. P.; Moore, T. Inelastic Scattering Dynamics of Hyperthermal Fluorine Atoms on a Fluorinated Silicon Surface. **1997,** *101*, 6549-6555.

[79] Caledonia, G. E.; Krech, R. H.; Green, B. D. A High-Flux Source of Energyetic Oxygen-Atoms for Material Degradation Studies. *AIAA J.* **1987,** *25*, 59-63.

[80] Garton, D. J.; Brunsvold, A. L.; Minton, T. K.; Troya, D.; Maiti, B.; Schatz, G. C. Experimental and Theoretical Investigations of the Inelastic and Reactive Scattering Dynamics of $O(^3P) + D_2$. *J. Phys. Chem. A* **2005,** *110*, 1327-1341.

[81] Garton, D. J.; Minton, T. K.; Maiti, B.; Troya, D.; Schatz, G. C. A Crossed Molecular Beams Study of the $O(^3P)+H_2$ Reaction: Comparison of Excitation Function with Accurate Quantum Reactive Scattering Calculations. *J. Chem. Phys.* **2003,** *118*, 1585-1588.

[82] Troya, D.; Schatz, G. C.; Garton, D. J.; Brunsvold, A. L.; Minton, T. K. Crossed Beams and Theoretical Studies of the $O(^3P)+CH_4 \rightarrow H+OCH_3$ Reaction Excitation Function. *J. Chem. Phys.* **2004,** *120*, 731-739.

[83] SPI http://www.2spi.com/catalog/mounts/glassy-vitreous-carbon-glass-substrates.php (accessed March, 2015).

[84] Gibson, K. D.; Sibener, S. J.; Upadhyaya, H. P.; Brunsvold, A. L.; Zhang, J.; Minton, T. K.; Troya, D. Hyperthermal Ar Atom Scattering from a C(0001) Surface. *J. Chem. Phys.* **2008,** *128*, 224708.

[85] Garton, D. J.; Minton, T. K.; Alagia, M.; Balucani, N.; Casavecchia, P.; Gualberto Volpi, G. Reactive Scattering of Ground-State and Electronically Excited Oxygen Atoms on a Liquid Hydrocarbon Surface. *Faraday Discuss.* **1997,** *108*, 387-399.

[86] Garton, D. J.; Minton, T. K.; Alagia, M.; Balucani, N.; Casavecchia, P.; Gualberto Volpi, G. Comparative Dynamics of $Cl(^2P)$ and $O(^3P)$ Interactions with a Hydrocarbon Surface. *J. Chem. Phys.* **2000,** *112*, 5975-5984.

[87] Rettner, C. T.; Auerbach, D. J.; Tully, J. C.; Kleyn, A. W. Chemical Dynamics at the Gas−Surface Interface. *J. Phys. Chem.* **1996,** *100*, 13021-13033.

[88] Rettner, C. T.; Barker, J. A.; Bethune, D. S. Angular and Velocity Distributions Characteristic of the Transition between the Thermal and Structure Regimes of Gas-Surface Scattering. **1991,** *67*, 2183-2186.

[89] Rettner, C. T.; Auerbach, D. J. Distinuguishing the Direct and Indirect Products of a Gas-Surface Reaction. *Science* **1994,** *263*, 365-367.

[90] Marton, D.; Boyd, K. J.; Lytle, T.; Rabalais, J. W. Near-Threshold Ion-Induced Defect Production in Graphite. *Phys. Rev. B* **1993,** *48*, 6757-6766.

[91] Pratihar, S.; Kohale, S. C.; Yang, L.; Manikandan, P.; Gibson, K. D.; Killelea, D. R.; Yuan, H.; Sibener, S. J.; Hase, W. L. Chemical Dynamics Simulations of High Energy Xenon Atom Collisions with the {0001} Surface of Hexagonal Ice. *J. Phys. Chem. C* **2013,** *117*, 2183-2193.

[92] King, M. E.; Fiehrer, K. M.; Nathanson, G. M.; Minton, T. K. Effects of Thermal Roughening on the Angular Distributions of Trapping and Scattering in Gas−Liquid Collisions. **1997,** *101*, 6556-6561.

[93] Hurst, J. E.; Wharton, L.; Janda, K. C.; Auerbach, D. J. Direct Inelastic Scattering Ar from Pt(111). *J. Chem. Phys.* **1983,** *78*, 1559-1581.

[94] Yan, T.; Hase, W. L. Origin of the Boltzmann Translational Energy Distribution in the Scattering of Hyperthermal Ne Atoms off a Self-Assembled Monolayer. *Phys. Chem. Chem. Phys.* **2000,** *2*, 901-910.

[95] Hunt, J.; Ferrari, A.; Lita, A.; Crosswhite, M.; Ashley, B.; Stiegman, A. E. Microwave-Specific Enhancement of the Carbon–Carbon Dioxide (Boudouard) Reaction. *J. Phys. Chem. C* **2013,** *117*, 26871-26880.

[96] Ergun, S. Kinetics of the Reaction of Carbon with Carbon Dioxide. *J. Phys. Chem.* **1956,** *60*, 480-485.

[97] Mahzari, M.; Braun, R. D.; White, T. R.; Bose, D. Inverse Estimation of the Mars Science Laboratory Entry Aeroheating and Heatshield Response. *J. Spacecr. Rockets* **2015,** *52*, 1203-1216.

[98] Milos, F. S.; Chen, Y.-K. Ablation and Thermal Response Property Model Validation for Phenolic Impregnated Carbon Ablator. *J. Spacecr. Rockets* **2010,** *47*, 786-805.

[99] Yoshida, A.; Hishiyama, Y. Electron Channeling Effect on Highly Oriented Graphites–Size Evaluation and Oriented Mapping of Crystals. *J. Mater. Res.* **1992,** *7*, 1400-1405.

[100] Baskin, Y.; Meyer, L. Lattice Constants of Graphite at Low Temperatures. *Phys. Rev.* **1955,** *100*, 544.

[101] Takeo, I.; Hiroaki, S.; Hiroyuki, N. Observation of Surface Corrugation of Highly Oriented Pyrolytic Graphite by Scanning Tunneling Microscope in Air. *Jpn. J. Appl. Phys.* **1992,** *31*, 1441.

[102] Murray, V. J.; Pilinski, M. D.; Smoll, E. J.; Qian, M.; Minton, T. K.; Madzunkov, S. M.; Darrach, M. R. Gas–Surface Scattering Dynamics Applied to Concentration of Gases for Mass Spectrometry in Tenuous Atmospheres. *J. Phys. Chem. C* **2017,** *121*, 7903-7922.

[103] Walker Jr, P. L.; Rusinko Jr, F.; Austin, L. G., Gas Reactions of Carbon. In *Advances in Catalysis*, D.D. Eley, P. W. S.; Paul, B. W., Eds. Academic Press: 1959; Vol. Volume 11, pp 133-221.

[104] Barber, M.; Evans, E. L.; Thomas, J. M. Oxygen Chemisorption on the Basal Faces of Graphite: an XPS Study. *Chem. Phys. Lett.* **1973,** *18*, 423-425.

[105] Morón, V.; Martin-Gondre, L.; Crespos, C.; Larregaray, P.; Gamallo, P.; Sayós, R. Classical Dynamics Study of Atomic Oxygen Over Graphite (0001) aith New Interpolated and Analytical Potential Energy Surfaces. *Comp. Theor. Chem.* **2012,** *990*, 132-143.

[106] Sun, T.; Yao, X.; Fabris, S. Effects of Thermal Electronic Excitations on the Diffusion of Oxygen Adatoms on Graphene. *J. Phys. Chem. A* **2016,** *120*, 2607-2613.

[107] Rosner, D. E.; D., A. H. Comparative Studies of Attack of Pyrolytic and Isotropic Graphite by Atomic and Molecular Oxygen. *AIAA J.* **1968,** *6*, 650-654.

[108] Murray, V. J.; Marshall, B. C.; Woodburn, P. J.; Minton, T. K. Inelastic and Reactive Scattering Dynamics of Hyperthermal O and O_2 on Hot Vitreous Carbon Surfaces. *J. Phys. Chem. C* **2015,** *119*, 14780-14796.

[109] Dempsey, L. P.; Faust, J. A.; Nathanson, G. M. Near-Interfacial Halogen Atom Exchange in Collisions of Cl_2 with 2.7 M NaBr–Glycerol. *J. Chem. Phys. B* **2012,** *116*, 12306-12318.

[110] Quintas-Sánchez, E.; Crespos, C.; Larrégaray, P.; Rayez, J.-C.; Martin-Gondre, L.; Rubayo-Soneira, J. Surface Temperature Effects on the Dynamics of N_2 Eley-Rideal Recombination on W(100). *J. Chem. Phys.* **2013,** *138*, 024706.

[111] King, M. E.; Saecker, M. E.; Nathanson, G. M. The Thermal Roughening of Liquid Surfaces and its Effect on Gas–Liquid Collisions. *J. Chem. Phys.* **1994,** *101*, 2539-2547.

[112] Steurer, P.; Wissert, R.; Thomann, R.; Mülhaupt, R. Functionalized Graphenes and Thermoplastic Nanocomposites Based upon Expanded Graphite Oxide. *Macromol. Rapid Commun.* **2009,** *30*, 316-327.

[113] Gråsäs, E.; Knudsen, J.; Schröder, U. A.; Gerber, T.; Busse, C.; Arman, M. A.; Schulte, K.; Andersen, J. N.; Michely, T. Oxygen Intercalation under Graphene on Ir(111): Energetics, Kinetics, and the Role of Graphene Edges. *ACS Nano* **2012,** *6*, 9951-9963.

[114] Blume, R.; Kidambi, P. R.; Bayer, B. C.; Weatherup, R. S.; Wang, Z.-J.; Weinberg, G.; Willinger, M.-G.; Greiner, M.; Hofmann, S.; Knop-Gericke, A.; Schlogl, R. The Influence of Intercalated Oxygen on the Properties of Graphene on Polycrystalline Cu Under Various Environmental Conditions. *Phys. Chem. Chem. Phys.* **2014,** *16*, 25989-26003.

[115] Incze, A.; Pasturel, A.; Chatillon, C. First-Principles Study of the Atomic Oxygen Adsorption on the (0001) Graphite Surface and Dissolution. *Appl. Surf. Sci.* **2001,** *177*, 226-229.

[116] Galparsoro, O.; Juaristi, J. I.; Crespos, C.; Alducin, M.; Larrégaray, P. Stereodynamics of Diatom Formation through Eley–Rideal Abstraction. *J. Phys. Chem. C* **2017,** *121*, 19849-19858.

[117] Blanco-Rey, M.; Díaz, E.; Bocan, G. A.; Díez Muiño, R.; Alducin, M.; Juaristi, J. I. Efficient N_2 Formation on Ag(111) by Eley–Rideal Recombination of Hyperthermal Atoms. *J. Phys. Chem. Lett.* **2013,** *4*, 3704-3709.

[118] Ueta, H.; Gleeson, M. A.; Kleyn, A. W. The Interaction of Hyperthermal Nitrogen with N-Covered Ag(111). *J. Chem. Phys.* **2011,** *135*, 074702.

[119] Pierson, H. O., Graphite Structure and Properties. In *Handbook of Carbon, Graphite, Diamonds and Fullerenes*, William Andrew Publishing: Oxford, 1993; pp 43-69.

[120] Jiang, H. Dynamics of Hydrogen Atoms Scattering from Surfaces. The Georg-August University of Göttingen, December 2016.

[121] Jaramillo-Botero, A.; An, Q.; Cheng, M.-J.; Goddard, W. A.; Beegle, L. W.; Hodyss, R. Hypervelocity Impact Effect of Molecules from Enceladus' Plume and Titan's Upper Atmosphere on NASA's Cassini Spectrometer from Reactive Dynamics Simulation. *Phys. Rev. Lett.* **2012,** *109*, 213201.

[122] Teolis, B. D.; Perry, M. E.; Magee, B. A.; Westlake, J.; Waite, J. H. Detection and Measurement of Ice Grains and Gas Distribution in the Enceladus Plume by Cassini's Ion Neutral Mass Spectrometer. *J. Geophys. Res. Space* **2010,** *115*, A09222.

[123] Smith, J. N.; Saltsburg, H. Atomic□Beam Scattering from Epitaxially Grown Gold Films. *J. Chem. Phys.* **1964,** *40*, 3585-3591.

[124] West, L. A.; Kozak, E. I.; Somorjai, G. A. Molecular Beam Scattering from Single Crystal Surfaces under Ultrahigh Vacuum Conditions. *J. Vac. Sci. Technol.* **1971,** *8*, 430-436.

[125] Butler, D. A.; Berenbak, B.; Stolte, S.; Kleyn, A. W. Elastic Scattering in a Reactive Environment: NO on Ru(0001)−(1×1)H. *Phys. Rev. Lett.* **1997,** *78*, 4653-4656.

[126] Murray, V. J.; Marshall, B. C.; Woodburn, P. J.; Minton, T. K. Inelastic and Reactive Scattering Dynamics of Hyperthermal O and O_2 on Hot Vitreous Carbon Surfaces. *J. Phys. Chem. C* **2015,** *119*, 14780-14796.

[127] Riedmüller, B.; Ciobîcă, I. M.; Papageorgopoulos, D. C.; Berenbak, B.; van Santen, R. A.; Kleyn, A. W. The Dynamic Interaction of CO with Ru(0001) in the Presence of Adsorbed CO and Hydrogen. *Surf. Sci.* **2000,** *465*, 347-360.

[128] Che, L.; Gardenghi, D. J.; Szilagyi, R. K.; Minton, T. K. Production of a Biomimetic Fe-(I)-S Phase on Pyrite by Atomic Hydrogen Beam Surface Reactive Scattering. *Langmuir* **2011,** *27*, 6814-6821.

[129] Leger, L. J. *Oxygen Atom Reaction with Shuttle Materials at Orbital Altitutes*; 1982.

[130] Silverman, E. M. *Space Environmental Effects on Spacecraft: LEO Materials Selection Guide, Part 1*; 1995.

[131] Minton, T. K.; Garton, D. J., Dynamics of Atomic-Oxygen-Induced Polymer Degradation in Low Earth Orbit. In *Chemical Dynamics in Extreme Environments*, Dressler, R. A., Ed. World Scientific: Singapore, 2001; pp 420-489.

[132] Garton, D. J.; Brunsvold, A. L.; Minton, T. K.; Troya, D.; Maiti, B.; Schatz, G. C. Experimental and Theoretical Investigations of the Inelastic and Reactive Scattering Dynamics of $O(^3P)$ + D_2. *J. Phys. Chem. A* **2005,** *110*, 1327-1341.

[133] Outka, D. A.; Madix, R. J. Broensted Basicity of Atomic Oxygen on the Gold(110) Surface: Reactions with Methanol, Acetylene, Water, and Ethylene. *J. Am. Chem. Soc.* **1987,** *109*, 1708-1714.

[134] Outka, D. A.; Madix, R. J. Acid-base and Nucleophilic Chemistry of Atomic Oxygen on the Au(110) Surface: Reactions with Formic Acid and Formaldehyde. *Surf. Sci.* **1987,** *179*, 361-376.

[135] Syomin, D.; Koel, B. E. IRAS Studies of the Orientation of Acetone Molecules in Monolayer and Multilayer Films on Au(111) Surfaces. *Surf. Sci.* **2002,** *498*, 53-60.

[136] Meyer, R.; Lemire, C.; Shaikhutdinov, S. K.; Freund, H.-J. Surface Chemistry of Catalysis by Gold. *Gold Bull.* **2004,** *37*, 72-124.

[137] Tsai, H.; Hu, E.; Perng, K.; Chen, M.; Wu, J.-C.; Chang, Y.-S. Instability of Gold Oxide Au_2O_3. *Surf. Sci.* **2003,** *537*, L447-L450.

[138] Canning, N. D. S.; Outka, D.; Madix, R. J. The Adsorption of Oxygen on Gold. *Surf. Sci.* **1984,** *141*, 240-254.

[139] Neergaard Waltenburg, H.; Yates, J. T. Surface Chemistry of Silicon. *Chem. Rev.* **1995,** *95*, 1589-1673.

[140] Kisa, M.; Minton, T. K.; Yang, J. C. Structural Comparisons of SiO_x and Si/SiO_x Formed by the Exposure of Silicon (100) to Molecular Oxygen and to Hyperthermal Atomic Oxygen. *J. Appl. Phys.* **2005,** *97*, 023520.

[141] Masahito, T.; Kumiko, Y.; Nobuo, O.; Hiroshi, K.; Masataka, U. Oxidation Properties of Hydrogen-Terminated Si(001) Surfaces Following Use of a Hyperthermal Broad Atomic Oxygen Beam at Low Temperatures. *Jpn. J. Appl. Phys.* **2001,** *40*, 6152.

[142] Tagawa, M.; Matsumoto, K.; Doi, H.; Yokota, K. Computer Simulation and its Experimental Verification of Atomic Oxygen Concentration. *J. Spacecr. Rockets* **2006,** *43*, 999-1003.

[143] Tagawa, M.; Doi, H.; Yokota, K. Atomic Oxygen Concentrators for Material Exposure Acceleration Tests in Low Earth Orbit. *J. Spacecr. Rockets* **2009,** *46*, 226-229.

[144] Gibson, K. D.; Sibener, S. J.; Upadhyaya, H. P.; Brunsvold, A. L.; Zhang, J.; Minton, T. K.; Troya, D. Hyperthermal Ar Atom Scattering from a C(0001) Surface. *J. Chem. Phys.* **2008,** *128*, 224708.

[145] Chu, X.; Schmidt, L. D. Reactions of NO, O_2, H_2O, and CO_2 with the Basal Plane of Graphite. *Surf. Sci.* **1992,** *268*, 325-332.

[146] Arnold, G. S.; Peplinski, D. R. Reaction of Atomic Oxygen with Vitreous Carbon - Laboratory and STS-5 Data Comparisons. *AIAA J.* **1985,** *23*, 976-977.

[147] Park, C. Effects of Atomic Oxygen on Graphite Ablation. *AIAA J.* **1976,** *14*, 1640-1642.

[148] Paci, J. T.; Upadhyaya, H. P.; Zhang, J.; Schatz, G. C.; Minton, T. K. Theoretical and Experimental Studies of the Reactions between Hyperthermal $O(^3P)$ and Graphite: Graphene-Based Direct Dynamics and Beam-Surface Scattering Approaches. *J. Phys. Chem. A* **2009,** *113*, 4677-4685.

[149] Lee, Y. T.; McDonald, J. D.; LeBreton, P. R.; Herschbach, D. R. Molecular Beam Reactive Scattering Apparatus with Electron Bombardment Detector. *Rev. Sci. Instrum.* **1969,** *40*, 1402-1408.

[150] Brink, G. O. Electron Bombardment Molecular Beam Detector. *Rev. Sci. Instrum.* **1966,** *37*, 857-860.

[151] Daly, N. R. Scintillation Type Mass Spectrometer Ion Detector. *Rev. Sci. Instrum.* **1960,** *31*, 264-267.

[152] Marshall, B. C.; Smoll, E. J.; Purcell, S. M.; Costen, M. L.; McKendrick, K. G.; Minton, T. K. Scattering Dynamics of Oxygen Atoms on Imidazolium Tetrafluoroborate Ionic Liquid Surfaces: Dependence on Alkyl Chain Length. *J. Phys. Chem. C* **2016,** *120*, 12472-12483.

[153] Troya, D.; Schatz, G. C.; Garton, D. J.; Brunsvold, A. L.; Minton, T. K. Crossed Beams and Theoretical Studies of the $O(^3P)+CH_4 \rightarrow H+OCH_3$ Reaction Excitation Function. *J. Chem. Phys.* **2004,** *120*, 731-739.

[154] Garton, D. J.; Minton, T. K.; Maiti, B.; Troya, D.; Schatz, G. C. A Crossed Molecular Beams Study of the $O(^3P)+H_2$ Reaction: Comparison of Excitation Function with Accurate Quantum Reactive Scattering Calculations. *J. Chem. Phys.* **2003,** *118*, 1585-1588.

[155] Pilinski, M. D. Dynamic Gas-Surface Interaction Modeling for Satellite Aerodynamic Computations. Ph.D Dissertation, University of Colorado, Boulder, CO, 2011.

[156] Logan, R. M.; Stickney, R. E. Simple Classical Model for the Scattering of Gas Atoms from a Solid Surface. *J. Chem. Phys.* **1966,** *44*, 195-201.

[157] Schamberg, R. *Analytic Representation of Surface Interaction for Free Molecule Flow with Application to Drag of Various Bodies*; Santa Monica, Calif., 1959; pp 12-11 to 12-41.

[158] Cook, G. E. Satellite Drag Coefficients. *Planet. Space Sci.* **1965,** *13*, 929-946.

[159] Cercignani, C.; Lampis, M. Kinetic Models for Gas-Surface Interactions. *Transp. Theory Stat. Phys.* **1971,** *1*, 101-114.

[160] Nocilla, S. In *On the Interaction between Stream and Body in Free-Molecule Flow*, Proceedings of the Second International Symposium University of California, Berkeley, 1961; Talbot, L., Ed. Academic Press: University of California, Berkeley, 1960; pp 169-208.

[161] Masel, R. I., *Principles of Adsorption and Reaction on Solid Surfaces*. John Wiley and Sons, Inc: New York, NY, 1996.

[162] Pilinski, M. D.; Argrow, B. M. Aerodynamic Analysis Based on Challenging Minisatellite Payload Satellite Lift-to-Drag Measurements. *J. Spacecr. Rockets* **2013,** *50*, 1162-1170.

[163] Schaaf, S. A.; Chambré, P. L., *Flow of Rarefied Gases*. Princeton University Press: Princeton, NJ, 1961.

[164] Rettner, C. T.; Schweizer, E. K.; Mullins, C. B. Desorption and Trapping of Argon at a 2H–W(100) Surface and a Test of the Applicability of Detailed Balance to a Nonequilibrium System. *J. Chem. Phys.* **1989,** *90*, 3800-3813.

[165] Engel, T.; Rieder, K. H., *Structural Studies of Surfaces with Atomic and Molecular Beam Diffraction*. Springer Berlin Heidelberg: Berlin, Heidelberg, 1982; p 55-180.

[166] Moe, K.; Moe, M. M. Gas–Surface Interactions and Satellite Drag Coefficients. *Planet. Space Sci.* **2005,** *53*, 793-801.

[167] Pilinski, M. D.; Argrow, B. M.; Palo, S. E.; Bowman, B. R. Semi-Empirical Satellite Accommodation Model for Spherical and Randomly Tumbling Objects. *J. Spacecr. Rockets* **2013,** *50*, 556-571.

[168] Pippin, H. G. *Final Report on Analysis of Boeing Specimens Flown on the Effects of Space Environment on Materials Experiment*; 1999.

[169] Blanchard, R. C.; Wilmoth, R. G.; Lebeau, G. J. Rarefied-Flow Transition Regime Orbiter Aerodynamic Acceleration Flight Measurements. *J. Spacecr. Rockets* **1997,** *34*, 8-15.

[170] Lake, L. R.; Nier, A. O. Loss of Atomic Oxygen in Mass Spectrometer Ion Sources. *J. Geophys. Res.* **1973,** *78*, 1645-1653.

[171] Rettner, C. T.; Schweizer, E. K.; Stein, H. Dynamics of the Chemisorption of N_2 on W(100): Precursor□Mediated and Activated Dissociation. *J. Chem. Phys.* **1990,** *93*, 1442-1454.

[172] Raukema, A.; Dirksen, R. J.; Kleyn, A. W. Probing the (Dual) Repulsive Wall in the Interaction of O_2, N_2, and Ar with the Ag(111) Surface. *J. Chem. Phys.* **1995,** *103*, 6217-6231.

[173] Berenbak, B.; Zboray, S.; Riedmuller, B.; Papageorgopoulos, D. C.; Stolte, S.; Kleyn, A. W. Ar Scattering on Ru (0001): a Comparison to the Washboard Model. *Phys. Chem. Chem. Phys.* **2002,** *4*, 68-74.

[174] Grimmelmann, E. K.; Tully, J. C.; Cardillo, M. J. Hard□Cube Model Analysis of Gas□Surface Energy Accommodation. *J. Chem. Phys.* **1980,** *72*, 1039-1043.

[175] Goodman, F. O.; Wachman, H. Y., *Dynamics of Gas-Surface Scattering*. Academic: New York, 1976.

[176] Watanabe, Y.; Yamaguchi, H.; Hashinokuchi, M.; Sawabe, K.; Maruyama, S.; Matsumoto, Y.; Shobatake, K. Energy Transfer in Hyperthermal Xe-Graphite Surface Scattering. *Eur. Phys. J. D* **2006,** *38*, 103-109.

[177] Junepyo, O.; Takahiro, K.; Keitaro, A.; Yoshihiko, S.; Junji, N.; Hayes, W. W.; Manson, J. R. Scattering of CO and N_2 Molecules by a Graphite Surface. *J. Phys. Condens. Matter* **2012,** *24*, 354001.

[178] Mehta, N. A.; Levin, D. A.; Murray, V. J.; Minton, T. K. Study Of Non-Reactive Scattering from Graphene using Molecular Beam Experiments and Molecular Dynamics. *AIP Conf. Proc.* **2016,** *1786*, 100003.

[179] King, M. E.; Fiehrer, K. M.; Nathanson, G. M.; Minton, T. K. Effects of Thermal Roughening on the Angular Distributions of Trapping and Scattering in Gas−Liquid Collisions. *J. Phys. Chem. A* **1997,** *101*, 6556-6561.

[180] Mehta, N. A.; Levin, D. A. Molecular-Dynamics-Derived Gas–Surface Models for Use in Direct-Simulation Monte Carlo. *J. Thermophys. Heat Transfer* **2017**, 1-15.

[181] Mehta, N. A.; Levin, D. A.; Murray, V. J.; Xu, C.; Minton, T. K. Non-Reactive Scattering of N_2 from Layered Graphene using Molecular Beam Experiments and Molecular Dynamics. *J. Phys. Chem. C* **2018,** *Under Review*, March 1, 2018.

[182] Rettner, C. T.; Mullins, C. B.; Bethune, D. S.; Auerbach, D. J.; Schweizer, E. K.; Weinberg, W. H. Molecular Beam Studies of Trapping Dynamics. *J. Vac. Sci. Technol. A* **1990,** *8*, 2699-2704.

[183] Gibson, K. D.; Sibener, S. J. Scattering Dynamics, Survival, and Dispersal of Dimethyl Methylphosphonate Interacting with the Surface of Multilayer Graphene. *J. Phys. Chem. A* **2016,** *120*, 4863-4871.

[184] Rahaman, A.; Zhou, J. B.; Hase, W. L. Effects of Projectile Orientation and Surface Impact Site on the Efficiency of Projectile Excitation in Surface-Induced Dissociation: Protonated Diglycine Collisions with Diamond {111}. *Int. J. Mass Spectrom.* **2006,** *249-250*, 321-329.

[185] Liang, S.; Hemberger, P.; Neisius, N. M.; Bodi, A.; Grützmacher, H.; Levalois-Grützmacher, J.; Gaan, S. Elucidating the Thermal Decomposition of Dimethyl Methylphosphonate by Vacuum Ultraviolet (VUV) Photoionization: Pathways to the PO Radical, a Key Species in Flame-Retardant Mechanisms. *Chem. Eur. J.* **2015,** *21*, 1073-1080.

[186] Andersson, M. B.; Petterson, J. B. C. Vibrational Excitation of SF_6 Scattering from Graphite. *Chem. Phys. Lett.* **1996,** *250*, 555-559.

[187] Andersson, M. B.; Pettersson, J. B. C.; Marković, N. Vibrational Excitation of CF_3Br Scattering from Graphite. *Surf. Sci.* **1997,** *384*, L880-L885.

[188] Stinnett, J. A.; Madix, R. J.; Tully, J. C. Stochastic Simulations of the Trapping of Ethane on Pt(111) from a Realistic Potential: the Roles of Energy Transfer Processes and Surface Corrugation. *J. Chem. Phys.*
1996, *104*, 3134-3142.

[189] Hurkmans, A.; Overbosch, E. G.; Los, J. Trapping Probabilities and Desorption Energies of Alkali Atoms on a Clean and an Oxygen Covered Tungsten (110) Surface. *Surf. Sci.* **1976,** *59*, 488-508.

[190] Hurkmans, A.; Overbosch, E. G.; Los, J. The Trapping of K and Na Atoms by a Clean W(110) Surface Trajectory Calculations. *Surf. Sci.* **1977,** *62*, 621-638.

[191] Luo, Y. R., *Handbook of Bond Dissociation Energies in Organic Compounds*. CRC Press: Baca Raton, Fl, 2003.

[192] Plimpton, S. Fast Parallel Algorithms for Short-Range Molecular Dynamics. *J. Comput. Phys.* **1995,** *117*, 1-19.

[193] Aktulga, H. M.; Fogarty, J. C.; Pandit, S. A.; Grama, A. Y. Parallel Reactive Molecular Dynamics: Numerical Methods and Algorithmic Techniques. *Parallel Comput.* **2012,** *38*, 245-259.

[194] Kamat, A. M.; van Duin, A. C. T.; Yakovlev, A. Molecular Dynamics Simulations of Laser-Induced Incandescence of Soot Using an Extended ReaxFF Reactive Force Field. *J. Chem. Phys. A* **2010,** *114*, 12561-12572.

[195] Burke, D. J.; Puletti, F.; Woods, P. M.; Viti, S.; Slater, B.; Brown, W. A. Adsorption and Thermal Processing of Glycolaldehyde, Methyl Formate, and Acetic Acid on Graphite at 20 K. *J. Phys. Chem. A* **2015,** *119*, 6837-6849.